University of Nottingham



School of Mathematical Sciences

Quantitative analysis of fluorescence recovery after photobleaching and fluorescence loss in photobleaching, with a focus on the dynamics of yes-associated protein

Daniel Williamson

A thesis submitted to the University of Nottingham for the degree of

Doctor of Philosophy

August 2020

Abstract

Yes-associated protein (YAP) is a transcription regulator with a highly significant role in a wide variety of cancers. When YAP is transported into the cell nucleus, it activates a programme of genes which promote cell proliferation and confer resistance to regulatory signals that normally limit tissue growth. YAP has been shown to promote malignancy and metastasis in tumours and is thus the object of much current biological and medical research. The aim of this thesis is to investigate quantitatively the factors which cause excessive nuclear accumulation of YAP in cancer-associated fibroblasts. To this end, we utilise data from two common experimental techniques, fluorescence recovery after photobleaching (FRAP) and fluorescence loss in photobleaching (FLIP).

We develop the theory of FRAP, deriving several new (to our knowledge) approximation formulas. We establish conditions to ensure the viability of parameter estimation and propose a fitting protocol which can theoretically produce, at the very least, estimates of the ratio of bound to unbound molecules at chemical equilibrium. We implement a numerical cell simulation which we then fit to empirical FRAP data from fibroblast nuclei.

FLIP can be used to estimate the rate of shuttling between the nucleus and cytoplasm. This process depends on the 3D geometry of the nuclear membrane, yet often only 2D imaging data are available. We propose a simple ODE model which can account for 3D effects when only 2D data are available. We also implement a numerical FLIP model which incorporates active transport across the nuclear membrane and cell motion during the experiment. Using both the ODE and PDE FLIP models, we are able to investigate quantitatively YAP nucleocytoplasmic shuttling, and the ratio of bound to unbound YAP molecules at equilibrium in fibroblast cytoplasm.

Combing FRAP and FLIP results, we quantify the differences in YAP regulation between normal fibroblasts (NFs) and cancer-associated fibroblasts (CAFs). We find that, in order of importance, increased nuclear import, reduced nuclear export, weaker binding reactions in the cytoplasm and stronger binding reactions in the nucleus all contribute to the localisation of YAP to the nucleus in CAFs. Though YAP is the immediate focus of the thesis, the methodology we develop could be applied to a wide variety of other proteins.

Acknowledgements

I wish to thank my supervisors, John King and Reuben O'Dea, for all of their support and guidance over the past few years. I would also like to thank Rob Jenkins and Erik Sahai from the Crick Institute for much helpful input and for providing experimental data for the thesis.

CONTENTS

1 INTRODUCTION 1

1.1 Fluorescence recovery after photobleaching . . . 3

1.1.1 Laser intensity profile . . . 5

1.1.2 Photobleaching . . . 6

1.1.3 Static laser FRAP . . . 8

1.1.4 Scanning laser FRAP . . . 9

1.2 FRAP mathematical analysis . . . 12

1.2.1 Diffusion . . . 13

1.2.2 Scanning FRAP . . . 17

1.2.3 3D FRAP . . . 19

1.2.4 Multi-photon excitation . . . 23

1.2.5 Reaction-diffusion . . . 27

1.2.6 Reaction-diffusion approximations . . . 30

1.2.7 Exponential models . . . 32

1.2.8 Numerical model analysis . . . 33

1.2.9 Integral transform methods . . . 35

1.2.10 Other uses of FRAP . . . 36

1.2.11 Complications . . . 39

1.3 Fluorescence loss in photobleaching . . . 39

1.4 FLIP mathematical analysis . . . 41

1.4.1 ODE modelling . . . 42

1.4.2 PDE modelling . . . 43

1.5 Parameter estimation/non-linear optimisation . . . 44

1.5.1 Nonlinear least squares . . . 44

1.5.2 Maximum likelihood . . . 45

1.5.3 Variance methods . . . 46

1.5.4 Maximum entropy methods 46
1.5.5 Fisher information and parameter estimability 48
1.6 YAP biology 49
1.6.1 Protein localisation 50
1.6.2 Contact inhibition of proliferation and mechanotransduction 50
1.6.3 YAP at the roots of cancer 51
1.6.4 YAP and contact inhibition 52
1.6.5 Mechanotransduction and the ECM 54
1.6.6 Wnt signalling and heat shock factors 55
1.6.7 YAP feedback loop in fibroblasts 56
1.6.8 Summary of YAP biology 57

2 MATHEMATICAL ANALYSIS OF FLUORESCENCE RECOVERY AFTER PHOTOBLEACHING 59
2.1 Mathematical model 60
2.1.1 The FRAP forward reaction rate 61
2.2 Two-species reaction-diffusion model 62
2.2.1 Radial symmetry 64
2.2.2 Asymptotic analysis 66
2.2.3 Rapid equilibration ($\eta \gg 1$) 66
2.2.4 Intermediate equilibration ($\eta = O(1)$) 74
2.2.5 Slow equilibration ($\eta \ll 1$) 77
2.2.6 Parameter identifiability in static laser FRAP 83
2.2.7 Parameter identifiability scanning laser FRAP 84
2.3 General results for multi-species model 86
2.3.1 Linearity 87
2.3.2 Balanced reaction rates 88
2.3.3 High mobility 88
2.3.4 Effective diffusion 90
2.4 Multi-species sequential reactions 91

2.4.1 Three disparate diffusive time scales 92
2.4.2 Two highly mobile species 95
2.4.3 Two immobile species 96
2.4.4 Determining the order of reaction 97
2.5 Multi-species parallel reactions 100
2.5.1 Rapid equilibration 101
2.6 Chapter summary 102

3 NUMERICAL ANALYSIS OF FLUORESCENCE RECOVERY AFTER PHOTOBLEACHING AND A GENERAL PARAMETER FITTING SCHEME 103
3.1 Methodology 104
3.1.1 Parameter generation 106
3.1.2 Procedure summary 107
3.2 Computational results 108
3.3 Model uncertainty and multiple curve fitting 113
3.3.1 The value of multiple recovery fitting 115
3.4 Regime identification 116
3.4.1 The effect of varying η 117
3.4.2 The effect of varying κ 120
3.4.3 The quasi-diffusive regimes, $\eta \ll 1$, $\kappa \gg 1$ and $\kappa \ll 1$. 123
3.5 General fitting algorithm 124
3.6 Chapter summary 127

4 APPLYING NUMERICAL PARAMETER FITTING TO EMPIRICAL FLUORESCENCE RECOVERY AFTER PHOTOBLEACHING DATA 129
4.1 Mathematical model 130
4.1.1 The bleaching/imaging laser $I(\mathbf{x}, t)$ 132
4.1.2 Parameter estimation 133
4.2 Numerical methods 134
4.3 The bleaching laser $I_{\text{pre}}(\mathbf{x})$ 135
4.4 Fitting preliminaries 140
4.4.1 Identifying the active domain 141

4.4.2 Passive bleaching $I_{\text{post}}(\mathbf{x})$ . . . 143
4.4.3 The initial condition, $w_{\text{eq}}(\mathbf{x})$ . . . 145
4.5 Biological context and experimental data . . . 147
4.6 Main results . . . 156
4.7 Evaluating model limitations . . . 163
4.7.1 Transfer of protein across the nuclear membrane. . . . 163
4.7.2 Cell motion . . . 165
4.8 Chapter summary . . . 166

5 FLUORESCENCE LOSS IN PHOTOBLEACHING 168
5.1 FLIP model . . . 170
5.2 Asymptotic analysis of the FLIP model . . . 173
5.2.1 Nucleus shape and the surface area to volume ratio . . 177
5.3 Numerical simulation of the FLIP model . . . 179
5.3.1 Compensating for cell motion . . . 179
5.3.2 The bleaching laser . . . 182
5.3.3 The simulation mesh . . . 184
5.3.4 Finite element matrices . . . 186
5.3.5 Example simulations . . . 189
5.4 Methodology . . . 192
5.5 Results . . . 194
5.5.1 Concordance between FRAP and FLIP . . . 197
5.6 Chapter summary . . . 198

6 CONCLUSION 200
6.1 Mathematical analysis of FRAP . . . 200
6.2 Numerical analysis of FRAP and a general parameter fitting scheme . . . 201
6.3 Investigating YAP with FRAP model fitting . . . 201
6.4 Fluorescence loss in photobleaching . . . 202
6.5 Summary of empirical results: the difference between CAFs and NFs . . . 203

6.6 Possibilities for future work 204

1

INTRODUCTION

Yes-associated protein 1 (hereafter referred to as YAP) is the focus of intense interest given its remarkable biological properties in development, tissue homeostasis and cancer. When localised to the nucleus, YAP activates a programme of genes which boost cell growth, mitosis, and resistance to apoptosis [1–4]. It also possesses the ability to un-differentiate cells [5–7]. YAP is essential in embryonic development, organ growth and wound healing [5,8–10]. Yet its ability to promote tissue growth is potentially fatal when activated errantly. Elevated YAP activity has been identified in dozens of different solid cancers [8, 9]. In tumours, YAP promotes malignancy and metastasis [11–13], and is associated with poor clinical outcomes [14, 15]. As such, YAP is an appealing therapeutic target in cancer and regenerative medicine [9, 12].

Most pertinently to this project, elevated nuclear localisation of YAP may cause fibroblasts (cells which possess the ability to remodel surrounding tissue) to adopt a 'cancer-associated' phenotype. Cancer-associated fibroblasts (CAFs) promote tumour progression and metastasis and have been identified in many types of solid tumour [16, 17]. In some cases, they partially dissolve the extra-cellular matrix (ECM), creating tracks that enable subsequent cancer cell invasion [17]. Furthermore, neighbouring fibroblasts can, via mechanosensing, detect remodelling of the ECM by CAFs, increasing YAP activity in response [18]. This process may establish a potent feedback

loop where CAFs recruit nearby fibroblasts, while simultaneously promoting tumour growth and metastasis [18].

The objective of this thesis is to investigate the elevated YAP activity in cancer-associated fibroblasts. Current literature (summarised in 1.6.8) suggests that YAP is proximally regulated by four processes: binding reactions in the cytoplasm, binding reactions in the nucleus, nuclear import and nuclear export.

To investigate protein dynamics and localisation within living cells, researchers often utilise fluorescence microscopy techniques; in particular fluorescence recovery after photobleaching (FRAP) and fluorescence loss in photobleaching (FLIP). FRAP can be used to investigate protein diffusion and binding reactions within cellular compartments (such as the cytoplasm or nucleus), while FLIP can be used to investigate transfer between compartments. This is accomplished by fitting mathematical models to empirical data, with the model parameter values thereby obtained representing rates of reaction and translocation.

The question naturally arises: under which circumstances can binding kinetics be accurately dissected using quantitative FRAP analysis? This thesis is essentially split between this theoretical problem, and the empirical problem of YAP dynamics in fibroblasts.

The remainder of this chapter is a literature review concerned with mathematical modelling of FRAP and FLIP, parameter estimation and the biology of YAP. In chapter 2 we derive conditions which guarantee the viability of parameter estimation in FRAP. In chapter 3 we test our predictions numerically and go on to propose a general parameter fitting scheme. We then turn to the empirical YAP problem in chapter 4, applying a pixel-based computational model to investigate binding kinetics in the nucleus. Finally, in chapter 5 we use a FLIP modelling approach to investigate binding kinetics in the cytoplasm and transfer across the nuclear membrane.

1.1 FLUORESCENCE RECOVERY AFTER PHOTOBLEACHING

The development of live cell fluorescence microscopy has revolutionised molecular cell research. Much modern fluorescence microscopy depends upon the use of the green fluorescence protein (GFP) and its variants. GFP, first isolated from the jellyfish *Aequorea Victoria*, has the ability to absorb energy from light in the ultra violet to blue wavelength range, which is then released by radiating green light [19]. By modifying cells to express a fusion of GFP with a particular target protein (tagging or labelling), researchers are able to study gene expression and protein localisation within the living cell [20]. This is done by illuminating the target cell with light of an appropriate wavelength and detecting the fluorescent emission.

GFP and other fluorescent proteins have a finite fluorescent lifetime, so the fluorescent emission will decline given continued exposure to high intensity light (this process is known as photobleaching). FRAP is a deliberate exploitation of photobleaching to measure the mobility of molecules in living cells.

In typical FRAP experiments, a short sequence of images is acquired prior to photobleaching. These serve to document the initial spatial distribution of the fluorescent molecule. The next step is photobleaching: a small defined region of interest is briefly illuminated with high intensity light, usually delivered by a laser. This creates a high concentration of photobleached (or simply bleached) protein molecules within the region of interest. Next, the laser intensity is attenuated in order to acquire a longer sequence of images, ideally with minimal photobleaching. During this period, the motion of both non-bleached and bleached GFP molecules will lead to the spatial re-distribution of the fluorescent signal. Passive transport processes, such as Brownian motion, will create a net transfer of bleached molecules out of (and a net transfer of unbleached molecules into) the region of interest, causing a relaxation towards equilibrium. This is referred to as the fluorescence recovery. The speed of the fluorescence recovery is a measure of the mobil-

ity of the target species. The average intensity of fluorescent emission from the region of interest is recorded against time to construct the fluorescence recovery curve [21–24].

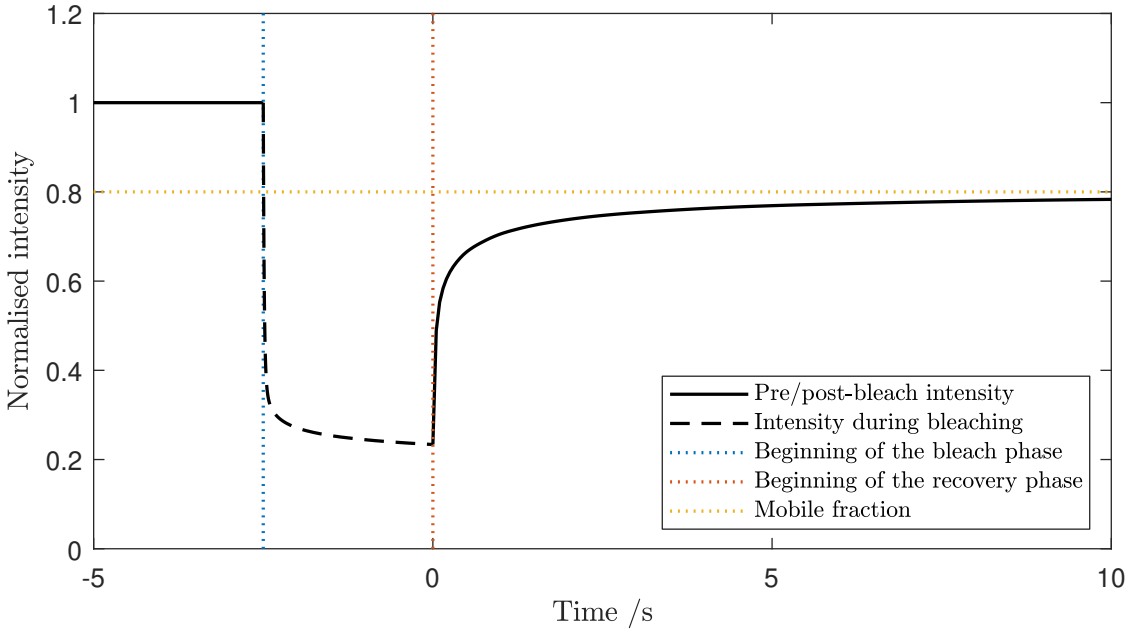


Figure 1: Normalised intensity during a simulated FRAP experiment. Prior to photobleaching it is assumed the intensity is 1. The intensity drops during the bleaching phase, although this could not be observed experimentally due to the high light intensity required for photobleaching. After photobleaching, the recovery, following equation (7), may be observed. In this example, the recovery curve approaches 80% of its pre-bleach value because 20% of the protein is immobile.

An idealised example of FRAP data is presented in figure 1 which represents the average intensity of the fluorescent emission from within the bleach region. Photobleaching causes a sharp decline in intensity, followed by the fluorescence recovery. The cell does not necessarily fully recover to the pre-bleach equilibrium as some of the protein may be immobile.

The early development of FRAP was quite highly collaborative and decentralised [28]. Poo and Cone pioneered the use of photobleaching to measure the mobility of the light sensitive receptor protein, rhodopsin, in the photoreceptor membranes of rod cells [31–33]. Peters *et al.* subsequently studied the motion of fluorescence-labelled proteins in erythrocyte membranes

using a static laser with photo-multiplier tube as a detector [34]. FRAP has since been widely adopted by researchers; over the past decade, FRAP has featured in over 150 studies per year [44]. Although numerous improvements have been made to FRAP procedure since it was first introduced, the fundamental idea has not changed [25].

1.1.1 *Laser intensity profile*

Let $I(\mathbf{x}, t)$ be the intensity of the laser light at coordinate $\mathbf{x}$ and time t. We refer to I as the intensity profile. The intensity profile is given a solution of the Fraunhofer diffraction equation. For a circular aperture, this is the Airy

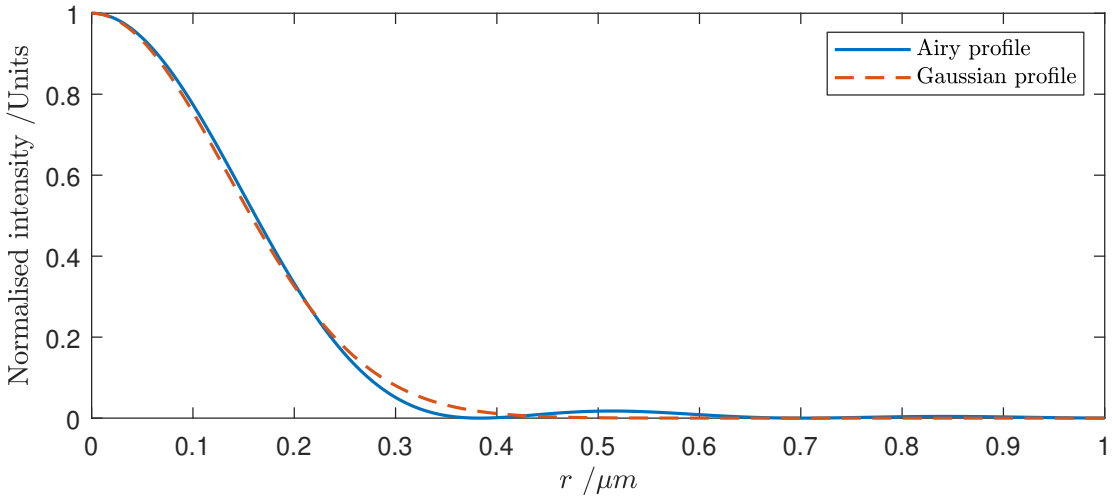


Figure 2: Example intensity profile, $I(r, t)$, given by formula (1), normalised so that the maximum intensity is 1. Also plotted is the best-fit Gaussian function, which is clearly a good approximation for small r, yet the approximation breaks down for larger r due to the presence of high order diffraction rings.

pattern [26],

$$I(\mathbf{x}, t) = I(r, t) = \frac{\Phi_0(t)\pi a^2}{\lambda^2 z_0^2} \left(\frac{2\mathbf{J}_1(2\pi a r/(\lambda z_0))}{2\pi a r/(\lambda z)} \right)^2, \tag{1}$$

where r is the distance in the focal plane from the centre of the beam. Additionally, $\Phi_0(t)$ is the radiant flux admitted by the aperture (which is dependent on t due to variations in laser power), a is the radius of the aperture, λ

is the wavelength of light and z_0 is the image distance. Here $\mathbf{J}_1$ is a first order Bessel function of the first kind. An example intensity profile is plotted in figure 2. For the purposes of fluorescence imaging, the intensity profile, I, can also be thought of as the point spread function (PSF) of the imaging system, which we discuss further in section 1.1.4.

1.1.2 *Photobleaching*

In this subsection we provide a more detailed physical description of the process of photobleaching. Prior to photobleaching, the vast majority of molecules exist in a ground energy singlet state, in which all electrons are paired [44]. Let S_0 be the singlet ground energy state. Irradiated by light of wavelength ν, the fluorophore has a probability to absorb the photon energy, E, given by the Planck-Einstein relation, $E = h\nu$, which causes it to transition into an excitation singlet state, S_1. The excess energy is rapidly dissipated (the lifetime of the excitation state is of the order of 10^{-9} seconds) in one of a variety of ways; significantly, by fluorescent emission, or by transition into a triplet state, T_1 in which there are two unpaired electrons [44]. The triplet state has a far greater characteristic decay time than S_1, typically of the order of 10^{-6} to 10^{-3} seconds, which is sufficient time for the fluorophore to react chemically with other excited molecules or free oxygen in the environment [44]. In that event, the reaction induces conformational change in the fluorophore, yielding a non-fluorescent product, which is the main mechanism by which photobleaching occurs [44]. In a well-mixed system, this process can be described by the system of ordinary differential equations,

$$\begin{cases} \frac{\mathrm{d}[S_0]}{\mathrm{d}t} = -k_1[S_0] + k_2[S_1] + k_4[T_1], \\ \frac{\mathrm{d}[S_1]}{\mathrm{d}t} = k_1[S_0] - k_2[S_1] - k_3[S_1], \\ \frac{\mathrm{d}[T_1]}{\mathrm{d}t} = k_3[S_1] - k_4[T_1], \end{cases} \tag{2}$$

where $[S_0]$ is the concentration of fluorophore molecules in the ground energy singlet state, $[S_1]$ is the concentration of molecules in the excited singlet state, and $[T_1]$ is the concentration of molecules in the triplet state. The rate k_1 is proportional to light intensity,

$$k_1 = k_I I,$$

where I is the excitation light intensity, given by formula (1), and k_I is a constant of proportionality. Given the average lifetime of the excitation states, k_4 must be of the order of $10^3\ s^{-1}$ to $10^6\ s^{-1}$, while k_2 and k_3 must be of the order of $10^9\ s^{-1}$ [44]. In the limit $I \to \infty$, the system of equations (2) will rapidly approach equilibrium, so we may make a quasi-steady state assumption. If we assume that $[S_0] + [S_1] + [T_1] = 1$ (in which case, S_0, S_1 and T_1 are the fractions of molecules in the ground, excitation and triplet states respectively) then the steady state of (2) is

$$[T_1] = \frac{k_1 k_3}{k_1(k_3 + k_4) + k_4(k_2 + k_3)}. \tag{3}$$

As $I \to \infty$, $k_1 \to \infty$, therefore $[T_1] \to k_3/(k_3 + k_4)$.

If we assume that the availability of free oxygen and other excited molecules is much greater than the availability of T_1 molecules, then the extent to which they are depleted by reaction with T_1 is effectively negligible. In this case, the rate of reaction is approximately proportional to $[T_1]$. Recalling that it is these reactions between T_1 and other molecules which are responsible for photobleaching, then the rate of photobleaching per unit concentration of fluorophore molecules is approximately $R_{\text{bleach}}[T_1]$, for some constant, R_{bleach}. Hence it follow from equation (3) that, as $I \to \infty$, the rate of photobleaching per unit concentration asymptotically approaches $R_{\text{bleach}} k_3/(k_3 + k_4)$.

Let $w(\mathbf{x}, t)$ be the concentration of fluorescent (*i.e.* not yet photobleached) molecules at position $\mathbf{x}$ and time t. Assume, for the moment, that these

molecules are immobile and non-reactive. The rate of photobleaching, $\frac{\partial w}{\partial t}$, is

$$\frac{\partial w}{\partial t}(\mathbf{x}, t) = -R_{\text{bleach}}[\mathrm{T}_1](\mathbf{x}, t)w(\mathbf{x}, t). \tag{4}$$

Substituting (3) into (4) yields,

$$\frac{\partial w}{\partial t} = -\frac{\alpha_1 I(\mathbf{x}, t)}{\alpha_2 I(\mathbf{x}, t) + \alpha_3} w(\mathbf{x}, t), \tag{5}$$

where $\alpha_1 = R_{\text{bleach}} k_3$, $\alpha_2 = k_1(k_3 + k_4)k_I$, and $\alpha_3 = k_4(k_2 + k_3)$. The rate of photobleaching is a saturating function of laser intensity, I. If $I \ll \alpha_3/\alpha_2$, then it is clear from (5) that

$$\frac{\partial w}{\partial t} \approx -\alpha I(\mathbf{x}, t)w(\mathbf{x}, t), \tag{6}$$

where $\alpha = \alpha_1/\alpha_3$.

1.1.3 *Static laser FRAP*

The earliest FRAP experiments were performed with a static laser beam [29, 30]. In static laser FRAP, both bleaching and imaging are typically performed with the same laser. At the end of the photobleaching phase of the experiment, the laser intensity is attenuated so the fluorescence recovery can be observed. Observation of the sample requires continual exposure to light, because the delay between a fluorophore absorbing energy from a photon and re-radiating that energy is typically a few milliseconds long (see section 1.1.2 or [44]). Ideally this exposure will causes minimal further photobleaching.

Let $w(x, y, t)$ be the local concentration of fluorescent molecules at coordinate (x, y) and time t. For a static laser FRAP experiment, the observed fluorescent light intensity across the bleach region, F, is given by

$$F(t) = q \iint_{\mathbf{R}^2} w(x', y', t) I(x', y', t) \mathrm{d}x' \mathrm{d}y', \tag{7}$$

where q is the quantum yield of the fluorophore and F is also known as the fluorescence recovery curve [29, 30].

In some cases, a fraction of the protein of interest may be stably bound to a cellular structure, rendering it immobile. In this case, there will be an incomplete fluorescence recovery. Figure 1 includes a theoretical example in which 20% of the protein is immobile. If there is an immobile fraction, the recovery curve can be normalised as follows,

$$F(t) = \bar{F}(t)M_f + (1 - M_f)F_0 \tag{8}$$

where $\bar{F}(t)$ is the fluorescence recovery curve supposing complete recovery, $M_f \in [0, 1]$ is the mobile fraction and F_0 is the initial post-bleach recovery.

1.1.4 *Scanning laser FRAP*

Perhaps the single most significant development in FRAP protocol was the adoption of the confocal scanning laser microscope (CSLM). In scanning FRAP, the beam is scanned repeatedly across the sample under observation in a raster pattern. Whereas conventional static FRAP can only provide temporal information as indicated by equation (7), scanning FRAP yields spatio-temporal information, producing a series of images (frames) of the entire sample region under observation [39–43]. The observed fluorescence intensity, f is the product convolution of the fluorophore concentration, w with the PSF [27],

$$f(x, y, t) = w(x, y, t) \circledast I(x, y) = q \iint_{\mathbf{R}^2} w(x - x', y - y', t) I(x', y') \mathrm{d}x' \mathrm{d}y'. \tag{9}$$

Bleaching with a CSLM

The CSLM can also be used for photobleaching. As the laser scans across the sample, an acousto-optical modulator (AOM) dynamically varies the intensity of the beam based on its position so that the beam has intensity $B(x, y)$ at position (x, y) [286].

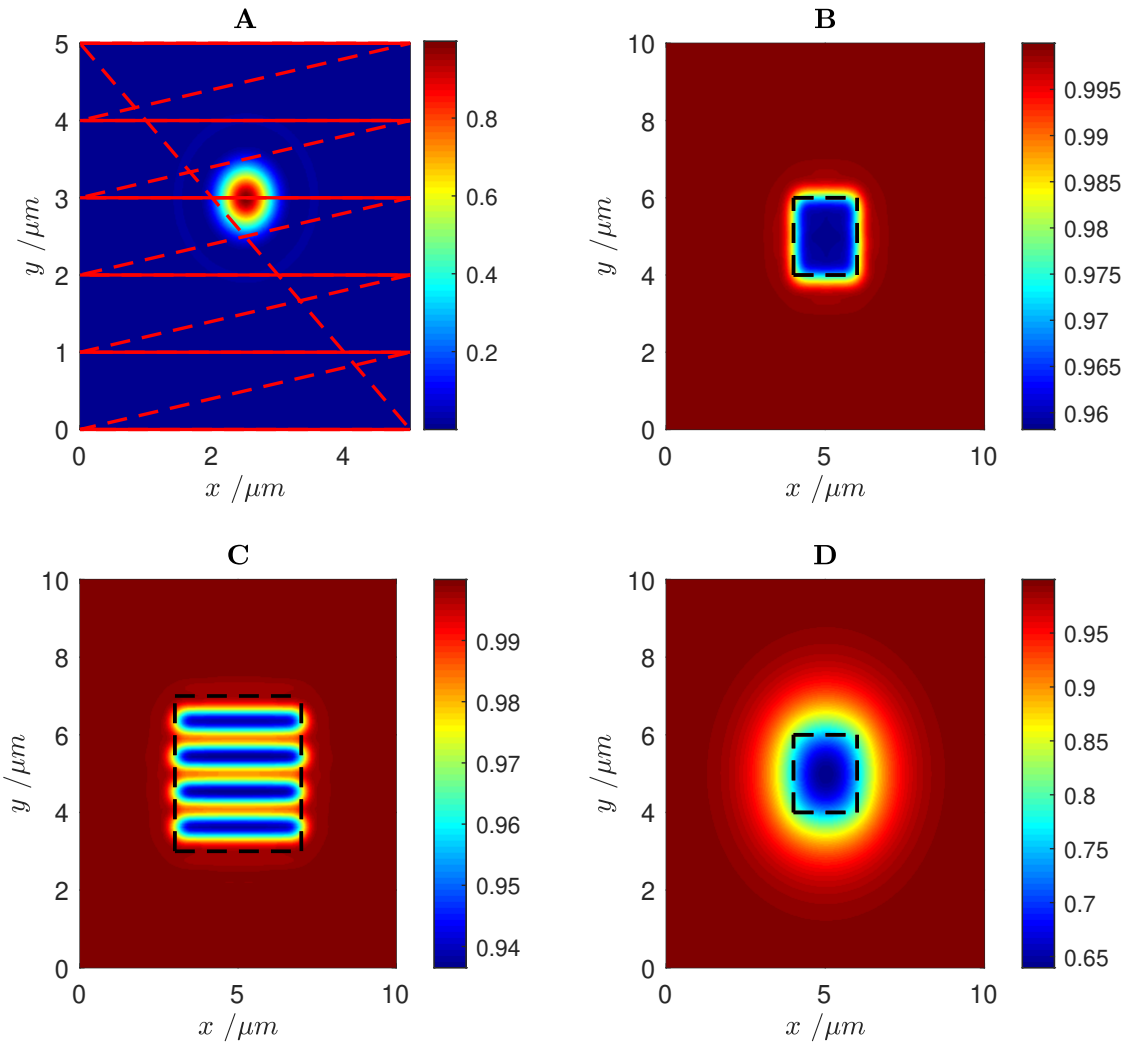


Figure 3: (A) A raster scan pattern and an Airy disk-type intensity distribution. Solid lines indicate that the beam is on, while dashed lines indicate it is off. (B) Raster bleaching of a square bleach region after a single scan. The profile does not perfectly conform to the geometry of the bleach region, but is slightly rounded, due to the effect of convolution with the PSF. It is assumed that the pre-bleach intensity is 1. (C) Raster bleaching of a square bleach region after a single scan. The scan lines have been set too far apart so that visible gaps emerge. (D) Concurrent bleaching and diffusion. The effect of 20 scans (*i.e.* lasting 1 second) over a sample with diffusivity $D = 1\mu m^2 s^{-1}$. Repeated scanning causes a much greater drop in intensity than is observed in (B) or (C).

The effective bleaching profile (functionally equivalent to intensity), $K(x,y)$, is the convolution of the beam intensity, B with the PSF, I, [61]

$$K(x,y) = B \circledast I = \iint_{\mathbb{R}^2} B(x',y')I(x-x',y-y')\mathrm{d}x'\mathrm{d}y'. \tag{10}$$

The unbleached fluorophore concentration is [61]

$$\frac{\mathrm{d}w}{\mathrm{d}t}(x,y,t) = -\alpha K(x,y)w(x,y,t). \tag{11}$$

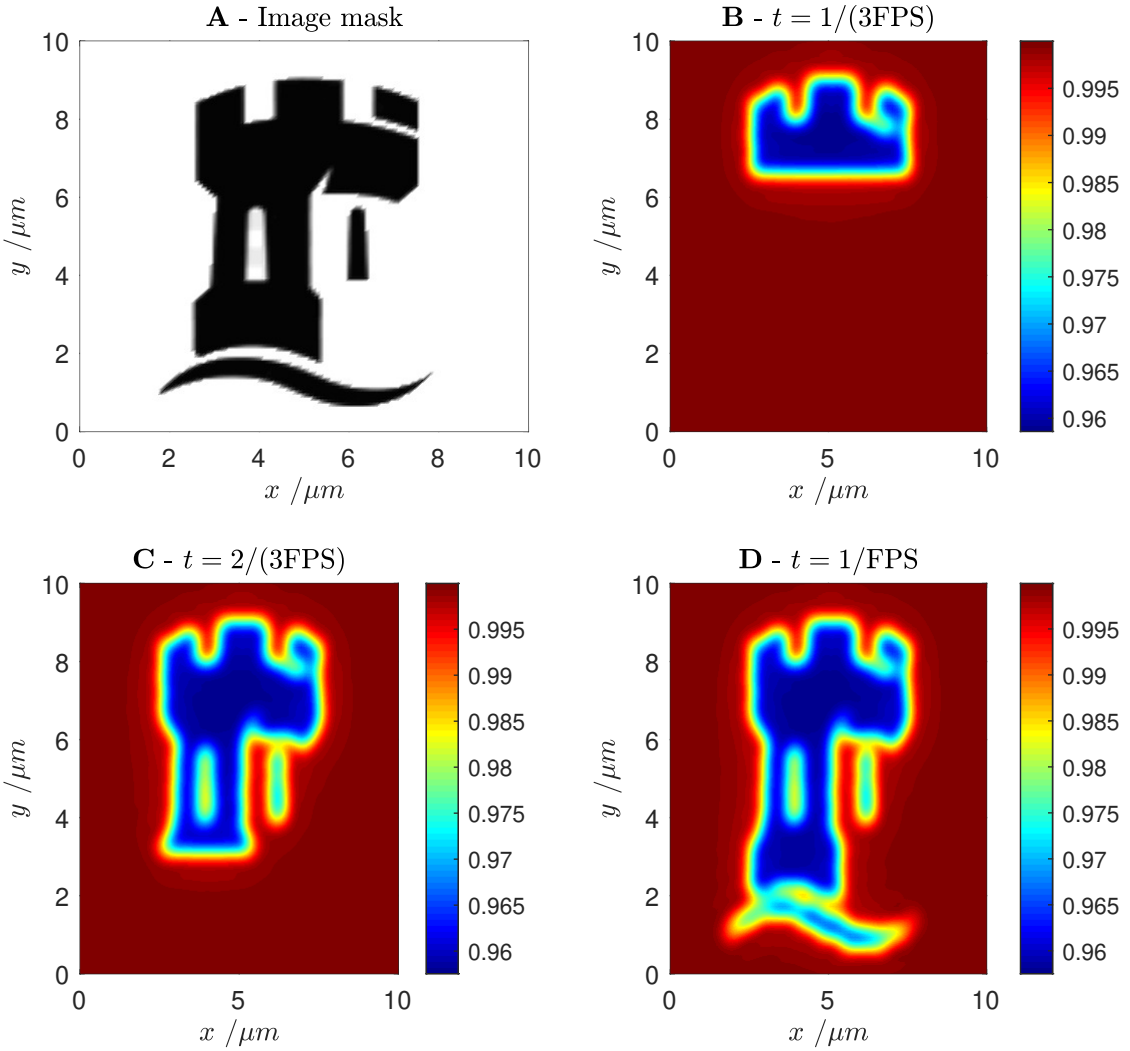


Figure 4: (A) A user-defined image mask. (B-D) Photobleaching at three different times after the beginning of photobleaching, as indicated where FPS $= 20\ s^{-1}$. (B) One third of the way through a complete scan. (C) Two thirds of the way through a complete scan. (D) Immediately after a single complete scan.

Two figures are included which were produced by numerical simulation of scanning FRAP. Figure 3A illustrates the PSF and the raster scan. The beam traces horizontally from left to right until it reached the end of the right boundary of the imaged region. Then the laser intensity is set to 0 and the beam retraces diagonally to the next scan line. This process repeats,

forming a sawtooth wave, until the beam reaches the bottom right, from where it retraces back to the top left diagonally and repeats. In figure 3B we can observe the effect of scanning photobleaching. When the beam is outside of the defined bleach region, the laser intensity is set to 0. The resulting bleaching profile is not perfectly square, but slightly rounded due to the effect of the convolution with the PSF, as indicated by formula (10). Figure 3C is similar, except that the distance between the scan lines is greater than the diameter of the beam, leaving gaps in the post-bleach profile. In figure 3D, despite the fact that the bleach region is square, diffusion during photobleaching drives the post-bleach profile towards circular symmetry.

Figure 4 shows the process of photobleaching according to an arbitrary image mask during a single scan. The image is produced by varying the laser intensity as it scans across the sample, based on position. Whenever the beam is centred on a point at which the image mask 4A is white, the intensity is set to 0. This means that only the black pixels in 4A are 'written' into the sample. This shows how photobleaching of an arbitrary image may be conducted, as well as the distortion of the image by convolution with the PSF (figure 4B-D) as predicted by equation (10).

1.2 FRAP MATHEMATICAL ANALYSIS

The earliest FRAP experiments involved the use of a static laser beam to investigate the lateral diffusion of proteins in biological membranes [32–38]. Naturally, the earliest quantitative FRAP studies were based on models of diffusion in 2D domains. With time, however, both FRAP experimental practice and FRAP modelling grew in scope and complexity. The introduction of the confocal scanning laser microscope in FRAP enabled the use of spatio-temporal information, while early studies had used only temporal information. Whereas early experiments had been focused on flat membranes, the application of FRAP to voluminous cellular compartments, such as the cytoplasm and the nucleus, necessitated the development of new 3D

FRAP models. Additionally, models were developed to incorporate other processes, such as binding kinetics. In this section we review the origin of quantitative FRAP modelling, and its subsequent development, with reference to a collection of significant examples.

1.2.1 *Diffusion*

To begin, we will consider models of 'Fickian' diffusion. It is assumed that protein mobility is solely due to diffusion, which can be described by Fick's second law,

$$\frac{\partial w}{\partial t} = D\nabla^2 w. \tag{12}$$

Axelrod et al., *1976*

The earliest quantitative study of FRAP was published by Axelrod *et al.* in 1976 [29]. It assumes the protein is mobile in an infinite 2D plane with radial symmetry about the origin, hence

$$\nabla^2 w = \frac{1}{r}\frac{\partial}{\partial r}\left(r\frac{\partial w}{\partial r}\right), \tag{13}$$

where r is the distance from the origin. The FRAP experiment is split into three phases: a pre-bleach phase, $t \in (\infty, -T)$, a bleach phase, $t \in [-T, 0)$, and a post-bleach observation phase $[0, \infty)$.

It is assumed that the protein has reached homogeneous equilibrium before the beginning of the experiment; for $t < -T$, $w(r,t) = w_{\text{eq}}$. It is further assumed that diffusion during the bleach phase is negligible, so that

$$\frac{\partial w}{\partial t}(r,t) = -\alpha I(r) w(r,t), \tag{14}$$

for $t \in [-T, 0)$. Although $I(r)$ is strictly speaking an Airy-disk (formula (1)), this results in a system which is not amenable to analysis, so Axelrod *et al.* model the intensity distribution as a Gaussian function,

$$I(r) \approx I_0 e^{-2r^2/{r_n}^2}. \tag{15}$$

A Gaussian function is a reasonably good fit to the real intensity distribution (see figure 2); however, for several reasons, the nominal radius of the Gaussian beam, r_n is greater than the optical resolution of the microscope. First, the light contained within the high order diffraction rings causes more photobleaching far from the origin than a Gaussian function would predict. Secondly, saturation effects (see equation (5)) result in less bleaching close to the origin. The combination of these two factors have the effect of flattening the best-fit Gaussian profile [64, 66]. Additionally, membrane curvature tends to expose more bleachable surface area, creating a larger effective bleach region [99]. Because r_n is hard to predict, it is best to take it as a fitting parameter.

Solving (14) with a Gaussian laser profile (15) implies that

$$w(r, 0) = w_{\text{eq}} \exp\left(-\alpha I(r) T\right) = w_{\text{eq}} \exp\left(-K e^{-2r^2/r_n^2}\right), \tag{16}$$

where $K = \alpha T I_0$ is considered to be the bleaching depth. Next comes the recovery phase for $t \in [0, \infty)$ during which it is assumed that photobleaching is negligible so fluorescent protein dynamics can be modelled by Fick's law (12). It is assumed that the domain has infinite spatial extent, so that the far field conditions,

$$\lim_{r \to \infty} w(r, t) = w_{\text{eq}}, \quad \forall t \in \mathbb{R}, \tag{17}$$

apply, which closes the model. This assumption is clearly appropriate if the membrane is much larger than the bleach spot, but not otherwise. Axelrod *et al.* then solve the diffusion equation (12) subject to the far-field condition (17) and the initial condition (16). The solution, $w(x, y, t)$ is given

by the product convolution of the initial condition with the Green's function for 2D radially symmetrical diffusion,

$$w(x,y,t) = \int_{-\infty}^{\infty}\int_{-\infty}^{\infty} w(x',y',0)\frac{1}{4\pi Dt}\exp\left(-\frac{(x-x')^2+(y-y')^2}{4Dt}\right)\mathrm{d}x'\mathrm{d}y'. \tag{18}$$

Axelrod *et al.* evaluate (18) to obtain and expression for w. The fluorescence recovery curve is then the product convolution of w with the laser intensity, according to (7). Of course, the intensity, I, is assumed to be Gaussain, in accordance with (15). The resulting recovery curve may be written as a series,

$$F(t)/F_\infty = \sum_{n=0}^{\infty}\frac{(-K)^n}{n!(1+n[1+2t/\tau_D])}, \tag{19}$$

where $F_\infty = \lim_{t\to\infty} F(t)$ and

$$\tau_D = \frac{r_n^2}{4D}.$$

The authors also considered a uniform circular disk model of laser intensity,

$$I(r) = \begin{cases} I_0 \text{ if } r \le r_n, \\ 0 \text{ if } r > r_n. \end{cases} \tag{20}$$

In this case, they obtained another series solution,

$$\frac{F(t)-F_0}{F_\infty - F_0} = 1 - \frac{\tau_D}{t}\exp\left(\frac{2\tau_D}{t}\right)\left[\mathbf{I}_0\left(\frac{2\tau_D}{t}\right)+\mathbf{I}_1\left(\frac{2\tau_D}{t}\right)\right] \tag{21}$$
$$+2\sum_{n=0}^{\infty}\frac{(-1)^n(2n+2)!(n+1)!(\tau_D/t)^{n+2}}{(n!)^2[(n+2)!]^2},$$

where $F_0 = F(0)$, and $\mathbf{I}_0$ and $\mathbf{I}_1$ are modified Bessel functions of the first kind. Note that (19) is semi-normalised (it asymptotically approaches 1 as $t \to \infty$) while (21) is fully normalised (it both approaches 1 and equals to 0 at $t = 0$).

By fitting the recovery formulas (19) or (21) to empirical data, estimates of the diffusivity, D, can be obtained from which inferences about molecular

mobility may be made. Naturally, the model of Axelrod *et al.* has some limitations. Due to the assumption of an infinite domain, it works only for bleach spots much smaller than the membranes under investigation. Because of the assumption of instantaneous photobleaching, it works only for slow-diffusing proteins. It also fails to account for photobleaching during the observation phase of the experiment. Nevertheless, it is the seminal quantitative FRAP study and, as we will see in the remainder of the section, many of the more sophisticated models which have since been proposed are in fact generalisations of this original model.

Soumpasis, 1983

One minor drawback of the analysis of Axelrod *et al.* is the expression of the recovery curves in terms of infinite series. Starting from identical assumptions, Soumpasis was able to derive an analytically closed expression for the recovery curve [30]. Assuming a uniform disk laser profile, (20), Soumpasis derived the following expression for the fully normalised recovery curve,

$$\frac{F(t) - F_0}{F_\infty - F_0} = \exp\left(-\frac{2\tau_D}{t}\right)\left[\mathbf{I}_0\left(\frac{2\tau_D}{t}\right) + \mathbf{I}_1\left(\frac{2\tau_D}{t}\right)\right], \tag{22}$$

where $\mathbf{I}_0$ and $\mathbf{I}_1$ are modified Bessel functions of the first kind. Formula (22) is tidier than the infinite series of Axelrod *et al.*. However, in practice, the asymptotic expansion,

$$\mathbf{I}_\nu(z) = \frac{e^z}{\sqrt{2\pi z}}\left(1 - \frac{4\nu^2 - 1}{8z} + \frac{(4\nu^2 - 1)(4\nu^2 - 9)}{2!(8z)^2} - \ldots\right), \tag{23}$$

is necessary to compute $F(t)$ for small values of t, so the problem of using infinite series is not totally avoided. Much like the model of Axelrod *et al.*, generalisations of (22) are featured in much subsequent model analysis.

1.2.2 *Scanning FRAP*

In section 1.1.4 we discussed how scanning FRAP differs from conventional static FRAP in that the laser scans repeatedly across the target sample. This process of repeated scanning typically takes several seconds, during which time there may be non-negligible diffusion. Applying the conventional FRAP models of Axelrod *et al.* and Soumpasis, both of which assume no concurrent bleaching and diffusion, to scanning FRAP yields underestimates of D, with the degree of the underestimation dependent upon the bleach spot size and scan time [45–47].

Strictly, it is necessary to solve the combined bleaching-diffusion equation,

$$\frac{\partial w}{\partial t}(r,t) = D\nabla^2 w(r,t) - \alpha I(r) w(r,t), \tag{24}$$

but this has no known analytic solutions for general $I(r)$. To apply conventional FRAP theory to scanning FRAP, it is therefore required to make some phenomenological assumptions.

Kang et al.*, 2009*

One method, provided by Kang *et al.* [48], is a modification of the conventional theory of Axelrod *et al.*. All model assumptions are identical except that, to account for diffusion during the bleaching phase, the model assumes that the sample is instantaneously bleached by a laser of radius r_e, the effective radius,

$$I_{\text{eff}}(r) = I_0 e^{-2r^2/r_e^2}. \tag{25}$$

The initial conditions of the recovery phase are then

$$w(r,0) = w_{\text{eq}} \exp\left(-K_e e^{-2r^2/r_e^2}\right). \tag{26}$$

The approach from this point is similar to Axelrod *et al.* The diffusion equation (12) is solved subject to initial conditions (26) and far field condition (17). This amounts to an experiment in which the sample is bleached with a

laser of radius r_e and then imaged with a laser of radius r_n, as per (15). The resulting recovery curve is

$$\frac{F(t)}{F_\infty} = \sum_{n=0}^{\infty} \frac{(-K)^n}{n!(1 + n[(r_n/r_e)^2 + 8Dt/r_e^2])}. \tag{27}$$

Satisfyingly, (27) exactly coincides with the series solution of Axelrod *et al.* (19) in the case where $r_e = r_n$. Further, (27) can be rewritten more concisely as

$$\frac{F(t)}{F_\infty} = \frac{\zeta}{K^\zeta}\gamma(\zeta, K), \tag{28}$$

where

$$\zeta = \frac{1}{\frac{2t}{\tau_D} + \frac{r_n^2}{r_e^2}},$$

and

$$\gamma(\zeta, K) = \int_0^K x^{\zeta-1}e^{-x}\mathrm{d}x,$$

is the incomplete gamma function.

The main advantage of this model is that it is a conceptually simple generalisation of established theory. The effective radius, r_e, can easily be determined by fitting (28) to the first post-bleach frame, using spatial information provided by the CSLM. Although spatial information is available (and, indeed, required to fit r_e), it is not utilised for the purposes of fitting the diffusion coefficient, D, as the recovery curve formula (27) involves only temporal data. It is arguably a disadvantage of the method of Kang *et al.* that it under-utilises data in this way.

Jonasson et al., *2008*

An alternative approach, which does utilise spatio-temporal information, is the model of Jonasson *et al.* [49]. The authors make no assumptions about the shape of post-bleach profile. Instead, they reason that diffusion will eventually blur the distribution of unbleached molecules until a Gaussian concentration profile develops. Let the time at which this occurs be $t = 0$

and suppose that the concentration profile at that time is w_0, a Gaussian function of radius r_0, *i.e.*

$$w_0(r) = a_0 - \frac{a_1}{r_0^2} \exp\left(\frac{r^2}{r_0^2}\right), \tag{29}$$

where a_0, a_1 and r_0 must be obtained by fitting (29) to data. Solving the diffusion equation (12) with initial conditions (29) yields,

$$w(r,t) = a_0 - \frac{a_1}{r_0^2 + 4Dt} \exp\left(\frac{r^2}{r_0^2 + 4Dt}\right). \tag{30}$$

Fitting (30) to data yields an estimate of the diffusivity coefficient, D. This method has its own disadvantages, however. Most significantly, information before $t = 0$ is discarded, which is a problem because early time data are actually more characteristic of a diffusive recovery [48] so we might expect this method to produce less accurate estimates of D than other methods.

1.2.3 3D FRAP

Over time, researchers became increasingly interested in the use of FRAP to investigate protein mobility in cellular compartments such as the cytoplasm [50–53], the nucleus [51–54], and also extracellular media [55–59]. Within these media, unlike membranes, proteins have genuine three dimensional mobility, and so three dimensional FRAP models were required. One of the problems of adapting FRAP modelling to three dimensional space is to describe mathematically the three dimensional intensity profile of the confocal laser. If the optical equipment has large numerical aperture, out of focus light above and below the focal plane forms a conical shape which is difficult to deal with analytically [60], and to our knowledge, no modellers have attempted to do so.

There are two common methods to approximate the 3D intensity profile, given a small numerical aperture. The first method assumes that the light is highly columnar, so that the beam has approximately uniform intensity

throughout the depth of the sample. If this is the case, the intensity distribution is approximately cylindrical and totally penetrates the sample in the axial direction. Hence the concentration gradient of bleached molecules is entirely radial, and there is no net axial transport of fluorescent material, so a 2D model is applicable [61,62].

In the second case, it is assumed that the high intensity light is somewhat constrained to the focal plane, so that photobleaching creates a concentration gradient of fluorescent material in the axial direction (as well as the radial direction). In this case, there is genuine 3D diffusion. It is common practice to model the intensity distribution phemonologically as radially and axially Gaussian [43,61], so that

$$I(r,z) = I_0 \exp\left(-2\left(\frac{r^2}{r_n^2} + \frac{z^2}{z_n^2}\right)\right). \tag{31}$$

To be clear, the Gaussian function (31) is used mainly for reasons of analytic convenience.

Blonk et al., *1993*

An early example of a three dimensional FRAP model (as well as the earliest scanning FRAP model) is Blonk *et al.* [43]. Despite seeking to describe scanning FRAP, this model actually assumes that the bleaching beam is static and that diffusion during the bleaching phase is negligible. Hence the post-bleach profile is

$$w(r,z,0) = w_{\text{eq}} \exp(-\alpha T I(r,z)) = w_{\text{eq}} \exp\left(-K \exp\left(-2\left(\frac{r^2}{r_n^2} + \frac{z^2}{z_n^2}\right)\right)\right). \tag{32}$$

It remains to solve the diffusion equation (12) subject to initial conditions (32). This model utilises spatio-temporal data, so it is required to take the product convolution of the concentration, $w(r,z,t)$ and the point spread function, $I(r,z)$.

The authors assume that the fluorescent emission is observed via a detector with a cylindrical space window centred in the focal plane, of total height $2\Delta z_0$ and radius r_0. Note that r_0 and Δz_0 are not the same as r_n and z_n in general, as the laser and the imaging apparatus may have different optical resolutions. The visible fluorescent light intensity is given by

$$f(r,z,t) = \int_0^{r_0} \int_0^{2\pi} \int_{-\Delta z_0}^{\Delta z_0} I(r',z') w(r-r', z-z', t) r' \mathrm{d}r' \mathrm{d}\theta' \mathrm{d}z'. \tag{33}$$

Blonk *et al.* obtained explicitly an expression for f, but it is omitted here for the sake of space. The expression readily simplifies, however, in the limit $r_0, \Delta z_0 \to \infty$, which is valid in the case of a fully open aperture,

$$\frac{f(r,z,t)}{f_\infty} = \sum_{m=0}^{\infty} \frac{(-K)^m}{m!} \frac{e^{-2mz^2/(z_n^2 \alpha_m)}}{\sqrt{\alpha_m}} \frac{e^{-2mr^2/(r_n^2 \beta_m)}}{\beta_m}, \tag{34}$$

where

$$\alpha_m = 1 + m\left(1 + \frac{2t}{\tau_z}\right), \quad \tau_z = \frac{z_n^2}{4D},$$

and

$$\beta_m = 1 + m\left(1 + \frac{2t}{\tau_D}\right), \quad \tau_D = \frac{r_n^2}{4D}.$$

While this is a significant early example of scanning FRAP modelling, the assumption of a static bleaching beam in scanning FRAP is highly unrealistic.

Braeckmans et al., *2003*

A subsequent model by Braeckmans *et al.* explicitly incorporates CSLM scanning effects in both bleaching and imaging [61]. The model assumes that the extent of diffusion during photobleaching is insignificant. Braeckmans *et al.* began by considering a single line scan, then extended their analysis to show that, in general, the post-bleach profile is

$$w(x,y,0) = w_{\mathrm{eq}} \exp\left(-\frac{\alpha}{c\Delta y} K(x,y,z)\right), \tag{35}$$

where c is the scanning speed and Δy is the spacing between scan lines. The bleaching function, $K(x,y,z)$, is the product convolution of the bleach region geometry $B(x,y)$ with the laser intensity,

$$K(x,y,z) = B \circledast I = \iint_{\mathbb{R}^2} B(x',y')I(x-x',y-y',z)\mathrm{d}x'\mathrm{d}y'. \tag{36}$$

Recall that $B(x,y)$ is the pre-programmed intensity of the beam at position (x,y). The authors assume that B is a uniform disk of radius r_b,

$$B(r) = \begin{cases} 1 \text{ if } r \leq r_b, \\ 0 \text{ if } r > r_b. \end{cases} \tag{37}$$

If $r_b \gg r_n$ then the laser can be considered to have negligible radius, in which case it is approximated by the Dirac delta function,

$$I(x,y,z) = I_0\delta(x,y)e^{-2z/z_n^2}. \tag{38}$$

By the sifting property of the Dirac delta function it follows that

$$K(r,z) = \begin{cases} I_0 e^{-2z/z_n^2} \text{ if } r \leq r_b, \\ 0 \text{ if } r > r_b. \end{cases} \tag{39}$$

The bleaching depth, K_0 is defined as

$$K_0 = \frac{\alpha I_0}{c\Delta y}. \tag{40}$$

In the case of a fully open aperture, the fluorescence recovery curve is

$$\frac{F(t)}{F_\infty} = 1 + \sum_{m=1}^{\infty} \left(\frac{(-K_0)^m}{m!\sqrt{\alpha_m}} \right) \left(1 - \frac{\tau_D}{t} \exp\left(\frac{2\tau_D}{t} \right) \left[\mathbf{I}_0\left(\frac{2\tau_D}{t} \right) + \mathbf{I}_1\left(\frac{2\tau_D}{t} \right) \right] \right), \tag{41}$$

where

$$\alpha_m = 1 + m\left(1 + \frac{2t}{\tau_z}\right), \quad \tau_z = \frac{z_n^2}{4D}.$$

The similarity to Soumpasis model (the term involving zeroth and first order modified Bessel functions of the first kind, $\mathbf{I}_0$ and $\mathbf{I}_1$) is a consequence

of the similar assumption of bleaching a uniform disk. The assumption of a Dirac delta PSF simplifies the analysis, yet the approximation is valid only if the radius of the bleach spot is at least 10 times greater than optical resolution [44]. However, the model assumes that space is infinitely expansive so it requires the bleach spot to be much smaller than the object being investigated. Consequently, the range of length scales over which the model is valid may be rather limited.

1.2.4 *Multi-photon excitation*

We have seen models that incorporate 3D protein mobility, but so far they have all been concerned with 2D bleaching and imaging, which is a limitation of single photon excitation FRAP. Genuine 3D imaging is possible using multi-photon excitation. Multi-photon excitation is similar in principle to single photon excitation except that the fluorophore must absorb the energy of two or more photons, potentially of different wavelengths, to enter an excitation state [67, 68].

In single photon excitation there is always substantial bleaching above and below the focal plane. In multi-photon excitation, the volume of excitation (hence of photobleaching and fluorescent emission) is more closely confined to the focal plane [60]. In this section we review some examples of fully three dimensional FRAP modelling which utilise multi-photon excitation.

Mazza et al. *2008*

We begin with the multi-photon excitation model of Mazza *et al.* [63]. Assuming that a fluorophore must absorb the energy of n photons simultaneously to enter an excitation state, then the local rate of photobleaching is not proportional to the local intensity, I, but rather the *n-th* power of the intensity, I^n.

Mazza *et al.* allow for the possibility that the laser light is pulsed, but they assume that photobleaching is effectively instantaneous compared with diffusion. Under these assumptions, the rate of photobleaching is proportional to the time average of I^n during the bleach phase,

$$\langle I^n(r,z)\rangle = \frac{1}{T}\int_{-T}^{0} I^n(r,z,t)\mathrm{d}t.$$

It remains to determine the functional form of the time average n-photon intensity, $\langle I^n\rangle$. Empirical studies suggest that $\langle I^n\rangle$ is well-approximated by a Gaussian function, even for a system with large numerical aperture [60]. Hence we can set

$$\langle I^n(r,z)\rangle = \langle I_0^n\rangle \exp\left(-2\left(\frac{r^2}{r_{en}^2}+\frac{z^2}{z_{en}^2}\right)\right), \tag{42}$$

where $r_{en} = r_e/\sqrt{n}$ and $z_{en} = z/\sqrt{n}$ are the effective radial and axial resolution of the n-photon beam.

As with the model of Braeckmans *et al.*, we suppose that radius of the bleach spot radius is much greater than the optical resolution of the microscope, so that the point spread function has effectively negligible radius and can therefore be approximated by the Dirac delta function. In this case, we have

$$\langle I^n(r,z)\rangle = \langle I_0\rangle \delta(x,y)e^{-2z/z_{en}^2}. \tag{43}$$

The post-bleach intensity is given by,

$$w(x,y,z,0) = w_{\mathrm{eq}} \exp\left(-\frac{\alpha_n}{nc\Delta y}K(x,y,z)\right), \tag{44}$$

where α_n is the n-photon sensitivity of the fluorophore and $K(x,y,z)$ is the bleaching function. Note that (44) is a generalisation of the initial conditions of Braeckmans *et al.* (equation (35)). The bleaching function $K(x,y,z)$ is the convolution of the bleaching geometry $B(x,y)$ and the average intensity $\langle I^n(x,y,z,t)\rangle$ (*i.e.* the Dirac delta function as in (43)),

$$K(x,y,z) = B \circledast \langle I^n\rangle = \iint_{\mathbb{R}^2} B(x',y')\langle I^n(x-x',y-y',z)\rangle \mathrm{d}x'\mathrm{d}y'. \tag{45}$$

Mazza *et al.* assume that B is a uniform disk of radius r_b, as in (37). The bleaching depth parameter is

$$K_{0n} = \frac{\alpha_n}{nc\Delta y}. \tag{46}$$

Suppose fluorescence recovery is observed using m-photon excitation. The m-photon intensity profile, I^m, is assumed to be Gaussian with radial and axial resolution r_{dm} and z_{dm} respectively. Note that these are different because intensity saturation effects tend to flatten the bleaching laser intensity [62–64]. The observed fluorescence intensity may be written in cylindrical coordinates as,

$$\frac{f(r,z,t)}{f_\infty} = 1 - \left[1 - \sum_{i=1}^{\infty} \frac{(-K_{0n}^i)}{i!} \frac{z_{en}}{z_{en}^2 + 8iDt} \exp\left(-2\frac{iz^2}{z_{en}^2 + 8iDt}\right)\right] \tag{47}$$
$$\times \frac{1}{2Dt} e^{-\frac{r^2}{4Dt}} \int_0^{r_b} e^{-\frac{r'^2}{4Dt}} \mathbf{I}_0\left(\frac{rr'}{2Dt}\right) \mathrm{d}r'.$$

Equation (47) can be used to predict the fluorescent concentration at each point (r,z), although this does require numerically approximating the integral, which cannot be evaluated exactly. It is also possible to derive a fluorescence recovery curve for this model, which is

$$\frac{F(t)}{F_\infty} = 1 + \sum_{i=1}^{\infty} \frac{(-K_{0n}^i)}{i!} \frac{z_{en}}{z_{en}^2 + 8iDt} \left(1 - e^{\frac{2\tau_D}{t}} \left[\mathbf{I}_0\left(\frac{2\tau_D}{t}\right) + \mathbf{I}_1\left(\frac{2\tau_D}{t}\right)\right]\right). \tag{48}$$

Deschout et al., *2010*

All of the models we have so far considered require radially symmetric bleach geometries. The model of Deschout *et al.* is distinct in that it requires a rectangular bleach region. It is also an example of a confocal model which does not assume Dirac delta PSF, and so it remains a good approximation for bleach regions of smaller length scale than previous models [65].

The bleaching function, $K(x,y,z)$ is defined identically to equation (45), the product convolution of the intensity profile $\langle I^n(x,y,z)\rangle$ and and image mask $B(x,y)$, a rectangle of dimensions $l_x \times l_y$,

$$B(x,y) = \begin{cases} 1 \text{ if } (x,y) \in [-l_x/2, l_x/2] \times [-l_y/2, l_y/2], \\ 0 \text{ otherwise.} \end{cases} \tag{49}$$

The PSF is once again assumed to be radially and axially Gaussian as in (42). For simplicity Deschout *et al.* assume photobleaching to be a linear (as opposed to exponential) process, so that the post-bleach profile is

$$w(x,y,z,0) = w_{\text{eq}} \left(1 - \frac{\alpha_n}{nc\Delta y} K(x,y,z)\right). \tag{50}$$

Equation (50) is the linearisation (*i.e.* the Taylor expansion truncated to first order) of (44) which is a valid approximation if the amount of photobleaching is fairly limited.

Observations are made with m-photon excitation. The image of the sample is the product convolution of the fluorescent concentration and a Gaussian function with radial and axial resolution, r_d and z_d. The resolutions of the multi-photon PSF are $r_{dm} = r_d/\sqrt{m}$ and $z_{dm} = z_d/\sqrt{m}$. The bleaching depth is

$$K_0 = \frac{\pi \alpha_n}{2nc\Delta y} \langle I^n(0,0,0)\rangle \left(\frac{r_e}{n}\right)^2. \tag{51}$$

It is convenient to define the quantities,

$$r_{m,n}^2 = \frac{r_{dm}^2 + r_{en}^2}{2}, \quad z_{m,n}^2 = \frac{z_{dm}^2 + z_{en}^2}{2}.$$

The fluorescence intensity is given by

$$\frac{f(x,y,z,t)}{f_\infty} = 1 - \frac{K_0}{4} \frac{z_e}{\sqrt{2n}} \frac{1}{z_{m,n}^2 + 4Dt} \exp\left(-\frac{z^2}{z_{m,n}^2 + 4Dt}\right) \mathcal{F}_x(x)\mathcal{F}_x(y), \tag{52}$$

where

$$\mathcal{F}_x(x) = \left[\operatorname{erf}\left(\frac{x + l_x/2}{\sqrt{r_{m,n}^2 + 4Dt}}\right) - \operatorname{erf}\left(\frac{x - l_x/2}{\sqrt{r_{m,n}^2 + 4Dt}}\right)\right], \tag{53}$$

and

$$\mathcal{F}_y(y) = \left[\text{erf}\left(\frac{y + l_y/2}{\sqrt{r_{m,n}^2 + 4Dt}} \right) - \text{erf}\left(\frac{y - l_y/2}{\sqrt{r_{m,n}^2 + 4Dt}} \right) \right]. \tag{54}$$

The error function, $\text{erf}(x)$, is defined as

$$\text{erf}(x) = \frac{2}{\sqrt{\pi}} \int_0^x e^{-x'^2} \mathrm{d}x'.$$

Equation (52) can also be reduced to two dimensional FRAP. In this case, there would be single photon excitation so $m = n = 1$. Also, $z = 0$ and $z_e \to \infty$, leaving

$$\frac{f(x, y, z, t)}{f_\infty} = 1 - \frac{K_0}{4} \mathcal{F}_x(x) \mathcal{F}_y(y). \tag{55}$$

This model has many appealing features: being pixel-based it allows fitting with spatio-temporal information, it works even for small bleach regions close to the optical resolution limit, and it is analytically closed. Arguably the most significant disadvantage is the assumption of instantaneous photobleaching. In figure 3D, we saw the post-bleach profile after bleaching material with diffusivity $D = 1\ \mu m s^{-1}$ for 1 second was almost entirely radially symmetric and could in no way be fitted by a rectangular function (50). Yet GFP in cytosol has a much greater diffusivity of approximately 30 $\mu m s^{-1}$ [70]. This suggests that the rectangular bleach region model is appropriate only for very short bleaching times or for slow-diffusing molecules.

1.2.5 *Reaction-diffusion*

FRAP is not limited to pure diffusion problems, it can also be used to study protein reaction kinetics. The simplest and most widely considered case is that of a single reversible reaction in which a protein, A, associates transiently with a binding partner, B, to form a complex C,

$$\mathrm{A} + \mathrm{B} \underset{\mathrm{k}^-}{\overset{\bar{k}^+}{\rightleftharpoons}} \mathrm{C}.$$

The law of mass action implies that, in a well-mixed system, the concentrations of A, B and C evolve according to

$$\begin{cases} \frac{\mathrm{d}[\mathrm{A}]}{\mathrm{d}t} = -\bar{k}^+[\mathrm{A}][\mathrm{B}] + k^-[\mathrm{C}], \\ \frac{\mathrm{d}[\mathrm{B}]}{\mathrm{d}t} = -\bar{k}^+[\mathrm{A}][\mathrm{B}] + k^-[\mathrm{C}], \\ \frac{\mathrm{d}[\mathrm{C}]}{\mathrm{d}t} = \bar{k}^+[\mathrm{A}][\mathrm{B}] - k^-[\mathrm{C}]. \end{cases} \tag{56}$$

Suppose that protein A is tagged with a fluorophore. Let u be the concentration of unbleached A, which has diffusivity D_u, and v the concentration of unbleached C with diffusivity D_v. Then, for u and v we have,

$$\begin{cases} \frac{\partial u}{\partial t} = -k^+ u + k^- v + D_u \nabla^2 u, \\ \frac{\partial v}{\partial t} = +k^+ u - k^- v + D_v \nabla^2 v, \end{cases} \tag{57}$$

where $k^+ = \bar{k}^+[\mathrm{B}]$. Note that, since B is not tagged, it contributes nothing to the fluorescence recovery and so does not appear in equation (57) except as a factor of k^+. Equation (57) has appeared widely in many FRAP studies, some of which consider the binding partners to be immobile ($D_v = 0$) [69–74] and others that allow $D_v > 0$ [75–78]. The total fluorescence is given by

$$w = u + v, \tag{58}$$

while the equilibrium concentrations are

$$u_{\mathrm{eq}} = \frac{k^-}{k^+ + k^-} w_{\mathrm{eq}}, \quad v_{\mathrm{eq}} = \frac{k^+}{k^+ + k^-} w_{\mathrm{eq}}. \tag{59}$$

Sprague et al., *2004*

One of the most widely cited studies of reversible binding kinetics is a 2004 paper by Sprague *et al.* [70]. The authors assume that the protein complexes, C, are immobile, hence $D_v = 0$. Analytically closed solutions to (57) are not

available, but a possible approach is to take the Laplace transform, which is defined by

$$\mathcal{L}\{g\} = \int_0^\infty g(t)e^{-st}\mathrm{d}t, \tag{60}$$

for a function g. It is assumed that there is a uniform bleach spot of radius r_n, hence the post-bleach conditions are

$$w(r,0) = \begin{cases} 1 \text{ if } r \leq r_n, \\ 0 \text{ if } r > r_n, \end{cases} \tag{61}$$

along with $u(r,0) = u_{\text{eq}}w(r,0)$ and $v(r,0) = v_{\text{eq}}w(r,0)$. This approach directly yields the fully normalised recovery curve $\mathrm{F}(t)$ which satisfies $\bar{F}(0) = 0$ and $\lim_{t\to\infty}\bar{F}(t) = 1$. The Laplace transform of $\bar{F}$ is

$$\mathcal{L}\{\bar{F}\}(s) = \frac{1}{s} - \frac{u_{\text{eq}}}{s}[1 - 2\mathbf{K}_1(r_n p(s))\mathbf{I}_1(r_n p(s))]\left(1 + \frac{k^+}{s+k^-}\right) - \frac{v_{\text{eq}}}{1+k^-}, \tag{62}$$

where

$$p(s) = \sqrt{\frac{s}{D_u}\left(1 + \frac{k^+}{s+k^-}\right)}.$$

This model has several limiting assumptions, most obviously instantaneous photobleaching. Additionally, the model works only for bleach spots of radius much greater than optical resolution due to the absence of convolution with the PSF.

Kang et al. *2010*

Kang *et al.* also published a reaction diffusion model which was a generalisation of earlier work on pure diffusion [76]. It makes several technical improvements on the model of Sprague *et al.*: it allows for protein redistribution during photobleaching and includes mobile binding sites. As with

the pure diffusion model of Kang *et al.* (2009) [48] it is assumed that the post-bleach profile is

$$w(r,0) = w_{\text{eq}} \exp\left(-Ke^{-r^2/r_e^2}\right), \tag{63}$$

where K and r_e are taken to be fitting parameters. The authors have derived the following fluorescence recovery curve,

$$F(t) = u_{\text{eq}} e^{-k^+ t}\mathcal{F}(D_u t) + v_{\text{eq}} e^{-k^- t}\mathcal{F}(D_v t) + \frac{t}{D_u - D_v}\mathcal{I}(t). \tag{64}$$

The various functions and constants included in (64) are defined as follows:

$$\mathcal{I}(t) = \int_{D_v}^{D_u} \frac{e^{\lambda t - \mu s t}\sqrt{k^+ k^-}}{k^+ + k^-}(F_1(s,t) + F_2(s,t))\mathcal{F}(st)\mathrm{d}s,$$

$$\lambda = \frac{k^+ D_v - k^- D_u}{D_u - D_v}, \quad \mu = \frac{k^+ - k^-}{D_u - D_v},$$

$$F_1(s,t) = \left(k^- \sqrt{\frac{s - D_v}{D_u - s}} + k^- \sqrt{\frac{D_u - s}{s - D_v}}\right)\mathbf{I}_1\left(\frac{2t\sqrt{k^+ k^-, (D_u - s)(s - D_v)}}{D_u - Dv}\right),$$

$$F_2(s,t) = 2\sqrt{k^+ k^-}\mathbf{I}_0\left(\frac{2t\sqrt{k^+ k^-(D_u - s)(s - D_v)}}{D_u - Dv}\right).$$

The function $\mathcal{F}$ is the solution to the pure diffusion problem with diffusivity s,

$$\mathcal{F}(st) = \sum_{n=0}^{\infty} \frac{(-K)^n}{n!(1 + n[(r_n/r_e)^2 + 8st/r_e^2])}. \tag{65}$$

Quite apparently, the major disadvantages of this model are its complexity and lack of analytic closure.

1.2.6 *Reaction-diffusion approximations*

Due to the complexity of the reaction-diffusion model, it is often preferable to consider simplifying limiting cases, which have been provided by

Sprague *et al.* [70]. Note that the time scale of diffusion of unbound molecules across the bleach region is $\tau_{D_u} = r_n^2/(4D_u)$. Similarly the average time between binding reactions is $\tau_{k^+} = 1/k^+$. Therefore the dimensionless ratio,

$$\eta = \frac{D_u}{k^+ r_n^2}, \tag{66}$$

is a measure of the mobility. The larger η, the greater the distance a protein can be expected to travel between binding events. Simplifying approximations may be applied if η is either extremely large or extremely small.

Reaction limited recovery

In the limit $\eta \to \infty$, the unbound protein is highly mobile so that the unbound fraction of protein (of concentration u) reaches equilibrium quasi-instantaneously. Hence (57) becomes

$$\begin{cases} u = u_{\text{eq}}, \\ \frac{\partial v}{\partial t} = k^+ u_{\text{eq}} - k^- v = k^-(v_{\text{eq}} - v). \end{cases} \tag{67}$$

System (67) can readily be solved to obtain

$$\frac{F(t)}{F_\infty} = 1 - v_{\text{eq}} e^{-k^- t}. \tag{68}$$

We will give this simple exponential model greater consideration in section 1.2.7.

Effective diffusion recovery

In the opposing case, $\eta \to 0$, reactions occur far more rapidly than diffusion, hence the system rapidly converges to local chemical equilibrium at each point in space so that $u(x, y, z, y) = u_{\text{eq}} w(x, y, z, t)$ and $v(x, y, z, y) = v_{\text{eq}} w(x, y, z, t)$. Taking the sum, $\frac{\partial u}{\partial t} + \frac{\partial v}{\partial t} = \frac{\partial w}{\partial t}$ yields

$$\frac{\partial w}{\partial t} = u_{\text{eq}} D_u \nabla^2 w + v_{\text{eq}} D_v \nabla^2 w = D_{\text{eff}} \nabla^2 w. \tag{69}$$

According to (69), the system closely resembles a pure diffusion model with effective diffusivity,

$$D_{\text{eff}} = \left(\frac{k^+ D_u + k^- D_v}{k^+ + k^-} \right), \tag{70}$$

which is a generalisation of the notion of effective diffusivity derived by Crank [274].

1.2.7 *Exponential models*

Arguably the simplest recovery curve models are the simple exponential model [79]

$$\frac{F(t)}{F_\infty} = 1 - Ae^{-t/\tau}, \tag{71}$$

where A is a constant and τ is the time scale of the recovery (both of which can be determined by fitting). The exponential model can be generalised to [80]

$$\frac{F(t)}{F_\infty} = 1 - \sum_{i=1}^{N} A_i e^{-t/\tau_i}, \tag{72}$$

where A_i is a constant which determines the size of the contribution of mode i to the recovery and τ_i is the time scale of the recovery of mode i.

Though useful, analytical FRAP models can be somewhat complicated and tend to have rather specific assumptions. It is perhaps not surprising that experimentalists have often preferred simply to analyse their data with the exponential formula [81–89]. As we saw in section 1.2.6, the exponential model is a perfectly reasonable approximation to a reaction-diffusion system with rapid diffusion, yet it is often applied to pure diffusion systems [90]. It is not obvious that this practice is theoretically justified, as the exponential formula (72) is not the solution to the equations which model pure diffusion fluorescence recoveries. Furthermore, it is common to assume that the number of exponential components required to fit the

recovery curve is the number of modes contributing to the fluorescence recovery [91–95] even though this is not necessarily the case and in fact it is not strictly speaking possible to fit a purely diffusive recovery (which would have only a single mode) with any finite number of exponentials [99].

Nevertheless, Taylor *et al.* [90] have provided a mathematical basis for the use of exponential formulas to model pure diffusion. If the diffusion equation is solved on a disk of radius r_n, using initial conditions,

$$w(r,0) = \begin{cases} 0 \text{ if } r < r_n, \\ w_{\text{eq}} \text{ if } r = 1, \end{cases} \tag{73}$$

and Dirichlet boundary conditions

$$w(1,t) = w_{\text{eq}}, \tag{74}$$

then the radially symmetric concentration profile can be written as an infinite series,

$$\frac{w(r,t)}{w_{\text{eq}}} = 1 - \sum_{m=1}^{\infty} \frac{2\mathbf{J}_0(\alpha_m r)}{\alpha_m r_n \mathbf{J}_1(\alpha_m r_n)} e^{-\alpha_m^2 D t}, \tag{75}$$

where α_m are the solutions to $\mathbf{J}_0(r_n \alpha_m) = 0$. Integrating over the disk yields the recovery curve.

$$\frac{F(t)}{F_\infty} = 1 - \sum_{m=1}^{\infty} \frac{4}{(\alpha_m r_n)^2} e^{-\alpha_m^2 D t}. \tag{76}$$

Truncating (76) to N terms yields the multi-exponential recovery curve (72).

1.2.8 *Numerical model analysis*

One of the weaknesses of the analytical approach is the lack of solutions to the bleaching-diffusion equation, which makes it technically impossible to account for diffusion during photobleaching and forces modellers to make potentially unphysical assumptions about the post-bleach profile.

Furthermore, analytical models typically do not directly account for unintended photobleaching caused by imaging during the recovery phase. A workaround is to normalise the recovery curve prior to analysis which can be approached in several ways. One way is to perform preliminary control experiments [73, 96], imaging a sample without any prior photobleaching, then recording the loss of fluorescence. Alternatively, one can measure the intensity drop in an external control region during the main experiment [61]. In either case, the recovery curve is normalised by the control intensity to account for passive photobleaching, though neither method is perfect. The former method fails to account for intensity fluctuations during the main FRAP experiment, while the latter method may introduce additional stochastic noise. Further, due to the potential presence of an immobile fraction, one cannot reliably make simple linear adjustments to the recovery curve, complicating the normalisation process [97].

Another significant, though unavoidable, limitation is the assumption of infinite space. This is essential because otherwise the exact solution cannot be derived from the product convolution of the initial post-bleach conditions with the Green's function. However, an infinite model necessarily fails to take into account cell geometry and boundary effects, which can introduce significant errors in parameter estimation [98, 99].

Numerical methods do not suffer from these limitations. For example, Braga *et al.* proposed a model of FRAP in the cell nucleus; a reaction-diffusion model which approximated the nucleus as a circular domain with homogeneous Neumann boundary conditions [75] (even this quite simple system cannot be solved analytically). Furthermore, numerical models can theoretically attain any level of biological realism (albeit with concomitant computational cost). Numerical models have been proposed which can handle anisotropic diffusion [100], inhomogeneous distribution of binding sites [72], simultaneous bleaching and diffusion [101, 102] and arbitrary photobleaching profiles [104]. Numerical software, such as Virtual Cell or

PyFRAP, can handle arbitrary cellular geometry [106], including tortuous effects exerted by obstacles [105].

A very comprehensive model for the raster scan motion of the laser during bleaching and imaging was published by Erdel and Rippe [103] in 2012. However, their approach requires computation times of several days for a single parameter set. More recently, a $3D$ computational FRAP model that incorporates particle diffusion, cell boundary effects, and the optical properties of the scanning confocal microscope, and which utilises general purpose computing on graphics processing units to reduce run time, was proposed by Kingsley *et al.* [99]. Besides deterministic FRAP models, there also exist stochastic approaches that track the diffusion and interactions of individual molecules and can be 'solved' using Monte Carlo methods [107, 109].

While the advantages of numerical models are clear, disadvantages include the increased computational cost of parameter fitting and the requirement of dedicated programming to implement numerical methods.

1.2.9 *Integral transform methods*

It is not always necessary to compute solutions to the diffusion equation explicitly. Numerous FRAP parameter fitting protocols exist which use integral transform methods, such as the Fourier transform [110], the Hankel transform [111], or the Laplace transform [70]. Taking the Fourier transform of the diffusion equation results in [110]

$$\frac{\mathrm{d}\tilde{w}}{\mathrm{d}t}(p,q,t) = -4\pi^2 D(p^2+q^2)\tilde{w}(p,q,t), \tag{77}$$

where p and q are the spatial frequencies. Being a linear ordinary differential equation, (77) is straightforward to solve,

$$\tilde{w}(p,q,t) = \tilde{w}(p,q,0)\exp\left(-4\pi^2 D(p^2+q^2)t\right). \tag{78}$$

Equation (78) can be rearranged in terms of D to give

$$D = \frac{\ln(\tilde{w}(p,q,t_2)/\tilde{w}(p,q,t_1))}{4\pi^2(p^2+q^2)(t_2-t_1)}, \tag{79}$$

for any times t_1 and t_2, $t_2 > t_1$. The Fourier transform is a rather simple and elegant method to obtain an explicit formula for D which has the highly desirable quality of being independent of the initial post-bleach distribution of fluorophores. Although it is necessary to measure empirically the distribution of fluorescent protein at two or more separate time points, formula (79) does not depend on an exact (or approximate) mathematical description of the post-bleach profile. The method is therefore compatible with arbitrary bleaching geometry, regardless of the extent of diffusion during the bleaching phase. However, the authors note that the Fourier method requires higher signal-to-noise ratio to achieve acceptable precision.

Additionally, the Fourier transform can also be used in numerical models. Röding *et al.* have recently published a reaction-diffusion (with immobile binding sites, $D_v = 0$) numerical model which is compatible with arbitrary bleach region geometry using spectral methods [112]. Spectral methods generally have exceptional convergence properties compared with more conventional methods such as finite differences [113].

1.2.10 *Other uses of FRAP*

Active transport models

Active transport has been incorporated into various models of bio-molecular transport, including neurofilament transport along axons in neurons [115, 116] motor-driven particles [117] and transport in microtubule networks [118]. Nevertheless, it has received far less attention in FRAP studies than passive transport by diffusion. Nevertheless, an early example of a directed transport model, concerned with electrophoresis in membranes, was proposed by Axelrod *et al.* (1976). The model includes simulataneous diffusion

and directed transport so that the concentration distribution of fluorescent protein, $w(x, y, t)$ is

$$\frac{\partial w}{\partial t} = D\nabla^2 w + V\frac{\partial w}{\partial y}, \tag{80}$$

where V is the transport velocity. Assuming quasi-instantaneous bleaching and an infinite spatial domain, the authors derived the following equation for the fluorescence recovery curve,

$$\frac{F(t)}{F_\infty} = \sum_{m=0}^{\infty} \frac{\left((-K)^m \exp\left[-2t^2/\tau_V^2 m(1+m(1+2t/\tau_D))\right]\right)}{m!(1+m(1+2t/\tau_D))}, \tag{81}$$

where $\tau_V = r_n/V$.

More recently, Ciocanel *et al.* [119] considered a slightly different model in which the molecules under investigation switch between an active transport state and a passive transport state. The dynamics are modelled by a system of partial differential equations,

$$\begin{cases} \frac{\partial u}{\partial t} = V\frac{\partial u}{\partial y} - k^+ u + k^- v, \\ \frac{\partial v}{\partial t} = D\nabla^2 v + k^+ u - k^- v, \end{cases} \tag{82}$$

which is solved numerically.

Anomalous diffusion

We have so far considered only models of normal diffusion. A characteristic of normal diffusion is that the mean square displacement of the distribution of particles, has a linear relationship with time,

$$\text{MSD} \propto t. \tag{83}$$

In reality the macro-molecular cellular environment is crowded and heterogeneous [122], which tends to obstruct diffusion. Molecules also undergo transient immobilisation due to binding events [127, 128] and hydrophobic/electrostatic interactions [129, 130]. For these reasons, it may be more appropriate to model protein transport with anomalous diffusion. There is a

consensus that in anomalous diffusion the MSD scales with time according to a power law [120–125]

$$\text{MSD} \propto t^{\alpha}, \tag{84}$$

which can be achieved if the diffusivity itself is time dependent,

$$D(t) = \Gamma t^{1-\alpha}. \tag{85}$$

It is worth noting that distinguishing anomalous from normal diffusion is very difficult without prior knowledge since in both cases the recovery curves have similar shape [120, 131]. Nevertheless, several FRAP models of anomalous diffusion have been proposed over the years.

One deterministic approach, which was taken by Lubelski and Klafter [132], is to use a fractional diffusion equation which is consistent with the power law (84). There are also stochastic models of anomalous diffusion, which can be implemented computationally using Monte Carlo methods [133]. Another approach, taken by Kang *et al.* [135] is to make no assumptions about the precise nature of the time dependence of the diffusivity coefficient, and instead to model D as an unknown function of time. Adapting a simplified equation to extract diffusion coefficient from FRAP data derived in previous work [134], the authors show that the time-dependent anomalous diffusivity equation is approximately

$$D(t) = \frac{r_e^2 + r_n^2}{8}\left(\frac{F'(t) - (F_\infty - F(0))}{(F_\infty - F(t))^2}\right), \tag{86}$$

where r_n is the nominal radius of the Gaussian bleaching profile and r_e is the effective radius of the post-bleach profile which must be determined by parameter fitting, and $F'(t)$ can be determined by numerical differentiation of the recovery curve. In this way, assumptions about the time-dependence of the diffusivity are avoided.

1.2.11 *Complications*

Having considered the theoretical aspects of FRAP, we will conclude this review by briefly discussing the effects which can complicate the procedure in practice. To begin with, emitted light will be attenuated as it passes through biological material above the focal plane before it can reach the detector apparatus. This is especially true if the emission wavelength of the fluorophore is close to its optimal absorption wavelength, since then photons emitted from flurophores within the focal plane will be absorbed by flurophores outside of the focal plane. Even if this leads to subsequent photon emission, the emitted light will be out of focus. This effect, known as inner filtering, is a well-document complication in fluorescence microscopy [136, 137].

Reversible photobleaching is another complication. The energy absorbed from a photon causes a fluorophore to enter an excitation state in which it can react chemically with other molecules in its surroundings. These reactions, which are the cause of photobleaching, may actually be reversible [138, 139]. In this case reversible photobleaching will accelerate the fluorescence recovery, causing overestimation of the mobility of the molecule under investigation. Conversely, the tagged protein of interest may oligomerise to form larger molecules. GFP and several other fluorescent proteins have been demonstrated to oligomerise at high concentrations [140]. As dimers and oligmers have greater mass than monomers, this process reduces the observed mobility of proteins in FRAP.

1.3 FLUORESCENCE LOSS IN PHOTOBLEACHING

Fluorescence loss in photobleaching (FLIP) is a fluorescence microscopy technique which is distinct from, though closely related to FRAP. FLIP can also be performed with a CSLM, and FLIP and FRAP are often used in con-

junction [141–143]. In FLIP, a target region is photobleached repeatedly, and the loss of fluorescence in a separate reporting region located elsewhere in the cell is monitored [141, 144, 145]. Bleaching in one cellular compartment (for example, the nucleus, the cytoplasm or an organelle) causes a loss of intensity in one or more adjacent compartments, which is evidence of transport of the target protein between them [21, 144, 146].

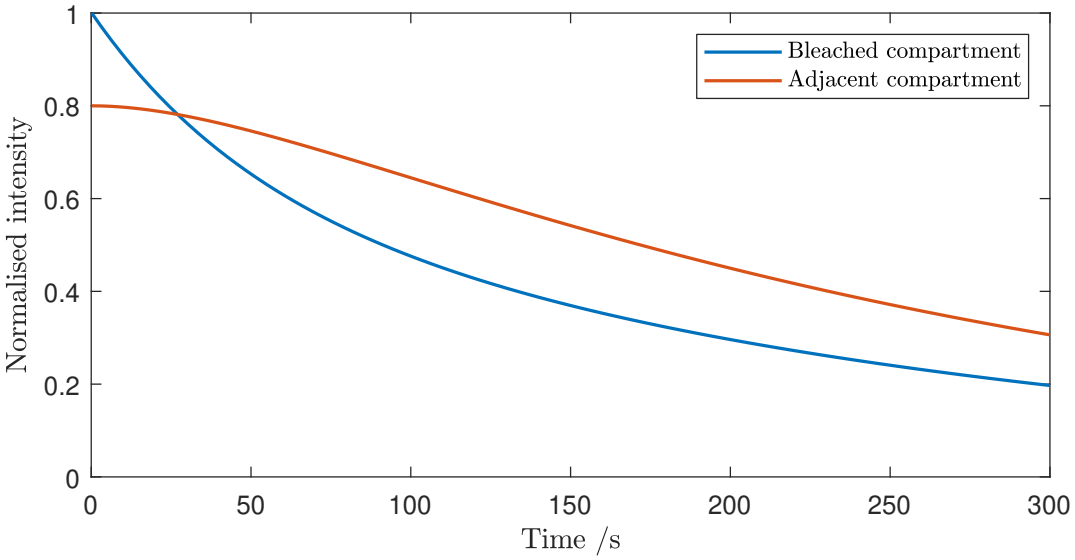


Figure 5: An idealised example a FLIP experiment showing the total intensity of fluorescent emission in the bleached compartment and the adjacent compartment.

In figure 5 we have included an idealised example of a FLIP experiment. The fluorescence intensity initially declines in the bleached compartment. This forces the gradient of bleached/unbleached molecules across the separating membrane between the compartments out of equilibrium, creating a net transfer of unbleached molecules into the bleached compartment, and bleached particles out of the bleached compartment. The greater the rate of fluorescence loss in the adjacent compartment, the greater the continuity across the separating membrane.

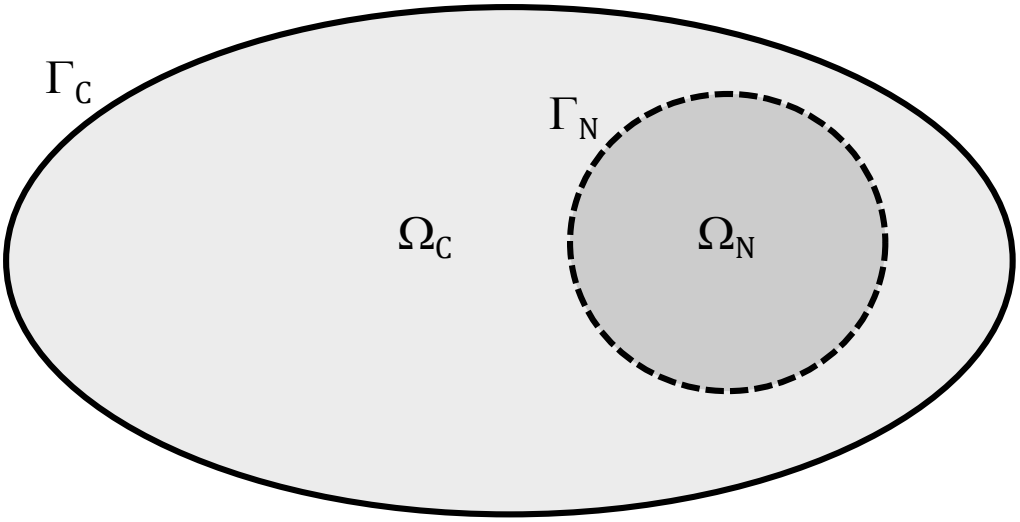


Figure 6: A simplified two compartment conception of a cell used in FLIP modelling. The main compartments are the nucleus, Ω_N, and the cytoplasm, Ω_C. The nuclear membrane, Γ_N, is denoted by a dotted line, as it is partially permeable. The cell membrane, Γ_C is a solid line, as it is assumed to be impermeable.

1.4 FLIP MATHEMATICAL ANALYSIS

Compared with FRAP, FLIP has received relatively little attention from mathematical modellers. Only a handful of FLIP models have been proposed, which can be split into two categories: ODEs [147–149] and PDEs [150–152]. In this section, we consider examples of both of these approaches. We assume that the cell is formed of two compartments, the cytoplasm and the nucleus (although FLIP studies of other structures, such as the endoplasmic reticulum, exist [147]).

Let Ω_C and Ω_N represent the cytoplasm and the nucleus respectively. Further, let Γ_N be the boundary between the cytoplasm and the nucleus (*i.e.* the nuclear membrane) and Γ_C be the outer boundary of the cytoplasm (*i.e.* the cell membrane). By assumption, there is protein flux across Γ_N, but not across Γ_C which is presumed impermeable. Of course, in reality there may be transfer of protein between adjacent cells, or perhaps between cells and extracellular media. These processes could potentially be investigated with a kind of generalised FLIP experiment; bleaching one cell and monitoring

the decline of fluorescence intensity in its neighbours, but they are neglected here.

The FLIP model is represented schematically in figure 6. Let $w_c(\mathbf{x}, t)$ be the fluorescent concentration at position $\mathbf{x}$ and time t in Ω_c and $w_n(\mathbf{x}, t)$ be likewise for Ω_n. We can also define the total masses of fluorescent protein in each compartment as follows:

$$W_c(t) = \int_{\Omega_c} w_c(\mathbf{x}, t)\mathrm{d}V, \quad W_n(t) = \int_{\Omega_n} w_n(\mathbf{x}, t)\mathrm{d}V.$$

1.4.1 *ODE modelling*

The simplest FLIP model involves linear ordinary differential equations. This approach assumes that the transfer of molecules between cellular compartments will generally evolve over a much slower time scale than molecular redistribution within compartments. Hence the redistributive dynamics within compartments can be neglected and the total concentrations, $W_c(t)$ and $W_n(t)$, will evolve according to a system of ODEs [148, 149]

$$\begin{cases} \frac{\mathrm{d}W_c}{\mathrm{d}t} = -k_1 W_c + k_{-1} W_n - k_0(t) W_c, \\ \frac{\mathrm{d}W_n}{\mathrm{d}t} = k_1 W_c - k_{-1} W_n, \end{cases} \tag{87}$$

where k_1 and k_{-1} are the aggregate cross-membrane transport rates and $k_0(t)$ is the time-dependent rate of bleaching. The simplicity of this model is both its most significant strength and weakness, in different respects. It is straightforward and computationally economical to fit (87) with experimental data to obtain estimates of k_1 and k_{-1}. Yet these transport rates give only a general idea of inter-compartmental continuity, and reveal nothing about the mechanisms which underpin cross-membrane transport.

1.4.2 *PDE modelling*

Systems of partial differential equations (PDEs) can model FLIP in greater detail than ODEs [150–152]. Here we consider a recent example published by Hansen *et al.* [152]. It is supposed that the protein is temporarily immobilised by transient binding reactions in both compartments, hence the equations for the entire cell are

$$\begin{cases} \frac{\partial u}{\partial t} = \nabla \cdot (D(\mathbf{x})\nabla u) + k^+(\mathbf{x})v - k^-(\mathbf{x})u - \alpha I(\mathbf{x},t)u, \\ \frac{\partial v}{\partial t} = k^+(\mathbf{x})u - k^-(\mathbf{x})v - \alpha I(\mathbf{x},t)v, \end{cases} \tag{88}$$

where $I(\mathbf{x},t)$ is the effective laser intensity at position $\mathbf{x}$ and time t, $u(\mathbf{x},t)$ is the concentration of mobile protein and $v(\mathbf{x},t)$ is the concentration of bound immobile protein. The diffusivity, D, and the reaction rates, k^+ and k^-, are spatially dependent because they vary between the nucleus and cytoplasm. While equation (88) is effectively identical to the reaction-diffusion models sometimes used in FRAP, the difference is that, in the FLIP model, there is an internal interface which represents the nuclear membrane, Γ_N.

The nuclear membrane is modelled as a semi-permeable membrane, across which there is flux of material dependent on the concentration difference of free protein, $\mathbf{J} = \pm p(u^+ - u^-)\hat{\mathbf{n}}$, where p is the permeability and $\hat{\mathbf{n}}$ is the unit outward normal vector of the nucleus. Transport across the nuclear membrane is modelled by a Robin boundary condition at Γ_N,

$$(D\nabla u)\cdot\hat{\mathbf{n}}|_{\Gamma_n^+} = -p(u^+ - u^-), \quad (D\nabla u)\cdot(-\hat{\mathbf{n}})|_{\Gamma_n^-} = -p(u^- - u^+), \tag{89}$$

where a $+$ superscript indicates that one is approaching Γ_N from within the nucleus and a $-$ superscript likewise from the cytoplasm. In addition, it is assumed that there is no transport of protein into or out of the cell, so a homogeneous Neumann boundary condition is imposed at the cell membrane, Γ_C,

$$(\nabla u \cdot \hat{\mathbf{n}})|_{\Gamma_C} = 0. \tag{90}$$

It is also assumed that bound protein is unable to cross any membranes, hence

$$(\nabla v \cdot \hat{\mathbf{n}})|_{\Gamma_C} = (\nabla v \cdot \hat{\mathbf{n}})|_{\Gamma_N} = 0. \tag{91}$$

Hansen *et al.* numerically solved the model equations using a Galerkin method implemented in FEniCS. Naturally, the PDE model provides more detailed insight in exchange for greater computational cost and more degrees of freedom in parameter fitting. The ODE model, (87), is an asymptotic limit of the PDE model which we will derive explicitly in chapter 5.

1.5 PARAMETER ESTIMATION/NON-LINEAR OPTIMISATION

The purpose of FRAP modelling is to obtain parameter estimates which reveal some biophysical information about the system under investigation. In this section we review a collection of common parameter fitting methods.

1.5.1 *Nonlinear least squares*

The most conventional parameter estimation method is the method of least squares. We begin by defining an objective function, ϕ, which represents the distance between some empirical FRAP data and the output of a theoretical model. Let θ be a vector of model parameter values, then for continuous time data

$$\phi(\theta) = \int_0^\infty (F(t;\theta) - F_{\text{data}}(t))^2 \mathrm{d}t. \tag{92}$$

where $F(t;\theta)$ is a fluorescence recovery curve generated by the model with parameters θ, and $F_{\text{data}}(t)$ is an empirical recovery curve. Similarly, for discrete time data we can define the objective function as the residual sum of squares,

$$\bar{\phi}(\theta) = \sum_{k=1}^{n_t} (F(t_k;\theta) - F_{\text{data}}(t_k))^2. \tag{93}$$

For spatio-temporal data, we have

$$\phi_{\text{space}}(\theta) = \int_0^\infty \left[\int_0^\infty \int_0^\infty (f(x,y,t;\theta) - f_{\text{Data}}(x,y,t))^2 \mathrm{d}x\mathrm{d}y \right] \mathrm{d}t, \qquad (94)$$

where $f(x,y,t;\theta)$ is the fluorescence intensity at position (x,y) and time t generated by the model with parameters θ, and $f_{\text{Data}}(x,y,t)$ is the empirically observed fluorescence intensity. Likewise for discrete data,

$$\bar{\phi}_{\text{space}}(\theta) = \sum_{k=1}^{n_t} \sum_{j=1}^{n_y} \sum_{i=1}^{n_x} (f(x_i,y_j,t_k;\theta) - f_{\text{Data}}(x_i,y_j,t_k))^2. \qquad (95)$$

The minimum of the objective function can be found algorithmically, for example using the well-known Nelder-Mead algorithm [278, 279]. The method of non-linear least squares is the most conceptually rudimentary, but also most adaptable fitting method.

1.5.2 *Maximum likelihood*

A closely related alternative to the least squares method is maximisation of the log-likelihood [49],

$$l(\theta) = \frac{M}{2} \log(2\pi\sigma) - \frac{1}{2\sigma^2} \sum_{k=1}^{n_t} \sum_{j=1}^{n_y} \sum_{i=1}^{n_x} (f(x_i,y_j,t_k;\theta) - f_{\text{data}}(x_i,y_j,t_k))^2, \quad (96)$$

where $M = n_x n_y n_t$ is the total number of data points and σ is the standard deviation of the noise. It is clear from (96) that, in practice, the log-likelihood method is functionally equivalent to the least squares fitting routine. However, it has the advantage that it readily yields an error estimate of the fitted parameters in terms of the Fisher information matrix, which we give greater consideration in section 1.5.5.

1.5.3 *Variance methods*

Kubitscheck *et al.* have argued that the statistical properties of diffusion can be used to estimate the diffusivity coefficient [39]. The central second moment, m_2 (equivalently, the variance) of the bleached molecules is

$$\mu_n(t) = \iint_{\mathbb{R}^2} (x^2 + y^2)(w_{\text{eq}} - w(x, y, t))\mathrm{d}x\mathrm{d}y, \tag{97}$$

where $(w_{\text{eq}} - w(x, y, t))$ is the concentration distribution of bleached molecules. Kubitscheck *et al.* showed that the variance follows a linear relationship,

$$\mu_n(t) = 4M_f Dt + \langle x_0^2 \rangle + \langle y_0^2 \rangle, \tag{98}$$

where

$$\langle x_0^2 \rangle = \iint_{\mathbb{R}^2} w(x, y, 0)x^2\mathrm{d}x\mathrm{d}y, \quad \langle y_0^2 \rangle = \iint_{\mathbb{R}^2} w(x, y, 0)y^2\mathrm{d}x\mathrm{d}y.$$

Fitting the variance of the spatial distribution of bleached material with a straight line, the gradient of which is precisely $4M_f D$, returns an estimate of D. The variance method is a significant advantage that it will work for any radially symmetric initial post-bleach profile, although only for pure diffusion systems.

1.5.4 *Maximum entropy methods*

So far we have only considered models with one or two diffusivity coefficients. However, a biological molecule may exist in multiple states with different diffusive properties. That is, it may be stably incorporated into many different complex molecules of different diffusivities. Supposing that there is negligible conversion between the different diffusive states on the time scale of the FRAP experiment, there will arise a heterogeneous fluorescence recovery which is the weighted sum of several pure diffusion fluorescence recoveries. Let

$$1 - \tilde{f}(x, y, t; D_i, r_i)$$

be the normalised fluorescence intensity at point (x, y) and time t for a pure diffusion system with diffusivity D_i and bleach region radius r_i. The general heterogeneous diffusive recovery can be written as

$$f(x, y, t) = 1 - \sum_{i=1}^{n_D} k_i \tilde{f}(x, y, t; D_i, r_i), \tag{99}$$

where n_D is the number of diffusive states. It is possible to attempt to fit (99) to empirical data using a conventional least-squares method. However, the quality of the data required to achieve a reliable fit increases substantially with n_D [154]. Furthermore, it would require extensive model selection to determine the optimal value of n_D. An alternative approach is to assume that n_D is large and then attempt to find the optimal probability, k_i, that a molecule has diffusivity D_i, $\forall i$. To give an example, Xiong *et al.* [153] have taken this approach, employing a maximum entropy method. The principle of maximum entropy states that the probability distribution which best represents a system is the one which maximises the Shannon-Claude entropy [155],

$$S = -\sum_{i=1}^{n} k_i \log k_i. \tag{100}$$

The entropy, S is maximised subject to the least squares constraint $\chi^2 = M$, where M is the total number of data points. The test statistic χ^2 is given by

$$\chi^2 = \sum_{k=1}^{n_t} \sum_{j=1}^{n_y} \sum_{i=1}^{n_x} \frac{(f(x_i, y_j, t_k) - f_{\text{data}}(x_i, y_j, t_k))^2}{\sigma(x_i, y_j, t_k)^2}, \tag{101}$$

where f_{data} is empirical fluorescence microscopy data, f is the simulated data given by formula (99) and σ^2 is the corresponding variance. The maximum entropy method ensures that the final distribution does not contain more features than statistically warranted by the data [156]. Deriving a probability distribution of diffusivities is far less limiting than estimating a small

number of parameter values. However, the maximum entropy method has greater computational cost than conventional least squares which may force the user to model $f(x, y, t)$ analytically (Xiong *et al.* chose the rectangular FRAP model of Deschout *et al.* [65]). Consequently, this method cannot realistically benefit from accurate descriptions of photobleaching, cell geometry, boundary conditions and other attractive features which are exclusive to numerical models.

1.5.5 *Fisher information and parameter estimability*

Parameter estimability can be predicted using the Fisher information matrix. Suppose we are given data collected at a set of time points, t_i. Let $\Delta t = t_{i+1} - t_i$, for all i, be the time step, so that $1/\Delta t$ is the frame rate of the imaging process; let Y_i be the fluorescence recovery curve data values at the sample times t_i; and $F_i(\theta) = F(t_i; \theta)$, with θ being the vector of model parameters. Assuming the fundamental accuracy of the model, empirical data may be described by the sum of the output of the mathematical model and a stochastic variable such that,

$$Y_i = F_i(\theta) + \sigma_i \xi_i, \tag{102}$$

where the ξ_i are normally distributed random variables and σ_i the standard deviations which account for the scale of the observational uncertainty. The objective function may be defined as

$$\phi(\theta) = \sum_i \frac{(F_i(\theta) - Y_i)^2}{2\sigma_i^2}, \tag{103}$$

where the factor of 2 is purely for notational convenience. The global minimum of the objective function, θ^*, corresponds to a maximum likelihood estimate of model parameters [157]. The Fisher information matrix is the Hessian matrix of the objective function [158, 159],

$$I_{\mu\nu} = \left. \frac{\partial^2 \phi}{\partial \theta_\mu \partial \theta_\nu} \right|_{\theta^*}, \tag{104}$$

where μ and ν are parameter indices. Substituting (103) into (104) gives

$$I_{\mu\nu} = \sum_i \frac{1}{\sigma_i^2} \frac{\partial}{\partial \theta_\mu} \left(F_i \frac{\partial F_i}{\partial \theta_\nu} - Y_i \frac{\partial F_i}{\partial \theta_\nu} \right) = \sum_i \frac{1}{\sigma_i^2} \left(\frac{\partial F_i}{\partial \theta_\mu} \frac{\partial F_i}{\partial \theta_\nu} + \frac{\partial^2 F_i}{\partial \theta_\nu \partial \theta_\mu} (F_i - Y_i) \right).$$

If the system is well-described by the model, then $F_i(\theta^*) = Y_i$, so the term involving second derivatives vanishes and the FIM simplifies to

$$I_{\mu\nu} = \sum_i \frac{1}{\sigma_i^2} \left. \frac{\partial F_i}{\partial \theta_\mu} \frac{\partial F_i}{\partial \theta_\nu} \right|_{\theta^*}. \tag{105}$$

If an eigenvector of the FIM has a large corresponding eigenvalue, then the combination of parameters given by the eigenvector is identifiable [160]. Models containing a mixture of identifiable and non-identifiable parameters (for which the eigenvalues of the FIM are spread across a logarithmic scale) are said to be sloppy [157]. Sloppy models characteristically include certain parameters, or combinations of parameters, in which even substantial variations do not significantly affect the behaviour of the dependent variables. In geometric terms, there is a manifold within the space of model parameters which is approximately a flat minimum of the objective function so that the unique exact global minimum cannot be easily located. Numerous sloppy models have been identified within the mathematical biology literature, usually those with large numbers of parameters [160–163].

1.6 YAP BIOLOGY

Since the discovery of YAP by Sudol [193], research on YAP has turned into a burgeoning field [169, 170]. The objective of this section is to review the literature on YAP, with a particular focus on its role in cancer and its regulation. We introduce the topic with a general discussion of certain biological phenomena: protein localisation, contact inhibition of proliferation and the related topic of mechanotransduction.

1.6.1 *Protein localisation*

Localisation refers to the distribution of protein molecules within a cell. Proteins may have different functions in different cellular compartments such as the cytoplasm, the nucleus, or various organelles. The same protein may serve different purposes depending on whether it is localised to the nucleus or the cytoplasm, for example. Hence protein localisation provides cells with an economical method to achieve functional diversity [166]. Aberrant protein localisation is associated with an array of human pathologies, crucially including a variety of cancers [167, 168].

1.6.2 *Contact inhibition of proliferation and mechanotransduction*

Cells possess the ability to detect the presence of adjacent cells and mechanical forces in their microenvironment. Sensing neighbouring cells is essential for tissue integrity. For example, contact inhibition of proliferation (cell–cell contact-induced arrest of cell growth) underlies homeostatic control of cell density and organ size [194, 195]. One of the characteristics of cancerous cells is their resistance to contact inhibition [164].

Many eukaryotic cells also possess the ability to convert local external mechanical cues into chemical signals which regulate cell behaviour [165]. These cues include three closely related factors; cell shape, internal cellular isometric tension and the stiffness of the extracellular matrix (ECM) [243–245]. The ECM is a collection of interstitial molecules which provide structural support to tissue. Its structural and mechanical properties are largely dependent upon three components; elastic fibres, collagen fibres, and proteoglycans. Elastic fibres endow tissue with extensibility, while collagen fibres provide material strength and increase the stiffness of the ECM. Proteoglycans have net negative electrostatic charge, attracting positively charged sodium ions and in turn attracting water via osmosis, ensuring

that the ECM and resident cells remain extensively hydrated, thereby contributing to the compressive stiffness of connective tissue [183].

Cells are in constant isometric tension with the ECM. The equilibrium of forces in the tissue microenvironment controls the shape and volume of cells while also regulating their function via mechanosensing [224, 225]. It has been suggested that cells probe the external resisting forces of the ECM and neighbouring cells by developing internal forces of increasing magnitude [228–230]. On a larger scale, regulation of cells by mechanical cues maintains organ functionality, while changes in the mechanical balance between the cells and the surrounding environment result in tissue malfunctioning or malignant transformation. Mechanical properties of tumours differ substantially from normal cells and tissues. Changes in stiffness or elasticity regulate pro-metastatic behaviours of cancer cells [226,227]. Localisation of YAP has been revealed as one of the central components in the regulation of contact inhibition and mechanotransduction [194, 196, 197].

1.6.3 *YAP at the roots of cancer*

YAP is a transcription co-regulator which, when localised to the nucleus, interacts with the TEAD family of transcription factors [4,171] to regulate gene transcription [3, 205–207]. Specifically, YAP regulates a coherent gene programme involved in proliferation, DNA replication and repair, nucleotide metabolism, and mitosis [1–3], while inhibiting apoptotic genes [4]. YAP promotes various processes which require cell proliferation. It is essential for embryonic development, organ growth and wound healing [5, 8–10]. YAP also regulates angiogenesis (the formation of new blood vessels by the extension of existing vasculature) and heart development [201–204].

Given its role in promoting tissue growth, it is not surprising that YAP dysregulation causes a variety of pathologies linked with hyperproliferation [1, 196, 197, 200]. The forced expression of YAP leads to organ overgrowth and, almost invariably, to the development of cancer [8, 9]. Indeed,

there is evidence that YAP is specifically required for proliferation and survival of tumour cells [8, 9]. Aberrant expression or localisation of YAP has been identified in a broad range of aggressive human solid cancers [11–13]. Furthermore YAP overexpression is associated with poor prognosis in cancer patients [14, 15] and is thought to confer resistance to targeted therapies [15].

Aside from promoting cell growth and inhibiting apoptosis, YAP also regulates the expression of genes that drive cell migration, potentially enhancing the risk of metastasis in cancer [3,208]. Additionally, YAP possesses the ability to 'reprogram' mature differentiated cells into their corresponding less-differentiated progenitors, possibly leading to the creation of cancer stem cells [5–7]. There is a compelling case for targeting YAP for therapeutic intervention, and the search for small-molecule drugs that are able to modulate YAP activity is an active field of research [9, 12]

1.6.4 *YAP and contact inhibition*

The Hippo pathway

YAP is a well-documented target of the Hippo signalling pathway [174]. Hippo is a highly evolutionarily conserved pathway which controls organ size and functions as a tumour-suppressor [172]. The upstream regulators of YAP include various kinases (proteins capable of phosphorylating other proteins [173]) involved in the Hippo pathway, including MST1/2, MOB1A/B and LATS1/2. MST1/2 and phosphorylated WW45 bind to form an active enzyme which phosphorylates LATS1/2. Phosphorylated LATS1/2 in turn binds with MOB1A/B to form a complex capable of phosphorylating YAP [8, 170, 174, 209].

Phosphorylated YAP is marked for degradation by proteasomes [176]. Additionally, phosphorylation creates binding sites for regulatory 14-3-3 proteins which form an anchor sequestering YAP in the cytoplasm [175],

though this effect alone is not sufficient fully to prevent YAP transport into the nucleus [177].

The suppression of YAP by the Hippo pathway is one of the cell regulatory mechanisms responsible for contact inhibition of proliferation [182]. The clearest link between YAP-mediated contact inhibition and Hippo is Merlin, a tumour-suppressor protein [178] and known upstream regulator of Hippo [8, 180, 209]. At low cell density, MST–LATS kinase complexes are inactive, and unphosphorylated YAP is free to enter the nucleus [288]. In confluent cell cultures, Merlin is preferentially located near to the tight junctions between adjacent cells, where it forms protein scaffolds [179] which promote the phosphorylation of LATS by MST/WW45 complexes. [180]. There is also evidence that Merlin negatively regulates YAP target gene expression by promoting the export of YAP from the nucleus [181].

αE-catenin

Another significant contact inhibition mechanism is the regulation of YAP by αE-catenin at adherens junctions (AJs). AJs are macromolecular complexes that mediate adhesion between cells [219, 220]. They are formed of various proteins, though the most relevant for our purposes is αE-catenin, a linking protein between AJs and the cell cytoskeleton, which has been identified as a mechanosensor at AJs [222, 223] essential for contact inhibition [194, 210].

Several studies have revealed important roles of AJ components in YAP regulation [194, 210, 216–218], and there is evidence that αE-catenin exerts tumour-suppressing functions by inactivating YAP [194, 210–213]. Cells possess the ability to sense mechanical stretching at AJs [214]. At high, but not low, cell density, YAP forms a tripartite complex with αE-catenin and 14-3-3 proteins [210]. Disengagement of cell–cell adhesions is sufficient to unleash YAP activity [215]. Similarly in αE-catenin-null cells, YAP has elevated nuclear concentration [194], which amounts to compelling evidence of YAP regulation by αE-catenin at AJs.

1.6.5 *Mechanotransduction and the ECM*

Many cells possess the ability to detect various physical signals in their surrounding environment, including mechanical forcing and ECM stiffness [242]. Under conditions of high ECM stiffness, cells tend to favour proliferation over apoptosis and experience reduced sensitivity to contact inhibition [187]. Softer substrates and cell crowding both act to diminish cell proliferation [243–245].

There is abundant evidence implicating YAP in mechanosensing. If YAP is knocked down, cells grown on a stiff substrate exhibit a phenotype similar to that of cells grown on soft substrate. On the other hand, overexpression of YAP in cells grown on a soft substrate causes cells to behave as if they were on a stiff substrate [177].

The regulation of YAP by mechanical forcing is dependent on the formation of actin stress fibres [239, 243]. Actins are a family of proteins that form microfilaments, and are a constituent of the cytoskeleton [233]. In response to mechanical forcing F-actin is polymerised to form stress fibres [18]. These stress fibres transmit forces to focal adhesions [231], structures which link the cell with the ECM [229, 232, 234]. Stress fibre formation is dependent on several proteins: the Rho family of GTPases, Rho-associated kinase enzymes (ROCK) and myosin light chain kinase [235–237]. Inhibition of any of these proteins prevents stress fibre formation and converts the cell to a state of low tensile forces [235–237] and also inactivates YAP [177, 238]. Conversely, F-actin polymerization results in increased activity of YAP [241].

In response to stress fibre formation, YAP is recruited to focal adhesions [185] where it is phosphorylated by Src family kinases. YAP which has been phosphorylated by Src is marked for translocation into the nucleus (note that phosphorylation by Src and phosphorylation by Hippo kinases occur at different locations on the YAP molecule, producing different effects) [186]. Src increases the association of YAP with TEAD and decreases its association with 14-3-3 proteins even where Hippo signalling remains ac-

tive [187]. A lower affinity for 14-3-3 proteins frees up a greater number of YAP molecules for translocation into the nucleus, while a greater affinity for TEAD anchors YAP molecules to chromatin in the nucleus, reducing the number of molecules available for export to the cytoplasm [149]. Some studies have suggested that Src has an inhibitory effect on LATS, which might decrease the inhibitory phosphorylation of YAP by the Hippo pathway [184, 240].

There is another important mechanism by which mechanical forcing, mediated by focal adhesions, activates YAP, dependent upon connections between focal adhesions and the nucleus. There are actomyosin fibres running from focal adhesions to the apical surface of the nucleus [246]. Contractile force generated by actomyosin activity flattens the nucleus and opens up nuclear pores. Such an opening increases the rate of YAP import without affecting the export rate [247]. To be clear, if YAP diffused passively across the nuclear membrane, opening nuclear pores would equally increase both the import and export rate. However, YAP, like other large proteins, is actively transported between the nucleus and cytoplasm using energy [302]. This process of stretching nuclear pores therefore increases the rate at which the cell is able to selectively import YAP into the nucleus, rather than increasing the rate of bidirectional passive transport between the nucleus and cytoplasm.

1.6.6 *Wnt signalling and heat shock factors*

Wnts are a family of growth factors involved in cell proliferation, stem cell expansion, regeneration, and tumorigenesis [254, 255]. The core of the Wnt pathway is the regulation of its nuclear transducer β-catenin by a cytoplasmic destruction complex, consisting of other proteins. The arrival of a Wnt ligand causes functional inactivation of the destruction complex, resulting into β-catenin accumulation [254]. YAP is a component of the β-catenin

destruction complex. Thus, whenever Wnt signalling is inactive, YAP is sequestered in the cytoplasm in the destruction complex [198, 199].

Recent research has revealed Wnt signalling as a link between YAP and heat shock factor 1 (HSF1) [258]. HSF1 is a regulatory protein that enhances cellular survival in the face of heat stress. In tumours, HSF1 promotes cancer cell survival and metastasis [256, 257]. HSF1 targets genes that promotes malignant behaviour in cancer by activating YAP via Wnt signalling [258].

1.6.7 *YAP feedback loop in fibroblasts*

While YAP is a target of various mechanisms including the Hippo pathway and mechanical forces, it also has the power to regulate these mechanisms, creating a feedback loop. YAP also controls the expression of upstream regulators of the Hippo pathway [248–250] and of the cytoskeletal machinery [18, 251–253]. YAP transcriptionally controls FA formation and cytoskeleton stability, in turn determining cell mechanics and the degree of cell adhesion to the ECM [251].

YAP feedback mechanisms are highly significant in fibroblasts, cells which possess the ability to remodel the ECM [16]. Fibroblasts respond to increases in ECM stiffness by increasing proliferation and suppressing apoptosis, but also by increasing collagen synthesis, thickening and strengthening the ECM [260, 261]. YAP knockdown reverses these outcomes, reverting cells to a state more indicative of a pliant ECM. [262, 263].

Consequently, there may arise a potent positive feedback loop whereby ECM rigidity activates YAP target gene transcription in fibroblasts, which in turn increases ECM rigidity [18]. 'Cancer-associated' fibroblasts, in which YAP is transcriptionally active, are found in many solid tumours, and are known to remodel the ECM to create conditions more favourable to metastasis [16, 17]. In some cases, they partially dissolve the ECM, creating tracks that enable subsequent cancer cell invasion [17].

1.6.8 *Summary of YAP biology*

The Hippo signalling pathway promotes the association between YAP and 14-3-3 anchoring proteins, sequestering YAP in the cytoplasm [170, 175, 177]. Src, activated downstream of stress fibre formation in response to mechanical forcing, possibly suppresses Hippo signalling to some extent and reduces the affinity between YAP and 14-3-3 proteins even if Hippo remains active. [184, 240]. YAP is involved in β-catenin destruction complexes. The presence of Wnt ligand releases YAP from these complexes, potentiating entry into the nucleus [198, 199]. In crowded environments, YAP forms a complex with αE-catenin, another route to cytoplasmic sequestration [194, 210–213].

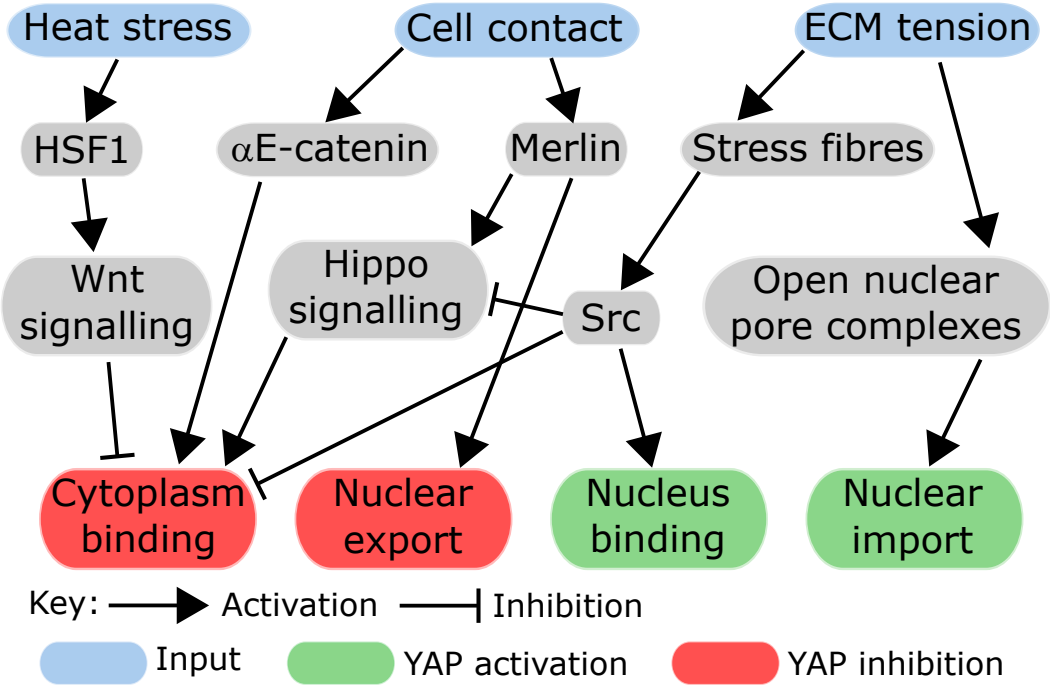


Figure 7: Schematic summary of YAP regulation.

There are connections between the apical surface of the nucleus and the cell outer membrane. External tension is transferred to the nucleus, pulling open nuclear pore complexes and facilitating YAP entry into the nucleus

[247]. Conversely, nuclear localised Merlin promotes the expulsion of YAP from the nucleus by active transport [181].

Src promotes interactions between YAP and TEAD, which by extension increases TEAD-mediated interactions between YAP and chromatin in the nucleus [187]. YAP binding with chromatin reduces the total rate of nuclear export just as binding with anchor proteins in the cytoplasm reduces the rate of nuclear import [149].

We notice that the direct regulation of YAP entry into the nucleus (and hence transcriptional activity) is influenced by four factors: binding reactions in the cytoplasm, nuclear export, binding reactions in the nucleus and nuclear import. The remainder of this thesis is dedicated to investigating these mechanisms quantitatively, in both cancer-associated and normal fibroblasts, using FRAP and FLIP empirical data.

2

MATHEMATICAL ANALYSIS OF FLUORESCENCE RECOVERY AFTER PHOTOBLEACHING

The focus of this chapter is the mathematical analysis of fluorescence recovery after photobleaching (FRAP). Many mathematical studies of FRAP have been published, mainly on pure diffusion models of FRAP, or two-species models with a single reversible binding reaction (reviewed in chapter 1). Analytically closed expressions for the fluorescence recovery curve have been derived for pure diffusion models, but it is not possible to do so in the case of two species models, though several approximations have been derived in limit cases. Although these well known approximation formulas are correct, to our knowledge they have never been formally mathematically derived. Furthermore, the precise form of the approximations, as they are commonly presented, may give the impression that fewer model parameters are estimable, in certain circumstance, than is actually the case.

In this chapter, we both re-derive established asymptotic formulas and derive new generalisations using using formal asymptotic methods. Using Fisher Information, we then use our new extended formulas to derive sufficient conditions under which every parameter of a two species reaction-diffusion FRAP model may be estimated from empirical data. We will apply this analysis both to the conventional analysis of FRAP recovery curves, and to confocal scanning FRAP.

Next we turn our attention to more general FRAP models. We derive several new limiting case approximations of multi-species FRAP models.

We also show that FRAP analysis can theoretically be used, not only to quantify model parameters, but also to deduce qualitative results, such as the order of reaction with systems with more than two interacting chemical species.

2.1 MATHEMATICAL MODEL

In its most general form, the FRAP model is based on a reaction-transport equation,

$$\frac{\partial \mathbf{u}}{\partial t} = \mathbf{f}(\mathbf{u}, \mathbf{x}, t) - \nabla \cdot (\mathbf{J}(\mathbf{u}, x, t)), \tag{106}$$

where $\mathbf{u}(\mathbf{x}, t) = (u_1(\mathbf{x}, t), \ldots, u_n(\mathbf{x}, t))^T$ is the vector of concentrations of each of species, u_i at spatial position $\mathbf{x} \in \mathbb{R}^m$ ($m = 1, 2, 3$) and time $t \in \mathbb{R}$. The vector-valued function $\mathbf{f} : \mathbb{R}^n \times \mathbb{R}^m \times \mathbb{R} \to \mathbb{R}^n$ gives the rates of conversion between each species due to chemical reaction. The flux term, $\mathbf{J} : \mathbb{R}^n \times \mathbb{R}^m \times \mathbb{R} \to \mathbb{R}^n$ determines the type of transport to which the chemical species, u_i, are subjected.

To begin with, we consider the single reversible reaction,

$$\mathrm{A} + \mathrm{B} \underset{\mathrm{k}^-}{\overset{\bar{k}^+}{\rightleftharpoons}} \mathrm{C},$$

though we consider more general problems in in sections 2.3, 2.4 and 2.5. The law of mass action implies that, in a well-mixed system, the concentrations of A, B and C evolve according to

$$\begin{cases} \frac{\mathrm{d}[\mathrm{A}]}{\mathrm{d}t} = -\bar{k}^+[\mathrm{A}][\mathrm{B}] + k^-[\mathrm{C}], \\ \frac{\mathrm{d}[\mathrm{B}]}{\mathrm{d}t} = -\bar{k}^+[\mathrm{A}][\mathrm{B}] + k^-[\mathrm{C}], \\ \frac{\mathrm{d}[\mathrm{C}]}{\mathrm{d}t} = \bar{k}^+[\mathrm{A}][\mathrm{B}] - k^-[\mathrm{C}], \end{cases} \tag{107}$$

where [X] denotes the concentration of X. In FRAP, a protein under investigation is tagged with a fluorescent probe. We assume that the system reaches steady state before the beginning of the experiment, so that

$[A] = [A]^*$, $[B] = [B]^*$, $[C] = [C]^*$. Photobleaching does not degrade any protein and so does not perturb the concentrations [A], [B] or [C], which remain in equilibrium. Let u be the concentration of the fluorescent (not photobleached) protein A, and v be the concentration of fluorescent C (a complex which contains fluorescent A). The equations arising from FRAP on protein A, which model there free and bound protein fractions (u and v respectively), are then

$$\begin{cases} \frac{du}{dt} = -k^+ u + k^- v, \\ \frac{dv}{dt} = k^+ u - k^- v, \end{cases} \tag{108}$$

where $k^+ = \bar{k}^+[B] = \bar{k}^+[B]^*$ ($[B] = [B]^*$ because the system is in equilibrium).

2.1.1 *The FRAP forward reaction rate*

It is important to note that the rate of reaction in the FRAP equation (108), k^+, is distinct from the rate of reaction per unit concentration in the mass action equation (107), $\bar{k}^+$. The forward reaction rate constant, k^+, is dependent upon the equilibrium concentration of unoccupied binding sites at chemical equilibrium, $[B]^*$, and hence on the total concentration of protein, $A_T = [A] + [C]$ (the greater the total concentration of protein, the greater the fraction of occupied binding sites at equilibrium). To make this relationship explicit, let $B_T = [B] + [C]$ be the total binding site concentration. The steady state of (107) can be re-written as

$$\begin{cases} \bar{k}^+[A]^*[B]^* = k^-[C]^*, \\ [A]^* + [C]^* = A_T, \\ [B]^* + [C]^* = B_T. \end{cases} \tag{109}$$

We can express $k^+ = \bar{k}^+[\mathrm{B}]^*$ in terms of A_T by solving (109) for $[\mathrm{B}]^*$. Setting $\beta = k^- + \bar{k}^+(A_T - B_T)$, (109) reduces to a quadratic,

$$\bar{k}^+[\mathrm{B}]^* + \beta B - \bar{k}^+ B_T = 0,$$

which has solution,

$$k^+ = \frac{-\beta + \sqrt{\beta^2 + 4\bar{k}^+ k^- B_T}}{2}. \tag{110}$$

The second solution of the quadratic is discarded as it always yields a negative value of k^+, which is unphysical.

Suppose we were to increase the total protein concentration, A_T. As $A_T \to \infty$, $\beta \to \infty$. Likewise, as $\beta \to \infty$, $\sqrt{\beta^2 + 4\bar{k}^+ k^- B_T} \to \beta$ in which case (110) implies that $k^+ \to 0$.

As the total concentration of protein increases, the concentration of unoccupied binding sites at chemical equilibrium decreases hence, all other factors being equal, the association rate, k^+, also decreases. This result must be taken into consideration when comparing FRAP data from different cells (as in chapter 4). For example, suppose we were comparing measurements of k^+ in the nuclei of two different cells. The total concentration of a protein in the nucleus is affected by various factors, including nuclear import and export rates, and the total level of expression of the protein by the cell. Hence, k^+ is not a pure measure of the chemical properties of the protein (as $\bar{k}^+$ would be); rather, it is somewhat confounded by other factors not directly related to the chemical reaction under investigation.

2.2 TWO-SPECIES REACTION-DIFFUSION MODEL

In this section we will analyse the common [69–78] two species FRAP model. We assume that a diffusible molecular species, A, associates reversibly with a binding partner, B, to form a complex, C, according to

$$\mathrm{A} + \mathrm{B} \underset{\mathrm{k}^-}{\overset{\bar{k}^+}{\rightleftharpoons}} \mathrm{C}.$$

We further assume that B is homogeneously distributed. Under the assumption of mass action, the concentrations of A, B and C are governed by

$$\begin{cases} \frac{\partial[\mathrm{A}]}{\partial t} = -\bar{k}^+[\mathrm{A}][\mathrm{B}] + k^-[\mathrm{C}] + D_A\nabla^2[\mathrm{A}], \\ \frac{\partial[\mathrm{B}]}{\partial t} = -\bar{k}^+[\mathrm{A}][\mathrm{B}] + k^-[\mathrm{C}] + D_B\nabla^2[\mathrm{B}], \\ \frac{\partial[\mathrm{C}]}{\partial t} = \bar{k}^+[\mathrm{A}][\mathrm{B}] - k^-[\mathrm{C}] + D_C\nabla^2[\mathrm{C}], \end{cases} \tag{111}$$

where [X] denotes the concentration of X. In the course of the FRAP experiment, the concentrations [A], [B] and [C] are assumed not to change. The reaction is assumed to have reached equilibrium before the start of the experiment and, since FRAP does not eliminate any of the existing molecules, this equilibrium is unperturbed.

Let $u(\mathbf{x}, t)$ be the concentration of species A at point $\mathbf{x}$ and time t that is fluorescent (not photobleached), and $D_u = D_A$ be the diffusivity of A (note that photobleaching is assumed not to alter the diffusivity or reactivity of the molecules). Likewise, let $v(\mathbf{x}, t)$ be the concentration of the fluorescent C species and $D_v = D_C$ be its diffusivity. The resulting FRAP model is

$$\begin{cases} \frac{\partial u}{\partial t}(\mathbf{x}, t) = -k^+u(\mathbf{x}, t) + k^-v(\mathbf{x}, t) + D_u\nabla^2u(\mathbf{x}, t) - \alpha I(\mathbf{x}, t)u(\mathbf{x}, t), \\ \frac{\partial v}{\partial t}(\mathbf{x}, t) = +k^+u(\mathbf{x}, t) - k^-v(\mathbf{x}, t) + D_v\nabla^2v(\mathbf{x}, t) - \alpha I(\mathbf{x}, t)v(\mathbf{x}, t), \end{cases} \tag{112}$$

where $I(\mathbf{x}, t)$ is the intensity profile of the laser acting upon the sample, and α is the sensitivity of the fluorescent tag to photobleaching. For convenience we measure fluorescence in units such that $u_{\mathrm{eq}} + v_{\mathrm{eq}} = 1$, where u_{eq} and v_{eq} are the pre-bleach homogeneous steady states,

$$u_{\mathrm{eq}} = \frac{k^-}{k^+ + k^-}, \quad v_{\mathrm{eq}} = \frac{k^+}{k^+ + k^-}. \tag{113}$$

Due to conservation of mass, the concentration of bleached A is $u_{\mathrm{bleach}} = u_{\mathrm{eq}} - u$ and that of bleached C is $v_{\mathrm{bleach}} = v_{\mathrm{eq}} - v$.

2.2.1 *Radial symmetry*

For analytic purposes, we assume the system (254) to be radially symmetric. Let $r = \sqrt{x^2 + y^2}$, and non-dimensionalise by setting $r' = r/r_n$, where r_n is the radius of the bleach region of interest and $t' = k^+ t$. The resulting equations (setting $I = 0$) are

$$\begin{cases} \frac{\partial u}{\partial t'} = -u + \kappa v + \eta \frac{1}{r'} \frac{\partial}{\partial r'} \left(r' \frac{\partial u}{\partial r'} \right), \\ \frac{\partial v}{\partial t'} = u - \kappa v + \delta\eta \frac{1}{r'} \frac{\partial}{\partial r'} \left(r' \frac{\partial v}{\partial r'} \right), \end{cases} \tag{114}$$

where

$$\delta = D_v/D_u, \quad \kappa = k^-/k^+, \quad \eta = D_u/(k^+ r_n^2), \tag{115}$$

are positive dimensionless numbers. We solve the initial value problem for (114) on an infinite spatial domain with far field conditions

$$\lim_{r' \to \infty} u(r', t') = u_{\text{eq}}, \quad \lim_{r' \to \infty} v(r', t') = v_{\text{eq}}, \tag{116}$$

and initial conditions

$$u(r', 0) = U_0(r') = u_{\text{eq}} H(r' - 1), \quad v(r, 0) = V_0(r') = v_{\text{eq}} H(r' - 1), \tag{117}$$

where H is the Heaviside step function. Initial conditions (117) are appropriate if all available material inside the region of interest is bleached instantaneously.

We will show that the orders of magnitude of the dimensionless parameters η, κ and δ determine whether the model parameters, D_u, D_v, k^+ and k^- are estimable. The region of interest, ROI, is a disk of radius r_n,

$$\text{ROI} = \{r \mid r \leq r_n\} = \{r' \mid r' \leq 1\}. \tag{118}$$

Let $w(r, t) = u(r, t) + v(r, t)$. Strictly, the fluorescence intensity that would be observed with a scanning laser microscope is the convolution of w with the optical point spread function, as in equation (9) of section 1.1.4 (chapter

1). However, we assume that the point spread function is the Dirac delta function, so that the observed fluorescence is exactly w [61, 63]. Similarly, the recovery curve, F, is simply

$$F(t) = \frac{1}{\pi r_n^2} \int_{\text{ROI}} w(r,t) \mathrm{d}r. \tag{119}$$

It is also useful at this stage to introduce the following function,

$$\mathcal{F}_S(z) = e^{-z}(\mathbf{I}_0(z) + \mathbf{I}_1(z)), \tag{120}$$

where $\mathbf{I}_0$ and $\mathbf{I}_1$ are modified Bessel functions of the first kind. The function, $\mathcal{F}_S$, is the recovery curve of a single species pure diffusion system,

$$\frac{\partial \tilde{w}}{\partial t} = D\nabla^2 \tilde{w},$$

with step function initial conditions and far-field conditions, the recovery curve is [30]

$$\mathcal{F}_S\left(\frac{r_n^2}{2Dt}\right) = \begin{cases} \frac{1}{\pi r_n^2} \int_{\text{ROI}} \tilde{w}(r,t) \mathrm{d}r \text{ if } t > 0, \\ 0 \text{ if } t = 0. \end{cases} \tag{121}$$

Note that $\mathcal{F}_S(0) = 1$, as $\mathbf{I}_0(0) = 1$ and $\mathbf{I}_1(0) = 0$. Also, the well known large limit asymptotic expansion of $\mathbf{I}_\nu(z)$ [267],

$$\mathbf{I}_\nu(z) \sim \frac{e^z}{\sqrt{2\pi z}},$$

implies that

$$e^{-z}(\mathbf{I}_0(z) + \mathbf{I}_1(z)) \sim e^{-z}\left(\frac{e^z}{\sqrt{2\pi z}} + \frac{e^z}{\sqrt{2\pi z}}\right) = \sqrt{\frac{2}{\pi z}}.$$

The small and large argument limits of $\mathcal{F}_S$ are then

$$\lim_{z\to 0} \mathcal{F}_S = 1. \quad \lim_{z\to\infty} \mathcal{F}_S = 0, \tag{122}$$

which justifies the imposition of $\mathcal{F}_S(r_n^2/(2Dt))|_{t=0} = 0$ and implies that $\lim_{t\to\infty} \mathcal{F}_S(r_n^2/(2Dt)) = 1$.

The full reaction-diffusion equation (114) does not have closed form analytic solutions, however approximations are possible in asymptotic limiting cases of the dimensionless parameters η and κ.

2.2.2 *Asymptotic analysis*

In the following subsections, we will derive approximation formulas in several limiting cases of the FRAP model. We will make repeated use of the asymptotic series expansion,

$$\begin{cases} u(r,t) = u_0(r,t) + \epsilon u_1(r,t) + \epsilon^2 u_2(r,t) + \dots, \\ v(r,t) = v_0(r,t) + \epsilon v_1(r,t) + \epsilon^2 v_2(r,t) + \dots, \end{cases} \tag{123}$$

where ϵ is a dimensionless variable which will be defined as appropriate.

2.2.3 *Rapid equilibration ($\eta \gg 1$)*

The larger the dimensionless parameter η, the more rapidly the unbound protein equilibrates across the bleach region. Suppose that $\eta \to \infty$ and the product $\eta\delta$ converges to a finite limit ($\lim_{\eta\to\infty}(\delta\eta) \in [0,\infty)$), then the fluorescence recovery curve reduces to:

$$F(t) = \frac{k^-}{k^+ + k^-}\mathcal{F}_S\left(\frac{r_n^2}{2D_u t}\right) + \frac{k^+}{k^+ + k^-}\left(1 - e^{-k^- t}\left[1 - \mathcal{F}_S\left(\frac{r_n^2}{2D_v t}\right)\right]\right). \tag{124}$$

Proof. To derive formula (124) we used used matched asymptotics, splitting the problem over a long time scale and a short time scale.

Long time scale

We begin by setting $\epsilon = 1/\eta$. Substituting expansion (123) into the non-dimensional system (114) yields

$$\begin{cases} \epsilon\frac{\partial u_0}{\partial t'} = \epsilon(\kappa v_0 - u_0) + \nabla'^2 u_0 + \epsilon\nabla'^2 u_1 + O(\epsilon^2), \\ \frac{\partial v_0}{\partial t'} + \epsilon\frac{\partial v_1}{\partial t'} = (u_0 - \kappa v_0) + \epsilon(u_1 - \kappa v_1) + \frac{\delta}{\epsilon}\nabla'^2 v_0 + \delta\nabla'^2 v_1 + \delta\epsilon\nabla'^2 v_2 + O(\epsilon^2), \end{cases} \tag{125}$$

where $O(\epsilon^2)$ denotes all terms of order ϵ^2 and higher. As $\epsilon \to 0$, clearly we are left with $\nabla'^2 u_0 = 0$. By the radial symmetry assumption,

$$\nabla'^2 u_0 = \frac{1}{r'}\frac{\partial}{\partial r'}\left(r'\frac{\partial u_0}{\partial r'}\right) = 0,$$

which can be integrated to give

$$r' \frac{\partial u_0}{\partial r'} = c_1(t'),$$

for some function $c_1(t')$. Further integration yields,

$$u_0(r', t') = c_1(t') \log(r') + c_2(t').$$

However, this would imply $\lim_{r' \to 0} u_0(r', t') = -\infty$, which is physically impossible, so $c_1 = 0$ and we are left with

$$u_0(r', t') = c_2(t').$$

We are able to solve for c_2 by applying the far-field condition to u_0,

$$u_{\text{eq}} = \lim_{r' \to \infty} u_0 = \lim_{r' \to \infty} c_2 = c_2.$$

Hence $u_0 = u_{\text{eq}}$, a constant. Our assumption that $\delta\eta = \delta/\epsilon$ converges to a finite value is important; if δ/ϵ were divergent, then we would also have $\nabla'^2 v_0 = 0$, which would imply that $v_0 = v_{\text{eq}}$. In this case, the concentration of fluorescent material would be constant to first order, yielding a practically imperceptible fluorescence recovery for large η. With the constraint that the limit of δ/ϵ is finite, as $\epsilon \to 0$, (125) reduces to

$$\frac{\partial v_0}{\partial t'} = u_{\text{eq}} - \kappa v_0 + \frac{\delta}{\epsilon} \nabla'^2 v_0, \tag{126}$$

where we have used the fact that $u_0 = u_{\text{eq}}$. Noting that $k^+ u_{\text{eq}} = k^- v_{\text{eq}}$ and making the substitution $v_0(r, t) = v_{\text{eq}} - \tilde{v}(r, t)$, we arrive at

$$\frac{\partial \tilde{v}}{\partial t} = -k^- \tilde{v} + D_v \nabla^2 \tilde{v}, \tag{127}$$

where we should note that (127) has been restored to dimensional form. The solution to (127) subject to Dirac delta initial conditions is [264]

$$\tilde{v}(r, t) = \frac{1}{4\pi D_v t} \exp\left(-k^- t\right) \exp\left(-\frac{r^2}{4 D_v t}\right). \tag{128}$$

The general solution of (127) is the product convolution of the initial condition with the Green's function,

$$\tilde{v}(x,y,t) = \iint_{\mathbb{R}^2} \tilde{v}(x',y',0)\frac{1}{4\pi D_v t}\exp\left(-k^- t - \frac{(x'-x)^2+(y'-y)^2}{4D_v t}\right)\mathrm{d}x\mathrm{d}y, \tag{129}$$

which can be translated to polar coordinates by setting $x = r\cos\theta$, $y = y\sin\theta$, $x' = r'\cos\theta'$, and $y' = r'\cos\theta'$ to give

$$\tilde{v}(r',t) = \frac{\exp(-k^- t)}{4\pi D_v t}\int_0^{2\pi}\int_0^{\infty}\tilde{v}(r',0)\exp\left(-\frac{r'^2+r^2-2rr'\cos(\theta'-\theta)}{4D_v t}\right)r'\mathrm{d}r'\mathrm{d}\theta'$$

$$= \frac{\exp(-k^- t)}{4\pi D_v t}\int_0^{\infty}\tilde{v}(r',0)\exp\left(-\frac{r'^2+r^2}{4D_v t}\right)\left[\int_0^{2\pi}\exp\left(\frac{rr'\cos(\theta'-\theta)}{2D_v t}\right)\mathrm{d}\theta'\right]r'\mathrm{d}r'. \tag{130}$$

Since $\cos\theta'$ is a 2π-periodic function,

$$\int_0^{2\pi}\exp\left(\frac{rr'\cos(\theta'-\theta)}{2D_v t}\right)\mathrm{d}\theta' = \int_0^{2\pi}\exp\left(\frac{rr'\cos(\theta')}{2D_v t}\right)\mathrm{d}\theta'$$

$$= 2\int_0^{\pi}\exp\left(\frac{rr'\cos(\theta')}{2D_v t}\right)\mathrm{d}\theta', \tag{131}$$

At this stage we can introduce the following integral definition of the Bessel function $\mathbf{I}_0$ [268],

$$\mathbf{I}_0(z) = \frac{1}{\pi}\int_0^{\pi}\exp(z\cos(\theta))\mathrm{d}\theta. \tag{132}$$

Now (131) and (132) may be applied to (130), yielding

$$\tilde{v}(r,t) = \frac{\exp(-k^- t)}{2D_v t}\int_0^{\infty}\tilde{v}(r',0)\exp\left(-\frac{r'^2+r^2}{4D_v t}\right)\mathbf{I}_0\left(\frac{rr'}{2D_v t}\right)r'\mathrm{d}r'. \tag{133}$$

We may make further progress by use of the integral identities [265]

$$\int_0^{\infty}\mathbf{J}_\nu(\alpha s)\mathbf{J}_\nu(\beta s)\exp(-\rho^2 s^2)s\mathrm{d}s = \frac{1}{2\rho^2}\exp\left(-\frac{\alpha^2+\beta^2}{4\rho^2}\right)\mathbf{I}_\nu\left(\frac{\alpha\beta}{2\rho^2}\right), \tag{134}$$

where $\mathbf{J}_\nu$ is an order ν Bessel function of the first kind, and [266]

$$\int_0^{r_n} r'\mathbf{J}_0(sr')\mathrm{d}r' = \frac{1}{s^2}\int_0^{sr_n} z\mathbf{J}_0(z)\mathrm{d}z = \frac{r_n}{s}\mathbf{J}_1(r_n s). \tag{135}$$

By applying (134) to (133) with $\alpha = r$, $\beta = r'$, $\rho^2 = D_v t$, $\nu = 0$ we get

$$\tilde{v}(r,t) = v_{\text{eq}} \exp(-k^- t) \int_0^\infty \left[\int_0^{r_n} \mathbf{J}_0(r's) r' \mathrm{d}r' \right] \mathbf{J}_0(rs) \exp(-D_v t s^2) s \mathrm{d}s$$

$$= v_{\text{eq}} r_n \exp(-k^- t) \int_0^\infty \mathbf{J}_0(rs) \mathbf{J}_1(r_n s) \exp(-D_v t s^2) \mathrm{d}s. \tag{136}$$

At this point we define the normalised integral $\tilde{V}(t) = \left(\int_{r \le r_n} \tilde{v} \mathrm{d}A \right) / (\pi r_n^2)$, by which (136) becomes,

$$\tilde{V}(t) = \frac{2\pi v_{\text{eq}} r_n \exp(-k^- t)}{\pi r_n^2} \int_0^\infty \left[\int_0^{r_n} \mathbf{J}_0(rs) \mathrm{d}r \right] \mathbf{J}_1(r_n s) \exp(-D t s^2) \mathrm{d}s.$$

Then with further application of (135) we obtain

$$\tilde{V}(t) = 2 v_{\text{eq}} \exp(-k^- t) \int_0^\infty \frac{1}{s} \mathbf{J}_1^2(r_n s) \exp(-D_v t s^2) \mathrm{d}s.$$

Setting $z = r_n s$,

$$\tilde{V}(t) \exp(k^- t) = 2 v_{\text{eq}} \int_0^\infty \frac{1}{z} \mathbf{J}_1^2(z) \exp\left(-\frac{D_v t}{r_n^2} z^2 \right) \mathrm{d}z. \tag{137}$$

It is possible to reduce (137) to a much simpler expression by differentiating both sides with respect to t,

$$\frac{\mathrm{d}}{\mathrm{d}t} (\tilde{V}(t) \exp(k^- t)) = -2 v_{\text{eq}} \int_0^\infty \frac{D_v}{r_n^2} \mathbf{J}_1^2(z) \exp\left(-\frac{D_v t}{r_n^2} z^2 \right) z \mathrm{d}z.$$

Now (134) is once again applicable with $\alpha = \beta = 1$, $\rho^2 = D_v t / r_n^2$, and $\nu = 1$.

$$\int_0^t \frac{\mathrm{d}}{\mathrm{d}t'} (\tilde{V}(t') \exp(k^- t')) \mathrm{d}t' = -v_{\text{eq}} \int_0^t \frac{1}{t'} \exp\left(-\frac{r_n^2}{2 D_v t'} \right) \mathbf{I}_1 \left(\frac{r_n^2}{2 D_v t'} \right) \mathrm{d}t'$$

Firstly, define the characteristic diffusion time of the bound fraction as $\tau_D^v = r_n^2 / (4 D_v)$. Next make the substitution $\zeta = 2\tau_D^v / t'$, which implies that $\mathrm{d}t'/t' = -\mathrm{d}\zeta/\zeta$, hence

$$\tilde{V}(t) \exp(k^- t) - \tilde{V}(0) = -v_{\text{eq}} \int_{2\tau_D^v / t}^\infty \frac{1}{\zeta} \exp(-\zeta) \mathbf{I}_1(\zeta) \mathrm{d}\zeta \tag{138}$$

It is possible to make progress with (138) firstly by simply noticing that $\tilde{V}(0) = v_{\text{eq}}$. Secondly, motivated by an appropriate identity [269], we can see that

$$-\int \frac{1}{z} e^{-z} \mathbf{I}_1(z) \mathrm{d}z = e^{-z} (\mathbf{I}_0(z) + \mathbf{I}_1(z)) + c. \tag{139}$$

The well known asymptotic large limit expansion of $\mathbf{I}_\nu(z)$ [267],

$$\mathbf{I}_\nu(z) \sim \frac{e^z}{\sqrt{2\pi z}},$$

implies that

$$e^{-z}(\mathbf{I}_0(z) + \mathbf{I}_1(z)) \sim e^{-z}\left(\frac{e^z}{\sqrt{2\pi z}} + \frac{e^z}{\sqrt{2\pi z}}\right) = \sqrt{\frac{2}{\pi z}},$$

for large real values of z. It is then obvious that as $z \to \infty$

$$\lim_{z\to\infty} e^{-z}(\mathbf{I}_0(z) + \mathbf{I}_1(z)) = 0. \tag{140}$$

With formula (139) and limit (140), (138) becomes

$$\tilde{V}(t)\exp(k^- t) - v_{\text{eq}} = -v_{\text{eq}}\exp\left(-\frac{2\tau_D^v}{t}\right)\left(\mathbf{I}_0\left(\frac{2\tau_D^v}{t}\right) + \mathbf{I}_1\left(\frac{2\tau_D^v}{t}\right)\right),$$

equivalently,

$$\tilde{V}(t) = v_{\text{eq}}\exp(-k^- t)\left(1 - \exp\left(-\frac{2\tau_D^v}{t}\right)\left(\mathbf{I}_0\left(\frac{2\tau_D^v}{t}\right) + \mathbf{I}_1\left(\frac{2\tau_D^v}{t}\right)\right)\right).$$

The contribution to the fluorescence recovery due to v_0 is $F_v(t) = \left(\int_{r\le r_n} v_0(r,t)\mathrm{d}A\right)/(\pi r_n^2) = v_{\text{eq}} - \tilde{V}(t)$. Finally, we arrive at

$$F_v(t) = v_{\text{eq}} - v_{\text{eq}}e^{-k^- t}\left[1 - e^{-2\tau_D^v/t}\left(\mathbf{I}_0\left(\frac{2\tau_D^v}{t}\right) + \mathbf{I}_1\left(\frac{2\tau_D^v}{t}\right)\right)\right].$$

Recalling our definition of $\mathcal{F}_S$ and substituting $\tau_D^v = r_n^2/(4D_v)$, we are left with,

$$F_v(t) = v_{\text{eq}} - v_{\text{eq}}e^{-k^- t}\left(1 - \mathcal{F}_S\left(\frac{r_n^2}{2D_v t}\right)\right). \tag{141}$$

Short time scale

The above approximation breaks down over the short time scale, $t' = O(\epsilon)$, so it is helpful to introduce the re-scaling $t' = \epsilon\tau$, under which the asymptotic expansion (125) becomes

$$\begin{cases} \frac{\partial u_0}{\partial \tau} + \epsilon\frac{\partial u_1}{\partial \tau} = \epsilon(\kappa v_0 - u_0) + \nabla'^2 u_0 + \epsilon\nabla'^2 u_1 + O(\epsilon^2), \\ \frac{\partial v_0}{\partial \tau} + \epsilon\frac{\partial v_1}{\partial \tau} = \epsilon(u_0 - \kappa v_0) + \delta\nabla'^2 v_0 + \delta\epsilon\nabla'^2 v_1 + O(\epsilon^2), \end{cases} \tag{142}$$

which reduces to

$$\frac{\partial u_0}{\partial \tau} = \nabla'^2 u_0, \quad \frac{\partial v_0}{\partial \tau} = 0, \tag{143}$$

as $\epsilon \to 0$. The dynamics of u_0 are governed purely by diffusion, implying that, if we define F_u analogously to F_v such that

$$F_u(t) = \frac{1}{\pi r_n^2} \int_0^{2\pi} \int_0^{r_n} u_0(r,t) \mathrm{d}r\mathrm{d}\theta, \tag{144}$$

we conclude that

$$F_u(t) = u_{\mathrm{eq}} \mathcal{F}_S \left(\frac{r_n^2}{2D_u t} \right). \tag{145}$$

Noting that the total fluorescence recovery curve is given by $F(t) = F_u(t) + F_v(t)$, we have

$$F(t) = u_{\mathrm{eq}} \mathcal{F}_S \left(\frac{r_n^2}{2D_u t} \right) + v_{\mathrm{eq}} \left(1 - e^{-k^- t} \left[1 - \mathcal{F}_S \left(\frac{r_n^2}{2D_v t} \right) \right] \right). \tag{146}$$

Finally, substituting $u_{\mathrm{eq}} = k^-/(k^+ + k^-)$, $v_{\mathrm{eq}} = k^+/(k^+ + k^-)$, we arrive at

$$F(t) = \frac{k^-}{k^+ + k^-} \mathcal{F}_S \left(\frac{r_n^2}{2D_u t} \right) + \frac{k^+}{k^+ + k^-} \left(1 - e^{-k^- t} \left[1 - \mathcal{F}_S \left(\frac{r_n^2}{2D_v t} \right) \right] \right). \tag{147}$$

□

In physical terms, the fluorescence recovery in this case is bi-phasic, which can be observed in figure 8. Over the short time scale, there is a brief, diffusion-driven equilibration of the unbound protein. Over a longer time scale, the fluorescence recovery is limited by the rate at which protein dissociates from binding sites.

Figure 9 gives a sense of the shape of the objective function in this case. It is clear that the objective function attains its minimum value on a manifold, which is approximately a one dimensional straight line parallel to the D_u axis. In practical terms, this suggests that recovery curves with different values of k^+, k^- and D_v would be easily distinguishable. However, recovery curves with different values of D_u, all other parameters being equal, will be almost identical. This result suggests that estimation of all parameters

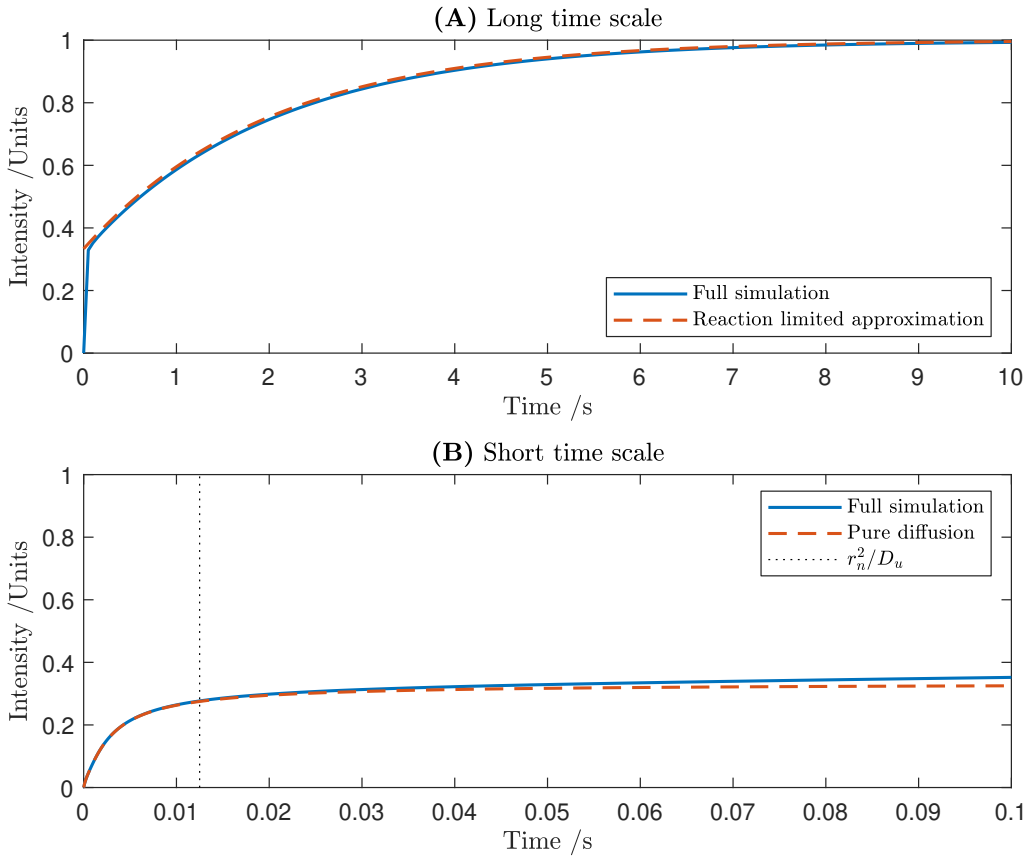


Figure 8: Numerically simulated fluorescence recovery curve with $\eta \gg 1$. (A) Long time scale recovery compared with the exponential model (149). (B) Short time scale recovery compared with a pure diffusion recovery with diffusivity D_u.

except D_u will be practicable. We will revisit this issue in section 2.2.5 where we derive the Fisher information matrix.

It is possible to derive a further sub-approximation of (147). The limits (122) state that $\lim_{z\to\infty} \mathcal{F}_S(z) = 0$ and $\lim_{z\to 0} \mathcal{F}_S(z) = 1$. Therefore,

$$\lim_{r_n^2/D_v\to\infty} \mathcal{F}_S\left(\frac{r_n^2}{2D_v t}\right) = 0, \quad \text{and} \quad \lim_{r_n^2/D_u\to 0} \mathcal{F}_S\left(\frac{r_n^2}{2D_u t}\right) = 1, \quad \forall t > 0.$$

Equivalently, if the slow diffusion time scale is sufficiently long ($r_n^2/D_v \gg 1$) and the time scale of rapid diffusion is sufficiently short ($r_n^2/D_u \ll 1$), then (124) reduces to the well known formula [70, 270, 271, 273, 282] for 'reaction limited' dynamics,

$$F(t) = \frac{k^-}{k^+ + k^-} + \frac{k^+}{k^+ + k^-}\left(1 - e^{-k^- t}\right) = 1 - \frac{k^+}{k^+ + k^-} e^{-k^- t}, \qquad (148)$$

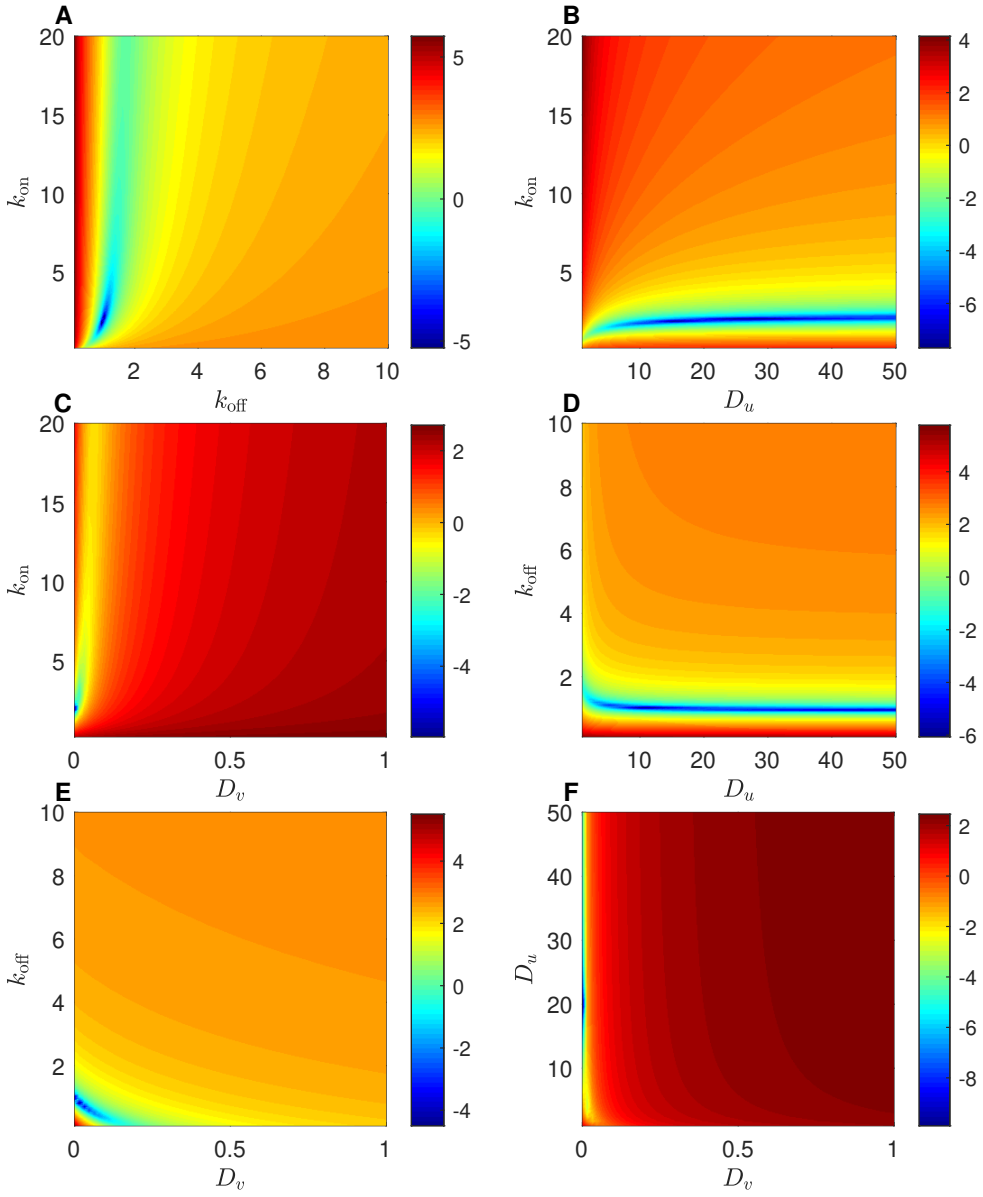


Figure 9: Logarithm of the numerically constructed objective function, $\log(\phi)$, in the rapid equilibration (reaction limited) regime. Colour indicates the size of the sum of square errors between a single simulated fluorescence recovery curve spanning 15 seconds (1024 data points) generated with parameter values $D_u = 20.0\mu m^2 s^{-1}, D_v = 0.00\mu m^2 s^{-1}, k^+ = 2.00 s^{-1}, k^- = 1.00 s^{-1}$, and a secondary simulated recovery curve generated with indicated parameter values. Each subplot displays variation in one of the six possible pairs of parameters, with the remaining two parameters held at the correct value in each case.

or equivalently,

$$F(t) = 1 - v_{\text{eq}} e^{-k^- t}. \tag{149}$$

2.2.4 *Intermediate equilibration ($\eta = O(1)$)*

No known approximations describe the dynamics of the intermediate case in which $\eta = O(1)$, but this does not mean that analysis is impossible. In order to derive formula (148) we introduced an asymptotic expansion in terms of a small parameter $\epsilon = 1/\eta$ to produce an approximation which holds whenever η is large. By extending this expansion to first order, we are able to produce an approximation which is accurate for somewhat smaller values of η and so gives some insight into the behaviour of the system as it approaches $\eta = O(1)$. The first-order extension of formula (148) is

$$F(t) = 1 - \frac{k^+}{k^+ + k^-} e^{-k^- t} - \frac{k^+ r_n}{3D_u} e^{-k^- t} \left(\frac{k^- + k^+ k^- t}{k^+ + k^-} \right), \tag{150}$$

which holds for $r_n^2 / D_v \ll 1$ and $t \gg \epsilon$.

Proof. We begin by taking the expansion (125) to first order, eliminating the 'zeroth' order terms, which we have already balanced, and cancelling ϵ throughout. Then, once again considering the limit $\delta, \epsilon \to 0$, we are left with

$$\begin{cases} \nabla'^2 u_1 = u_0 - \kappa v_0, \\ \frac{\partial v_1}{\partial t'} = +(u_1 - \kappa v_1) + \frac{\delta}{\epsilon} \nabla'^2 v_1. \end{cases} . \tag{151}$$

Since, u_0 and v_0 entirely satisfy the far field conditions (116), for consistency we impose

$$\lim_{r \to \infty} u_1(r', t') = 0 \quad \lim_{r \to \infty} v_1(r', t') = 0. \tag{152}$$

When $r' \geq 1$, we have $v_0(r', t') = v_{\text{eq}}$, hence $\nabla'^2 u_1 = u_{\text{eq}} - \kappa v_{\text{eq}} = 0$, which taken together with (152) implies that $u_1(r', t') = 0$ for $r' \geq 1$. Imposing the continuity condition $u_1(1^-, t') = 0$, we then solve for u_1 on $r' \leq 1$ to get

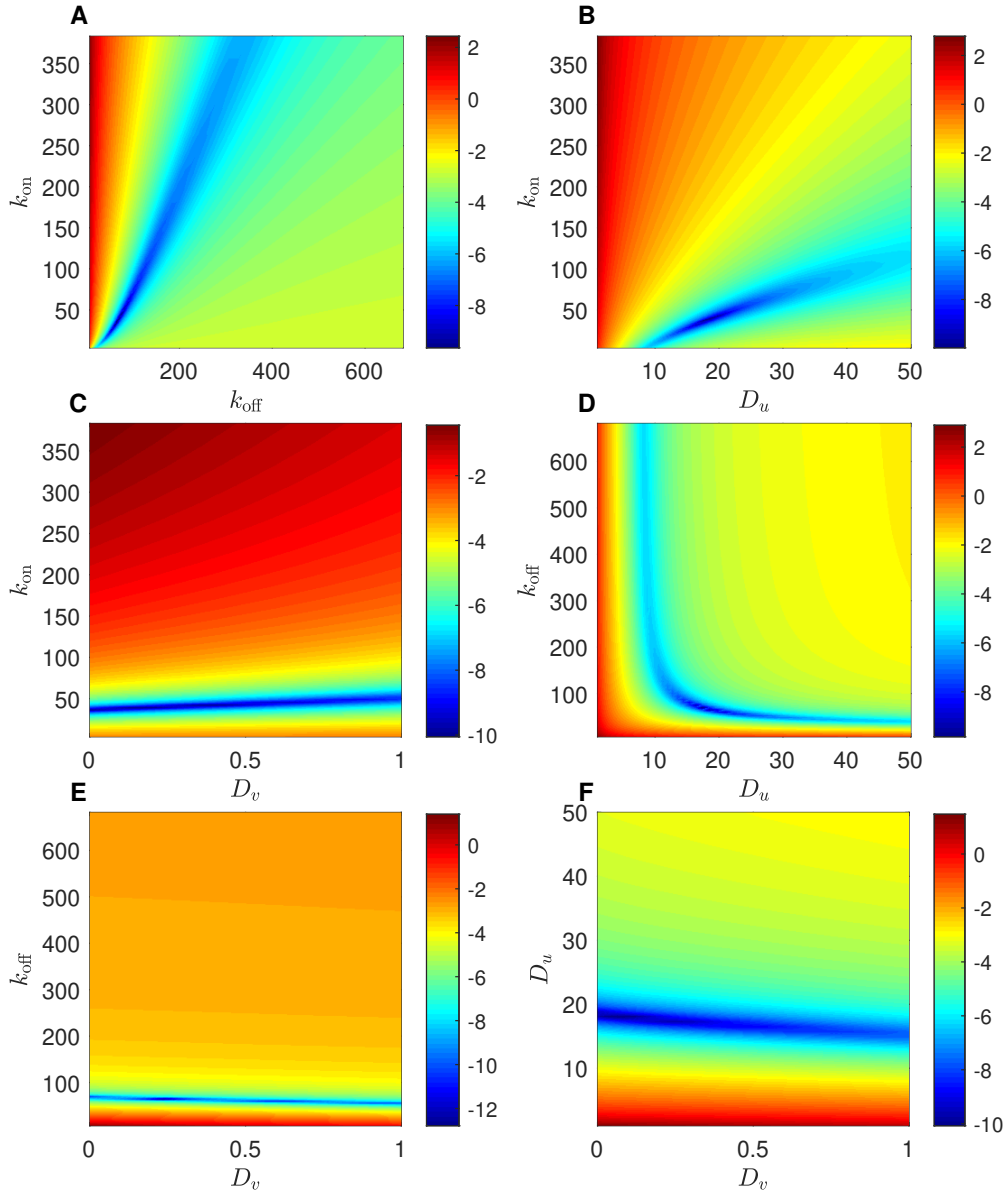


Figure 10: Logarithm of the numerically constructed objective function, $\log(\phi)$, in the intermediate equilibration regime. Colour indicates the size of the sum of square errors between a single simulated fluorescence recovery curve spanning 15 seconds (1024 data points) generated with parameter values $D_u = 18.1\mu m^2 s^{-1}, D_v = 0.0718\mu m^2 s^{-1}, k^+ = 38.3 s^{-1}, k^- = 68.2$, and a secondary simulated recovery curve generated with indicated parameter values. Each subplot displays variation in one of the six possible pairs of parameters, with the remaining two parameters held at the correct value in each case.

$$\frac{1}{r'}\frac{\partial}{\partial r'}\left(r'\frac{\partial u_1}{\partial r'}\right) = u_{eq} - \kappa v_{eq}(1 - e^{-\kappa t'}) = u_{eq}e^{-\kappa t'}, \tag{153}$$

which implies that

$$u_1(r', t') = \frac{1}{4} u_{\text{eq}} e^{-\kappa t'} (r'^2 - 1), \tag{154}$$

where we have used the symmetry condition $\frac{\partial u_1}{\partial r'}\Big|_{r=0} = 0$. Further analytic progress is possible in the limiting case $\delta/\epsilon \to 0$. Multiplying through (151) with the integrating factor $e^{\kappa t'}$ yields

$$e^{\kappa t'} \frac{\partial v_1}{\partial t'} + \kappa e^{\kappa t'} v_1 = \frac{\partial}{\partial t'} (v_1 e^{\kappa t'}) = \frac{1}{4} u_{\text{eq}} (r'^2 - 1). \tag{155}$$

Taking $v_1(r', 0) = 0$ as the initial condition, we are left with

$$v_1(r', t') = \frac{1}{4} u_{\text{eq}} (r'^2 - 1) t' e^{\kappa t'}. \tag{156}$$

We may precisely express the asymptotic expansion as follows

$$\begin{cases} u(r,t) = u_{\text{eq}} + \epsilon \frac{1}{4} u_{\text{eq}} e^{-\kappa t'} (r'^2 - 1) + O(\epsilon^2), \\ v(r,t) = v_{\text{eq}} (1 - e^{\kappa t'}) + \epsilon \frac{1}{4} u_{\text{eq}} t' e^{-\kappa t'} (r'^2 - 1) + O(\epsilon^2). \end{cases} \tag{157}$$

In dimensional form and truncated to first order, we have

$$\begin{cases} u(r,t) = u_{\text{eq}} \left(1 + \frac{k^+}{4D_u} e^{-k^- t} (r^2 - r_n^2)\right), \\ v(r,t) = v_{\text{eq}} \left(1 - e^{-k^- t} + \frac{k^+}{4D_u} k^- t e^{-k^- t} (r^2 - r_n^2)\right). \end{cases} \tag{158}$$

We are now able to evaluate the integral,

$$F(t) = \frac{1}{\pi r_n^2} \int_0^{2\pi} \int_0^{r_n} (u(r,t) + v(r,t)) \mathrm{d}r \mathrm{d}t, \tag{159}$$

to obtain the fluorescence recovery function,

$$F(t) = 1 - v_{\text{eq}} e^{-k^- t} - \frac{k^+ r_n}{3D_u} e^{-k^- t} (1 + k^- t), \tag{160}$$

□

In contrast with formula (149), D_u appears explicitly in (150), which implies that it could be estimated if the other model parameters were known. The full significance of this result will be discussed in section 2.2.7.

By contrasting figures 9 and 10, it can be seen quite clearly how reducing the value of the dimensionless parameter η changes the shape of the objective function. In particular, in the subplots that involve D_u (figure 10B,D,

and F), there is a clear unique local minimum of the objective function - in contrast with the manifold in figure 9B,D and F - which tends to support the prediction that D_u is estimable when $\eta = O(1)$ (at least when other parameters are known).

2.2.5 *Slow equilibration ($\eta \ll 1$)*

In the limit $\eta \to 0$, we define the small parameter by $\epsilon = \eta$. The fluorescence recovery approximation is simply

$$F(t) = \mathcal{F}_S\left(\frac{r_n^2}{2D_{\text{eff}}t}\right), \tag{161}$$

where D_{eff}, the effective diffusivity, is

$$D_{\text{eff}} = \frac{k^+ D_v + k^- D_u}{k^- + k^+}. \tag{162}$$

Proof. Set $\epsilon = \eta$ so that (114) becomes

$$\begin{cases} \frac{\partial u_0}{\partial t'} = \kappa v_0 - u_0 + \epsilon \nabla'^2 u_0, \\ \frac{\partial v_0}{\partial t'} = u_0 - \kappa v_0 + \delta\epsilon \nabla'^2 v_0 \end{cases} \tag{163}$$

Short time scale

In the limit $\epsilon \to 0$ (163) becomes

$$\begin{cases} \frac{\partial u_0}{\partial t'} = \kappa v_0 - u_0, \\ \frac{\partial v_0}{\partial t'} = u_0 - \kappa v_0. \end{cases} \tag{164}$$

Note that $w_0 = u_0 + v_0$ is time-invariant, as $\frac{\partial w_0}{\partial t'} = \frac{\partial u_0}{\partial t'} + \frac{\partial v_0}{\partial t'} = 0$. Further, we have $u_0 \to \kappa w_0/(1+\kappa), v_0 \to w_0/(1+\kappa)$ as $t' \to \infty$.

Long time scale

The time-invariant approximation of w_0 fails over sufficiently long time scales ($t' = O(1/\epsilon)$), which we may investigate by re-scaling time such that we have $t' = \tau/\epsilon$ for $\tau = O(1)$. Under this re-scaling (163) becomes

$$\begin{cases} \epsilon \frac{\partial u_0}{\partial \tau}(r', \tau/\epsilon) = \kappa v_0(r', \tau/\epsilon) - u_0(r', \tau/\epsilon) + \epsilon \nabla'^2 u_0(r', \tau/\epsilon), \\ \epsilon \frac{\partial v_0}{\partial \tau}(r', \tau/\epsilon) = u_0(r', \tau/\epsilon) - \kappa v_0(r', \tau/\epsilon) + \delta\epsilon \nabla'^2 v_0(r', \tau/\epsilon). \end{cases} \tag{165}$$

Adding the two equations in system (165) neutralises the zeroth order terms

$$\frac{\partial u_0}{\partial \tau} + \frac{\partial v_0}{\partial \tau} = \nabla'^2 u_0(r', \tau/\epsilon) + \delta \nabla'^2 v_0, (r', \tau/\epsilon), \tag{166}$$

where we have cancelled ϵ throughout. As $\epsilon \to \infty$, $t' \to \infty$, leaving $u_0 = \kappa w_0/(1+\kappa), v_0 = w_0/(1+\kappa)$. Therefore, (166) becomes

$$\frac{\partial w_0}{\partial \tau} = \left(\frac{\kappa}{1+\kappa} + \frac{\delta}{1+\kappa} \right) \nabla'^2 w_0. \tag{167}$$

At this point it is convenient to re-dimensionalise, finally yielding

$$\frac{\partial w_0}{\partial t} = \frac{k^- D_u + k^+ D_v}{k^+ + k^-} \nabla^2 w_0 = D_{\text{eff}} \nabla^2 w_0, \tag{168}$$

hence the total fluorescence concentration recapitulates the behaviour of a pure diffusion system and the fluorescence recovery function is

$$F(t) = \mathcal{F}_S \left(\frac{r_n^2}{2 D_{\text{eff}} t} \right). \tag{169}$$

□

As the recovery curve (161) depends only on D_{eff}, this is the only estimable combination of parameters. As $\eta \to 0$, a manifold within the parameter space, defined by (162), emerges upon which the value of the objective function is approximately zero, which is clearly visible in any subplot of figure 11. No pair of parameters could be estimated even if the values of the other two were known. It would be necessary to determine three of the parameters to determine the fourth. If the diffusivities, D_u and D_v, could

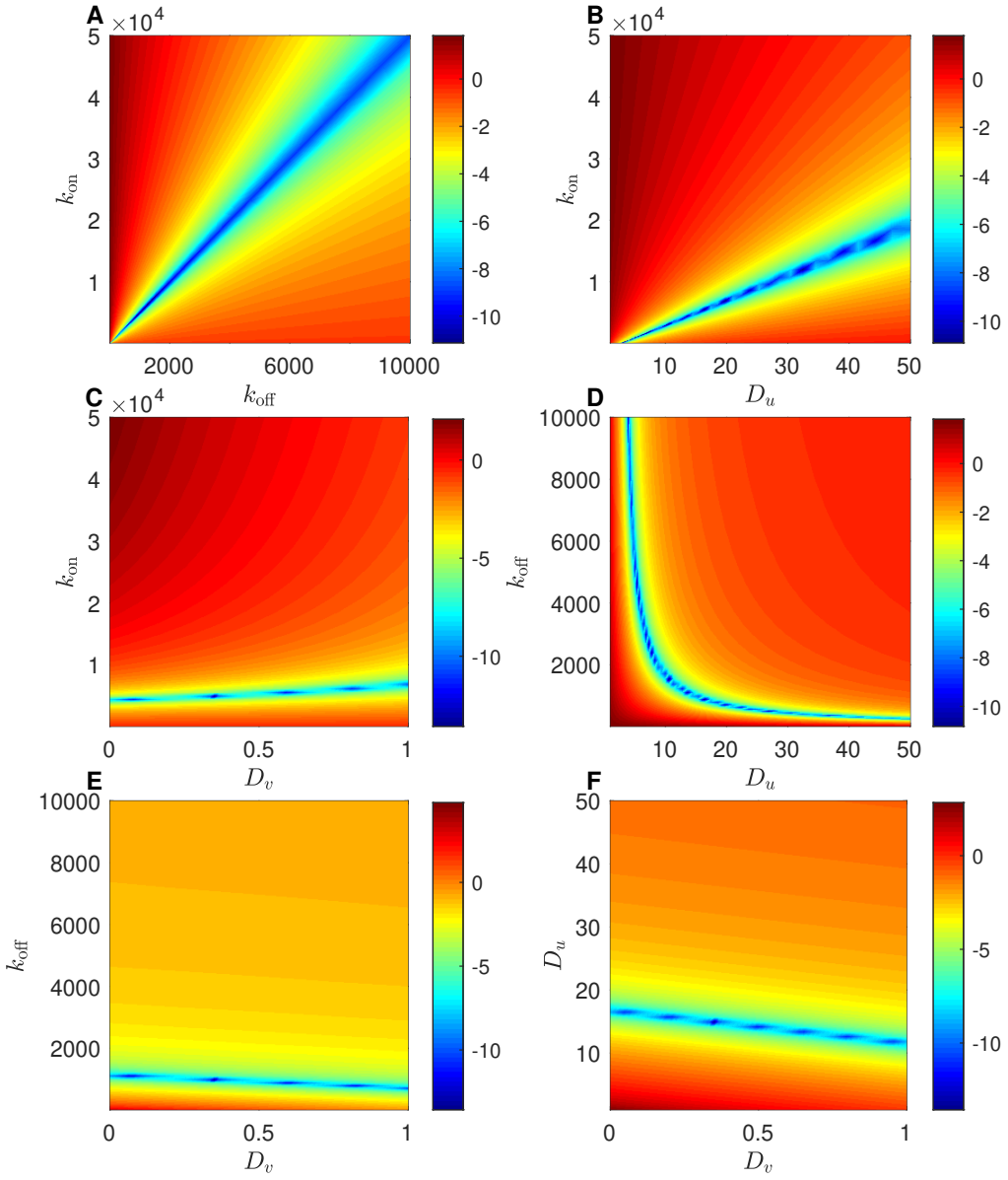


Figure 11: Logarithm of the numerically constructed objective function, $\log(\phi)$, in the slow equilibration (effective diffusion) regime. Colour indicates the size of the sum of square errors between a single simulated fluorescence recovery curve spanning 15 seconds (1024 data points) generated with parameter values $D_u = 15.0\mu m^2 s^{-1}, D_v = 0.374\mu m^2 s^{-1}, k^+ = 1000 s^{-1}, k^- = 5000$, and a secondary simulated recovery curve generated with indicated parameter values. Each subplot displays variation in one of the six possible pairs of parameters, with the remaining two parameters held at the correct value in each case.

be independently determined, then at most the ratio of the reaction rates, $\kappa = k^-/k^+$ could be estimated.

Like the rapid equilibration case, the slow equilibration recovery is biphasic. The early phase consists of a rapid convergence to local chemical equilibrium between the bound and unbound species (v and u respectively) which is imperceptible because it does not alter the total concentration of fluorescent protein, w.

Dissimilar reaction rates ($\kappa \gg 1$)

If we take $\kappa \to \infty$, we find that $u_{\text{eq}} = \kappa/(1+\kappa) \to 1$, so almost all available material will be in the unbound state, and the system will be closely approximated by pure diffusion. The recovery curve is

$$F(t) = \mathcal{F}_S\left(\frac{r_n^2}{2D_u t}\right). \tag{170}$$

Since,

$$D_{\text{eff}} = \frac{D_v + \kappa D_u}{\kappa + 1}, \tag{171}$$

it is clear that $D_{\text{eff}} \to D_u$ as $\kappa \to \infty$. In effect, the $\kappa \gg 1$ case coincides with the $\eta \ll 1$ case, except that $\kappa = k^-/k^+$ could not be estimated in the $\kappa \gg 1$ case even if D_u and D_v could be independently measured.

Dissimilar reaction rates ($\kappa \ll 1$)

As $\kappa \to 0$ almost all available molecules are in a bound state, such that the recovery curve can be approximated by

$$F(t) = \mathcal{F}_S\left(\frac{r_n^2}{2D_v t}\right), \tag{172}$$

and D_v is the only measurable parameter. As $\kappa \to 0$, $D_{\text{eff}} \to D_v$, so this case coincides with the $\eta \ll 1$ case, except that κ itself is always inestimable.

Fisher information and parameter estimation

In this section we derive the Fisher information matrix from the ($\eta \gg 1$) asymptotic formula (124). Recalling the definition given in section 1.5.5, the Fisher information matrix is

$$I_{\mu\nu} = \sum_i \frac{1}{\sigma_i^2} \frac{\partial F_i}{\partial \theta_\mu} \frac{\partial F_i}{\partial \theta_\nu}\bigg|_{\theta^*}. \tag{173}$$

where $F_i = F(t_i)$ (F is defined in (124)), and θ_μ and θ_ν are model parameters. The eigenvalues of the Fisher information matrix (173) derived from formula (124) are plotted in figure 12 (see below for a derivation). One of the eigenvalues (figure 12A) is many orders of magnitude smaller than the other three. On this basis we expect that there will be a manifold within the parameter space which represents a flat minimum of the objective function,

$$\phi(\theta) = \sum_i (F(t_i;\theta) - F_{\text{data}}(t_i))^2, \tag{174}$$

$$\Delta t \ll \frac{r_n^2}{D_u}. \tag{175}$$

Returning briefly to figure 12A, it is quite clear that the magnitude of the smallest eigenvalue is increased as Δt decreases and r_n increases. Interestingly, two other eigenvalues (figure 12C and D) visibly decline, for fixed Δt, as r_n increases. Nonetheless, it is clear that every model parameter is estimable in this case provided condition (175) holds.

Derivation of the FIM

We begin by differentiating the function

$$\mathcal{F}_S(z) = e^{-z}(\mathbf{I}_0(z) + \mathbf{I}_1(z)),$$

using the identities,

$$\frac{\mathrm{d}}{\mathrm{d}z}\mathbf{I}_0(z) = \mathbf{I}_1(z), \tag{176}$$

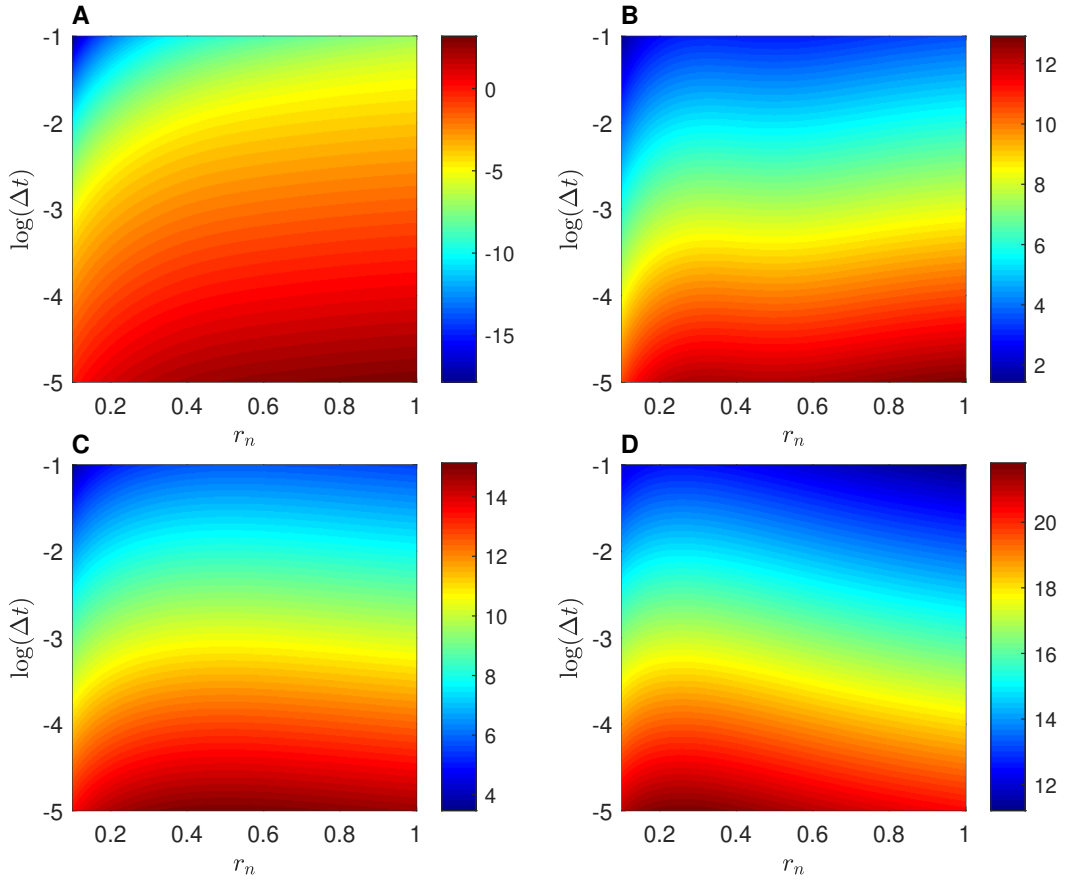


Figure 12: Logarithm of the eigenvalues, $\log(\lambda_i)$, of the Fisher information matrix computed from formula (124) for different values of the r_n and Δt. Each subplot corresponds to one of the four eigenvalues, (A) λ_1, (B) λ_2, (C) λ_3 and (D) λ_4.

and

$$\frac{\mathrm{d}}{\mathrm{d}z}\mathbf{I}_\alpha(z) = \mathbf{I}_{\alpha-1}(z) + \frac{\alpha}{z}\mathbf{I}_\alpha(z) \therefore \frac{\mathrm{d}}{\mathrm{d}z}\mathbf{I}_1(z) = \mathbf{I}_0 + \frac{1}{z}\mathbf{I}_1(z). \tag{177}$$

From (176) and (177) it follows that

$$\frac{\mathrm{d}\mathcal{F}_S}{\mathrm{d}z} = -\frac{e^{-z}\mathbf{I}_1(z)}{z}. \tag{178}$$

Then, taking $z = (r_n^2)(2Dt)^{-1}$ it remains to apply to chain rule to conclude that

$$\frac{\partial}{\partial D}\mathcal{F}_S\left(\frac{r_n^2}{2Dt}\right) = \frac{e^{-\frac{r_n^2}{2Dt}}\mathbf{I}_1\left(\frac{r_n^2}{2Dt}\right)}{D}. \tag{179}$$

It follows that

$$\frac{\partial F}{\partial D_u} = \frac{k^-}{k^+ + k^-}\frac{e^{-\frac{r_n^2}{2D_u t}}\mathbf{I}_1\left(\frac{r_n^2}{2D_u t}\right)}{D_u}, \tag{180}$$

and

$$\frac{\partial F}{\partial D_v} = \frac{k^+}{k^+ + k^-} e^{-k^- t} \frac{e^{-\frac{r_n^2}{2D_v t}} \mathbf{I}_1\left(\frac{r_n^2}{2D_v t}\right)}{D_v}. \tag{181}$$

It follows from the quotient rule that

$$\frac{\partial F}{\partial k^+} = \frac{k^- e^{-k^- t}\left(\mathcal{F}_S\left(\frac{r_n^2}{2D_v t}\right) + e^{k^- t} - \mathcal{F}_S\left(\frac{r_n^2}{2D_u t}\right) e^{k^- t} - 1\right)}{(k^+ + k^-)^2}, \tag{182}$$

and

$$\frac{\partial F}{\partial k^-} = \frac{k^+ e^{-k^- t}\left(\mathcal{F}_S\left(\frac{r_n^2}{2D_v t}\right)(1 + k^+ t) + e^{k^- t} - (k^+ + k^-)t - \mathcal{F}_S\left(\frac{r_n^2}{2D_u t}\right) e^{k^- t} - 1\right)}{(k^+ + k^-)^2}. \tag{183}$$

Now that we have explicitly derived the partial derivatives of F with respect to each of the four model parameters, we can define the matrix

$$I_i = \begin{pmatrix} \left(\frac{\partial F}{\partial D_u}\right)^2 & \frac{\partial F}{\partial D_u}\frac{\partial F}{\partial D_v} & \frac{\partial F}{\partial D_u}\frac{\partial F}{\partial k^+} & \frac{\partial F}{\partial D_u}\frac{\partial F}{\partial k^-} \\ \frac{\partial F}{\partial D_u}\frac{\partial F}{\partial D_v} & \left(\frac{\partial F}{\partial D_v}\right)^2 & \frac{\partial F}{\partial D_v}\frac{\partial F}{\partial k^+} & \frac{\partial F}{\partial D_v}\frac{\partial F}{\partial k^-} \\ \frac{\partial F}{\partial D_u}\frac{\partial F}{\partial k^+} & \frac{\partial F}{\partial D_v}\frac{\partial F}{\partial k^+} & \left(\frac{\partial F}{\partial k^+}\right)^2 & \frac{\partial F}{\partial k^+}\frac{\partial F}{\partial k^-} \\ \frac{\partial F}{\partial D_u}\frac{\partial F}{\partial k^-} & \frac{\partial F}{\partial D_v}\frac{\partial F}{\partial k^-} & \frac{\partial F}{\partial k^+}\frac{\partial F}{\partial k^-} & \left(\frac{\partial F}{\partial k^-}\right)^2 \end{pmatrix}(t_i). \tag{184}$$

Then the Fisher information matrix is simply,

$$I = \sum_i \frac{1}{\sigma_i^2} I_i. \tag{185}$$

2.2.6 *Parameter identifiability in static laser FRAP*

Here we summarise the conditions which guarantee parameter identifiability in static laser FRAP modelling. Suppose we have a theoretical recovery curve based on the solution to a mathematical model $F(t;\theta)$ for parameter values θ, and some recovery curve data $F_{\text{Data}}(t)$. Recall that in static laser FRAP the only observable quantity is the convolution of fluorescent protein concentration, w, and laser intensity. Under our assumptions this is simply

$$F(t) = \frac{1}{\pi r_n^2} \int_{\text{ROI}} w(r,t)\mathrm{d}r.$$

The objective function, ϕ, is then defined as the residual sum of squared errors,

$$\phi(\theta) = \sum_i (F(t_i;\theta) - F_{\text{Data}}(t_i))^2. \tag{186}$$

The model includes four physical parameters that are unknown, $\theta = (D_u, D_v, k^+, k^-)$ and two experimental parameters: r_n, the radius of the bleach region of interest and $\Delta t = t_{i+1} - t_i$, the time interval between data points.

All model parameters are estimable if $\eta \gg 1$, when condition (175) holds. This means that we require the following conditions on the physical parameters

$$\frac{k^-}{k^+} = O(1), \quad D_v \ll D_u, \tag{187}$$

and the following conditions on the experimental parameters

$$\frac{D_u}{k^+ r_n^2} \ll 1 \quad \Delta t \ll \frac{r_n^2}{D_u}. \tag{188}$$

These results imply that smaller bleach region radius and higher frame rate data acquisition are generally preferable in principle. However, this is not necessarily practical; r_n cannot be reduced arbitrarily as the resolution of an optical system is limited by diffraction.

2.2.7 *Parameter identifiability scanning laser FRAP*

Scanning laser FRAP, unlike static laser FRAP, may yield a detailed recording of an entire cell. In this case, we may attempt to fit the total fluorescence $w(\mathbf{x}, t)$, not just the recovery curve $F(t)$. Under the assumption of radial symmetry, let

$$w(r, t;\theta) = u(r, t;\theta) + v(r, t;\theta), \tag{189}$$

for some parameter values, θ, and let $w_{\text{Data}}(r,t)$ be some appropriate fluorescence microscopy data. The objective function in this case is defined as

$$\phi_{\text{space}}(\theta) = \sum_i \sum_j (w_{\text{Data}}(r_j,t_i) - w(r_j,t_i))^2. \tag{190}$$

It has already been observed that the process of averaging across the bleach region of interest to compute the recovery curve effectively destroys a significant amount of information [41, 275], so we expect that it will be advantageous to define the objective function as in (190). Here we will propose simple conditions to ensure parameter estimability in confocal scanning FRAP.

Once again, we have four physical parameters, $\theta = (D_u, D_v, k^+, k^-)$, though this time we have three experimental parameters: Δr, the length scale of a pixel of the micrograph, Δt, the duration of one frame, and L, the length scale of the whole field of view.

We could, in principle, construct a recovery curve, F_1, of radius r_n so that $\eta = D_u/(k^+ r_n) \gg 1$ provided that $\Delta r < r_n$ (clearly we cannot have a recovery curve radius smaller than one pixel),

$$F_1(t_i;\theta) = \sum_{\{j|r_j \le r_n\}} (w_{\text{Data}}(r_j,t_i) - w(r_j,t_i))^2.$$

As we saw in section 2.2.3, we could use this recovery curve to estimate k^+, k^- and D_v, but not necessarily D_u except for very high frame rate data. Likewise, we could construct a second recovery curve, F_2, of radius r_n' so that $\eta' = D_u/(k^+ r_n') = O(1)$ provided that $L > r_n'$.

$$F_2(t_i;\theta) = \sum_{\{j|r_j \le r_n'\}} (w_{\text{Data}}(r_j,t_i) - w(r_j,t_i))^2.$$

From the results of section 2.2.4 (formula (150)) we know that D_u will be estimable if $\eta' = O(1)$ or greater, as long as the other model parameters are known, but this is certainly the case because estimates can be obtained from the first recovery curve of radius r_n. However, certainly all the information contained within F_1 and F_2 is contained within w (indeed, w contains information about the fluorescence recovery on all length scales between Δr

and L). Therefore, fitting w by minimising ϕ_{space} will produce accurate estimates of all desired parameters. In summation, we expect that all model parameters will be estimable as long as

$$\frac{k^-}{k^+} = O(1), \quad D_v \ll D_u, \tag{191}$$

and

$$\frac{D_u}{k^+ \Delta r^2} \gg 1, \quad \frac{D_u}{k^+ L^2} \lesssim 1. \tag{192}$$

There is also an extremely weak implicit constraint on Δt, that the frame rate is not so low that the fluorescence recovery is totally imperceptible. These theoretical predictions are tested numerically in chapter 3.

2.3 GENERAL RESULTS FOR MULTI-SPECIES MODEL

In the next sections, 2.4 and 2.5, we will consider some special cases of multi-species FRAP models. We will make repeated use of a handful of general results which we will discuss in detail here and then reference later on to avoid repetition. We begin with the n species linear reaction-diffusion system

$$\frac{\partial \mathbf{u}}{\partial t} = K\mathbf{u} + D\nabla^2 \mathbf{u}, \tag{193}$$

where $\mathbf{u} = (u_1, \ldots, u_n)^T$ is the vector of concentrations, K is an $n \times n$ matrix of rank $n-1$ and D is a diagonal matrix. Here K contains all the reaction rates, and D contains all the diffusivities. There is a unique homogeneous steady state of (193), $\mathbf{u}_{\text{eq}} = ((u_{\text{eq}})_1, \ldots, (u_{\text{eq}})_n)^T$ which satisfies

$$K\mathbf{u}_{\text{eq}} = 0, \quad \sum_{j=1}^{n} (u_{\text{eq}})_j = 1.$$

Equation (193) is subject to the initial conditions

$$u_j(r, 0) = (u_{\text{eq}})_j H(r - r_n), \quad \forall j \in \{1, \ldots, n\},$$

where H is the Heaviside step function, and far-field conditions

$$\lim_{r \to \infty} u_j(r, 0) = (u_{\text{eq}})_j, \quad \forall j \in \{1, \ldots, n\}. \tag{194}$$

The four general notions which can be invoked to derive approximation formulas for multi-species systems are as follows, and are discussed in detail in the following sections.

- Linearity - the fluorescence recovery curve is the sum of the partial recovery curves for each species.
- Similar reaction rates - all reaction terms must be of a similar order of magnitude (equivalently, all reactions must occur of a similar time scale) or else the concentration of at least one of the species will be negligibly small.
- High mobility - any species which diffuses rapidly relative to the rate of reaction approximately obeys a pure diffusion equation.
- Effective diffusion - if the rate of reaction is much greater than the rate of diffusion of each species across the bleach region, the entire system will resemble a pure diffusion system with an effective diffusivity which can be explicitly calculated.

2.3.1 *Linearity*

The recovery curve is the average of the total fluorescent material across the bleach region

$$F(t) = \text{Avg}\left(\sum_{i=1}^{n} u_i(r,t)\right) = \frac{1}{\pi r_n^2}\int_{\text{ROI}} \sum_{i=1}^{n} u_i(r,t) r \mathrm{d}r\mathrm{d}\theta$$

$$= \sum_{i=1}^{n} \frac{1}{\pi r_n^2}\int_{\text{ROI}} u_i(r,t) r \mathrm{d}r\mathrm{d}\theta = \sum_{i=1}^{n} \text{Avg}\left(u_i(r,t)\right).$$

In a decoupled system, it suffices to solve for each species individually. The general solution is a linear combination of the solutions of each individual species.

2.3.2 *Balanced reaction rates*

Consider a reaction which converts between two species, u_i and u_j,

$$\mathrm{u}_i \underset{\mathrm{k}_{\mathrm{ij}}^-}{\overset{\mathrm{k}_{\mathrm{ij}}^+}{\rightleftharpoons}} \mathrm{u}_j.$$

We can define a dimensionless parameter $\kappa_{ij} = k_{ij}^-/k_{ij}^+$. For all i, j, $\kappa_{i,j} = O(1)$. At steady state, each reaction must be in equilibrium, so $k_{ij}^+(u_{\mathrm{eq}})_i = k_{ij}^+(u_{\mathrm{eq}})_j$, which means that $(u_{\mathrm{eq}})_i = \kappa_{ij}(u_{\mathrm{eq}})_j$. Due to the condition $\sum_{j=1}^n (u_{\mathrm{eq}})_j = 1$, we must have $0 \leq (u_{\mathrm{eq}})_j \leq 1$. Since $(u_{\mathrm{eq}})_j$ is upper-bounded by 1, in the limit as $\kappa_{ij} \to 0$, $(u_{\mathrm{eq}})_i = \kappa_{ij}(u_{\mathrm{eq}})_j \to 0$. Recall that $u_i(r,t) = (u_{\mathrm{eq}})_i$ in the pre-photobleached state. Clearly the concentration of fluorescent protein can never exceed the pre-bleach concentration, so $u_i(r,t) \leq (u_{\mathrm{eq}})_i \ \forall r, t$, which implies that $u_i(r,t) \to 0$ as $(u_{\mathrm{eq}})_i \to 0$. One can follow a similar argument to show that $u_j(r,t) \to 0$ as $\kappa_{ij} \to \infty$. We must have $\kappa_{ij} = O(1) \ \forall i, j$ or else the concentration of one or more of the species is approximately 0 and the order of the system is thereby reduced.

2.3.3 *High mobility*

Assume that the balanced reaction rates property (section 2.3.2) is satisfied. The general equations (193) can be rewritten as follows,

$$\frac{\partial u_i}{\partial t} = \sum_j (K_{ij}u_j) + D_{u_i}\nabla^2 u_i = \sum_{j \neq i} (K_{ij}u_j) - (-K_{ii})u_i + D_{u_i}\nabla^2 u_i. \tag{195}$$

The rate of change of concentration of species i is the sum of all reactions which convert species j to species $i \ \forall j$ minus the sum of the rates of all the reactions which consume species i, plus diffusion. Let $k_i = -K_{ii}$ and introduce dimensionless parameters, r', t', so that $r = r_n r'$, $t = t'/(k_i)$. Equation (195) becomes

$$\frac{\partial u_i}{\partial t'} = \frac{1}{k_i}\sum_{j \neq i} (K_{ij}u_j) - u_i + \eta_i \nabla'^2 u_i, \tag{196}$$

where $\eta_i = D_{u_i}/(k_i r_n^2)$. The species u_i is highly mobile in the limiting case where $\eta_i \to \infty$. Now consider a second species u_m,

$$\frac{\partial u_m}{\partial t'} = \frac{1}{k_i}\sum_j (K_{mj}u_j) + \delta_{mi}\eta_i \nabla^2 u_m, \tag{197}$$

where $\delta_{mi} = D_{u_m}/D_{u_i}$. The dynamics of u_m depend on the product $\delta_{mi}\eta_i$. If $\delta_{mi}\eta_i \to \infty$, then both u_m and u_i are highly mobile. However, if as $\eta_i \to \infty$, we allow $\delta_{mi} \to 0$ in such a way that the product $\delta_{mi}\eta_i$ converges to a finite value, then u_m is not highly mobile. Set $\eta_i = 1/\epsilon$ and (196) becomes

$$\frac{\partial u_i}{\partial t'} = \frac{1}{k_i}\sum_{j\neq i} (K_{ij}u_j) - u_i + \frac{1}{\epsilon_i}\nabla'^2 u_i \Rightarrow \nabla'^2 u_i + O(\epsilon) = 0. \tag{198}$$

As $\epsilon_i \to 0$, we are left with $\nabla'^2 u_i = 0$. To be consistent with the far-field conditions (194), we must have $u_i = (u_{\text{eq}})_i$. Hence, (197) becomes

$$\frac{\partial u_m}{\partial t'} = \frac{1}{k_i}\sum_{j\in R} (K_{mj}(u_{\text{eq}})_j) + \frac{1}{k_i}\sum_{j\notin R} (K_{mj}u_j) + \delta_{mi}\eta_i \nabla^2 u_m, \tag{199}$$

where $R \subset \{1, \ldots, n\}$ is the set of highly mobile species. If we re-scale (198) by setting $t = \epsilon_i \tau$, we get

$$\frac{\partial u_i}{\partial \tau} = \nabla'^2 u_i + O(\epsilon). \tag{200}$$

Over a short time scale $t = O(\epsilon)$, the highly mobile species follow independent, pure diffusion dynamics. Over the long time scale $t = O(1)$, the high mobility species reach equilibrium and thus their concentrations are constants in the remaining equations for the low mobility species. By linearity, the recovery curve, is the sum of the concentration averages of the high mobility species and the remaining low mobility species,

$$F(t) = \sum_{i\in R} \text{Avg}(u_i) + \text{Avg}\left(\sum_{i\notin R} u_i\right). \tag{201}$$

Since the high mobility species obey pure diffusion, (201) can be re-written as

$$F(t) = \sum_{i\in R} \mathcal{F}_S\left(\frac{r_n^2}{2D_{u_i}t}\right) + \text{Avg}\left(\sum_{i\notin R} u_i\right). \tag{202}$$

In summary, in systems with high mobility species, the solution can be found by setting all of the highly mobile species to their equilibrium values, $u_i = (u_{\text{eq}})_i$, solving the remaining system, then adding in the contributions to the recovery curve from the highly mobile species at the end.

2.3.4 *Effective diffusion*

Without loss of generality, let u_i be the species with the highest diffusivity, $D_{u_i} = \max_{j=1,\dots,n}\{D_{u_j}\}$. Recall the non-dimensionalised rate equation for an arbitrary species, u_m (which may be u_i),

$$\frac{\partial u_m}{\partial t'} = \frac{1}{k_i}\sum_j (K_{mj}u_j) + \delta_{mi}\eta_i \nabla'^2 u_m, \tag{203}$$

where $\delta_{mi} = D_{u_m}/D_{u_i} \in [0,1]$. If we set $\epsilon = \eta_i$ and take $\epsilon \to 0$, (203) reduces to

$$\frac{\partial u_m}{\partial t'} = \frac{1}{k_i}\sum_j (K_{mj}u_j). \tag{204}$$

As $t \to \infty$, (204) must converge to equilibrium at each point in space.

$$\lim_{t\to\infty} u_m = (u_{\text{eq}})_m \sum_{j=1}^{n} u_j = (u_{\text{eq}})_m w, \tag{205}$$

where $w = \sum_{j=1}^{n} u_j$. Now, set $t' = \tau/\epsilon$ and (203) becomes

$$\epsilon\frac{\partial u_m}{\partial \tau} = \frac{1}{k_i}\sum_j (K_{mj}u_j) + \delta_{mi}\epsilon \nabla'^2 u_m. \tag{206}$$

If we add each instance of (206) for $m = 1,\dots,n$, the reaction terms will cancel. We can then cancel ϵ, leaving

$$\sum_{m=1}^{n}\frac{\partial u_m}{\partial t} = \sum_{m=1}^{n}(D_{u_m}\nabla^2 u_m), \tag{207}$$

where we have returned to dimensional units. However, evaluating (207) in the limit case (205) yields

$$\frac{\partial w}{\partial t} = \sum_{i=1}^{n}((u_{\text{eq}})_i D_{u_i})\nabla^2 w_i,$$

which is equivalent to a pure diffusion system with effective diffusivity

$$D_{\text{eff}} = \sum_{i=1}^{n}((u_{\text{eq}})_i D_{u_i}).$$

2.4 MULTI-SPECIES SEQUENTIAL REACTIONS

In this section we consider the interactions between five molecules, A, B, C, D and E. A binds reversibly with B to form a complex C, which is stabilised by a further reversible reaction with D to form a second complex, E.

$$\begin{aligned} \mathrm{A} + \mathrm{B} &\underset{\mathrm{k}_1^-}{\overset{\bar{k}_1^+}{\rightleftharpoons}} \mathrm{C}, \\ \mathrm{C} + \mathrm{D} &\underset{\mathrm{k}_2^-}{\overset{\bar{k}_2^+}{\rightleftharpoons}} \mathrm{E}. \end{aligned}$$

Assuming mass action kinetics, the governing equations are

$$\begin{cases} \frac{\partial[\mathrm{A}]}{\partial t} = -\bar{k}_1^+[\mathrm{A}][\mathrm{B}] + k_1^-[\mathrm{C}] + D_A\nabla^2[\mathrm{A}], \\ \frac{\partial[\mathrm{B}]}{\partial t} = -\bar{k}_1^+[\mathrm{A}][\mathrm{B}] + k_1^-[\mathrm{C}] + D_B\nabla^2[\mathrm{B}], \\ \frac{\partial[\mathrm{C}]}{\partial t} = \bar{k}_1^+[\mathrm{A}][\mathrm{B}] - k_1^-[\mathrm{C}] - \bar{k}_2^+[\mathrm{C}][\mathrm{D}] + k_2^-[\mathrm{E}] + D_B\nabla^2[\mathrm{C}], \\ \frac{\partial[\mathrm{D}]}{\partial t} = -\bar{k}_2^+[\mathrm{C}][\mathrm{D}] + k_1^-[\mathrm{E}] + D_D\nabla^2[\mathrm{D}], \\ \frac{\partial[\mathrm{E}]}{\partial t} = \bar{k}_2^+[\mathrm{C}][\mathrm{D}] - k_2^-[\mathrm{E}] + D_C\nabla^2[\mathrm{E}]. \end{cases} \tag{208}$$

Suppose that species A is tagged, and a FRAP experiment is conducted. Only molecules that contain fluorescent A will be perceptible. Let u, v and w be the fluorescent fractions of A, B, and C respectively. The resulting FRAP system is

$$\begin{cases} \frac{\partial u}{\partial t} = -k_1^+ u + k_1^- v + D_u\nabla^2 u, \\ \frac{\partial v}{\partial t} = k_1^+ u - (k_1^- + k_2^+)v + k_2^- w + D_v\nabla^2 v, \\ \frac{\partial w}{\partial t} = k_2^+ v - k_2^- + D_w\nabla^2 w, \end{cases} \tag{209}$$

where the forward rates of reaction are given by

$$k_1^+ = \bar{k}_1^+[\mathrm{B}], \quad k_2^+ = \bar{k}_2^+[\mathrm{D}].$$

System (209) has a homogeneous steady state which satisfies

$$k_1^+ u_{\text{eq}} = k_1^- v_{\text{eq}}, \quad k_2^+ v_{\text{eq}} = k_2^- w_{\text{eq}}, \quad u_{\text{eq}} + v_{\text{eq}} + w_{\text{eq}} = 1,$$

which can be rearranged to give

$$u_{\text{eq}} = \frac{\kappa_1\kappa_2}{\kappa_1\kappa_2 + \kappa_2 + 1}, \; v_{\text{eq}} = \frac{\kappa_2}{\kappa_1\kappa_2 + \kappa_2 + 1}, \; w_{\text{eq}} = \frac{1}{\kappa_1\kappa_2 + \kappa_2 + 1}, \tag{210}$$

where the dimensionless parameters κ_1 and κ_2 are defined as

$$\kappa_1 = \frac{k_1^-}{k_1^+}, \quad \kappa_2 = \frac{k_2^-}{k_2^+}.$$

By the principle of effective diffusivity, if the reactive time scale of (209) is much faster than the diffusive time scale, the system will appear indistinguishable from a single species pure diffusion system with diffusivity,

$$D_{\text{eff}} = u_{\text{eq}} D_u + v_{\text{eq}} D_v + w_{\text{eq}} D_w = \frac{\kappa_1\kappa_2 D_u + \kappa_2 D_v + D_v}{\kappa_1\kappa_2 + \kappa_2 + 1}. \tag{211}$$

The system of equations (209) has no closed form solutions, however much like the two species model, we are able to derive approximation formulas in several limiting cases. In section 2.4.1 we consider the case where u is highly diffusive, w is immobile and v has some non-zero intermediate diffusivity. In section 2.4.2 we consider the case in which u and v are highly mobile but w is immobile, then in section 2.4.3 we consider the case where u is highly mobile but v and w are immobile. Having solutions in these particular cases is potentially useful as it theoretically enables us to determine the order of reaction when two proteins interact mutually dependently with an immobile binding partner, as explained in section 2.4.4.

2.4.1 *Three disparate diffusive time scales*

It is clear that E must be a larger molecule than C, which must be larger than A. It is therefore possible that A, C, and E have three disparate diffusive time scales. We begin by considering the case in which A is highly mobile ($D_u/(k_1^+ r_n^2) \to \infty$), E is immobile $D_w/r_n^2 \to 0$ and C has some intermediate

mobility. In this case, by the principle of high mobility, we can set $u = u_{\text{eq}}$ and attempt to solve the remaining system for v and w, which is

$$\begin{cases} \frac{\partial v}{\partial t} = k_1^+ u_{\text{eq}} - (k_1^- + k_2^+)v + k_2^- w + D_v \nabla^2 v, \\ \frac{\partial w}{\partial t} = k_2^+ v - k_2^- + D_w \nabla^2 w. \end{cases} \tag{212}$$

We can simplify (212) by making the substitution, $v = v_{\text{eq}} - \tilde{v}$, $w = w_{\text{eq}} - \tilde{w}$, to give

$$\begin{cases} \frac{\partial \tilde{v}}{\partial t} = -(k_1^- + k_2^+)\tilde{v} + k_2^- \tilde{w} + D_v \nabla^2 \tilde{v}, \\ \frac{\partial \tilde{w}}{\partial t} = k_2^+ \tilde{v} - k_2^- \tilde{w}. \end{cases} \tag{213}$$

Note that

$$\tilde{v}(r,0) = \tilde{v}_0(r) = \begin{cases} v_{\text{eq}}, r \leq r_n, \\ 0, r \leq r_n, \end{cases}$$

and

$$\tilde{w}(r,0) = \tilde{w}_0 = \begin{cases} w_{\text{eq}}, r \leq r_n, \\ 0, r \leq r_n. \end{cases}$$

System (213) does not have a closed form solution, but some analytical progress is possible by taking the Laplace transform,

$$V(s) = \mathcal{L}\{\tilde{v}\}, \quad W(s) = \mathcal{L}\{\tilde{w}\}.$$

The Laplace transform of the time derivative is

$$\mathcal{L}\left\{\frac{\partial \tilde{v}}{\partial t}\right\}(s) = \int_0^\infty \frac{\partial \tilde{v}}{\partial t}(r,t)e^{-st}\mathrm{d}t = \left[\tilde{v}e^{-st}\right]_0^\infty + s\int_0^\infty \tilde{v}e^{-st}\mathrm{d}t = sV - \tilde{v}_0(r),$$

and likewise for W. The Laplace transform of (213) is

$$\begin{cases} sV = -(k_1^- + k_2^+)V + k_2^- W + D_v \nabla^2 V + \tilde{v}_0, \\ sW = k_2^+ V - k_2^- W + \tilde{w}_0. \end{cases} \tag{214}$$

Clearly,

$$W = \frac{k_2^+ V + \tilde{w}_0}{s + k_2^-},$$

which can be substituted into, (214), yielding

$$sV + -(k_1^- + k_2^+)V + k_2^- \left(\frac{k_2^+ V + \tilde{w}_0}{s + k_2^-}\right) + D_v \nabla^2 V + \tilde{v}_0. \tag{215}$$

Equation (215) can be re-arranged to get

$$\nabla^2 V - \frac{s}{D_v}\left(1 + \frac{k_2^+ + k_1^-}{s + k_2^-} + \frac{k_1^- k_2^-}{s(s + k_2^-)}\right) V = -\frac{1}{D_v}\left(\tilde{v}_0 + \frac{k_2^- \tilde{w}_0}{s + k_2^-}\right). \quad (216)$$

We can then make the substitution

$$q^2 = \frac{s}{D_v}\left(1 + \frac{k_2^+ + k_1^-}{s + k_2^-} + \frac{k_1^- k_2^-}{s(s + k_2^-)}\right), \quad U = \frac{1}{D_v}\left(v_{\text{eq}} + \frac{k_2^- w_{\text{eq}}}{s + k_2^-}\right).$$

Then, (216) becomes

$$\nabla^2 V - q^2 V = \begin{cases} -U, r \leq r_n, \\ 0, r > r_n. \end{cases} \quad (217)$$

If we make the substitution $r = r'/q$, we end up with

$$\nabla'^2 V - V = \frac{\partial^2 V}{\partial r'^2} + \frac{1}{r'}\frac{\partial V}{\partial r'} - V^2 = \begin{cases} -\frac{U}{q^2}, r \leq r_n, \\ 0, r > r_n. \end{cases} \quad (218)$$

For $r > r_n$, (218) is Bessel's differential equation. For $r \leq r_n$, the substitution $V = U/q - V'$, reduces (218) to Bessel's equation. Hence,

$$\begin{cases} V = \frac{U}{q^2} - \alpha_1 \mathbf{I}_0(qr), r \leq r_n, \\ V = \alpha_2 \mathbf{K}_0(qr), r > r_n, \end{cases} \quad (219)$$

where $\mathbf{I}_0$ and $\mathbf{K}_0$ are modified Bessel functions of the first and second kind respectively. The solution, V, must not depend on $\mathbf{K}_0$ for $r \leq r_n$, nor on $\mathbf{I}_0$ for $r_n > r$, as $\mathbf{K}_0$ is divergent at $r = 0$, and $\mathbf{I}_0$ is diverges as $r \to \infty$. Continuity implies V and $\frac{\partial V}{\partial r}$ must coincide at $r = r_n$, so

$$\begin{cases} \alpha_1 \mathbf{I}_0(qr_n) + \alpha_2 \mathbf{K}_0(qr_n) = \frac{U}{q^2}, \\ \alpha_1 \mathbf{I}_1(qr_n) - \alpha_2 \mathbf{K}_1(qr_n) = 0. \end{cases}$$

It follows that

$$\alpha_1 = \frac{U r_n \mathbf{K}_1(qr_n)}{q},$$

We know that $u + v + w = u_{\text{eq}} + v_{\text{eq}} - \tilde{v} + w_{\text{eq}} - \tilde{w}$ since u is highly mobile. By assumption $u_{\text{eq}} + v_{\text{eq}} + w_{\text{eq}} = 1$, therefore $u + v + w = 1 - \tilde{v} - \tilde{w}$. The Laplace transform is

$$\mathcal{L}\{u + v + w\} = \frac{1}{s} - V - W = \frac{1}{s} - V - \frac{k_2^+ V + w_0}{s + k_2^-},$$

so the Laplace transform of the recovery curve is

$$\mathcal{L}\{F\} = \text{Avg}(\mathcal{L}\{u+v+w\}) = \frac{1}{s} - \left(1 + \frac{k_2^+}{s+k_2^-}\right)\text{Avg}(V) - \frac{w_{\text{eq}}}{s+k_2^-}. \quad (220)$$

Now we only require the average of V, which is

$$\text{Avg}(V) = \frac{1}{\pi r_n^2}\int_0^{2\pi}\int_0^{r_n}\left[\frac{U}{q^2} - \alpha_1 \mathbf{I}_0(qr)\right] r\mathrm{d}r\mathrm{d}\theta.$$

Using the fact that $\frac{\mathrm{d}\mathbf{I}_1}{\mathrm{d}r} = r\mathbf{I}_0$, we have that

$$\text{V} = \frac{U}{q^2} - \frac{2\alpha_1}{r_n q}\mathbf{I}_1(r_n q). \quad (221)$$

Finally, substituting the expression for V (221) into (220), using the definition of α_1, the Laplace transformed recovery curve is

$$\mathcal{L}(F) = \frac{1}{s} - \frac{1}{q^2 D_v}\left(v_{\text{eq}} + \frac{k_2^- w_{\text{eq}}}{s+k_2^-}\right)\left(1 + \frac{k_2^+}{s+k_2^-}\right)(1 - 2\mathbf{I}_1(r_n q)\mathbf{K}_1(qr_n)) - \frac{w_{\text{eq}}}{s+k_2^-},$$

which can be numerically inverted to yield $F(t)$.

2.4.2 *Two highly mobile species*

The analysis is considerably simpler if both A and C are highly mobile. Following the high mobility principle we can set, $u = u_{\text{eq}}$ and $v = v_{\text{eq}}$, then solve the remaining system, which is simply

$$\frac{\partial w}{\partial t} = k_2^-(w_{\text{eq}} - w) + D_w \nabla^2 w. \quad (222)$$

Equation (222) is virtually identical to the problem which was considered in section 2.2.3, so we can follow a similar procedure to get

$$F(t) = u_{\text{eq}}\mathcal{F}_S\left(\frac{r_n^2}{2D_u t}\right) + v_{\text{eq}}\mathcal{F}_S\left(\frac{r_n^2}{2D_v t}\right) + w_{\text{eq}}\left(1 - e^{-k_2^- t}\left[1 - \mathcal{F}_S\left(\frac{r_n^2}{2D_w t}\right)\right]\right). \quad (223)$$

If we let $r_n^2/D_v \to 0$ (hence $r_n^2/D_u \to 0$ also, as $D_u > D_v$) we are left with

$$F(t) = 1 - w_{\text{eq}} e^{-k_2^- t}\left[1 - \mathcal{F}_S\left(\frac{r_n^2}{2D_w t}\right)\right]. \quad (224)$$

Likewise, if $r_n^2/D_w \to \infty$ (w is immobile on the time scale of the experiment)

$$F(t) = 1 - w_{\text{eq}} e^{-k_2^- t}. \tag{225}$$

In this case the recovery curve of the three species system is indistinguishable from a two-species reaction limited system.

2.4.3 *Two immobile species*

We now consider the special case in which v and w are immobile ($D_v = D_w = 0$), but u is highly mobile ($D_u/(k_1^+ r_n^2) \to \infty$). As u is highly mobile, we set $u = u_{\text{eq}}$ and attempt to solve the remaining system,

$$\begin{cases} \frac{\partial v}{\partial t} = k_1^- v_{\text{eq}} - (k_1^- + k_2^+)v + k_2^- w, \\ \frac{\partial w}{\partial t} = k_2^+ v - k_2^- w, \end{cases} \tag{226}$$

where we have used the fact that $k_1^+ u_{\text{eq}} = k_1^- v_{\text{eq}}$. As in section 2.4.1 the transformation $v = v_{\text{eq}} - \tilde{v}$ and $w = w_{\text{eq}} - \tilde{w}$ simplifies system (226) to

$$\begin{cases} \frac{\partial \tilde{v}}{\partial t} = -(k_1^- + k_2^+)\tilde{v} + k_2^- \tilde{w}, \\ \frac{\partial \tilde{w}}{\partial t} = k_2^+ \tilde{v} - k_2^- \tilde{w}, \end{cases} \tag{227}$$

where

$$\tilde{v}(r,0) = \tilde{v}_0(r) = \begin{cases} v_{\text{eq}}, r \le r_n, \\ 0, r \le r_n, \end{cases}$$

and

$$\tilde{w}(r,0) = \tilde{w}_0 = \begin{cases} w_{\text{eq}}, r \le r_n, \\ 0, r \le r_n. \end{cases}$$

The solution of system (227) is

$$\begin{pmatrix} \tilde{v} \\ \tilde{w} \end{pmatrix} = c_1(r) e^{-\lambda_1} \mathbf{v_1} + c_2(r) e^{-\lambda_2} \mathbf{v_2}, \tag{228}$$

where λ_1, λ_2 and $\mathbf{v}_1, \mathbf{v}_2$ are respectively the eigenvalues and eigenvectors of the matrix

$$A = \begin{pmatrix} -(k_1^- + k_2^+) & k_2^- \\ k_2^+ & -k_2^- \end{pmatrix}.$$

The functions $c_1(r)$ and $c_2(r)$ are determined by the initial conditions, $c_1(r) = c_2(r)$ for $r > r_n$,

$$\begin{pmatrix} \tilde{v}_0(r) \\ \tilde{w}_0(r) \end{pmatrix} = c_1(r)\mathbf{v_1} + c_2(r)\mathbf{v_2}.$$

Though the eigenvalues and eigenvectors of matrix A can be computed in terms of the reaction rates, the resulting expression is lengthy and does not readily simplify. Instead, set $\alpha = c_1 v_{11} + c_1 v_{12}$, $\beta = c_2 v_{21} + c_2 v_{22}$ where v_{ij} is the jth element of eigenvector $\mathbf{v}_i$,

$$\tilde{v} + \tilde{w} = \alpha e^{-\lambda_1} + \beta e^{-\lambda_2}. \tag{229}$$

If we take $D_u / r_n^2 \to \infty$, then $u + v + w = u + v_{\text{eq}} - \tilde{v} + w_{\text{eq}} - \tilde{w}$. By linearity, the recovery curve is then

$$F(t) = u_{\text{eq}} \mathcal{F}_S \left(\frac{r_n^2}{2D_u t} \right) + v_{\text{eq}} + w_{\text{eq}} - \alpha e^{-\lambda_1 t} - \beta e^{-\lambda_2 t}. \tag{230}$$

Taking $D_u / r_n^2 \to \infty$, (230) becomes

$$F(t) = 1 - \alpha e^{-\lambda_1 t} - \beta e^{-\lambda_2 t}. \tag{231}$$

2.4.4 *Determining the order of reaction*

Suppose we have two highly mobile proteins, A and B, which interact with an immobile molecule or cellular structure, D, to form an immobile complex, ABD,

$$\text{A} + \text{B} + \text{D} \rightleftharpoons \text{ABD}.$$

This system could model the interaction between a transcription factor, a transcription co-regulator and DNA. The trasnscription factor and transcription co-regulator are proteins which interact with DNA to activate or inhibit

the expression of certain genes. As the transcription factor and co-regulator are both proteins localised to the cell nucleus, they are likely to have high mobility [276, 277], while the chromatin (DNA molecule) is totally immobile [282].

Suppose that it is known that A, B and D interact, but that the order of reaction is unknown. It may be informative, if it is possible, to determine the order of reaction by performing separate FRAP experiments on the proteins A and B.

The first possibility is that A and B react to form a complex that binds with D,

$$\begin{aligned} \mathrm{A} + \mathrm{B} &\rightleftharpoons \mathrm{AB}, \\ \mathrm{AB} + \mathrm{D} &\rightleftharpoons \mathrm{ABD}. \end{aligned}$$

If this is the case, then the recovery curve will depend on the mobility of the complex, AB. If AB is not highly mobile, then both A and B will fall into the regime with three disparate diffusive timescales discussed in section 2.4.1. The recovery curves for both A and B will depend on the size of the bleach region radius, so this regime can be identified by repeating the FRAP experiment with bleach spots of different sizes. If protein complex AB is itself highly mobile, then both A and B will be highly mobile, which is the scenario discussed in section 2.4.2. FRAP experiments on A and B will produce single exponent recovery curves with identical dissociation rates (the rate of dissociation of AB from D).

Alternatively, it may be that A reacts with D to induce some conformational change which enables B to bind, forming the complex ABD,

$$\begin{aligned} \mathrm{A} + \mathrm{D} &\rightleftharpoons \mathrm{AD}, \\ \mathrm{B} + \mathrm{AD} &\rightleftharpoons \mathrm{ABD}. \end{aligned}$$

In this case, A and B will have different recovery curves; B will obey a two species model and so its recovery curve will be approximately equal to a single exponential expression, while A will follow the three species

model discussed in section 2.4.3. The recovery curve for A will be composed of two exponential terms, although the exponents will be eigenvalues, not dissociation rates. There is also a third case in which B reacts with D first, followed by A,

$$\mathrm{B} + \mathrm{D} \rightleftharpoons \mathrm{BD},$$
$$\mathrm{A} + \mathrm{BD} \rightleftharpoons \mathrm{ABD}.$$

However, as A and B are arbitrary labels, there is no need to consider this case separately.

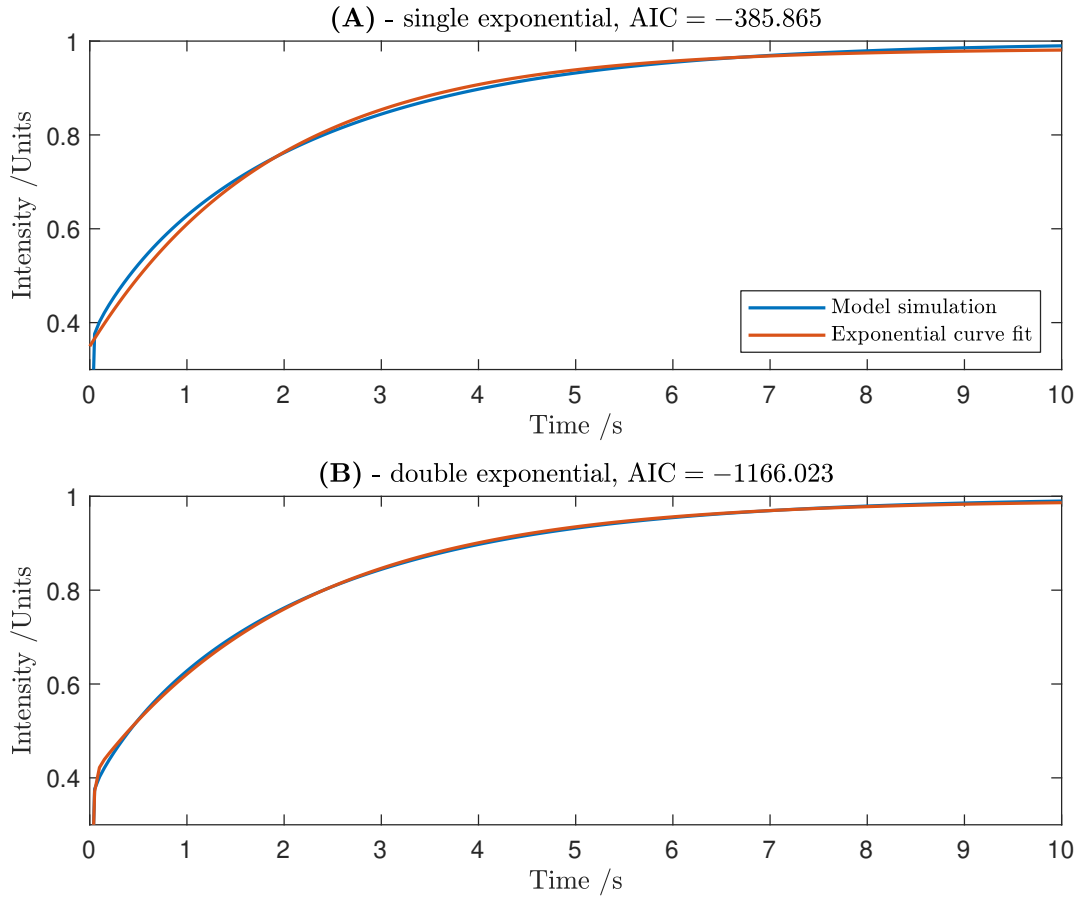


Figure 13: Numerical simulation of the three species sequential reaction, fitted with (A) a single exponential and (B) a double exponential according to formula (232). The double exponential formula, as expected, provides a better fit, which is visually apparent. The Akaike information critereon (AIC) also has a much lower value in the case of the double exponential formula which implies a better fit to data.

In summary, it is in principle possible to determine the order of reaction in a three species system with two highly mobile proteins and an immobile binding partner. It is simply necessary to perform FRAP experiments on both proteins, then attempt to fit the recovery curves with the formula

$$F(t) = 1 - \sum_{i=1}^{n} \alpha_i e^{-\lambda_i t}, \tag{232}$$

for $n = 1, 2$.

The Akaike information criterion [159] can be used to determine whether the single or double exponent model is a better fit. If the best fit for the recovery curve is a single exponent for both proteins, A and B, and both recovery curves have identical dissociation rates, λ_i, then the proteins react with each other before binding with D. If this is not the case, then one of the proteins must bind with D before the other is able to do so. In this case, one of the recovery curves will be best approximated by a single exponent model, while the other will be best approximated by a double exponent model. The protein with the double exponential recovery curve is the first to react with the immobile binding partner.

2.5 MULTI-SPECIES PARALLEL REACTIONS

In this section we consider a molecular species which is subject to n independent reversible reactions with n different types of binding site,

$$\mathrm{A} + \mathrm{B}_i \underset{\mathrm{k}_i^-}{\overset{\bar{k}_i^+}{\rightleftharpoons}} \mathrm{C}_i.$$

Assuming mass action kinetics, the governing equations are

$$\begin{cases} \frac{\partial [\mathrm{A}]}{\partial t} = \sum_{i=1}^{n} \left(-\bar{k}_i^+ [\mathrm{A}][\mathrm{B_i}] + k_i^- [\mathrm{C_i}] \right) + D_A \nabla^2 A, \\ \frac{\partial [\mathrm{B}]_i}{\partial t} = \sum_{i=1}^{n} \left(-\bar{k}_i^+ [\mathrm{A}][\mathrm{B_i}] + k_i^- [\mathrm{C_i}] \right) + D_{B_i} \nabla^2 B, \\ \frac{\partial [\mathrm{C_i}]}{\partial t} = \bar{k}_i^+ [\mathrm{A}][\mathrm{B_i}] - k_i^- [\mathrm{C_i}] + D_{C_i} \nabla^2 C_i. \end{cases} \tag{233}$$

If A is tagged, then the equations governing the FRAP experiment are

$$\begin{cases} \frac{\partial u}{\partial t} = \sum_{i=1}^{n} \left(-k_i^+ u + k_i^- v_i\right) + D_u \nabla^2 u, \\ \frac{\partial v_i}{\partial t} = k_i^+ u - k_i^- v_i + D_{v_i} \nabla^2 v_i, \end{cases} \tag{234}$$

where u is the normalised concentration of fluorescent A, and v_i is the normalised concentration of fluorescent C_i. The forward reaction rates are $k_i^+ = \bar{k}_i^+ [\mathrm{B_i}]$. The homogeneous steady states of (234) satisfy $k_i^+ u_{\mathrm{eq}} = k_i^- (v_{\mathrm{eq}})_i$ for $i = 1, \ldots, n$. Therefore,

$$u_{\mathrm{eq}} = \frac{1}{1 + \sum_{i=1}^{n} \kappa_i}, \quad (v_{\mathrm{eq}})_j = \frac{\kappa_j}{1 + \sum_{i=1}^{n} \kappa_i}, \tag{235}$$

where $\kappa_i = k_i^+ / k_i^-$.

If the rate of reaction is much greater than the rate of diffusion across the bleach region, then (234) resembles a single species pure diffusion system with effective diffusivity

$$D_{\mathrm{eff}} = \frac{D_u + \sum_{i=1}^{n} \kappa_i D_{v_i}}{1 + \sum_{i=1}^{n} \kappa_i}.$$

2.5.1 *Rapid equilibration*

If u is highly mobile, we can set $u = u_{\mathrm{eq}}$ and solve

$$\frac{\partial v_i}{\partial t} = k_i^- (v_{\mathrm{eq}} - v_i) + D_{v_i} \nabla^2 v_i, \tag{236}$$

using the fact that $k_i^+ u_{\mathrm{eq}} = k_i^- v_{\mathrm{eq}}$. The system is now decoupled, so we can solve for each v_i separately following the method in section 2.2.3. By linearity, the recovery curve is the sum of the average of each separate solution,

$$F(t) = u_{\mathrm{eq}} \mathcal{F}_S \left(\frac{r_n^2}{2 D_u t} \right) + \sum_{i=1}^{n} \left[(v_{\mathrm{eq}})_i \left(1 - e^{-k_i^- t} \left[1 - \mathcal{F}_S \left(\frac{r_n^2}{2 D_{v_i} t} \right) \right] \right) \right]. \tag{237}$$

As $D_u / r_n^2 \to \infty$ and $D_{v_i} / r_n^2 \to 0$ (237) reduces to

$$F(t) = 1 - \sum_{i=1}^{n} (v_{\mathrm{eq}})_i e^{-k_i^- t}, \tag{238}$$

which has appeared in previous quantitative FRAP studies [80].

2.6 CHAPTER SUMMARY

In this chapter we used formal asymptotic methods to derive new approximations in limiting cases of of the linear reaction-diffusion FRAP model. We found that not every parameter even in a two species FRAP model is estimable in general. Using Fisher information, combined with our new approximations, we proposed sufficient conditions to ensure that every model parameter is estimable. For conventional recovery curve analysis, the conditions are

$$\frac{k^-}{k^+} = O(1), \quad D_v \ll D_u,$$

and

$$\frac{D_u}{k^+ r_n^2} \ll 1 \quad \Delta t \ll \frac{r_n^2}{D_u},$$

where r_n is the radius of the bleach region and Δt is the regular time interval between data points. In scanning FRAP, the use of spatial information relaxes the requirement on Δt, so that the model parameters are fully estimable whenever

$$\frac{D_u}{k^+ \Delta r^2} \gg 1, \quad \frac{D_u}{k^+ L^2} \lesssim 1,$$

where L is the length scale of the imaged region. In the next chapter, we will numerically test these theoretical predictions.

We also considered the problem of multi-species FRAP modelling. We derived several approximation formula which can potentially be used to determine the order of reaction when two proteins interact mutually dependently with an immobile binding partner.

3

NUMERICAL ANALYSIS OF FLUORESCENCE RECOVERY AFTER PHOTOBLEACHING AND A GENERAL PARAMETER FITTING SCHEME

In chapter 2 we posited conditions that ensure the estimability of FRAP model parameters in terms of the values of the parameters themselves. In this chapter, we aim to revisit briefly our earlier predictions, and test them against numerically simulated synthetic data. In addition, the analysis in chapter 2 has two limitations. First, it is local to the optimal point and does not reveal anything about the viability of global parameter fitting with general initial guesses that may be far from the global minimum. Secondly, it applies only to the idealised case with step function initial conditions. We will use numerical data to broaden our earlier results and test predictions in this chapter.

We find that, consistent with our theoretical predictions, estimability is determined by the parameter regime; the magnitudes of the dimensionless constants η and κ. There is full parameter estimability only when $\eta \gg 1$ and $\kappa = O(1)$. In other regimes, progress is possible only if the diffusion coefficients D_u and D_v are separately measured.

Methodology is discussed in section 3.1 and main results are presented in sections 3.2 and 3.3. In section 3.4 we present a test to determine the parameter regimes; hence, what additional experiments, if any, will be required. This chapter concludes with section 3.5 in which we propose a simple, yet general parameter fitting algorithm.

3.1 METHODOLOGY

Our first aim is to test the feasibility of fitting the two species reaction-diffusion FRAP model to data,

$$\begin{cases} \frac{\partial u}{\partial t} = -k^+ u + k^- v + D_u \nabla^2 u - I(r,t)u(r,t), \\ \frac{\partial v}{\partial t} = k^+ u - k^- v + D_v \nabla^2 v - I(r,t)v(r,t). \end{cases} \tag{239}$$

Note that we are assuming radial symmetry, hence u (the free protein fraction) and v (the bound protein fraction) depend on r, the distance from the centre of the bleach region. System (239) is solved numerically with the laser profile $I(r,t)$ defined for $t \in [-t_{\text{bleach}}, \infty)$,

$$I(r,t) = \begin{cases} H(r_n - r), \text{ if } t \in [-t_{\text{bleach}}, 0) \\ 0 \text{ if } t \in [0, \infty), \end{cases} \tag{240}$$

where H is the Heaviside step function. We impose zero-flux boundary conditions on a disk of radius R,

$$\left.\frac{\partial u}{\partial r}\right|_{r=0} = \left.\frac{\partial u}{\partial r}\right|_{r=R} = 0, \tag{241}$$

and likewise for v. The radially symmetric Laplacian is

$$\nabla^2 u = \begin{cases} 2\frac{\partial^2 u}{\partial r^2} \text{ if } r = 0, \\ \frac{1}{r}\frac{\partial u}{\partial r} + \frac{\partial^2 u}{\partial r^2} \text{ if } r > 0, \end{cases} \tag{242}$$

where the result at $r = 0$ is a consequence of l'Hôpital's rule. Using a central difference approximation of the Laplacian (243),

$$\nabla_j^2 u(r_j, t_i) = \begin{cases} 2\frac{u(r_{j+1},t_i) + u(r_{j-1},t_i) - 2u(r_j,t_i)}{\delta r^2} \text{ if } r_j = 0, \\ \frac{1}{r_j}\frac{\partial u(r_{j+1},t_i) - u(r_{j-1},t_i)}{2\delta r} + \frac{u(r_{j+1},t_i) + u(r_{j-1},t_i) - 2u(r_j,t_i)}{\delta r^2} \text{ if } r_j > 0, \end{cases} \tag{243}$$

where δr is the mesh spacing, we produce a semi-descretised approximation to (254) to which we apply a stiff ODE solver (MATLAB's ode23s function) to obtain numerical solutions $u_{\text{Data}}(r_j, t_i)$, $v_{\text{Data}}(r_j, t_i)$, which represent the

mobile and bound fluorescent fractions at position r_j and time t_i. We use the subscript 'Data' to denote (synthetic) experimental data. The total fluorescence intensity is

$$w_{\text{Data}}(r_j, t_i) = u_{\text{Data}}(r_j, t_i) + v_{\text{Data}}(r_j, t_i). \tag{244}$$

For continuous data the recovery curve is

$$F_{\text{Data}}(t) = \frac{1}{\pi r_n^2} \int_0^{2\pi} \int_0^{r_n} w_{\text{Data}}(r, t) r \mathrm{d}r \mathrm{d}\theta = \frac{2}{r_n^2} \int_0^{r_n} w_{\text{Data}}(r, t) r \mathrm{d}r.$$

Discretising, with $r_j = j\delta r$, gives

$$F_{\text{Data}}(t_i) = \frac{2}{r_n^2} \sum_{\{j \in \mathbb{N} | r_j \leq r_n\}} w_{\text{Data}}(r_j, t_i) i \delta r^2. \tag{245}$$

There is evidence that bleaching a cell multiple times with different bleach spot radii can improve parameter estimation [102]. We certainly want to include this option in our synthetic tests. Suppose we bleach a cell n_{bleach} times, and that the bleaches are indexed by a number, $k = 1, ..., n_{\text{bleach}}$. Let r_n^k be the nominal bleach region radius used in experiment k, w_{Data}^k the total fluorescence, and F_{Data}^k the recovery curve (note the superscript k is an index and is not intended to mean 'raised to the power of k').

For each instance, k, with bleach region radius, r_n^k, we solve (239) numerically to obtain $u^k(r_j, t_i)$ and $v^k(r_j, t_i)$. We define the total fluorescence $w^k(r_j, t_i)$ and the fluorescence recovery curve $F^k(r_j, t_i)$ as in (244) and (245) respectively. We define the objective functions, ϕ and ϕ_{Space}, as

$$\phi = \sum_{k=1}^{n_{\text{bleach}}} \left[\sum_i (F_{\text{Data}}^k(t_i) - F^k(t_i))^2 \right], \tag{246}$$

and

$$\phi_{\text{Space}} = \sum_{k=1}^{n_{\text{bleach}}} \left[\sum_j \sum_i (w_{\text{Data}}^k(r_j, t_i) - w^k(r_j, t_i))^2 \right], \tag{247}$$

whose minima we attempt to find with the Nelder-Mead downhill simplex algorithm [278, 279] (using the fminsearch function of MATLAB). Note that scanning laser FRAP would be required in practice to obtain w_{Data}. Since we know the values of the parameters used to generate w_{Data}, we can easily

measure the accuracy of the fitting procedure. Let θ_l be any model parameter (D_u, D_v, k^+, k^-) used to generate w_{Data}, and $\bar{\theta}_l$ be the fitting procedure output, then the proportional estimation error is

$$\mu_l^h = \frac{\mid \bar{\theta}_l^h - \theta_l^h \mid}{\theta_l^h}, \tag{248}$$

where once more the superscript h is an index (the index of the experiment). The mean error is then simply

$$\mu_l = \frac{1}{n_{\text{run}}} \sum_{h=1}^{n_{\text{run}}} \mu_l^h. \tag{249}$$

In each case we take $n_{\text{run}} = 1024$. In this way we are able to condense information about the accuracy of parameter estimation in the various dynamic regimes (rapid equilibration, intermediate and so on) into a single variable. However, we have found that the distribution of parameter estimates may be thick-tailed such that neither the mean nor the median errors are especially informative. In these cases, the mean error is skewed by a minority of outliers, while the median error is approximately 0. For this reason we also recorded the number of instances, $n_l(\mu)$, which returned values $\bar{\theta}_l^h$ such that $\mu_l^h < \mu$. The fraction of such cases is simply

$$f_l(\mu) = \frac{n_l(\mu)}{n_{\text{run}}}, \tag{250}$$

where μ has a chosen value. For example, if $\mu = 0.01$, then $f_l(\mu)$ would be the fraction of instances which returned estimation errors of less than 1%.

3.1.1 *Parameter generation*

The parameter inputs for each synthetic experiment were generated randomly following a process which is described below.

1. Generate a uniformly distributed positive random value for D_u. We set $D_u \leq 50\ \mu m^2 s^{-1}$ to keep the diffusivity in a biologically realistic range [48].

2. Pick a random real number $\tilde{\eta} \in [-3, 3]$ from a uniform distribution, and set the dimensionless parameter $\eta = 10^{\tilde{\eta}}$. If $\tilde{\eta} \geq 1$, we consider the dynamics to be 'rapid equilibration'. If $-1 < \tilde{\eta} < 1$ we consider the dynamics to be 'intermediate'. Finally, if $\tilde{\eta} \leq 1$ we consider the dynamics to be 'slow equilibration' (effective diffusion).

3. Set the association rate $k^+ = D_u/(r_n^2\eta)$.

4. Pick a random real number $\tilde{\kappa} \in [-1, 1]$ from a uniform distribution, and set the dimensionless parameter $\kappa = 10^{\tilde{\kappa}}$. Cases where $\tilde{\kappa} > 1$ or $\tilde{\kappa} < 1$ are handled separately.

5. Set the dissociation rate $k^- = \kappa k^+$.

6. Pick a random real number $\delta \in [0, 10^{-1}]$ from a uniform distribution.

7. Set the slow diffusivity $D_v = \delta D_u$.

Initial guesses are generated in two different ways. In the first method, the 'local' method, each initial guess, $\tilde{\theta}_l^k$, is of the form

$$\tilde{\theta}_l^k = \theta_l^k(1 + p), \tag{251}$$

where $p \in [-0.5, 0.5]$ is a uniform random variable. This ensures that initial guesses are within 50% of the correct parameter value in each case. For the second method, the 'global' method, steps 1-7 were repeated to generate independent random initial guesses.

3.1.2 *Procedure summary*

It may be helpful at this stage to recap some of the key details of the process used to produce the aggregate measures of parameter estimation accuracy, μ_l and f_l. Note that there are n_{run} separate synthetic experiments included in each data set (each table in section 3.2 is one data set), the experiments are indexed by $h = 1, ..., n_{\text{run}} = 1024$. Each experiment involves bleaching

n_{bleach} times with different bleach region radii, indexed by $k = 1, ..., n_{\text{bleach}}$ (n_{bleach} is varied to investigate the effects of fitting multiple fluorescence recoveries on parameter estimation accuracy). The steps involved in the procedure are outlined below.

1. Generate a set of parameters as described in section 3.1.1.
2. Simulate a FRAP experiment using n_{bleach} different bleaches with different bleach region radii, and record the n_{bleach} fluorescence recoveries (all these synthetic data use the parameters generated in step 1 as inputs).
3. Generate a set of initial guesses as described in section 3.1.1.
4. Attempt parameter estimation by minimising the objective function (either ϕ (246) or ϕ_{Space} (247), as appropriate).

This process is repeated n_{run} times for each data set.

3.2 COMPUTATIONAL RESULTS

This section contains the results obtained by the methodology described in section 3.1, the results being collated in tables. Odd numbered tables display the mean estimation error, μ_l as defined in (249). These estimates were obtained using 'local' initial guesses, as defined in section 3.1. Even numbered tables display the fraction of parameter estimates which were within 1% of the correct value, $f_l(0.01)$ as defined in (250). These estimates were obtained using 'global' initial guesses, as defined in section 3.1.

We have included fitting results for each of the four model parameters, D_u, D_v, k^+ and k^-, as well as D_{eff} and v_{eq}, defined as

$$D_{\text{eff}} = \frac{D_u k^- + D_v k^+}{k^+ + k^-}, \quad v_{\text{eq}} = \frac{k^+}{k^+ + k^-}.$$

In chapter 2 we predicted that parameter estimability would be determined by the parameter 'regime' which is the magnitude of the dimensionless constants

$$\eta = \frac{D_u}{k^+ r_n^2}, \quad \kappa = \frac{k^-}{k^+}.$$

To investigate the effect of varying η and κ on parameter estimation accuracy, we have broken down the results by regime.

We investigated the effects of fluorescence recovery frame rate and the use of spatial information. We used two values for the interval between frames, Δt: $\Delta t = 5 \times 10^{-2}$ s (standard frame rate), and $\Delta t = 1 \times 10^{-4}$ s (high frame rate). Where spatial information was utilised, we used ϕ_{Space}, formula (247), as the objective function. Otherwise, we used ϕ, formula (246). We also investigated the possibility of fitting certain parameters separately and then using the FRAP experiments only to measure the remaining parameters. For some of the parameter fits (as indicated), we simply supplied the correct values of D_u and D_v and attempted to estimate only k^+ and k^-. Of course, in reality, this process of separately determining D_u and D_v would require some additional experiments.

$\eta \gg 1$

In the case when $\eta \gg 1$ and $\kappa = O(1)$ we predicted that the reaction rates, k^+ and k^-, and the slow diffusivity, D_v would be estimable from either recovery curve or spatial data. We predicted that the fast diffusivity, D_u, would be estimable using recovery curve data of sufficiently high frame rate (but not in general). We further predicted that the use of spatial information would greatly reduce the frame rate necessary to estimate D_u accurately.

Computational results, presented in table 1, are consistent with all of our predictions. In row 1, we see that fitting a low frame rate recovery curve produced estimates of D_v, k^+ and k^- with mean errors of less than 2%, but the error was much higher for D_u. Using a high frame rate recovery curve (row 2) reduced the error in the estimate of D_u to a similar level to the other pa-

Row	Spatial	HFR	D_u	D_v	k^+	k^-	D_{eff}	v_{eq}
1	-	-	26.1	1.15	0.48	0.43	21.4	0.51
2	-	✓	1.51	1.71	0.22	1.02	1.59	0.63
3	✓	-	0.00	0.00	0.00	0.00	0.00	0.00

Table 1: Mean percentage estimation error, μ_l, generated using local initial guesses, for the indicated parameters. A checkmark in the 'HFR' column indicates that a high frame rate fluorescence recovery was used. A checkmark in the 'Spatial' column indicates that the spatial objective function, ϕ_{Space} equation (247), was used; otherwise the conventional objective function ϕ equation (246) was used. Regime: $\eta \gg 1$.

rameters. The use of spatial information (row 3) even at conventional frame rate produced highly accurate estimates of all the parameters, as expected.

Row	η_0	D_u	D_v	k^+	k^-	D_{eff}	v_{eq}
1	$\eta_0 \gg 1$	94.0	94.0	94.1	94.0	94.0	94.0
2	$\eta_0 = O(1)$	26.6	26.6	29.1	29.3	27.3	28.7
3	$\eta_0 \gg 1$	-	-	100	100	100	100

Table 2: Percentage of estimates of the indicated parameters which were accurate to within 1% of the correct values, $f_l(0.01)$. Initial guesses were generated using the 'global' method. The regime of the initial guess is η_0. A hyphen (-) in a cell indicates that the corresponding parameter was not estimated, but was 'separately determined' by supplying the correct value directly. Regime $\eta \gg 1$.

Next turning our attention to table 2, we see that, using generic initial guesses in the $\eta \gg 1$ regime (row 1), accurate estimates (*i.e.* having an error of less than 1% of the correct value) of all four model parameters were obtained in 94% of cases. We notice (row 2) that the accuracy fell substantially when initial guesses were made in the $\eta = O(1)$ regime. When the initial guess was far from the correct parameter values, the fitting algorithm often

became stuck at a local minimum of the objective function and so never located the global minimum.

$\eta = O(1)$

We did not make any strong predictions about the feasibility of parameter estimation in the $\eta = O(1)$ regime. However, we conjectured that there would be increasing parameter multiplicity as the value of η declined, that different combinations of parameters would yield almost identical model outputs, making it very difficult in practice to choose the correct parameter values. Results in table 3 indicate large estimation errors for each of the four parameters, even when using spatial information and high frame rate data. An interesting exception is the effective diffusivity, D_{eff} which was estimated with a mean error of less than 2%. This is surprising, as we would not necessarily, on the basis of the results in sections 2.2.4 and 2.2.5 (chapter 2) expect D_{eff} to be estimable unless $\eta \ll 1$.

Row	Spatial	HFR	D_u	D_v	k^+	k^-	D_{eff}	v_{eq}
1	✓	✓	453	3730	1290	318	1.95	378

Table 3: Mean percentage estimation error, μ_l, generated using local initial guesses, for the indicated parameters. A checkmark in the 'HFR' column indicates that a high frame rate fluorescence recovery was used. A checkmark in the 'Spatial' column indicates that the spatial objective function, ϕ_{Space} equation (247), was used; otherwise the conventional objective function ϕ equation (246) was used. Regime: $\eta = O(1)$.

One method to circumvent the problem of multiplicity is to determine certain parameters independently using separate experiments. We investigated the effect of measuring the diffusivities, D_u and D_v separately. Results (table 4) imply that accurate estimation of the reaction rates, k^+ and k^-, is possible if D_u and D_v are known, but only if the initial guesses of k^+ and k^- are in the $\eta = O(1)$ regime.

Row	η_0	D_u	D_v	k^+	k^-	D_{eff}	v_{eq}
1	$\eta_0 = O(1)$	23.0	20.1	20.7	24.2	99.6	22.3
2	$\eta_0 \gg 1$	-	-	19.1	19.1	19.1	19.1
3	$\eta_0 = O(1)$	-	-	97.5	97.5	98.0	97.8

Table 4: Percentage of estimates of the indicated parameters which were accurate to within 1% of the correct values, $f_l(0.01)$. Initial guesses were generated using the 'global' method. The regime of the initial guess is η_0. A hyphen (-) in a cell indicates that the corresponding parameter was not estimated, but was 'separately determined' by supplying the correct value directly. Regime: $\eta = O(1)$.

$\eta \ll 1$

We predicted (in agreement with previous studies [70,76]) that in the $\eta \ll 1$ regime, only the effective diffusion coefficient,

$$D_{\text{eff}} = \frac{D_u k^- + D_v k^+}{k^+ + k^-},$$

would be estimable.

Row	Spatial	HFR	D_u	D_v	k^+	k^-	D_{eff}	v_{eq}
1	✓	✓	1270	5130	3670	1110	0.53	992
2	-	-	2430	6150	9730	1350	0.34	1210

Table 5: Mean percentage estimation error, μ_l, generated using local initial guesses, for the indicated parameters. A checkmark in the 'HFR' column indicates that a high frame rate fluorescence recovery was used. A checkmark in the 'Spatial' column indicates that the spatial objective function, ϕ_{Space} equation (247), was used; otherwise the conventional objective function ϕ equation (246) was used. Regime: $\eta \ll 1$.

Results (table 5) support this prediction. It is not possible (row 1) to estimate any parameters accurately, even with high frame rate spatial data,

yet D_{eff} can be accurately estimated given only low frame rate recovery curve data (row 2).

Row	η_0	D_u	D_v	k^+	k^-	D_{eff}	v_{eq}
1	$\eta_0 \ll 1$	2.54	0.78	0.59	0.59	98.0	1.95
2	$\eta_0 \ll 1$	-	-	92.2	92.2	100	100

Table 6: Percentage of estimates of the indicated parameters which were accurate to within 1% of the correct values, $f_l(0.01)$. Initial guesses were generated using the 'global' method. The regime of the initial guess is η_0. A hyphen (-) in a cell indicates that the corresponding parameter was not estimated, but was 'separately determined' by supplying the correct value directly. Regime: $\eta \ll 1$.

If D_u and D_v are known, it ought to be possible to estimate the ratio k^-/k^+, and hence the bound fraction, v_{eq}. Predictably, v_{eq} was estimated accurately (within 1% of the correct value) in 100% of instances (row 2). Surprisingly, the individual reaction rates, k^+ and k^-, were accurately estimated in almost as many instances 92%. Bearing in mind that in these experiments we allowed $10^{-3} \leq \eta \leq 10^{-1}$, these results suggest that many of the instances of the synthetic data were actually closer to the $\eta = O(1)$ regime than the true $\eta \to 0$ limit. This indicates that it requires an extremely small value of η for data to fall fully into the $\eta \ll 1$ regime, which is of some biological significance. Recalling that $\eta = \left(\frac{1}{k^+}\right) / \left(\frac{r_n^2}{D_u}\right)$ is the ratio of the reactive timescale to the diffusive timescale across the bleach region of interest, our results imply that 'effective diffusion' will only be encountered in systems with extremely highly transient chemical interactions.

3.3 MODEL UNCERTAINTY AND MULTIPLE CURVE FITTING

Empirical data similar to the idealised (*i.e.* almost noise-free) synthetic data used in section 3.2 are unlikely to be encountered in reality. In this section

we reproduce the results of the section 3.2, but including explicit uncertainty in the synthetic data.

Empirical data points, Y_i may be described by the sum of the output of the mathematical model, F_i and a stochastic variable such that,

$$Y_i = F_i(\theta) + \sigma_i \xi_i, \tag{252}$$

where the ξ_i are normally distributed random variables with mean 0 and standard deviation 1, and the σ_i account for the scale of the observational uncertainty [157]. We let ξ_i be independent and identically distributed random variables drawn from a normal distribution with zero mean and unit variance, and $\sigma_i = \sigma \; \forall i$.

Row	σ	n_{bleach}	D_u	D_v	k^+	k^-	v_{eq}
1	0.00	1	100	100	100	100	100
2	0.025	1	56 (78)	48 (66)	73 (93)	84 (94)	92 (99)
3	0.025	2	54 (88)	66 (79)	83 (95)	85 (95)	96 (99)
4	0.025	3	70 (92)	74 (85)	92 (98)	96 (99)	97 (99)
5	0.05	1	26 (50)	35 (54)	46 (72)	60 (80)	78 (90)
6	0.05	2	28(56)	41(63)	62(83)	70(88)	81(93)
7	0.05	3	43(66)	50(75)	70(94)	78(93)	88(97)

Table 7: Percentage of results within 5% of the correct value, $f_l(0.05)$ and, in brackets, percentage of results within 10% of the correct value, $f_l(0.1)$.

There are two other important methodological differences between this section and section 3.2. First, we used multiple start parameter estimation. We generated a sample of initial guesses, ran separate instances of the parameter fitting algorithm for each, and then selected the output which produced the lowest value of the objective function. The second important difference was that, for each instance of the synthetic data with certain parameter values, we attempted a fit using multiple fluorescence recoveries ($n_{\text{bleach}} = 1, 2, 3$) with different bleach region radii.

Fitting results for different values of σ and n_{bleach} are collated in table 7. Increased uncertainty, σ predictably reduced fitting reliability. Interestingly, v_{eq} turned out to be strongly estimable, more so than either k^+ of k^- individually.

3.3.1 *The value of multiple recovery fitting*

The quality of the parameter estimation is increased by fitting fluorescence recoveries with different bleach region sizes (table 7). With this in mind, one approach might be to conduct FRAP experiments with different bleach region sizes on separate cells; however, fitting a sample of cells with a single set of parameters is not ideal, as there is natural variation between cells. For this reason, we propose bleaching the same cell multiple times, varying the size of the bleach region. This would, of course, lengthen the duration of experiments which is time-consuming and increase the risk of non-negligible cell motion during the experiment. We suggest that a reasonable compromise might be to use only two different bleach region radii. The outline of the FRAP protocol is:

1. Record pre-bleach frames.
2. Bleach using first user-defined bleach region radius (radius 1).
3. Record fluorescence recovery until the cell reaches equilibrium.
4. Bleach using second user-defined bleach region radius (radius 2).
5. Record fluorescence recovery until the cell reaches equilibrium.

A theoretical example of how a FRAP experiment might look with this procedure is plotted in figure 14.

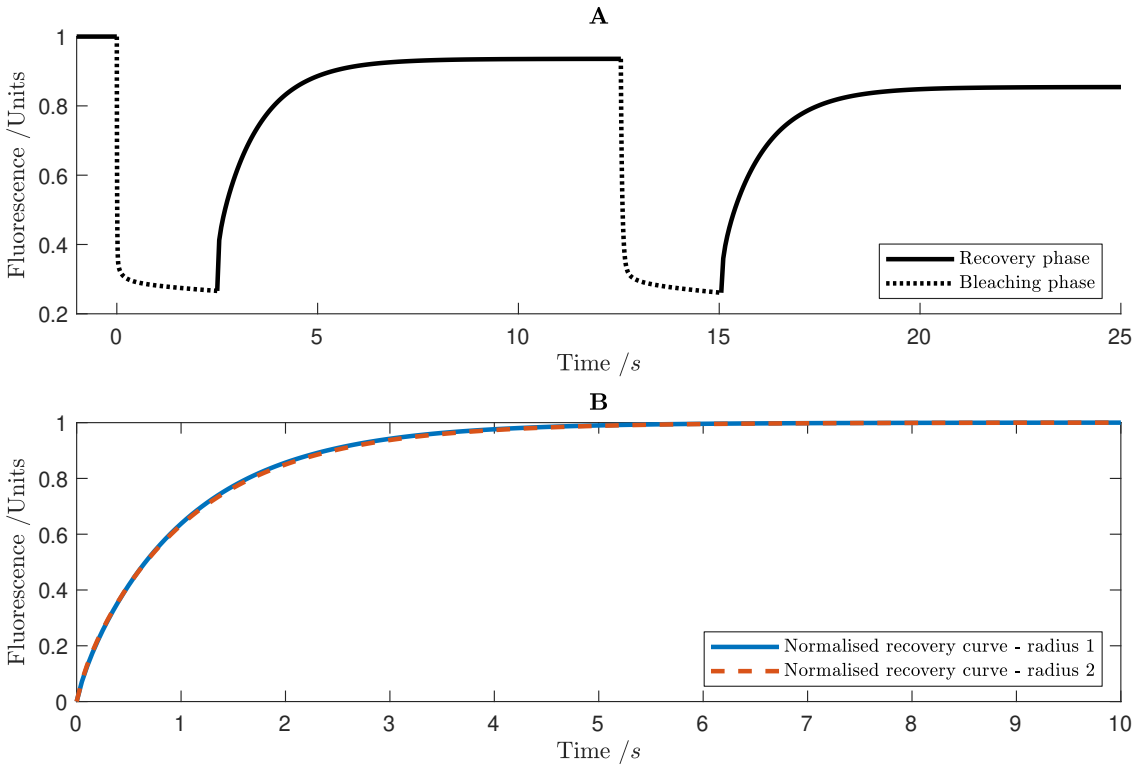


Figure 14: A simulated example of FRAP with double photobleaching. Circular bleach regions with two different radii, 0.3 μm and 0.7 μm, were used. The biophysical parameters were; $D_u = 20\mu m^2 s^{-1}, D_v = 0, k^+ = k^- = 1 s^{-1}$. (A) The averaged intensity across the bleach region of interest over time. Intensity during photobleaching is presented by a dotted line since this would not be measurable in practice. (B) The two recovery curves, both normalised to begin at 0 and end at 1, overlaid. Note that the fact that these recovery curves are almost identical suggests that the recovery curve is well-approximated by the reaction limited formula (149), which would imply that $\eta \gg 1$ and $D_v = 0$.

3.4 REGIME IDENTIFICATION

We have so far determined that the reliability and accuracy of parameter estimation are determined by the parameter regime of the data. However, one does not automatically know the regime of experimental data. The objective of this section is therefore to determine the precise boundary between the regimes and propose a method to determine the regime of arbitrary FRAP data. To this end, we ran numerical experiments in which we attempted

fitting on synthetic data with procedurally generated parameter inputs, as described in section 3.1, but precisely controlling the values of the dimensionless quantities, η and κ. We consider η in section 3.4.1 and κ in section 3.4.2.

3.4.1 *The effect of varying η*

In order to locate the boundary between the regimes we ran a sample of parameter fitting experiments with η values in a set of intervals, $\eta \in [10^{\tilde{\eta}}, 10^{\tilde{\eta}+0.1}]$ with $\tilde{\eta} \in \{..., -0.2, -0.1, 0, 0.1, 0.2, ...\}$, and recorded the fraction of output parameter estimates with an error of less than 1% relative to the correct corresponding parameter input value ($f_l(0.01)$ as defined in (250)).

Results (figure 15) indicate that, as expected, the reliability of the fit generally increased with the value of η. When D_u and D_v were known, fits of the reaction rates, k^+ and k^-, were consistently accurate for $\eta > 10^{0.4} \approx 2.51$ (figure 15A). Fitting all four parameters reliably, however, required $\eta > 10^{1.7} \approx 50.1$ (figure 15B).

We would expect that, in the regime where accurate estimation of all model parameters is possible, the rapid equilibration formula (124) ought to approximate the recovery curve. Accordingly, it is clear in figure 15C that the error between formula (124) and simulated data, ϕ_R, decreases as η increases, and is negligible for $\eta > 10^{1.7}$. Similarly, we would expect the slow equilibration (effective diffusion) formula (161) to be a good approximation where estimation of k^+ and k^- is not possible. Although the error, ϕ_D, decreases as η decreases, as we would expect, it does not appear that the effective diffusion formula is a good approximation when $\eta = 10^{0.4}$. This suggests that for $\eta \approx 1$, neither the effective diffusivity D_{eff}, nor k^+ and k^- individually, are estimable with total accuracy.

We can place data into one of three regimes: rapid equilibration ($\eta > 10^{1.7}$), intermediate ($10^{0.4} \leq \eta \leq 10^{1.7}$), and slow equilibration $\eta < 10^{0.4}$. If

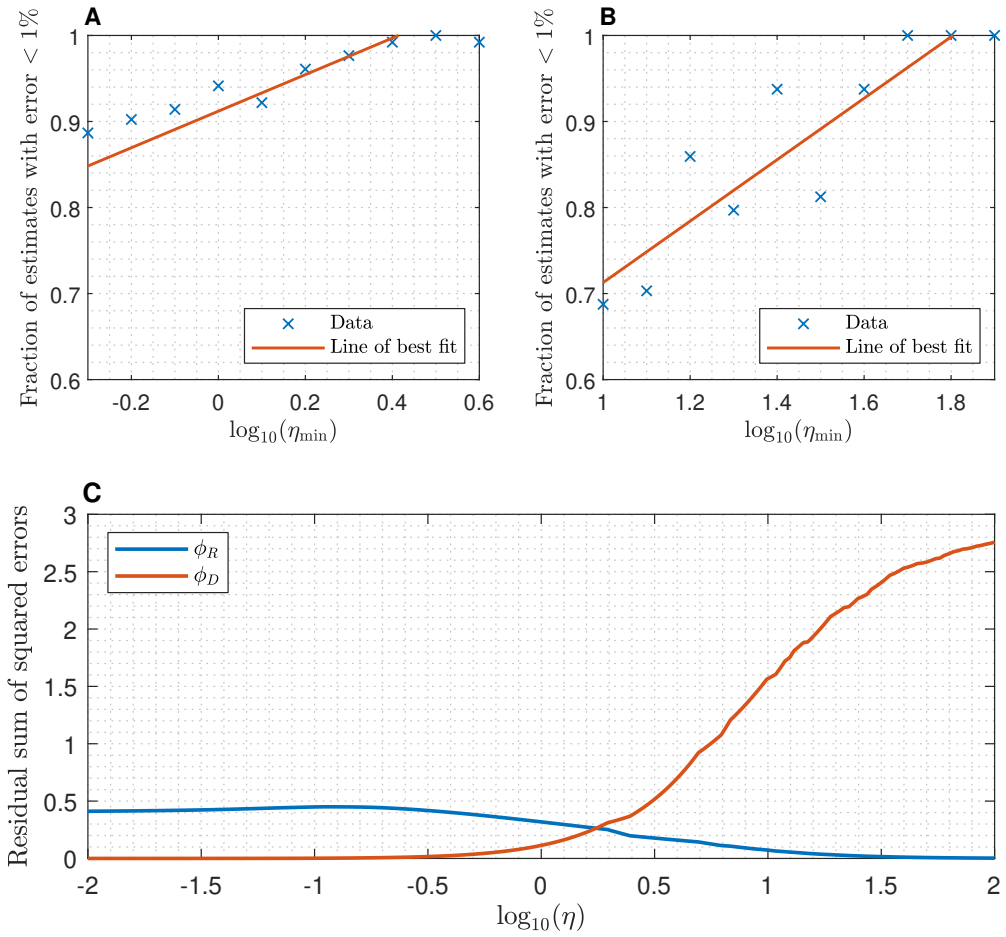


Figure 15: (A) Fraction of parameter estimates within 1% of the correct value ($f_l(0.01)$ as defined in (250)) when attempting to fit just k^+ and k^-. Each data point is calculated from $n_{\text{run}} = 128$ instances of fitting with $\eta \in [\eta_{\min}, \eta_{\max}]$ where $\eta_{\min}$ is indicated and $\log_{10}(\eta_{\max}) = \log_{10}(\eta_{\min}) + 0.1$. (B) identical to (A), except attempting to fit D_u, D_v, k^+ and k^-. (C) Residual sum of squared errors between a simulated fluorescence recovery curve and recovery curves computed by the rapid equilibration formula (124) (ϕ_R) and the slow equilibration (effective diffusion) formula (161) (ϕ_D). Parameters were $D_u = 30\ \mu m^2 s^{-1}$, $D_v = 0.01\ \mu m^2 s^{-1}$, $r_n = 0.5\ \mu m$, $k^+ = k^- = D_u/(r_n^2 \eta)$ for variable η. The rapid equilibration error, ϕ_R, decreases as η increases, while the effective diffusion error, ϕ_D, increases.

the regime can be determined, then the required course of action is obvious: in the rapid equilibration regime full parameter fitting is possible, in the intermediate regime the reaction rates can be estimated after separate

experiments to determine the diffusivities have been conducted, while in the slow equilibration regime at most the ratio of the reaction rates can be estimated.

We propose that the regime can be identified by attempting separate fits which are restricted to particular regimes. The best fit corresponds to the correct regime of the data. We measured goodness-of-fit with the Akaike information criterion [159],

$$\mathrm{AIC} = 2N_{\mathrm{param}} + N_{\mathrm{data}} \log(\phi), \tag{253}$$

where N_{param} is the number of model parameters, N_{data} is the number of data points and ϕ is the objective function/residual sum of squared errors. The model with the smallest AIC is in general the best fit with the least degree of over-fitting.

We tested procedurally generated data by fitting in the three major model regimes, as well as by fitting with a pure diffusion model. The restricted parameter estimation was implemented using MATLAB's constrained optimisation algorithm, fmincon. We define $\mathrm{AIC_{RE}}$ as the AIC resulting from a model fit which is limited to the rapid equilibration regime, while $\mathrm{AIC_I}$ and $\mathrm{AIC_{SE}}$ are likewise for the intermediate regime and the slow equilibration regimes respectively. $\mathrm{AIC_D}$ is the AIC of the pure diffusion model fit. Note that $N_{\mathrm{param}} = 4$ for $\mathrm{AIC_{RE}}$, $\mathrm{AIC_I}$ and $\mathrm{AIC_{SE}}$, while $N_{\mathrm{param}} = 1$ for $\mathrm{AIC_D}$. For this reason, the pure diffusion model yields a lower AIC than the full reaction-diffusion model in cases where the residual sum of squared errors, ϕ, are equal.

Results in table 8 indicate that, for both intermediate and rapid equilibration, constrained fitting in the correct regime produced the best fit in all cases, which strongly supports our contention that this method can be used for regime identification. In a minority of cases, the pure diffusion model provided a better fit than the full model in the slow equilibration regime, hence a slow equilibration recovery cannot reliably be distinguished from a purely diffusive recovery. This is to be expected, as the fluorescence re-

X (regime)	$AIC_X < AIC_{RE}$	$AIC_X < AIC_I$	$AIC_X < AIC_{SE}$	$AIC_X < AIC_D$
Large η (RE)	-	100%	100%	100%
Intermediate (I)	100%	-	100%	100%
Small η (SE)	100%	100%	-	84.4%

Table 8: Regime identification with constrained parameter fitting tested on a sample of 128 synthetic experiments for each regime. The leftmost row indicates the regime of the data: rapid equilibration (RE), intermediate (I) and slow equilibration (SE). Each cell displays the percentage of cases in which the AIC in a regime indicated by the column was greater than the AIC in the correct regime indicated by the row.

covery in slow equilibration regime tends to resemble pure diffusion with effective diffusivity, D_{eff}.

3.4.2 *The effect of varying κ*

As with η, we began investigating the effect of varying κ on parameter estimation by locating the boundary between the regimes. Computational results (figure 16A, B) indicate that parameter estimation deteriorates the further κ deviates from 1 in either direction. We found that $10^{-0.9} < \kappa < 10^{0.53}$ ensured reliably accurate estimation of all four model parameters.

As $\kappa \to \infty$, the system asymptotically approaches a pure diffusion recovery with diffusivity, D_u, and likewise for D_v as $\kappa \to 0$. Yet the pure diffusion model with the appropriate diffusivity is a better approximation for $\kappa = 10^{-0.9}$ than for $\kappa = 10^{0.53}$ (figure 16C). We believe that this asymmetry can be explained as follows. Since $D_u > D_v$, the diffusive recovery with diffusivity D_u is faster, hence there are comparatively fewer data points available with the fluorescence recovery in progress, ultimately leading to less accurate parameter estimates.

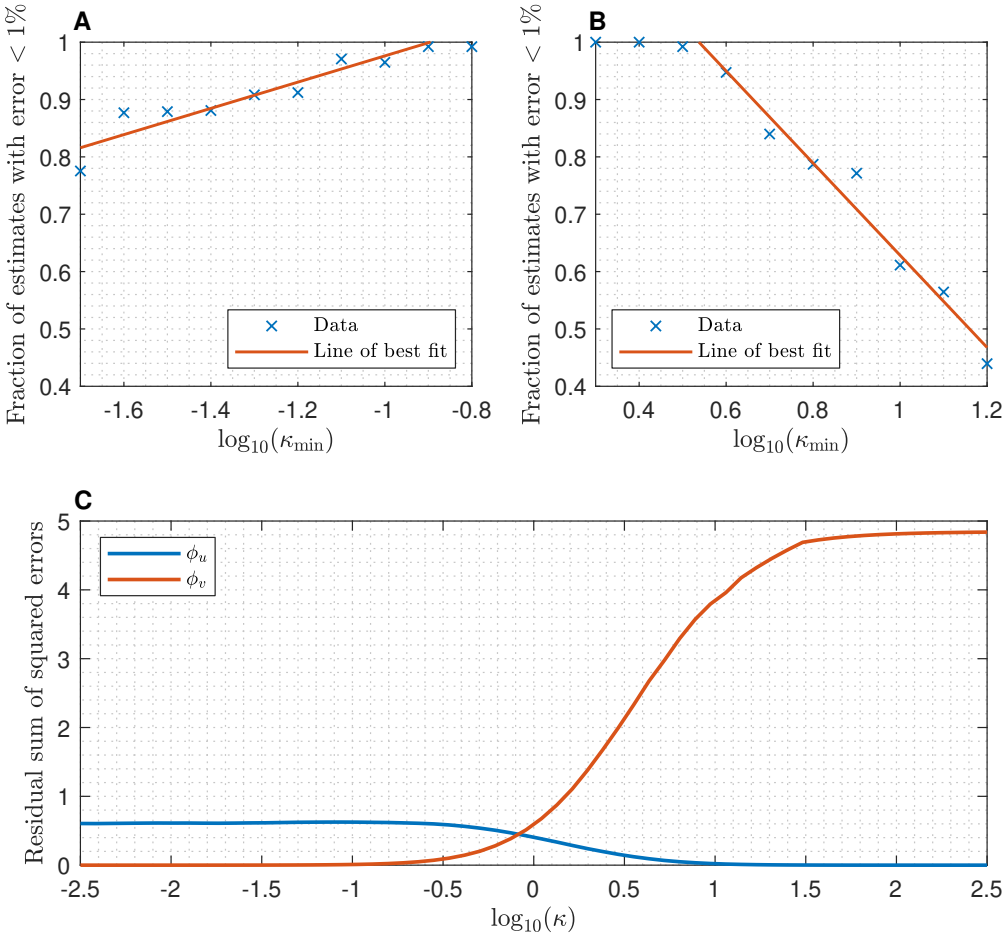


Figure 16: (A) Fraction of parameter estimates within 1% of the correct value ($f_l(0.01)$ as defined in (250)) when attempting to fit D_u, D_v, k^+ and k^-. Each data point is calculated from $n_{\text{run}} = 128$ instances of fitting with $\kappa \in [\kappa_{\min}, \kappa_{\max}]$ where $\kappa_{\min}$ is indicated and $\log_{10}(\kappa_{\max}) = \log_{10}(\kappa_{\min}) + 0.1$. (B) Similar to (A), except over a different range of values of $\kappa_{\min}$. (C) Residual sum of squared errors between a simulated fluorescence recovery curve and recovery curves computed by the pure diffusion formula with diffusivities D_u (170) (ϕ_u) and D_v (172) (ϕ_v). Parameters were $D_u = 8\ \mu m^2 s^{-1}$, $D_v = 1\ \mu m^2 s^{-1}$, $r_n = 0.5\ \mu m$, $k^+ = 1\ s^{-1}$ and $k^- = \kappa k^+$ for variable κ. The goodness-of-fit of pure diffusion with diffusivity D_u improves as κ increases, while the fit with diffusivity D_v improves as κ decreases.

Next, we tested whether constrained fitting can identify the magnitude of κ, similar to η in section 3.4.1. Again, we computed the Akaike information criterion of various fits limited to different regimes: AIC_U for $\kappa > 10^{0.53}$,

AIC_V for $\kappa < 10^{-0.9}$, and AIC_D for the pure diffusion model. For fits where κ was of intermediate magnitude ($10^{-0.9} < \kappa < 10^{0.53}$), we also imposed $\eta > 10^{1.7}$ (*i.e.* the rapid equilibration regime considered in section 3.4.1). We made this imposition because rapid equilibration is the sole regime in which full parameter estimation is possible, so identifying it is the most important problem.

X (regime)	$AIC_X < AIC_U$	$AIC_X < AIC_{RE}$	$AIC_X < AIC_V$	$AIC_X < AIC_D$
Large κ (U)	-	100%	82.0%	95.3%
Intermediate κ (RE)	100%	-	100%	100%
Small κ (V)	89.1%	88.3%*	-	100%

Table 9: Regime identification with constrained parameter fitting tested on a sample of 128 synthetic experiments for each regime. The leftmost row indicates the regime of the data: $\kappa > 10^{0.53}$ (U), rapid equilibration with intermediate κ (RE), and $\kappa < 10^{-0.9}$ (V). Each cell displays the percentage of cases in which the AIC in a regime indicated by the column was greater than the AIC in the correct regime indicated by the row. .

Results (table 9) clearly indicate that the $\kappa \gg 1$ and $\kappa \ll 1$ regimes cannot always be distinguished from one another, nor can they always be distinguished from pure diffusion; however this is unavoidable as both regimes are approximately diffusive.

For rapid equilibration data, the fit constrained to the rapid equilibration regime gave the best fit in all cases, which encouragingly suggests that this regime can be identified. On the other hand, for $\kappa \ll 1$ data, the fit constrained to the rapid equilibration regimes gave a better fit in 11.7% of cases. Judging by goodness-of-fit alone, we would erroneously conclude that these data were rapid equilibration, leading to potentially wildly inaccurate parameter estimates. However, in all of these instances we had $\bar{\kappa} \leq 10^{-0.9} + 10^{-3}$ where $\bar{\kappa}$ is the estimated value of κ. The algorithm clearly converged towards a point which was as close as possible to the $\kappa \ll 1$ regime (the correct regime). We therefore imposed the additional rule that

a regime is not considered viable if the constrained fit in that regime yields parameter estimates at the boundary between regimes. With the addition of this rule, in all of our numerical tests we were able to identify the rapid equilibration regime without any false positives or false negatives.

It is worthwhile noting that, even though the fluorescence recovery approximates pure diffusion as $\kappa \to \infty$ or $\kappa \to 0$, the $\kappa \gg 1$ and $\kappa \ll 1$ regimes could not be reliably identified with model selection alone. For $\kappa \gg 1$ and $\kappa \ll 1$, we found that $\mathrm{AIC}_{\mathrm{RE}} < \mathrm{AIC}_{\mathrm{D}}$ in 63.3% and 74.2% of cases respectively. In other words, the reaction-diffusion model produced a better fit than the pure diffusion model in the majority of cases. It is clear, then, that constrained fitting of the reaction-diffusion model is essential for the purposes of regime identification.

3.4.3 *The quasi-diffusive regimes, $\eta \ll 1$, $\kappa \gg 1$ and $\kappa \ll 1$*

Although the $\eta \gg 1$ and $\eta = O(1)$ regimes can be identified, the $\kappa \ll 1$, $\kappa \gg 1$ and $\eta \ll 1$ regimes cannot be differentiated from one another as they all somewhat resemble diffusive recoveries. However, this is no problem, as these regimes can easily be identified by other means. Suppose that D is optimum diffusivity obtained from fitting the pure diffusion model to data. If $D \approx D_u$ then $\kappa \gg 1$ and $v_{\mathrm{eq}} \approx 0$, while if $D \approx D_v$ then $\kappa \ll 1$ and $v_{\mathrm{eq}} \approx 1$. If it is clear that $D_v < D < D_u$, then $D = D_{\mathrm{eff}}$ and κ can be calculated. In summary, it is always possible, in principle, to determine the parameter regime, and by extension, which parameters are estimable and under what circumstances, of given FRAP data.

3.5 GENERAL FITTING ALGORITHM

The results of this chapter naturally lead us towards an idea of a general FRAP fitting algorithm. To conclude, we outline our proposed FRAP fitting procedure in this section (summarised as a flow chart in figure 17).

FRAP on an immobile species

To simulate a FRAP experiment as accurately as possible, it is essential to know the spatial profile of the bleaching laser - that is, the image mask which is 'written' into the sample by the laser during photobleaching. In testing we have found that this profile is surprisingly not well-approximated by any of the obvious candidate functions. We therefore believe that it will be advantageous to perform preliminary a photobleaching experiment on a protein which is known to be immobile. By observing the distribution of fluorescent immobile protein after photobleaching, it is easy to infer the profile of the bleaching laser, which can then be used in simulations of the main FRAP experiments without needing to know its functional form. An example of this process, using histone H2B, is detailed in chapter 4. Of course, this procedure requires a small number of additional experiments (we were able to construct a laser profile with four separate H2B instances), but removes a potentially inaccurate assumption and therefore eliminates one source of avoidable error. If different bleach region sizes are used, separate preliminary experiments are preferred for each size.

Main FRAP experiments

The FRAP experiments themselves proceed normally, with the only modification being the use of two different bleach rergion radii per cell, as described in section 3.3.1.

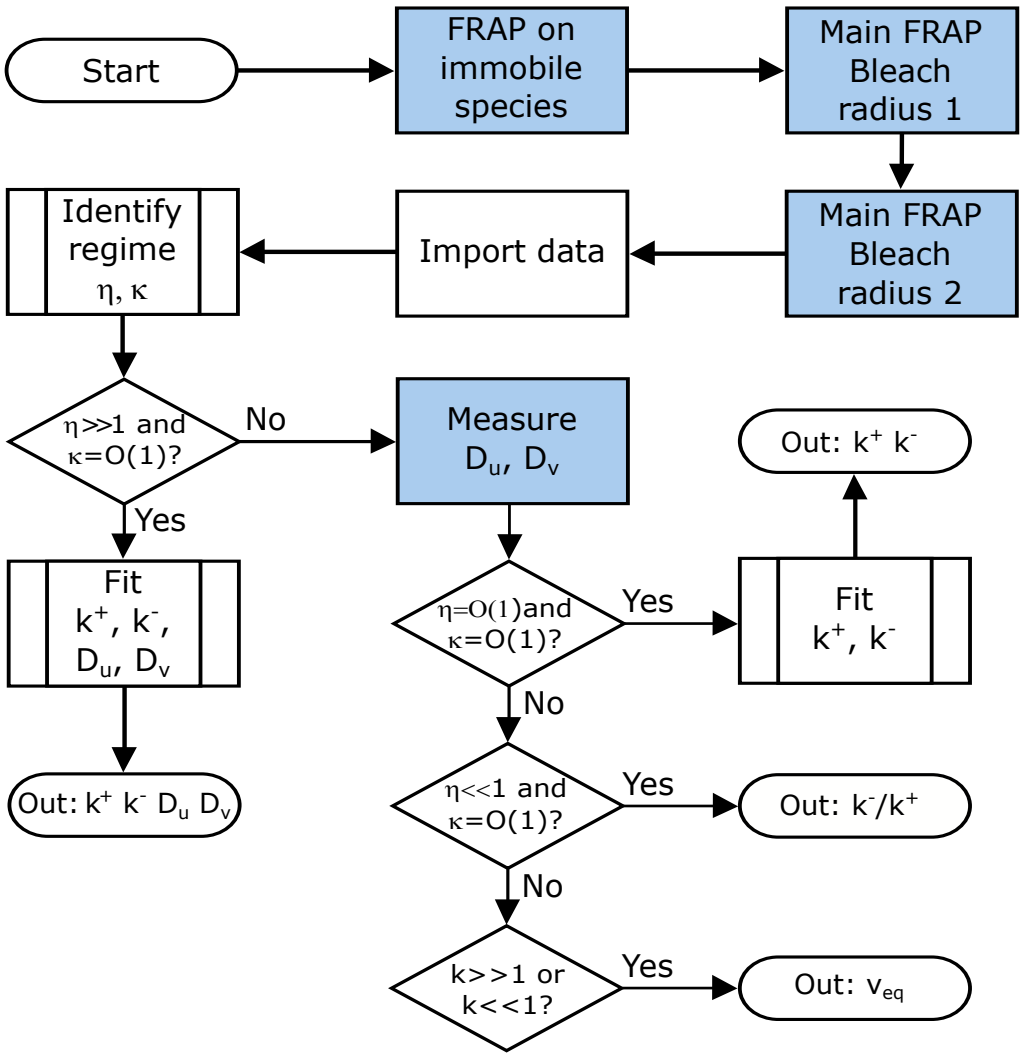


Figure 17: The FRAP parameter fitting algorithm. Steps highlighted in blue require direct actions by experimenters.

Importing data

Data acquisition being complete, the data must be converted into a usable format. We were given data in the form of a *.lsm file, which we converted to a series of images using ImageJ. The images were then imported into MATLAB with the imread function.

Initial regime identification

Initial regime identification proceeds just as described in section 3.4. Fitting the FRAP model to data using constrained parameter estimation can sort the data in one of three categories: the rapid equilibration regime ($\eta \gg 1$ and $\kappa = O(1)$), the intermediate regime ($\eta = O(1)$ and $\kappa = O(1)$) or one of the quasi-diffusive regimes ($\eta \ll 1$ and $\kappa = O(1)$, or $\kappa \gg 1$, or $\kappa \ll 1$).

The quasi-diffusive regimes cannot reliably be distinguished by this method of constrained optimisation; however, if the diffusivities, D_u and D_v, are known, then it is simple to identify which one of these regimes is correct. It is only necessary to fit a pure diffusion model to the data, obtaining an estimate of the diffusivity, D. If $D \approx D_u$, then $\kappa \gg 1$; if $D \approx D_v$, then $\kappa \ll 1$. Otherwise, if $D_v < D < D_u$, then the data are in the effective diffusion regime ($\eta \ll 1$ and $\kappa = O(1)$).

The rapid equilibration regime

In the rapid equilibration regime ($\eta \gg 1$ and $\kappa = O(1)$) all model parameters, D_u, D_v, k^+ and k^-, can be reliably estimated by fitting the FRAP model to data. No further experiments are required in this case.

Estimating D_u and D_v.

Outside of the rapid equilibration regime, it is necessary to measure the diffusivities, D_u and D_v, independently. It may be possible to estimate the diffusivity of the unbound protein of interest, D_u, with a FRAP experiment on a physically similar but inert protein (perhaps a binding-deficient mutant

of the protein of interest). The diffusivity of the binding partner molecule, D_v, might be estimated with FRAP on a protein constituent of the binding complex. If it is unfeasible to measure one or both diffusivities experimentally, they can be estimated with the Stokes-Einstein relation.

The intermediate regime

In the intermediate regime ($\eta = O(1)$ and $\kappa = O(1)$) the reaction rates, k^+ and k^-, can be estimated by fitting the FRAP model to data, although estimates of D_u and D_v must be supplied.

The quasi-diffusive regimes

There are three quasi-diffusive regimes: slow equilibration ($\eta \ll 1$ and $\kappa = O(1)$), fast diffusion ($\kappa \gg 1$), and slow diffusion ($\kappa \ll 1$). In the slow equilibration regime, the ratio of the reaction rates k^-/k^+ can be estimated using the formula

$$k^-/k^+ = \frac{D - D_v}{D_u - D}.$$

In the remaining two quasi-diffusive regimes, it is technically possible to estimate the fraction of bound protein at chemical equilibrium, v_{eq}. Simply, in the fast diffusion regime, $v_{\text{eq}} \approx 0$, while in the slow diffusion regime $v_{\text{eq}} \approx 1$.

3.6 CHAPTER SUMMARY

This chapter dealt exclusively with numerically simulated FRAP experiments. We found evidence support our prediction that the feasibility of parameter estimation depends on the regime of the data, determined by the dimensionless constants η and κ. In regimes where parameter estimation is not feasible, we found that progress can be made by estimating the diffusivities, D_u and D_v with separate experiments. We proposed a simple FRAP fitting protocol which relies on estimating the regime of the data, then per-

forming parameter estimation and additional experiments (as required) to maximise the amount of information which can be extracted from FRAP data.

4

APPLYING NUMERICAL PARAMETER FITTING TO EMPIRICAL FLUORESCENCE RECOVERY AFTER PHOTOBLEACHING DATA

In chapters 2 and 3 we theoretically established the feasibility of parameter estimation in FRAP. In this chapter we apply numerical parameter fitting (as discussed in chapter 3) to empirical fluorescence microscopy data which has been supplied by the tumour cell biology laboratory at the Crick Institute.

We have so far considered a rather idealised FRAP model, so we must slightly modify the FRAP model itself before we can apply it to empirical data. We must also make some adjustments to the data, for example to control for passive photobleaching during the recovery phase of the experiment. In section 4.1 we pose the mathematical model of FRAP and outline the numerical methods used in the model simulation in section 4.2. The focus of section 4.3 is the methodology we use to obtain an empirically validated numerical description of the laser bleaching profile. In section 4.4 we explain, with reference to an example, the additional steps required to utilise this model to practical ends.

In total, we analysed data from 264 individual FRAP experiments, including wild type YAP in both normal fibroblasts (NFs) and cancer-associated fibroblasts (CAFs), and wild type TEAD (CAFs and NFs). Also included are two mutant variants of YAP: 5SA (NFs and CAFs) and S94A (NFs and CAFs). In addition, we analysed data on enhanced green fluorescent protein (EGFP) which serves as a control. The data are placed in proper biological

context in section 4.5. Finally, results are presented in full and their implications discussed in section 4.6. We consider model limitations in section 4.8.

4.1 MATHEMATICAL MODEL

Following previous studies [70, 71, 76], we assume that a diffusible molecular species, A, associates reversibly with a binding partner, B, to form a complex, C. Departing from our work in previous chapters, we do not assume that the domain under investigation is infinite, nor do we assume that binding partner B is homogeneously distributed.

We suppose that the domain under investigation may be represented by the set $\Omega \subset \mathbb{R}^2$. Let $u(\mathbf{x}, t)$ be the concentration of species A at point $\mathbf{x} \in \mathbb{R}^2$ and time $t \in [0, \infty)$ that is fluorescent (not yet photobleached), and D_u be the diffusivity of free protein, A. Likewise, let $v(\mathbf{x}, t)$ be the concentration of the fluorescent bound protein, C, and D_v its diffusivity. The resulting FRAP model is

$$\begin{cases} \frac{\partial u}{\partial t}(\mathbf{x}, t) = -k^+(\mathbf{x})u(\mathbf{x}, t) + k^- v(\mathbf{x}, t) + D_u \nabla^2 u(\mathbf{x}, t) - \alpha I(\mathbf{x}, t)u(\mathbf{x}, t), \\ \frac{\partial v}{\partial t}(\mathbf{x}, t) = +k^+(\mathbf{x})u(\mathbf{x}, t) - k^- v(\mathbf{x}, t) + D_v \nabla^2 v(\mathbf{x}, t) - \alpha I(\mathbf{x}, t)v(\mathbf{x}, t), \end{cases} \tag{254}$$

where $I(\mathbf{x}, t)$ is the intensity profile of the laser acting upon the sample, and α is the sensitivity of the fluorophore to photobleaching. Note that u and v are not separately measurable. Only the total fluorescent protein concentration w,

$$w(\mathbf{x}, t) = u(\mathbf{x}, t) + v(\mathbf{x}, t), \tag{255}$$

can be measured empirically

We assume that, over the time scale of the FRAP experiment, minimal transfer of material takes place between cellular compartments (such as the

cell nucleus and cytoplasm), so we impose homogeneous Neumann boundary conditions

$$\nabla u \cdot \hat{\mathbf{n}}|_{\partial\Omega} = 0, \quad \nabla v \cdot \hat{\mathbf{n}}|_{\partial\Omega} = 0, \tag{256}$$

where $\partial\Omega$ is the boundary of the domain Ω and $\hat{\mathbf{n}}$ is the unit outward normal vector.

We assume that prior to photobleaching the cellular compartment has already reached equilibrium. This leads to the initial conditions

$$u(\mathbf{x}, 0) = u_{\text{eq}}, \quad v(\mathbf{x}, 0) = v_{\text{eq}}(\mathbf{x}, 0), \tag{257}$$

where u_{eq} and v_{eq} are the non-trivial steady states of system (254) when $I = 0$ (note that we have allowed v_{eq} to be heterogeneous, but not u_{eq} for reasons we will explain presently). Boundary conditions (256) and initial conditions (257) close the model (254) if $I(\mathbf{x}, t)$ is defined. Also, the total pre-bleach protein concentration, w_{eq}, is simply

$$w(\mathbf{x}, 0) = w_{\text{eq}}(\mathbf{x}) = u_{\text{eq}} + v_{\text{eq}}(\mathbf{x}). \tag{258}$$

In principle, formula (258) gives a constraint on the pre-bleach fluorescent protein concentration, u_{eq}. Since there cannot be negative amounts of bound protein at any point, it is clear that

$$u_{\text{eq}} \leq \min_{\mathbf{x}\in\Omega}(w_{\text{eq}}(\mathbf{x})), \tag{259}$$

yet in practice (259) does not strictly hold due to the stochasticity of experimental data.

If the binding partner, B, is diffusible, then it is distributed homogeneously throughout the cellular compartment at equilibrium, in which case k^+ is spatially invariant and there is a homogeneous steady state, $u_{\text{eq}}, v_{\text{eq}}$, satisfying

$$k^+ u_{\text{eq}} = k^- v_{\text{eq}}. \tag{260}$$

However, if the binding partner B is non-diffusible, then it may be heterogeneously distributed. In this case k^+ is a non-uniform function of $\mathbf{x}$ and not a

model parameter. Therefore, for the purposes of parameter fitting, we shall instead consider the steady state value u_{eq}, which is necessarily a constant. To prove this, we simply substitute u_{eq} and v_{eq} into (254),

$$\begin{cases} \frac{\partial u_{\text{eq}}}{\partial t}(\mathbf{x}) = 0 = -k^+(\mathbf{x})u_{\text{eq}}(\mathbf{x}) + k^-v_{\text{eq}}(\mathbf{x}) + D_u\nabla^2 u_{\text{eq}}(\mathbf{x}), \\ \frac{\partial v_{\text{eq}}}{\partial t}(\mathbf{x}) = 0 = +k^+(\mathbf{x})u_{\text{eq}}(\mathbf{x}) - k^-v_{\text{eq}}(\mathbf{x}) + D_v\nabla^2 v_{\text{eq}}(\mathbf{x}). \end{cases} \tag{261}$$

Adding both equations, the reaction terms cancel to give

$$D_u\nabla^2 u_{\text{eq}}(\mathbf{x}) + D_v\nabla^2 v_{\text{eq}}(\mathbf{x}) = 0. \tag{262}$$

Since $D_v = 0$ in this case, (262) reduces to Laplace's equation

$$\nabla^2 u_{\text{eq}} = 0, \tag{263}$$

Multiplying the boundary condition at equation (256) by u_{eq} gives

$$u_{\text{eq}}(\nabla u_{\text{eq}} \cdot \hat{\mathbf{n}}) \mid_{\partial\Omega} = (u_{\text{eq}}\nabla u_{\text{eq}}) \cdot \hat{\mathbf{n}} \mid_{\partial\Omega} = 0. \tag{264}$$

Let J be defined as the integral

$$J = \oint_{\partial\Omega} (u_{\text{eq}}\nabla u_{\text{eq}}) \cdot \hat{\mathbf{n}} \mathrm{d}S = 0. \tag{265}$$

Then, by the divergence theorem,

$$J = \int_\Omega \nabla \cdot (u_{\text{eq}}\nabla u_{\text{eq}}) \mathrm{d}V = \int_\Omega (\nabla u_{\text{eq}} \cdot \nabla u_{\text{eq}}) \mathrm{d}V + \int_\Omega u_{\text{eq}}\nabla^2 u_{\text{eq}} \mathrm{d}V. \tag{266}$$

Since $J = 0$ and $\nabla^2 u_{\text{eq}} = 0$,

$$J = \int_\Omega (\nabla u_{\text{eq}} \cdot \nabla u_{\text{eq}}) \mathrm{d}V = \int_\Omega \|\nabla u_{\text{eq}}\|^2 \mathrm{d}V = 0. \tag{267}$$

As $\|\nabla u_{\text{eq}}\|$ is non-negative, in order to have the integral (267) evaluate to zero we must have $\|\nabla u_{\text{eq}}(\mathbf{x})\| = 0 \; \forall \mathbf{x} \in \Omega$, which implies that $\nabla u_{\text{eq}} = \mathbf{0}$ or, equivalently, that u_{eq} is uniform, as required.

4.1.1 *The bleaching/imaging laser $I(\mathbf{x}, t)$*

To solve (254) numerically, we require a mathematical description of the bleaching laser, $I(\mathbf{x}, t)$. Let t_{bleach} be the duration of the bleach phase.

Although many conventional FRAP studies assume that $t_{\text{bleach}} = 0$, in confocal scanning FRAP the laser scans the sample repeatedly to achieve photobleaching, which typically takes several seconds [76]. At $t = t_{\text{bleach}}$ the bleaching phase ends and the recovery phase begins, which lasts until $t = t_{\text{end}}$; the duration of the recovery phase is then $t_{\text{end}} - t_{\text{bleach}}$.

The laser intensity, I, is given by

$$I(x,t) = \begin{cases} I_{\text{pre}}(\mathbf{x}) & \text{if } t \in [0, t_{\text{bleach}}), \\ I_{\text{post}}(t) & \text{if } t \in [t_{\text{bleach}}, t_{\text{end}}]. \end{cases} \tag{268}$$

We find that neither I_{pre} nor I_{post} can be easily described by common mathematical functions, and we instead derive numerical approximations from data. We discuss I_{pre} in detail in section 4.3, and I_{post} in section 4.4.2.

4.1.2 *Parameter estimation*

Here we briefly summarise the parameter estimation problem arising from system (254). The independent variables are the spatial coordinates, $\mathbf{x} \in \Omega$, and time elapsed since the start of photobleaching $t \in [0, t_{\text{end}}]$. The only empirically measurable dependent variable is the total concentration of fluorescent protein, $w(\mathbf{x}, t) = u(\mathbf{x}, t) + v(\mathbf{x}, t)$. The unknown model parameters are:

- $D_u \in [0, \infty)$ - the diffusivity of the unbound protein.
- $D_v \in [0, \infty)$ - the diffusivity of the bound protein complex.
- $k^- \in [0, \infty)$ - the reverse reaction rate, the rate of dissociation of protein from the complex.
- $u_{\text{eq}} \in [0, \max_{\mathbf{x}\in\Omega}(w_{\text{eq}}(\mathbf{x}))]$ - the initial pre-bleach concentration of unbound protein (note that this is a partial relaxation of constraint (259)).

- $\alpha \in [0, \infty)$ - the sensitivity of the fluorophore to photobleaching. It is possible that α could be determined in a separate experiment, but we will not assume so.

The association rate, $k^+(\mathbf{x})$, is not included in the above list because it is a function of space, rather than a parameter. Once u_{eq} and k^- are known, $k^+(\mathbf{x})$ can be inferred from $w_{\text{eq}}(\mathbf{x})$.

Let $w_{\text{Data}}(\mathbf{x}, t)$ be empirical fluorescence microscopy data and $\theta = (D_u, D_v, k^-, u_{\text{eq}}, \alpha)$ be the vector of fitting parameters. The objective function $\phi(\theta)$ is defined as

$$\phi(\theta) = \int_{t_{\text{bleach}}}^{t_{\text{end}}} \int_{\mathbf{x}\in\Omega} (w(\mathbf{x}, t; \theta) - w_{\text{Data}}(\mathbf{x}, t))^2 \mathrm{d}V \mathrm{d}t. \tag{269}$$

Note that only data from the recovery phase, $t \in (t_{\text{bleach}}, t_{\text{end}}]$, may be used to calculate ϕ; no data are collected during the bleaching phase. Similar to various prior studies [72, 104–106], we approximate system (254) numerically in order to compute the objective function (269), thereby enabling us to produce a maximum likelihood estimate of the values of the model parameters [157]. There are, however, several preliminary steps which we will first discuss in detail in the following section.

4.2 NUMERICAL METHODS

The FRAP model must be simulated numerically, which is accomplished using a finite difference method. First, the active domain, Ω, is decomposed into a set of grid points, $\mathbf{x}_i$, indexed by i. We begin with the regular grid,

$$G = \{(j\Delta x, k\Delta y) | j, k \in \mathbb{Z}\},$$

which has horizontal spacing Δx and vertical spacing Δy. The discrete active domain of the simulation, $\bar{\Omega}$, is just the grid points which are contained within Ω,

$$\bar{\Omega} = \Omega \cap G.$$

Having established the discrete domain, we define variables at each grid point equal to the value of the corresponding function at that point,

$$u_i(t) = u(\mathbf{x}_i, t), \quad v_i(t) = v(\mathbf{x}_i, t), \quad k_i^+ = k^+(\mathbf{x}_i), \quad I_i(t) = I(\mathbf{x}_i),$$

for $\mathbf{x}_i \in \bar{\Omega}$.

It remains to define the discrete Laplacian,

$$\nabla_i^2 u_i = \frac{1}{\Delta x^2} \sum_{j \in \text{nn}_x(i)} (u_j - u_i) + \frac{1}{\Delta y^2} \sum_{j \in \text{nn}_y(i)} (u_j - u_i),$$

where $\text{nn}_x(i)$ is the set of nearest neighbours (grid points adjacent to x_i) which are vertically aligned with $\mathbf{x}_i$, and likewise $\text{nn}_y(i)$ is the set of nearest neighbours which are horizontally aligned with $\mathbf{x}_i$. It is then simple to reduce the full FRAP PDE model (254) to the semi-discrete model,

$$\begin{cases} \frac{\mathrm{d}u_i}{\mathrm{d}t}(t) = -k_i^+ u_i(t) + k^- v_i(t) + D_u \nabla_i^2 u_i(t) - \alpha I_i(t) u_i(t), \\ \frac{\mathrm{d}v_i}{\mathrm{d}t}(t) = k_i^+ u_i(t) - k^- v_i(t) - \alpha I_i(t) v_i(t). \end{cases} \tag{270}$$

The solution to the system of equations, (270), can be approximated with an appropriate ODE solver. We chose MATLAB's variable order stiff solver, ode15s, as this method is numerically stable even for relatively large time step sizes, although it is required to compute the Jacobian. However, since (270) is linear, the Jacobian may be computed explicitly and supplied directly to the solver, so ODE15s is an efficient solver for our purposes.

4.3 THE BLEACHING LASER $I_{\text{pre}}(\mathbf{x})$

Quantitative studies of FRAP often assume that the intensity profile of the bleaching laser, $I_{\text{pre}}(\mathbf{x})$, is given by a standard function, such as a Gaussian function [29, 48, 74, 76, 280], or circular [30, 70] or square-shaped [65] step functions. However, since we have been supplied with fluorescence microscopy data from an immobile protein (histone H2B) we are able to obtain an empirical description of the bleaching laser intensity profile, $I_{\text{pre}}(\mathbf{x})$,

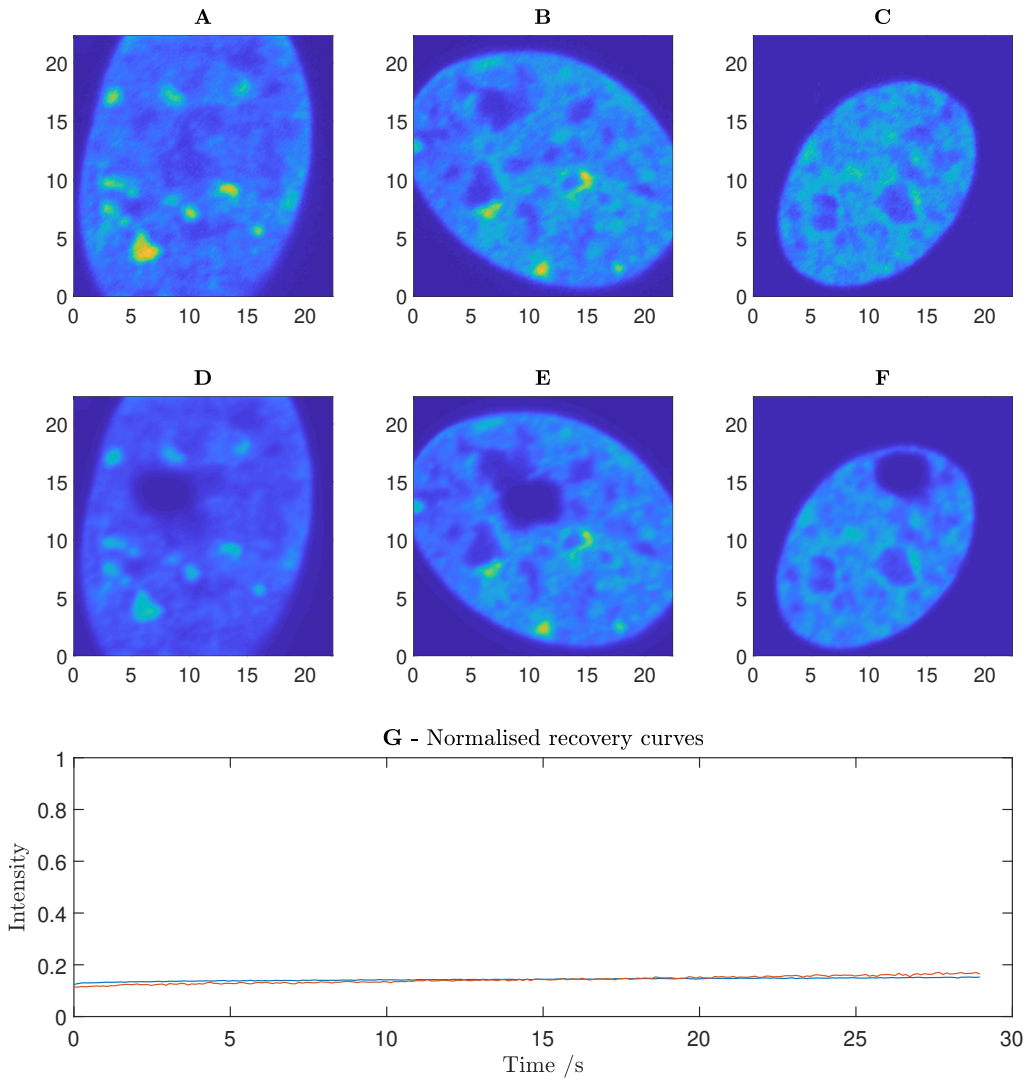


Figure 18: **(A-C)** H2B fluorescence intensity distributions in three separate cells at pre-bleach equilibrium. **(D-F)** The same three cells immediately after photobleaching. **(G)** Averaged H2B fluorescence intensity across the regions of interest in two sets of cells. The intensity recovers only to a minuscule extent during the experiment, which suggests that H2B has sufficiently low mobility that it can be used to infer the bleaching laser intensity distribution.

which we introduced in section 4.1.1. We can then use this laser profile in all subsequent instances of the FRAP simulation.

Suppose that an inert, non-diffusible molecule has a concentration $q(\mathbf{x}, t)$, which is scaled so that its sensitivity to photobleaching, $\alpha = 1$ (we are able to make this assumption because the photobleaching sensitivity is taken to be a fitting parameter in the analysis of the main proteins of interest, such

as YAP and TEAD). The governing equation of q during the bleaching phase is simply

$$\frac{\partial q}{\partial t}(\mathbf{x}, t) = -I_{\text{pre}}(\mathbf{x}) q(\mathbf{x}, t), \tag{271}$$

which has solution

$$q(\mathbf{x}, t) = q(\mathbf{x}, 0) e^{-I_{\text{pre}}(\mathbf{x}) t}, \tag{272}$$

for $t \in [0, t_{\text{bleach}}]$. Inversion of (272) at $t = t_{\text{bleach}}$ reveals that the bleaching laser profile is

$$I_{\text{pre}}(\mathbf{x}) = -\frac{1}{t_{\text{bleach}}} \log \left(\frac{q(\mathbf{x}, t_{\text{bleach}})}{q(\mathbf{x}, 0)} \right). \tag{273}$$

It is thus possible to infer $I_{\text{pre}}(\mathbf{x})$ from a pre-bleach frame, $q(\mathbf{x}, 0)$, and the first post-bleach frame, $q(\mathbf{x}, t_{\text{bleach}})$.

To measure $I_{\text{pre}}(\mathbf{x})$, we used FRAP data from histone H2B, a protein constituent of chromatin [281]. In figure 18, the pre-bleach (A-C) and post-bleach (D-F) frames from two different cells are shown. From the 'recovery' curves (figure 18, G) it is clear that H2B is immobile over the time scale of the experiment. Hence H2B can be used to estimate reliably the bleach laser profile.

Laser profiles derived from H2B data using formula (273) are shown in figure 19. Figure 19A displays the average of a sample of laser profiles re-centred on the same point, indicated by the red x. All available FRAP experiments on H2B had been photobleached using the largest bleach region size, the 17×17 pixel region; however, in the experiments on wild type YAP, two smaller bleach region sizes were used, the intermediate region size, 14×14 pixels, and the smallest region size, 11×11 pixels (where each pixel had a side length of 0.128 μm). In the absence of H2B data using these bleach region sizes, the smaller bleach region sizes were obtained by a linear re-scaling of the 17×17 region (figure 19B, C).

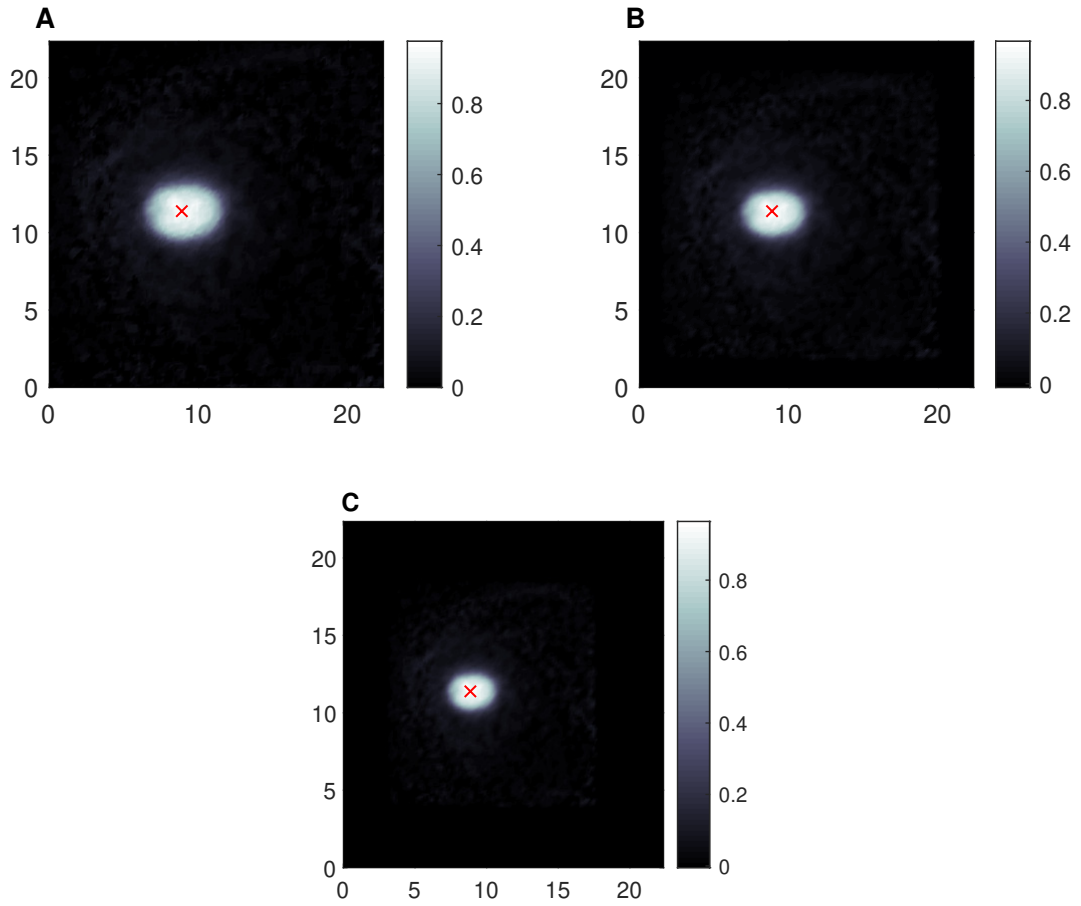


Figure 19: Laser profiles. The centre of the laser is in each case shown with a red x. **(A)** Laser profile for the 17×17 bleach spot, directly inferred from H2B data. **(B)** Laser profile for the 14×14 bleach spot, obtained by re-scaling the 17×17 profile. **(C)** Laser profile for the 11×11 bleach spot, obtained by re-scaling the 17×17 profile.

Previous quantitative studies of FRAP have commonly assumed that the bleaching laser profile is well-approximated by a simple mathematical function; such as a circular step function [30, 70]

$$I_{\text{pre}}(\mathbf{x}) = \begin{cases} 1 & \text{if } r \in [0, r_n] \\ 0 & \text{if } r > r_n, \end{cases} \tag{274}$$

or a Gaussian function [29, 48, 74, 76, 280]

$$I_{\text{pre}}(\mathbf{x}) = e^{-2\frac{r^2}{r_n^2}}, \tag{275}$$

where $r = \|\mathbf{x}\|$. Interestingly, our empirically-derived profiles do not resemble either of these functions. First, we notice that the shape of the laser profile is not perfectly symmetrical, but appears to be slightly elongated in the horizontal direction. We therefore also considered a more general Gaussian function, with mixed length scales x_n and y_n,

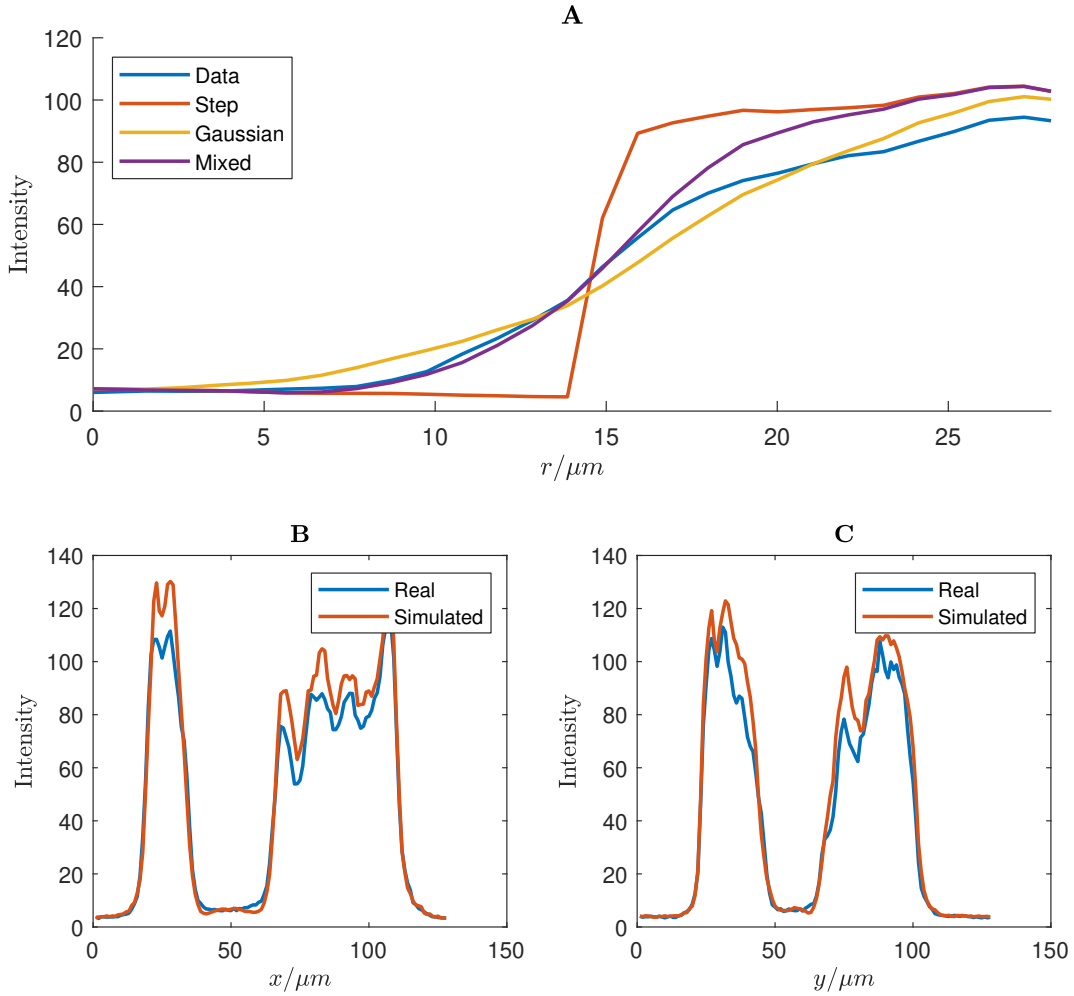


Figure 20: **(A)** Post-bleach H2B fluorescence intensity fitted with simulated post-bleach profiles generated using step function intensity (274), Gaussian intensity (275), and mixed Gaussian intensity (276). **(B)** Post-bleach H2B fluorescence intensity on a line through the centre of the bleach region which is parallel to the x-axis, fitted with the mixed Gaussian intensity (276) post-bleach profile. **(C)** Same as **(B)** for the y-axis.

$$I_{\text{pre}}(\mathbf{x}) = e^{-2\left(\frac{x^2}{x_n^2}+\frac{y^2}{y_n^2}\right)}, \tag{276}$$

where $\mathbf{x} = (x, y)$. Yet this also appears to be a poor fit to data (figure 20B, C). The Gaussian function underestimates the true extent of the photobleaching far from the centre of the region of interest.

We can only speculate about the reasons why the bleach profile is so unusual. In confocal scanning FRAP, the bleach profile is formed by modulated the intensity of the laser as it scans across the sample, so it can potentially take any shape [286]. As far as we are aware, the laser microscope was programmed to bleach a Gaussian profile. As we discussed in section 1.1 of chapter 1, at high light intensities the rate of photobleaching varies sub-linearly with intensity, which tends to flatten the bleach profile [62–64]. Consequently, the Gaussian model relatively overestimates the extent of bleaching close to the centre of the bleach region and relatively underestimates the extent of the bleaching at the periphery. We are unable to prove that this is the explanation, given the available data, but it is certainly consistent with our observations.

The asymmetry of the leach profile might also be explained as follows: as the laser scans across each raster line, it has high horizontal velocity and zero vertical velocity. If the rate of dynamic variation of laser intensity is not much larger than the horizontal scan rate, then the bleach profile may be stretched in the horizontal direction. Regardless of the reasons, the failure of typical mathematical models of the bleach profile to conform to data is clear. It would certainly be interesting to find out whether this phenomenon is common and, if so, how it has affected parameter estimation in studies which assume Gaussian or step function bleach profiles.

4.4 FITTING PRELIMINARIES

There are a few simple processes which must be applied to FRAP data in each instance prior to parameter fitting. First, it is necessary to determine the active domain, Ω, on which to run the numerical FRAP model (section 4.4.1). Next, we must determine the intensity of the light which causes

bleaching during the recovery phase, $I_{\text{post}}(t)$ (section 4.4.2). Additionally, we must prescribe the initial condition of the numerical model, $w_{\text{eq}}(\mathbf{x})$ (section 4.4.3). Once these steps are completed, the FRAP model (254) is closed and we may proceed with the parameter fitting simulation.

4.4.1 *Identifying the active domain*

For all the data we consider in this chapter, the active domain under consideration, Ω, is the cell nucleus (note that we will investigate translocation between the nucleus and the cytoplasm in chapter 5). For each assay, we are given a recording of a cell comprising 250 frames from which we seek to determine the precise geometry of Ω. As there is substantial noise in each individual frame, we begin by blending all of these frames into a single image by taking an average (figure 21A).

The proteins of interest, YAP and TEAD, associate with chromatin binding sites which are inhomogeneously distributed throughout the nucleus. Therefore YAP and TEAD themselves are inhomogeneously distributed at chemical equilibrium. Given the inhomogeneity of protein of interest concentration within the nucleus, as well as the complexity of nuclear boundary (specifically, the presence of internal obstructions), we found that edge detection algorithms such as the Sobel method were not consistently effective at identifying the geometry of the nucleus. For this reason, a GUI was implemented in MATLAB to allow the user to draw around the nucleus (or other relevant structure as the case may be) by selecting a sample of points (figure 21B). By interpolating between this points with a polynomial spline, a continuous closed curve is drawn. This curve is taken to be the nuclear boundary and all exterior points are excluded from the active domain (figure 21B,C).

In the example presented in figure 21 the cell nucleus is quite clear, an approximately elliptical region of relatively low YAP concentration. We also notice that there are a handful of dark regions inside the nucleus where the

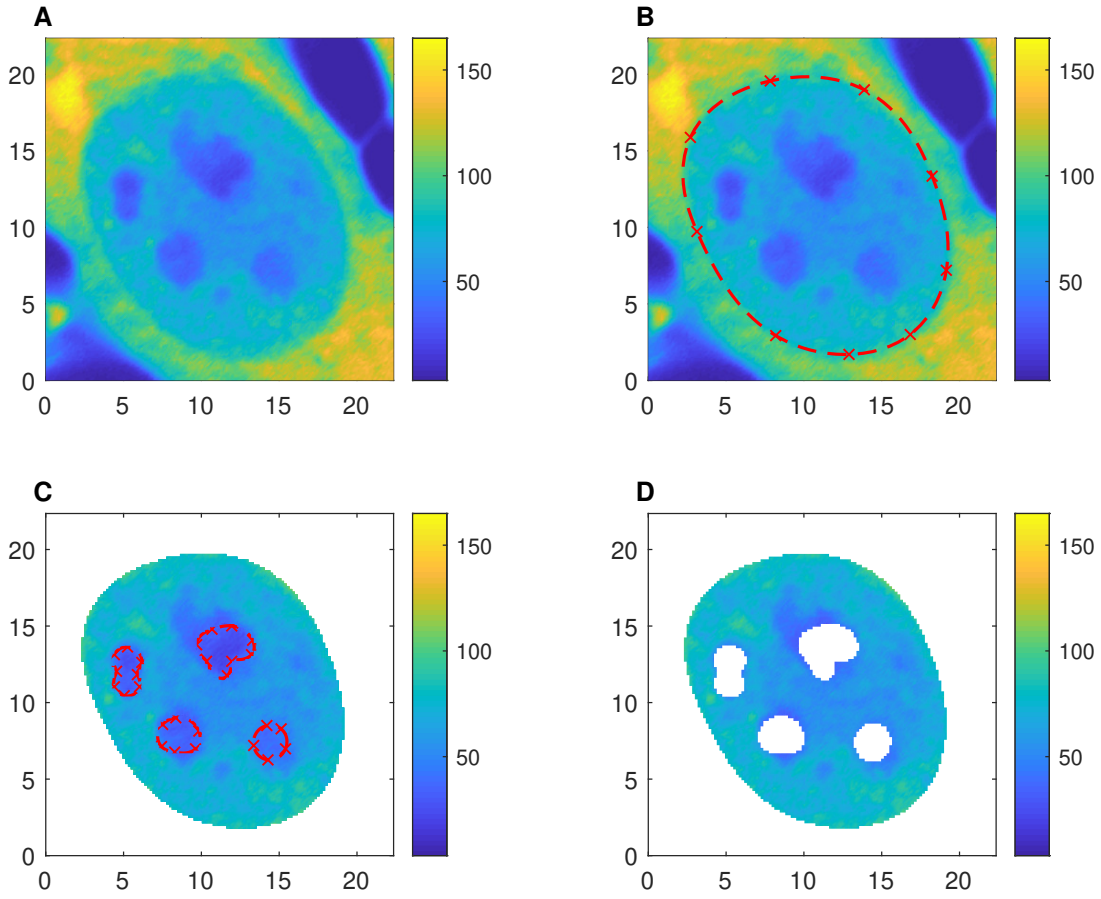


Figure 21: An illustration of the process of identifying the active domain for the simulation. **(A)** All 250 frames of fluorescence microscopy imaging of a cell during a FRAP experiment averaged to form a single image. **(B)** The cell nucleus is isolated by tracing its boundary with a closed curve shown in red. **(C)** The region outside the nucleus is excluded. Obstructions are isolated by tracing around them with closed curves shown in red. **(D)** The obstructions are excluded. The remaining region is taken to be the active domain for the simulation.

concentration of the protein of interest (YAP in this case) is much lower than elsewhere. It is possible that these dark regions are impermeable obstructions, such as nucleoli [287] or dense regions of DNA. We identify the dark regions as we identified the nuclear boundary, and then exclude them from the active domain (figure 21C,D).

It is possible that there could be diffusion across these dark, protein-deficient regions. We must bear in mind that we are posing a two-dimensional model of a three-dimensional structure and that there may well be diffusion

above and below the obstructions within the nucleus, which would resemble diffusion across the obstructed regions in the 2D plane. In this case it would be a mistake to exclude them form the active domain. For a sample of cells, we tested parameter fitting in both cases; including the chromatin deficient regions in Ω, and excluding them. We found that changing our assumptions about the chromatin-deficient regions had only a small effect on the fitting output. We believe that this is because the proteins we are investigating are highly mobile. They are able to diffuse around obstacles almost as quickly as they could diffuse through the space occupied by the obstacles. We expect that the precise details of cellular geometry would be more important if the proteins under investigation were less mobile, but have no available data to test this claim.

4.4.2 *Passive bleaching* $I_{\text{post}}(\mathbf{x})$

In practice, the imaging laser causes a small amount of unintentional photobleaching during the recording of the fluorescence recovery, so that the total amount of fluorescent protein inside the nucleus,

$$W(t) = \int_\Omega w(\mathbf{x}, t) \mathrm{d}V, \tag{277}$$

will decay over time. It follows that

$$\frac{\mathrm{d}W}{\mathrm{d}t} = \int_\Omega \frac{\partial w}{\partial t}(\mathbf{x}, t) \mathrm{d}V. \tag{278}$$

Since, $w(x, t) = u(\mathbf{x}, t) + v(\mathbf{x}, t)$,

$$\frac{\mathrm{d}W}{\mathrm{d}t} = \int_\Omega \left(\frac{\partial u}{\partial t} + \frac{\partial v}{\partial t} \right) \mathrm{d}V, \tag{279}$$

Substituting equation (254) yields

$$\frac{\mathrm{d}W}{\mathrm{d}t} = \int_\Omega \left(D_u \nabla^2 u + D_v \nabla^2 v - \alpha I_{\text{post}}(t) u - \alpha I_{\text{post}}(t) v \right) \mathrm{d}V. \tag{280}$$

By the divergence theorem

$$\int_\Omega D_u \nabla^2 u \mathrm{d}V = \oint_{\partial\Omega} D_u \nabla u \cdot \hat{\mathbf{n}} \mathrm{d}S = 0, \tag{281}$$

due to the zero-flux boundary condition (256). Likewise,

$$\int_\Omega D_v \nabla^2 v \mathrm{d}V = \oint_{\partial\Omega} D_v \nabla v \cdot \hat{\mathbf{n}} \mathrm{d}S = 0. \tag{282}$$

Therefore

$$\frac{\mathrm{d}W}{\mathrm{d}t} = \int_\Omega \left(-\alpha I_{\text{post}}(t) u - \alpha I_{\text{post}}(t) v\right) \mathrm{d}V = -\alpha I_{\text{post}}(t) \int_\Omega (u+v) \mathrm{d}V. \tag{283}$$

In conclusion,

$$\frac{\mathrm{d}W}{\mathrm{d}t} = -\alpha I_{\text{post}}(t) W(t) = a(t) W(t). \tag{284}$$

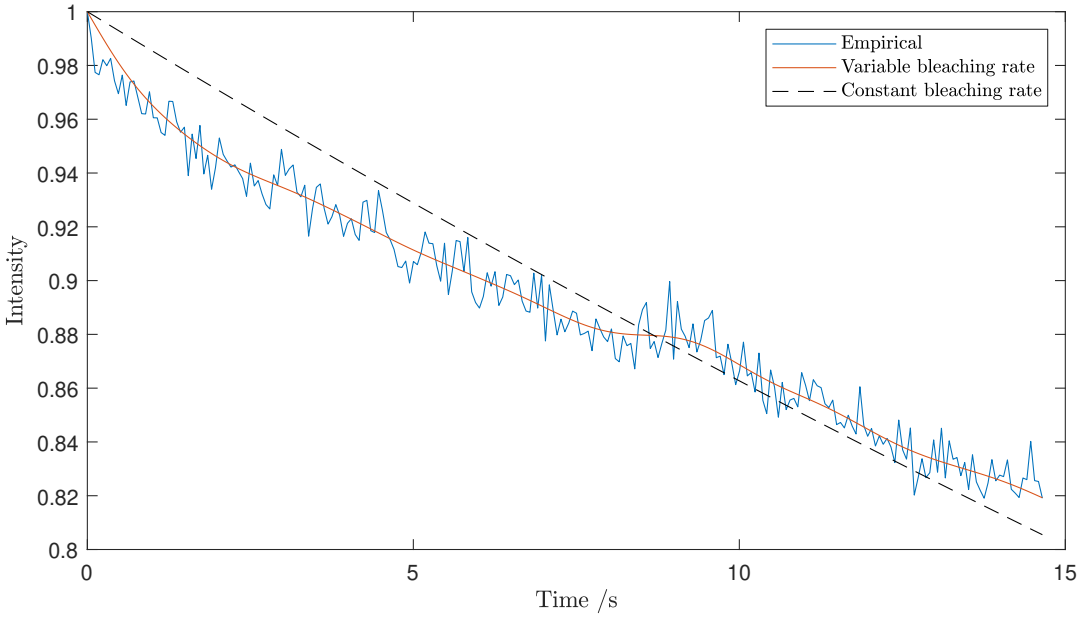


Figure 22: The decay of the total quantity of fluorescent material, W, inside the cell nucleus compared with two simulations. In the first simulation, the bleaching rate, $a(t)$, was variable as defined by formula (285). In the second simulation, a was assumed to be a constant which was determined by minimising the residual sum of squared errors.

The total fluorescence, $W(t)$ is measured empirically. A moving average filter is then applied to produce the smoothed function $\widetilde{W}(t)$ the derivative of which, $\widetilde{W}'(t)$, is then computed numerically. Finally, we are left with

$$a(t) = \frac{\widetilde{W}'(t)}{\widetilde{W}(t)}. \tag{285}$$

We might expect the passive bleaching function $a(t)$ to be a constant, yet surprisingly in experiments the rate of passive phototbleaching turns out to be unsteady, as shown in figure 22, with a constant bleaching rate model giving a poor fit to data, possibly due to laser intensity fluctuations [44].

4.4.3 *The initial condition, $w_{\text{eq}}(\mathbf{x})$*

In section 4.3 we saw that the protein binding partner, chromatin, is both immobile and imhomogeneously distributed. Since the distribution of chromatin varies from cell to cell, it will be necessary to determine the precise distribution in each case.

In principle, we could simply record the cell at pre-bleach steady state, but the data are noisy and we were provided with only three frames of pre-bleach recording. In this section we will outline in detail the process used to estimate the initial distribution of the protein of interest (YAP or TEAD) at pre-bleach equilibrium, $w_{\text{eq}}(\mathbf{x})$. Since the spatial structure of the cell is somewhat obscured by stochastic effects in any individual frame, it is necessary, as in section 4.4.1, to obtain a static image of the cell by averaging many frames. However, each recording includes only three frames of the cell pre-bleach, which is inadequate (figure 23C). If we simply average every frame of the recording we will obviously under-estimate the equilibrium concentration of protein (and hence chromatin) near to the bleach spot (figure 23A) because of photobleaching. We therefore wish to average only those frames for which the cell is close to chemical equilibrium.

It can be observed (for example in the recovery curves depicted in figure 22A) that the cells under investigation typically reach post-bleach equilibrium midway through the recording. Therefore, in each cell we identified a threshold time, which is the point at which the smoothed recovery curve attains 99% of its asymptotic limit, beyond which we assumed the cell to be in post-bleach equilibrium. We then simply averaged all the frames taken after the threshold time (figure 23C) as a form of noise reduction. One final

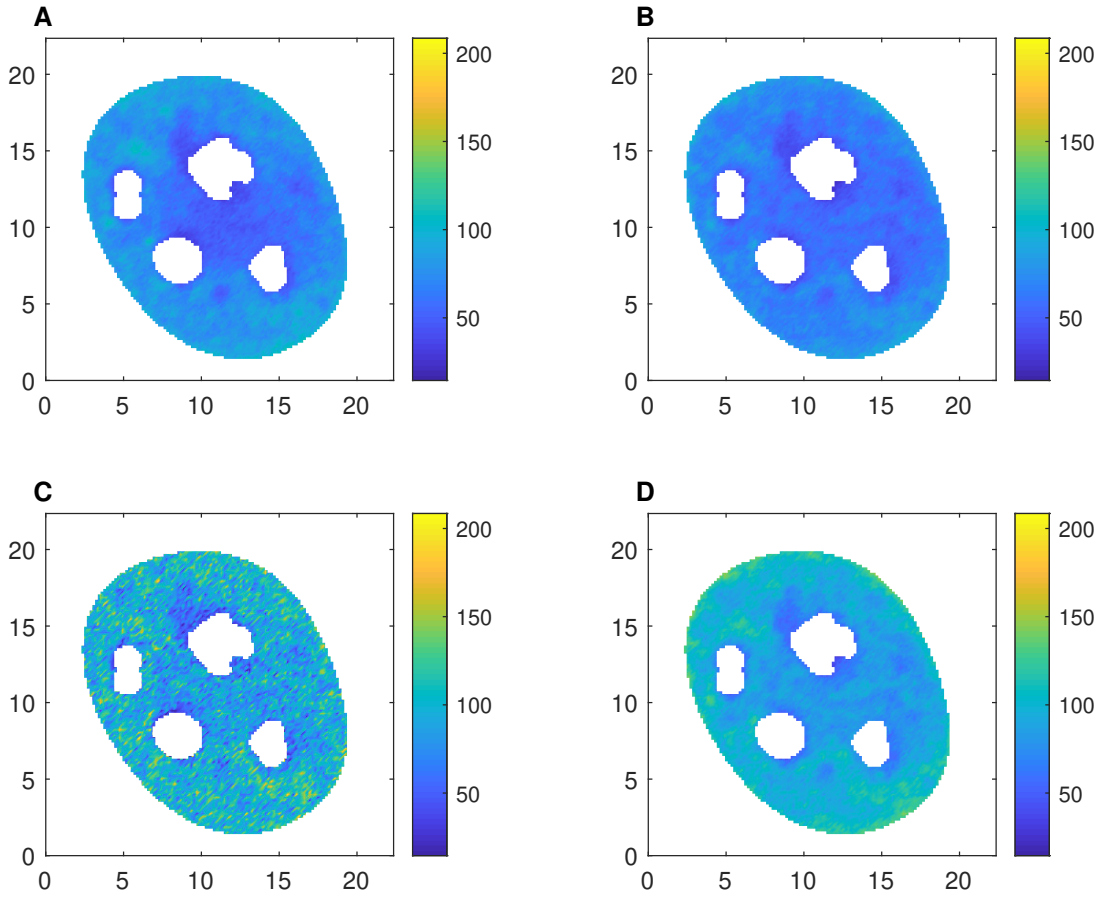


Figure 23: **(A)** An average of the frames before the cutoff time at which the cell has reached post-bleach equilibrium. Notice that there is a dark spot near the centre of the nucleus due to photobleaching. **(B)** An average of the frames after the cutoff time at which the cell has reached post-bleach equilibrium. Notice the absence of the dark spot near the centre of the nucleus since the cell has reached equilibrium. **(C)** The average of the three pre-bleach frames. This image is particularly noisy. **(D)** The estimate of the pre-bleach equilibrium which will be used in the cell simulation, created by linearly re-scaling the intensity of the post-bleach equilibrium to match the intensity of the pre-bleach equilibrium.

remaining problem is that the total quantity of protein at post-bleach equilibrium is significantly lower than at pre-bleach equilibrium. To resolve this we simply re-scale the post-bleach average intensity linearly to minimise the error between the post-bleach average intensity (figure 23B) and the empirical pre-bleach average (figure 23C) to produce the best fit of the noisy

pre-bleach profile with the relatively smooth, averaged post-bleach intensity profile. The output of this process can be seen in figure 23D.

4.5 BIOLOGICAL CONTEXT AND EXPERIMENTAL DATA

Before we discuss the model fitting results, let us briefly revisit the relevant biological background (discussed in greater detail in chapter 1). Recall that we are primarily interested in two interacting proteins, YAP and TEAD. YAP (yes-associated protein) is a transcription co-regulator which regulates various genes that promote cell growth and inhibit apoptosis [288, 289]. When YAP is aberrantly localised to the cell nucleus, it interacts with TEAD and chromatin (DNA) to cause tumorigenesis by promoting uncontrolled cell proliferation [9, 290]. The tumorigenic activity of YAP is dependent upon its interactions TEAD transcription factors [206, 291].

Under normal circumstances, YAP is regulated by the Hippo signalling pathway [10,170]. Hippo phosphorylates YAP, which inhibits its interactions with chromatin by a number of different mechanisms. Phosphorylated YAP is anchored in the cytoplasm by regulatory proteins [175], while its rate of degradation by proteasomes [176] and its rate of export from the cell nucleus [292, 293] are both increased.

We analysed data on the following proteins:

- Wild type YAP (WT YAP) - the typical form of the transcription co-regulator, YAP, as it appears in nature. Some WT YAP data are presented in figure 24 (NFs) and 25 (CAFs). The YAP concentration is visibly greater outside the nucleus in NFs, due to regulation by Hippo. Sample size: 30 NFs and 30 CAFs.

- Wild type TEAD (TEAD) - the typical form of the transcription factor and functional partner of YAP, TEAD, as it appears in nature. Some TEAD data are presented in figure 26 (NFs) and 27 (CAFs). Interest-

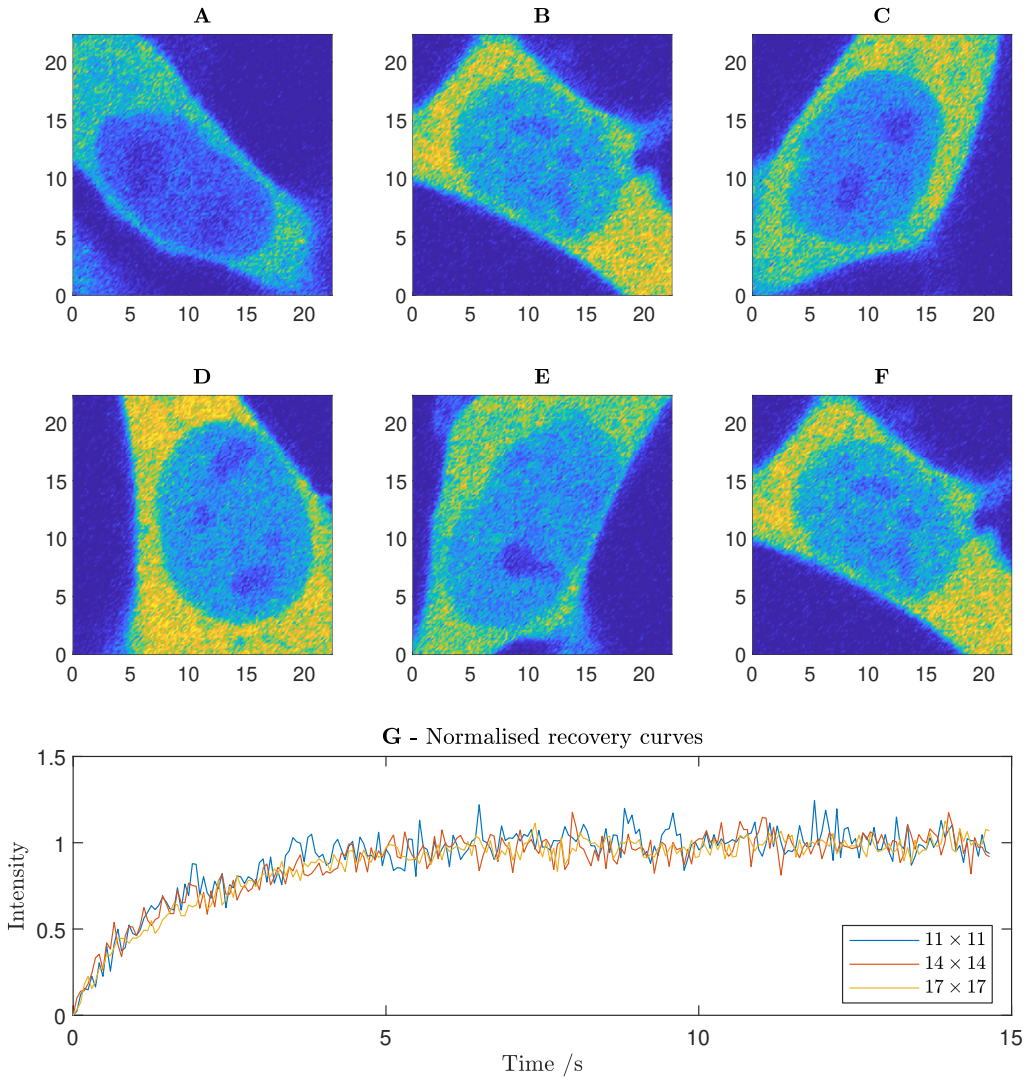


Figure 24: Wild type YAP, normal fibroblasts. (A-F) Images of six randomly selected cells obtained by averaging three pre-bleach frames. (G) Averaged, normalised fluorescence recovery curves from three different sets of experiments with different sizes of bleach region.

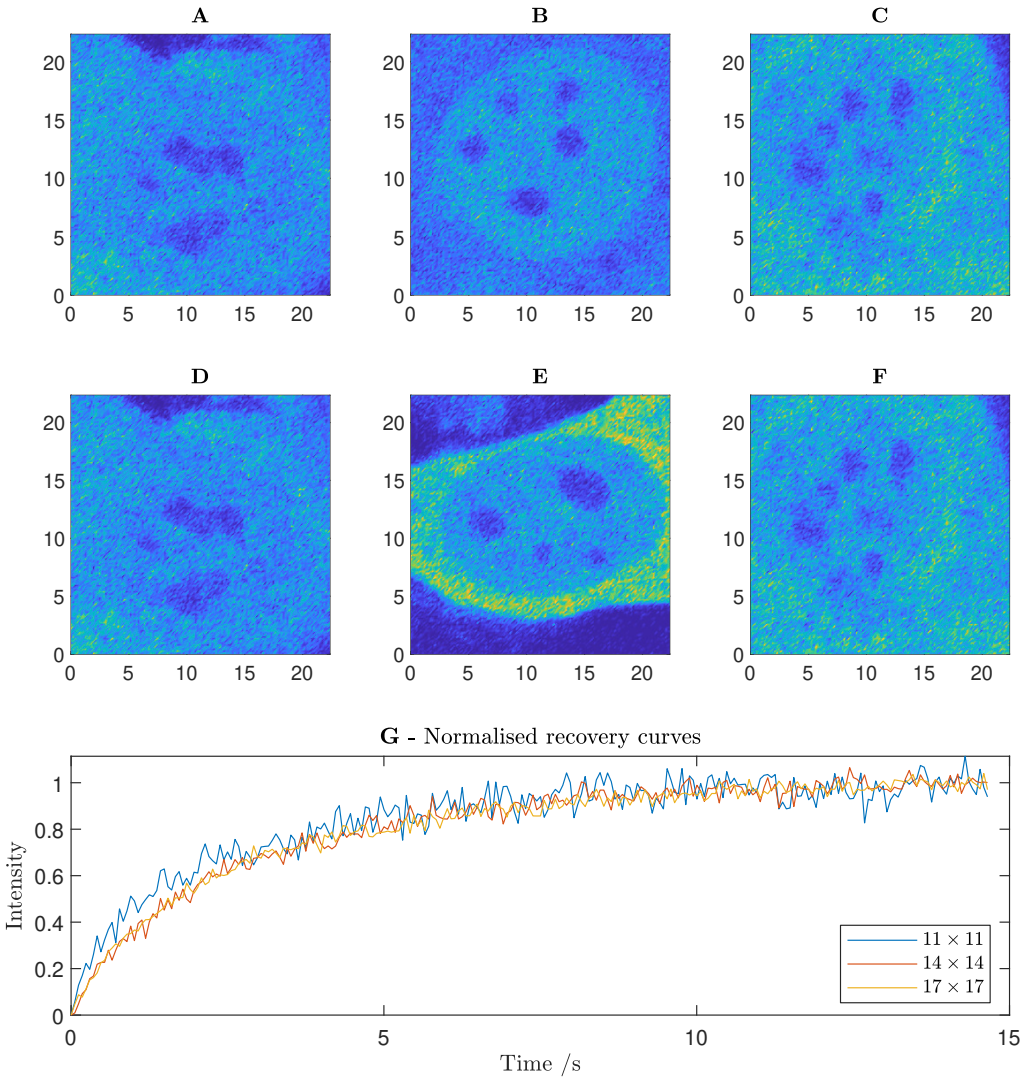


Figure 25: Wild type YAP, cancer-associated fibroblasts. (A-F) Images of six randomly selected cells obtained by averaging three pre-bleach frames. (G) Averaged, normalised fluorescence recovery curves from three different sets of experiments with different sizes of bleach region.

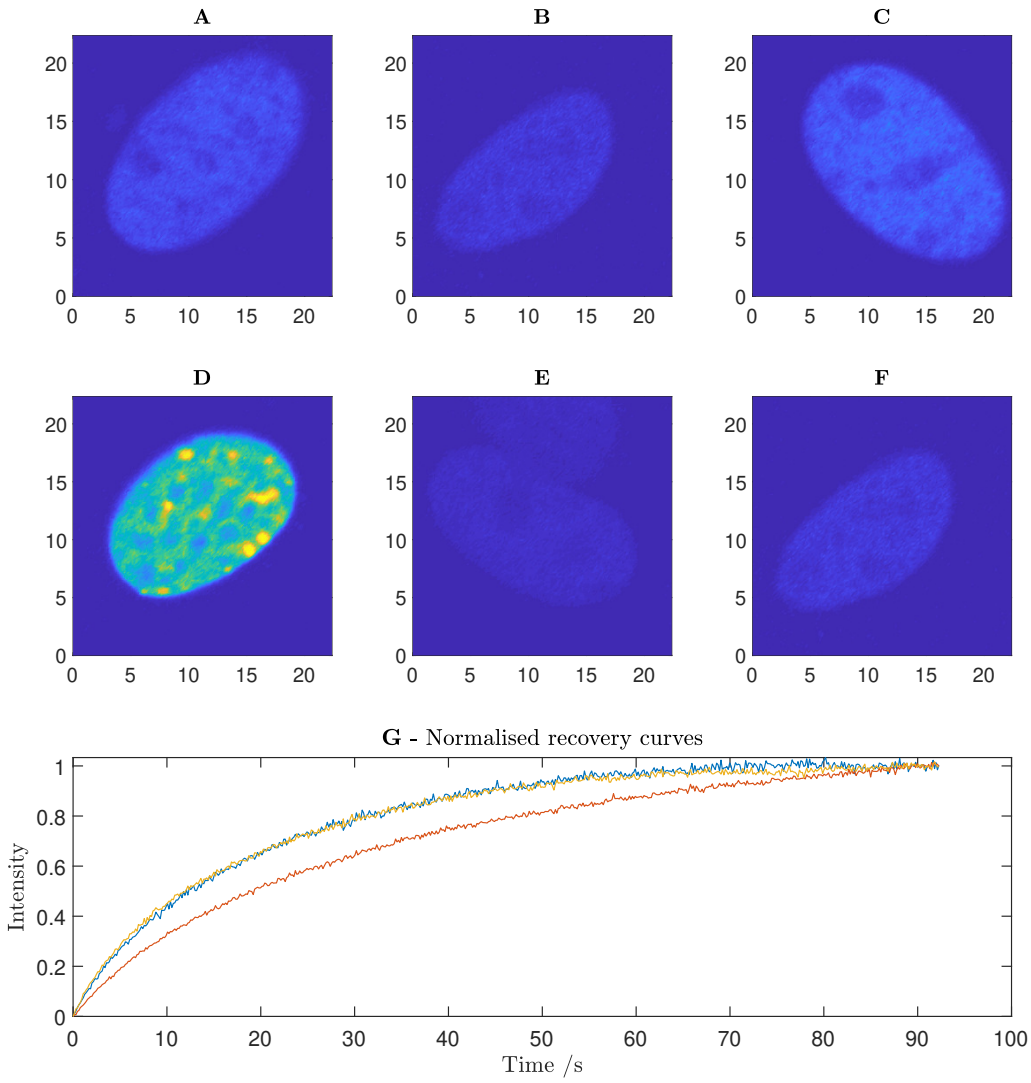


Figure 26: TEAD, normal fibroblasts. (A-F) Images of six randomly selected cells obtained by averaging three pre-bleach frames. (G) Averaged, normalised fluorescence recovery curves from three different sets of experiments. These different experiments used an identical bleach region radius (17×17). For this reason, the curves are unlabelled as the difference between the experiment sets is meaningless out of context. Note that, since the experiments used a single bleach region radius, the differences between the recovery curves are a product of variation between cells.

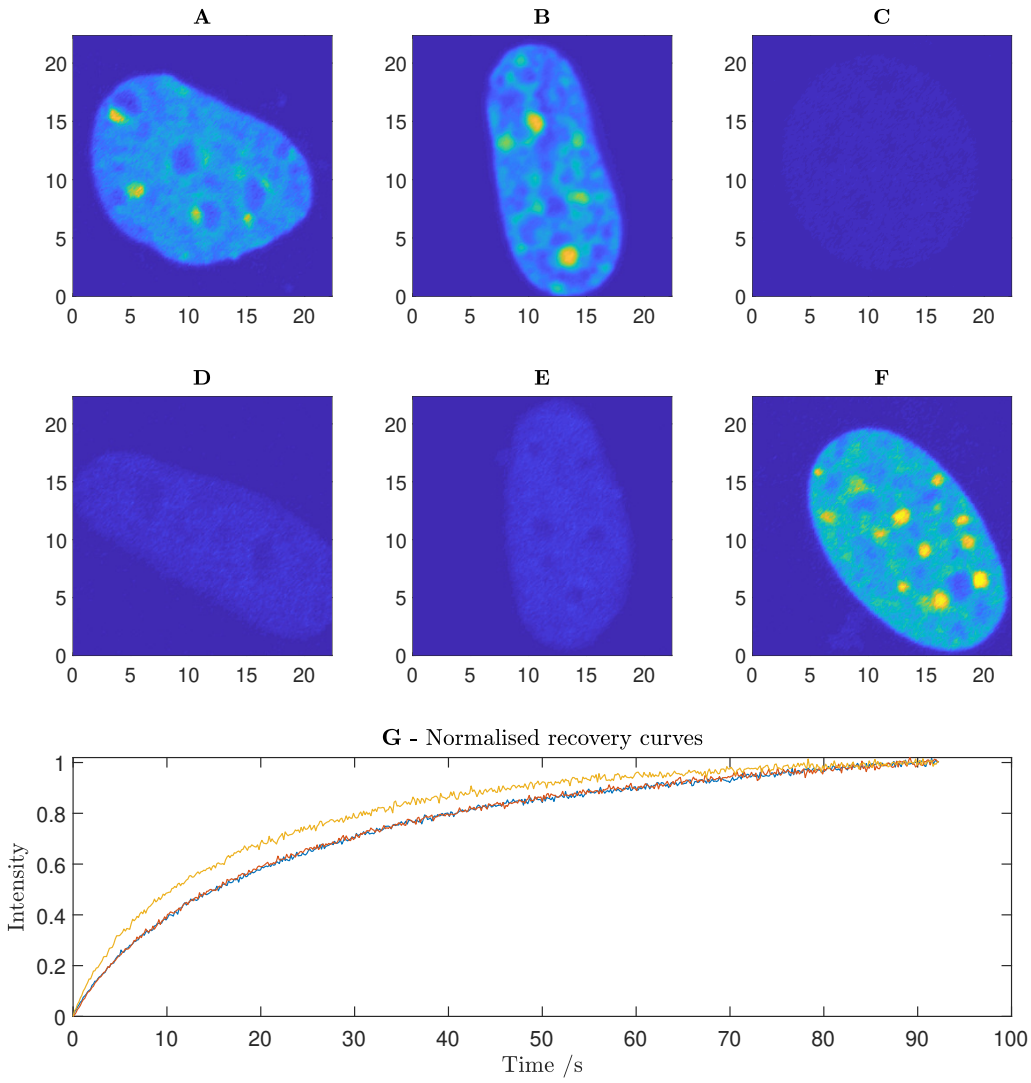


Figure 27: TEAD, cancer-associated fibroblasts. (A-F) Images of six randomly selected cells obtained by averaging three pre-bleach frames. (G) Averaged, normalised fluorescence recovery curves from three different sets of experiments. These different experiments used an identical bleach region radius (17×17). For this reason, the curves are unlabelled as the difference between the experiment sets is meaningless out of context. Note that, since the experiments used a single bleach region radius, the differences between the recovery curves are a product of variation between cells.

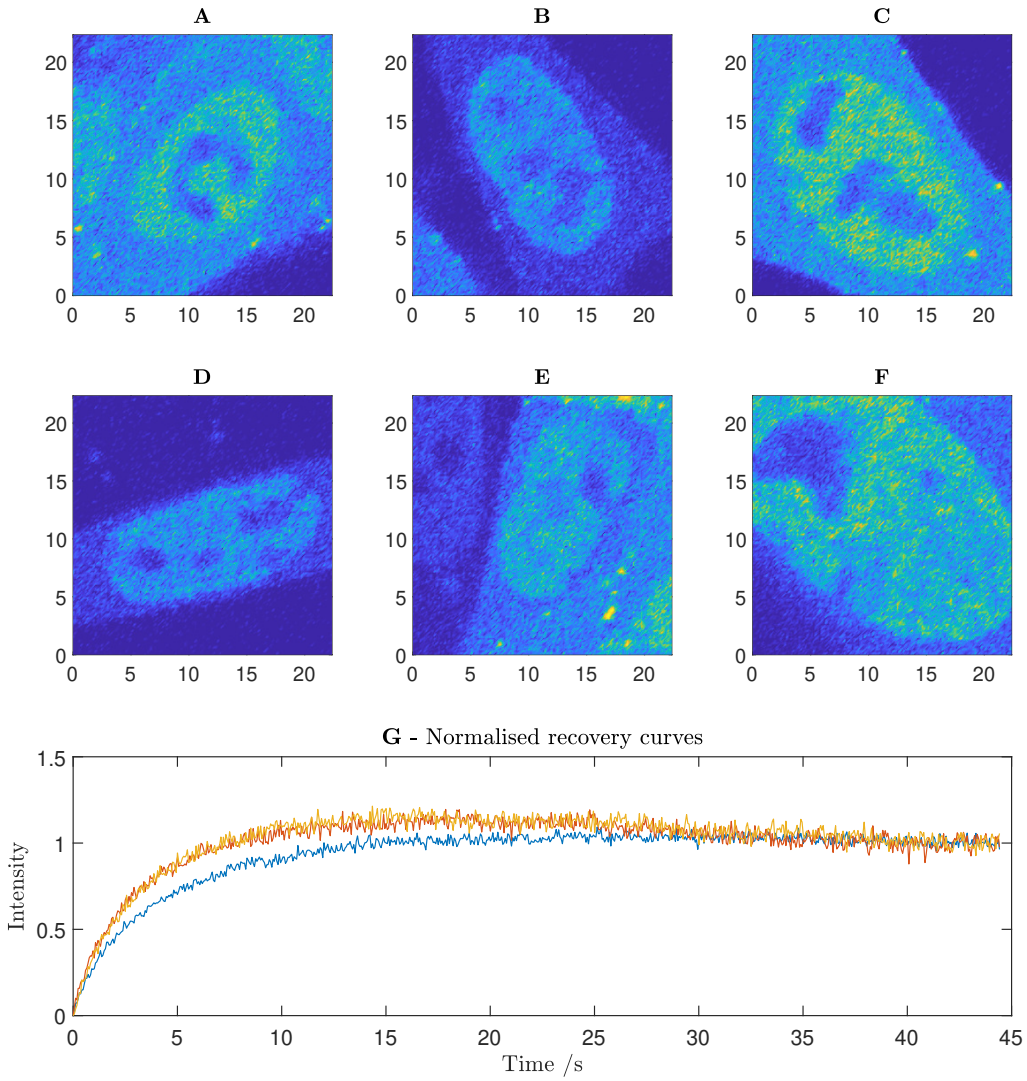


Figure 28: 5SA YAP, normal fibroblasts. (A-F) Images of six randomly selected cells obtained by averaging three pre-bleach frames. (G) Averaged, normalised fluorescence recovery curves from three different sets of experiments. These different experiments used an identical bleach region radius (17×17). For this reason, the curves are unlabelled as the difference between the experiment sets is meaningless out of context. Note that, since the experiments used a single bleach region radius, the differences between the recovery curves a product of variation between cells.

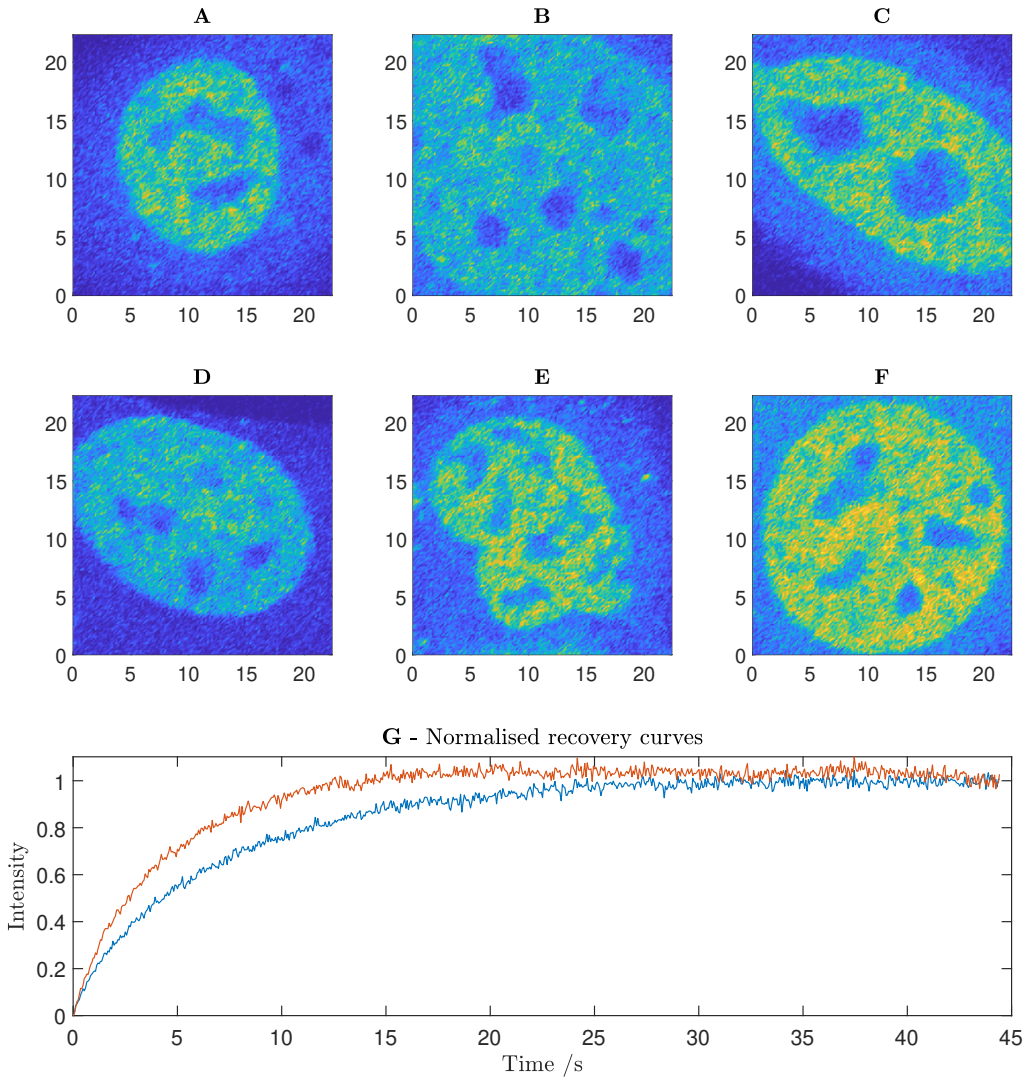


Figure 29: 5SA YAP, cancer-associated fibroblasts. (A-F) Images of six randomly selected cells obtained by averaging three pre-bleach frames. (G) Averaged, normalised fluorescence recovery curves from three different sets of experiments. These different experiments used an identical bleach region radius (17×17). For this reason, the curves are unlabelled as the difference between the experiment sets is meaningless out of context. Note that, since the experiments used a single bleach region radius, the differences between the recovery curves a product of variation between cells.

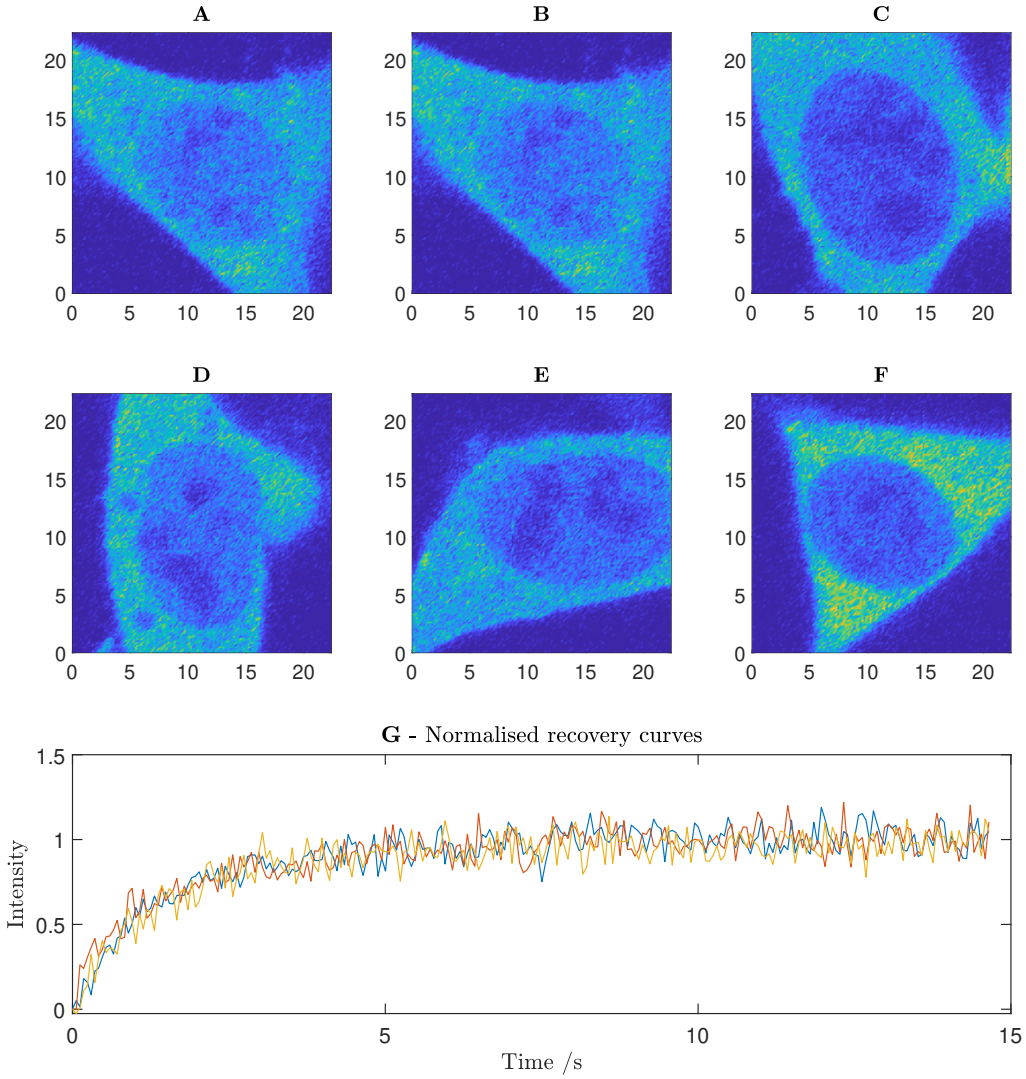


Figure 30: S94A YAP, normal fibroblasts. (A-F) Images of six randomly selected cells obtained by averaging three pre-bleach frames. (G) Averaged, normalised fluorescence recovery curves from three different sets of experiments. These different experiments used an identical bleach region radius (17×17). For this reason, the curves are unlabelled as the difference between the experiment sets is meaningless out of context. Note that, since the experiments used a single bleach region radius, the differences between the recovery curves a product of variation between cells.Also note that S94A has a lower signal-to-noise ratio than other proteins. This is simply because the concentration of S94A in the nucleus is lower than of other proteins.

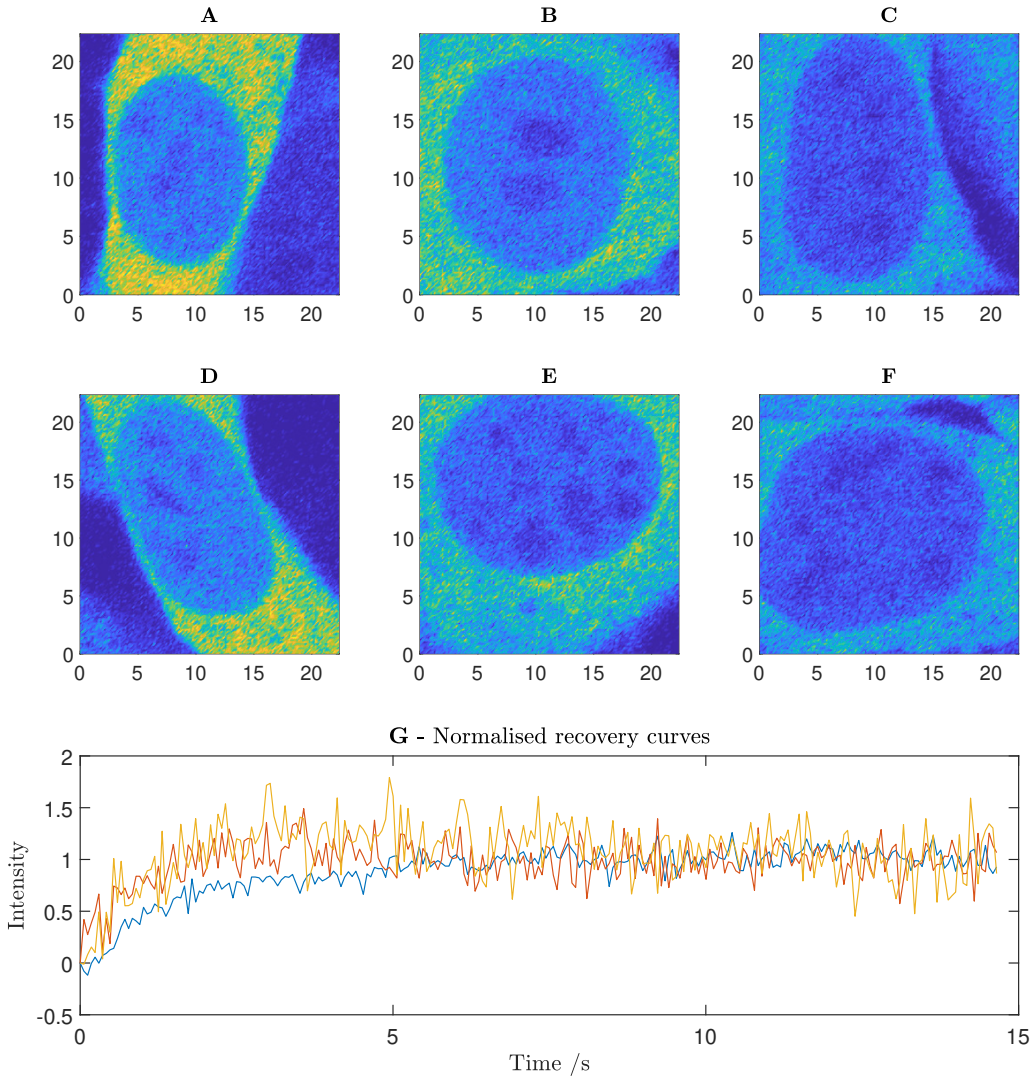


Figure 31: S94A, cancer-associated fibroblasts. (A-F) Images of six randomly selected cells obtained by averaging three pre-bleach frames. (G) Averaged, normalised fluorescence recovery curves from three different sets of experiments. These different experiments used an identical bleach region radius (17×17). For this reason, the curves are unlabelled as the difference between the experiment sets is meaningless out of context. Note that, since the experiments used a single bleach region radius, the differences between the recovery curves a product of variation between cells. Also note that S94A has a lower signal-to-noise ratio than other proteins. This is simply because the concentration of S94A in the nucleus is lower than of other proteins.

ingly, TEAD appears to be almost entirely absent from the cytoplasm. Sample size: 37 NFs and 36 CAFs.

- Mutant 5SA YAP (5SA YAP) - a mutant variant of YAP. The mutation substitutes serine amino acid for alanine in five sites preventing phosphorylation by the Hippo signalling pathway. 5SA YAP is highly tumorigenic [288, 294]. Some YAP 5SA data are presented in figure 28 (NFs) and 29 (CAFs). YAP concentration in the nucleus is visibly greater than in the cytoplasm (also contrast with figures 24 and 25) due to the absence of inhibition by the Hippo pathway. Sample size: 30 NFs and 26 CAFs.

- Mutant S94A (S94A YAP) - a mutant variant of YAP. The mutation substitutes a single serine for alanine. S94A YAP is physically incapable of interacting with TEAD [295, 296]. Some YAP S94A data are presented in figure 30 (NFs) and 31 (CAFs). Sample size: 30 NFs and 30 CAFs.

- Enhanced green fluorescent protein derived from the jellyfish *Aequorea victoria* [297]. In this context EGFP refers to the fluorescent protein itself, not a fusion with another protein of interest. Sample size: 15 cells.

All our results are from fibroblast nuclei; both normal (healthy) fibroblasts (NFs) and cancer-associated fibroblasts (CAFs).

4.6 MAIN RESULTS

In this section we present the results of the mathematical FRAP analysis, by which we obtained estimates of the following quantities:

- The aggregated pre-bleach concentration of protein inside the nucleus, $W_{\text{eq}} = \frac{\int_\Omega w_{\text{eq}} \mathrm{d}V}{\int_\Omega \mathrm{d}V}$.
- The rate of dissociation of protein from chromatin, k^-.

- The average dwell time of a protein molecule at a binding site, $\tau_{\text{dwell}} = 1/k^-$.
- The fraction of the total mass of protein inside the nucleus which is bound to chromatin at equilibrium, v_{eq}.
- The effective association rate, $k^+ = \frac{k^- v_{\text{eq}}}{1 - v_{\text{eq}}}$ (we use this measure since the true association rate is spatially inhomogeneous).
- The diffusivity of the protein, D_u.

Each cell was analysed individually and then mean parameter estimates were computed for each cell type. Estimates were excluded from the sample mean calculation if they were more than three median absolute deviations away from the median. If we revisit the results of table 2 in section 3.2, we find that, even for ideal data in the $\eta \gg 1$ regime, inaccurate parameter estimates were produced in about 6% of cases. We therefore believe it is sensible to remove outliers parameter estimates, as these outliers could be an artefact of the model fitting, rather than genuine results of biological relevance. Mean parameter estimates and 95% confidence intervals may be found in figure 32.

There is significant variation in estimates of W_{eq} and v_{eq} for different YAP variants, with 5SA being the greatest and S94A being the lowest (figure 32A, B). Dwell time (figure 32E) followed the same trend. This trend is strongly concordant with expectation based on the existing literature (explained in section 4.5). Of all the proteins, TEAD had the greatest fraction of molecules bound at equilibrium ($v_{\text{eq}} \approx 88\%$ for both CAFs and NFs), and was nearly entirely absent from the cytoplasm (figures 26 and 27). These results suggest that TEAD serves no important purposes in the cytoplasm in fibroblasts.

Diffusivity estimates for YAP and TEAD were between 20-40 $\mu m^2 s^{-1}$. The most mobile protein was EGFP with a diffusivity of approximately 56 $\mu m^2 s^{-1}$. These estimates were within the rage of free protein diffusivities reported in the existing literature [76]. The relatively high mobility of EGFP

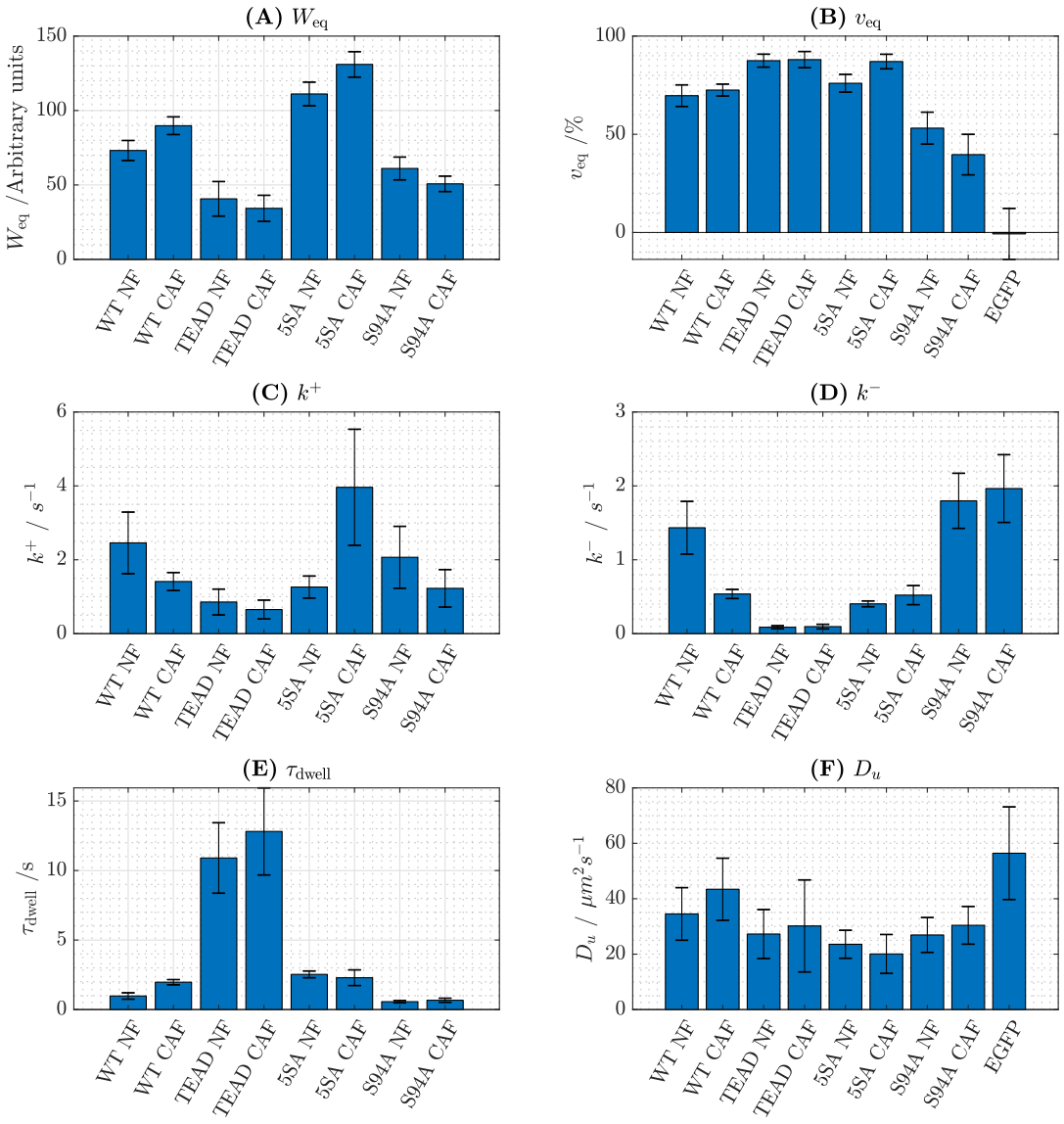


Figure 32: Mean parameter estimates for each of the six main model parameters and each of the eight cell types, as indicated. The error bars are the upper and lower bounds of the 95% confidence intervals.

is expected, as the proteins observed in FRAP are generally a fusion of a protein of interest (e.g. YAP or TEAD) with a fluorescent protein. Naturally, the fluorescent protein by itself, being a smaller molecule, can be expected to be more mobile.

We can compare different cell types with effect size calculations. The statistical size of the difference between two sets of data is measured by Cohen's d, defined as

$$d = \frac{\mu_1 - \mu_2}{\sqrt{\frac{(n_1-1)\sigma_1^2+(n_2-1)\sigma_2^2}{n_1+n_2-2}}}, \tag{286}$$

where μ_1 and μ_2 are the mean estimates of each parameter for the two cell types being compared, σ_1 and σ_2 are the standard deviations, and n_1 and n_2 are the sample sizes. Measures of effect size, such as the d index, give a clearer indication of biological importance than statistical significance alone [283, 284]. Results are illustrated in figures 33, 34 and 35.

The total average concentration, W_{eq}, of WT YAP is significantly greater in CAFs than in NFs, so that the quantity of YAP which is bound to chromatin at equilibrium (hence the biological effect) is much greater in CAFs, even though the bound fraction, v_{eq}, is only slightly greater in CAFs. The bonds between YAP and chromatin are much more stable in CAFs, evidenced by that fact that the dissociation rate k^- is significantly lower. Nonetheless, the association rate, k^+, is greater in NFs, which may seem counter-intuitive as it would be a waste of bioenergetic resources to transfer a greater mass of YAP into the nucleus only for it then to have a weaker affinity for chromatin. However, as we saw in section 2.1.1, chapter 2, all other things being equal, k^+ is a monotone decreasing function of the total protein concentration, W_{eq}. Since W_{eq} is greater in CAFs, it is natural that k^+ would be lower unless the affinity between YAP and chromatin were much stronger in CAFs. Equivalently, since there are fewer YAP molecules per unit of space in NF nuclei, there is less competition for binding sites and so association events

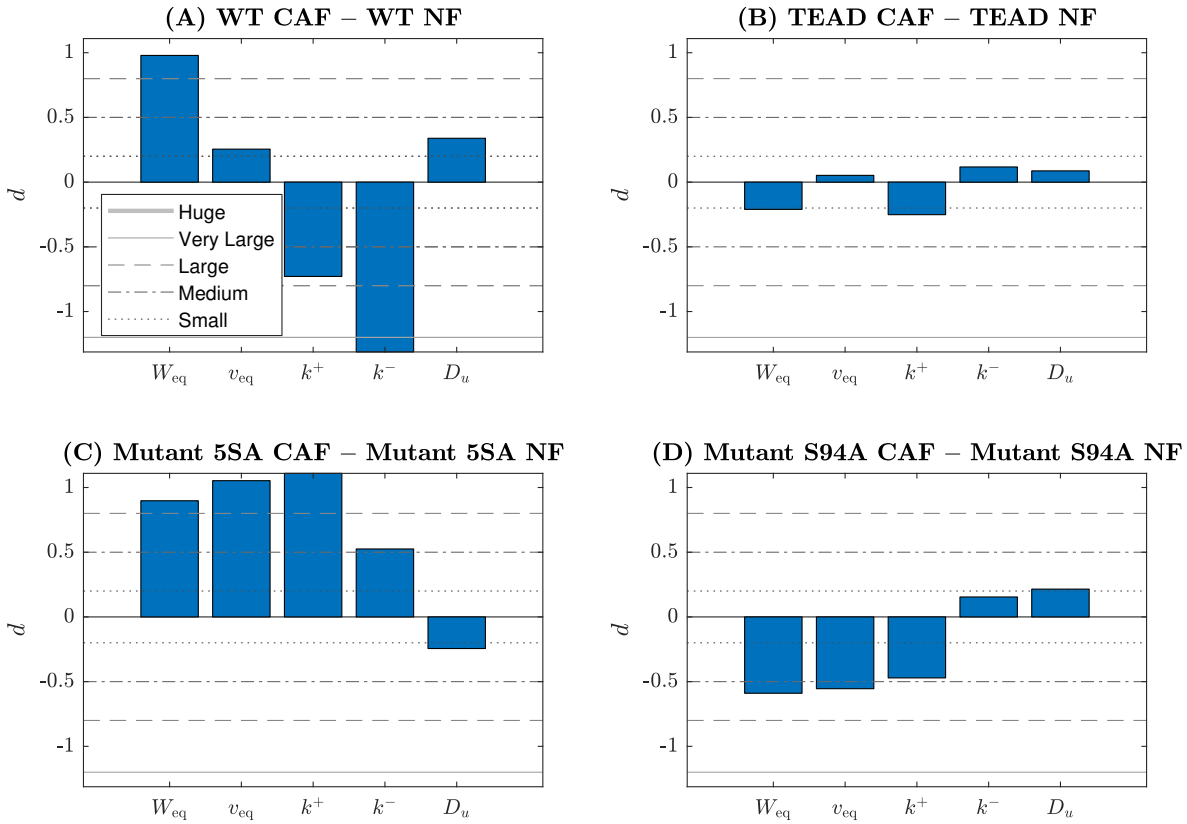


Figure 33: Comparison of parameter estimates between cancer-associated fibroblasts (CAFs) and normal fibroblasts (NFs) measured using Cohen's d (286). The canonical thresholds for small, medium, large and very large effect sizes are also plotted.

occur more frequently. It follows that there is a greater association rate in NFs.

The recorded differences between CAFs and NFs in terms of TEAD are so small that they are likely to be biologically insignificant (figure 33B). These results suggest that disregulation and overexpression of TEAD transcription factors do not contribute substantially to a fibroblast adopting the cancer-associated phenotype.

Mutant 5SA YAP, as with WT YAP, has a significantly greater equilibrium concentration in CAFs than in NFs (figure 33C). Unlike WT YAP, however, k^+ is greater which implies that YAP actually has greater avidity for chromatin in 5SA CAFs. Also unlike WT YAP, we found that the bonds between 5SA YAP and chromatin are less stable in CAFs, as the dissocation rate k^-

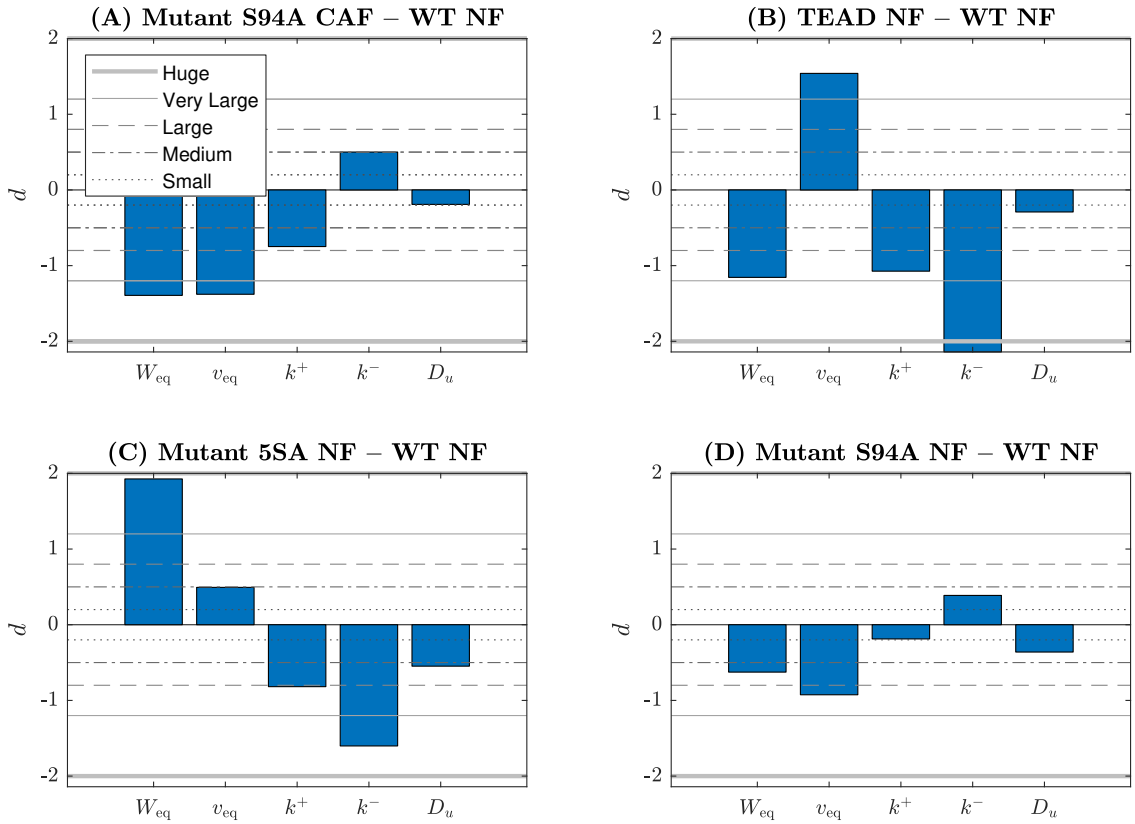


Figure 34: Comparison of parameter estimates between different variants of normal fibroblasts (NFs) measured using Cohen's d (286). The canonical thresholds for small, medium, large, very large and huge effect sizes are also plotted.

is greater, although this difference is moderate. In mutant S94A, the trend that CAFs have higher equilibrium YAP concentrations is actually reversed. Both the equilibrium concentration, W_{eq}, and the bound fraction, v_{eq}, are moderately lower in CAFs (figure 33D). We will return to the implications of this result presently.

The effect of the 5SA mutation in both CAFs and NFs is to increase the equilibrium concentration and the chromatin-bound fraction of YAP, although by different means. In NFs this increase in bound fraction is driven by stabilisation of YAP binding (figure 34C), while in CAFs it is driven by increasing the avidity of YAP (figure 35C). The equilibrium concentration is significantly greater in 5SA NFs than in WT CAFs, while the bound fraction is moderately greater. Again, this effect is driven by increased stabilisation of the reactions in the 5SA mutant cells (figure 35A). The fact that W_{eq}

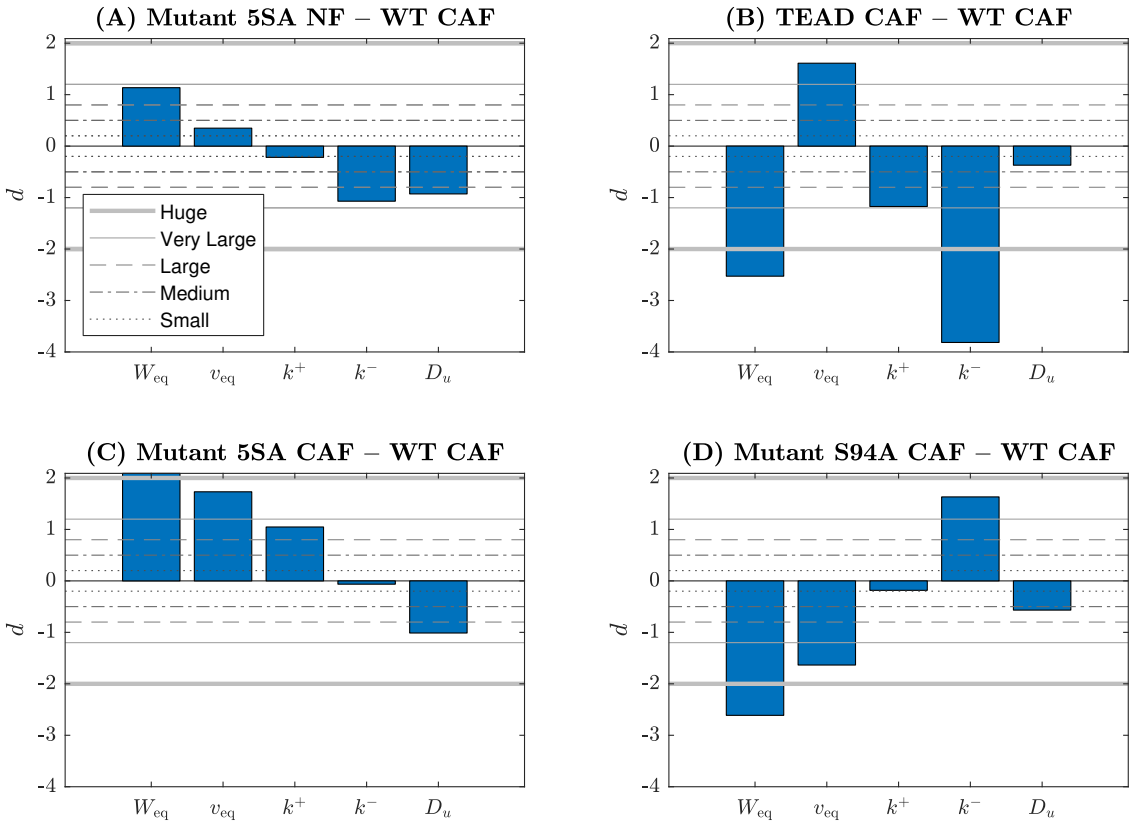


Figure 35: Comparison of parameter estimates between different variants of cancer-associated fibroblasts (CAFs) measured using Cohen's d (286). The canonical thresholds for small, medium, large, very large and huge effect sizes are also plotted.

and v_{eq} are both greater in 5SA mutants CAFs and NFs than in WT CAFs strongly suggests that the Hippo pathway must still, to some extent, remain active in CAFs, even if it is diminished, otherwise the 5SA mutation would have no effect in CAFs.

Inverse to the 5SA mutant, the S94A mutation decreases W_{eq} and v_{eq} in both CAFs and NFs. In CAFs, the reduction in W_{eq} is huge. There is also a very large reduction in v_{eq}, driven by a loss of bond stability, or equivalently an increase in k^- (figure 35D). In NFs there is an appreciable reduction in v_{eq} driven by a loss of binding stability, but this effect is far more moderate (figure 34D). The S94A mutation does not 'revert' the nuclear YAP concentration of a CAF to that of a NF; in S94A mutant CAFs W_{eq} and v_{eq} are even lower than in WT NFs (figure 34A). These facts, taken together, imply that

YAP undergoes some TEAD-mediated interactions with chromatin in NFs, otherwise the S94A mutation would have no effect in NFs.

Our results suggest that YAP undergoes some TEAD-independent interactions with chromatin, which are perhaps unrelated to its function as an oncogene, as approximately $40 - 50\%$ of S94A YAP is bound to chromatin at equilibrium. It is conceivable that the parameter fitting overestimates v_{eq}, but this is unlikely because it produced an estimate of $v_{\text{eq}} \approx 0$ for EGFP and there is no reason to believe that it would be incapable of doing so for YAP. The fact that the S94A causes a greater reduction of W_{eq} and v_{eq} in CAFs suggests that the TEAD-independent interactions between YAP and chromatin are favoured in NFs (figure 33D). If these TEAD-independent interactions do not lead to the activation of tumorigenic genes, that may explain part of the difference between the NF and CAF phenotypes.

4.7 EVALUATING MODEL LIMITATIONS

Naturally the FRAP model which we have used throughout this chapter has limitations. Most notably, we have simplified the complicated dynamics of a protein in the living cell to a set of simple reaction-diffusion equations. Of course, some degree of simplification is inevitable, as the greater the intricacy of the model, the higher its computational cost, and the greater the risk of over-fitting empirical data. Other limitations include our assumption of negligible protein transfer between the nucleus and the cytoplasm, and our assumption of negligible cell motion during the experiment. In this section, we show that both of these conditions approximately hold.

4.7.1 *Transfer of protein across the nuclear membrane.*

The FRAP model assumes that there is no transfer of protein between between the nucleus and the cytoplasm. This assumption is obviously unre-

alistic; however, given the data provided to us, including the cytoplasm in the model would have been difficult. The laser microscope was centred on the nucleus of each cell under investigation and was zoomed in so far that, for many cells, very little of the cytoplasm is visible in the recordings (this is particularly clear in figures 25, 29 and 31, for example). As a result, a FRAP model involving the cytoplasm would be largely unempirical, as the full geometry of the cytoplasm is unknown in most cases.

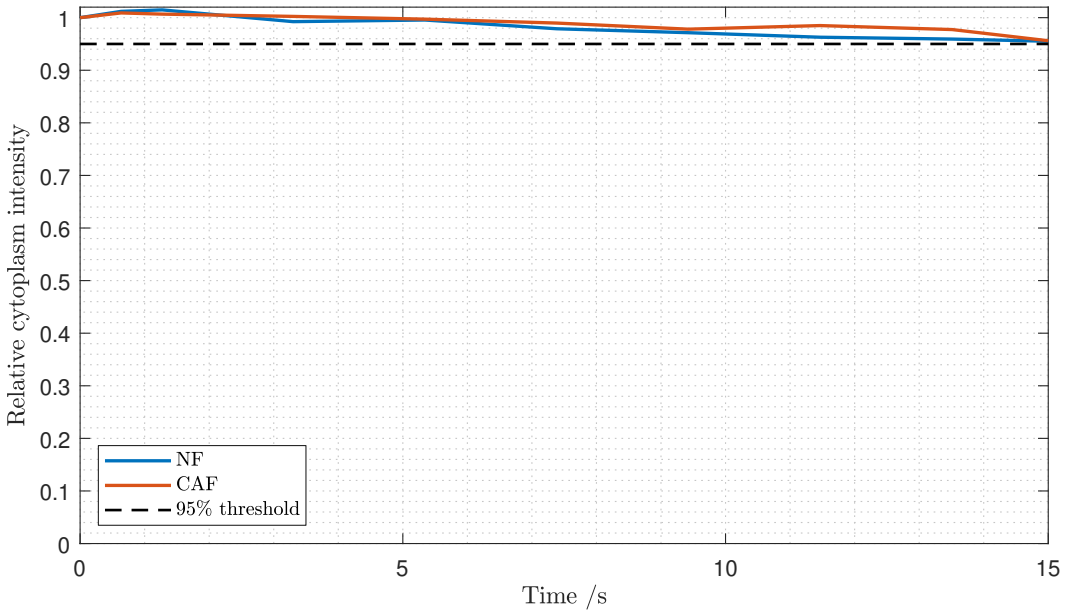


Figure 36: Average relative decline in intensity (due to the decline in the concentration of fluorescent YAP) in the cytoplasm of a sample of fibroblasts. Calculated using FLIP data from a sample of 24 NFs and 23 CAFs.

The model can nevertheless be considered reliable if the mass of protein exchanged between the nucleus and cytoplasm is relatively small on the time scale of the experiment. We can use fluorescence loss in photobleaching (FLIP) data to investigate whether this is the case. FLIP is a fluorescence microscopy technique which we will discuss in detail in chapter 5. For the purposes of this section, it is sufficient to note that FLIP experiments require the imaging of entire cells, and that FLIP data can therefore be used to investigate the transfer of protein across the nuclear membrane.

For our FRAP and FLIP data, bleaching takes place in the nucleus, creating a net transfer of fluorescent protein into the nucleus from the cytoplasm. The rate of decline of fluorescent protein concentration in the cytoplasm is therefore a measure of the degree of continuity between the two compartments. In figure 36 we plot the normalised concentration of YAP in the cytoplasm averaged across 24 NFs and 23 CAFs. For both cell phenotypes, the cytoplasmic YAP concentration remains above 95% of its initial value on the time scale of a FRAP experiment (approximately 15 s for YAP). This justifies our assumption that protein transfer between the nucleus and cytoplasm is negligible in FRAP.

4.7.2 *Cell motion*

The cells under investigation are not fixed and static, yet we have assumed that they experience negligible motion in the course of the FRAP experiments. We investigated the extent of cell motion in FRAP using the methodology described in section 5.3.1, chapter 5. For each FRAP experiment, we

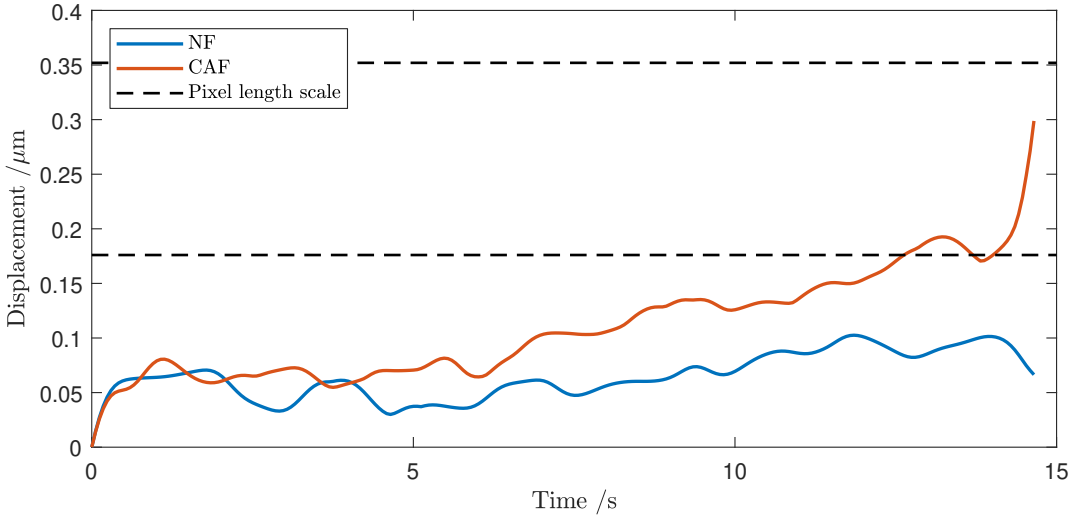


Figure 37: Average straight line distance (norm of the displacement) of cell nuclei from their positions at the beginning of the FRAP bleach phase. For reference, horizontal dashed lines represent integer multiples of the length scale of a single pixel (0.176 μm).

tracked the motion of the nucleus relative to its position at the start of the bleach phase, measured the straight line distance (*i.e.* the Euclidean norm of the displacement) of the nucleus from its original position, and then calculated the population average.

The average displacement of NFs and CAFs is plotted against time in figure 37. Results show that, while there was some degree of motion, it was generally small; equivalent to less than one pixel for NFs and less than two pixels for CAFs. We conclude that cell motion can be safely ignored in FRAP for our purposes.

4.8 CHAPTER SUMMARY

In this chapter we implemented a numerical FRAP model. We used a standard two-species mathematical FRAP model which incorporates diffusion and binding kinetics. Our method utilised an empirically derived model of the laser profile required to simulate the bleaching phase of the FRAP experiment, and also incorporated unintentional passive bleaching caused by the imaging laser during the recovery phase. Our method can be readily applied to almost any two-dimensional cellular geometry.

We applied the fitting method to empirical data obtained from two different fibroblast phenotypes: normal and cancer-associated. Two proteins were studied, YAP and TEAD. In addition to wild type YAP, two mutant variants, 5SA YAP and S94A YAP, were also studied. We found that there is greater localisation of YAP to the nuclei of cancer-associated fibroblasts than normal fibroblasts, although the proportion of YAP molecules bound to chromatin are similar in both phenotypes. Additionally, the 5SA mutation strongly increases YAP localisation to the nucleus and the affinity between YAP and chromatin. Inversely, the S94A mutation strongly decreases YAP localisation to the nucleus and the affinity of YAP and chromatin, especially in cancer-associated fibroblasts.

Recall that 5SA YAP is resistant to phosphorylation by the Hippo signalling pathway and is highly tumorigenic, and that S94A YAP is incapable of interacting with TEAD. Given that relevant background, knowing little else about YAP, our results adequately demonstrate that:

- YAP localisation to the nucleus and the total concentration of YAP bound to chromatin are much greater in CAFs, suggesting that YAP has a role in creating the CAF phenotype.
- The Hippo signalling pathway reduces YAP localisation to the nucleus (hence, activation of YAP target genes).
- Some of the interactions between YAP and chromatin are mediated by TEAD.

Of course, YAP is a thoroughly studied protein and these results are well-established. This being this case, the fact that our results agree strongly with the existing literature is an encouraging validation of our method of analysis.

We also found (non-dispositive) evidence that the Hippo pathway remains active in cancer-associated fibroblasts and that YAP has some TEAD-mediated interactions with chromatin even normal fibroblasts. We proposed that YAP undergoes multiple different kinds of interactions with chromatin which are independent of TEAD and that these reactions are prioritised in normal fibroblasts. We found that almost all available TEAD in a cell will be bound to chromatin at any given time and that TEAD molecules has a long dwell time on chromatin. Furthermore, we found no evidence of significant differences between TEAD in normal fibroblasts and cancer-associated fibroblasts, suggesting that disregulation of TEAD is not a significant factor in the formation of CAFs.

5

FLUORESCENCE LOSS IN PHOTOBLEACHING

The focus of this thesis so far has been fluorescence recovery after photobleaching (FRAP). In this chapter, we turn our attention to a different fluorescence microscopy technique: fluorescence loss in photobleaching (FLIP), which is often used in conjunction with FRAP [141–143]. In FRAP, a target region of interest within a cell is photobleached once by exposure to high intensity laser light, then the return to equilibrium is observed. In FLIP, by contrast, a target region is photobleached repeatedly, and the loss of fluorescence in a separate reporting region located elsewhere in the cell is monitored [141, 144, 145]. In this way, FLIP can be used to determine the continuity between organelles or cellular compartments [21, 144, 146].

Figure 38 displays an example of raw FLIP data which has been provided to us by the tumour cell biology laboratory at the Crick Institute. The bleaching laser is focused on a point within the nucleus of a chosen cell (indicated by the red x). Repeated photobleaching causes a loss of fluorescence intensity within the nucleus. Shuttling between the nucleus and cytoplasm creates a net transport of unbleached fluorescent molecules into the nucleus, reducing the intensity in the cytoplasm. The shorter the delay between the loss of fluorescence in the two compartments, the greater the rate of exchange of protein between them.

We begin this chapter in section 5.1 by posing a FLIP model. This model is an extension of the system of partial differential equations (PDEs) used to model FRAP in previous chapters to include two cellular compartments

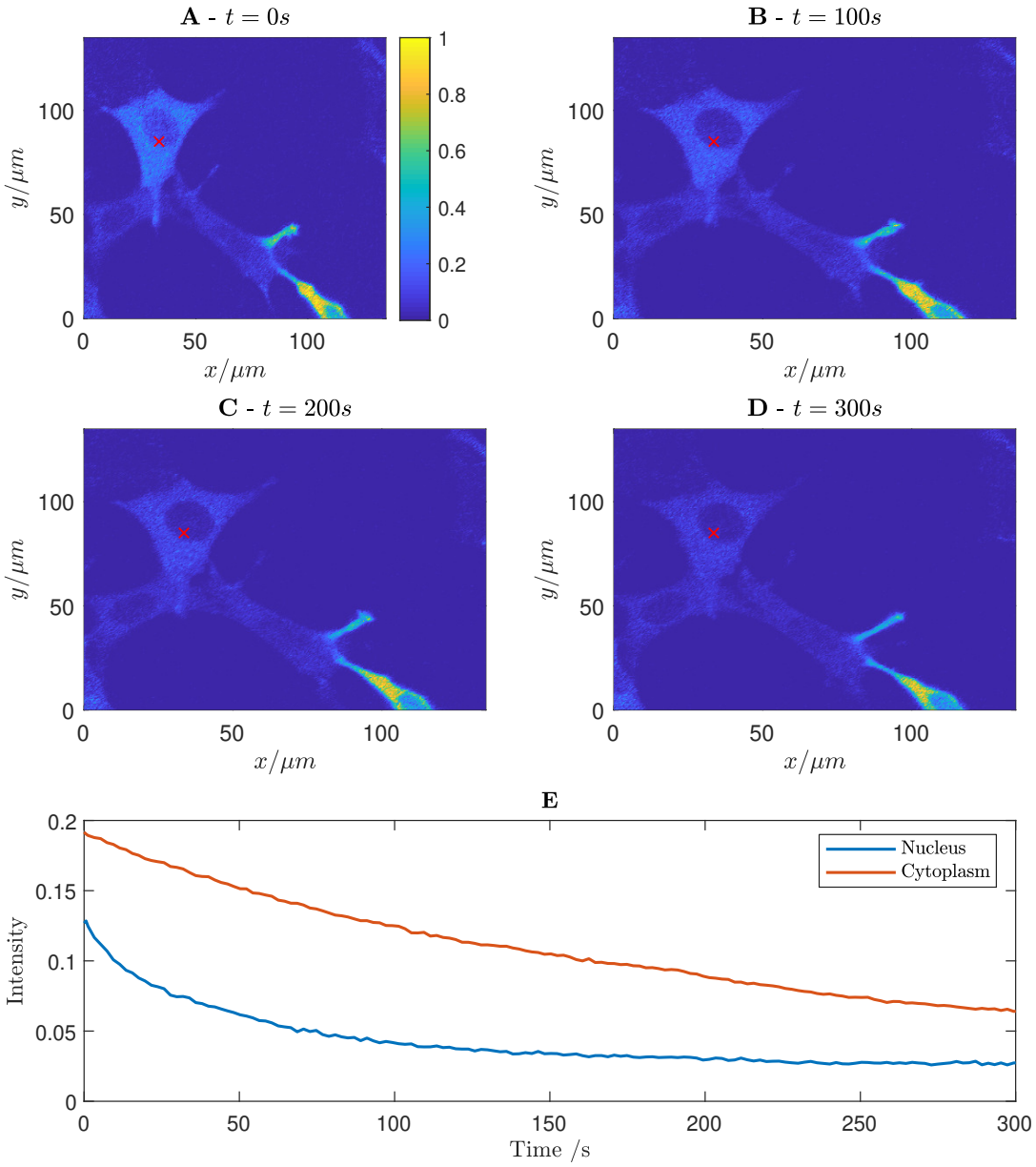


Figure 38: Raw FLIP data. (A-D) Frames from a recording taken with a scanning confocal laser microscope during a FLIP experiment. The bottom left corner of the square bleach region is marked with a red x. (E) average fluorescence intensity across the nucleus and cytoplasm of the cell under investigation over time.

and coupling between them. In section 5.2 we will carry out an asymptotic analysis of the FLIP model in the limiting case where transfer of protein between compartments is much slower than the redistribution of protein within compartments. We will rigorously demonstrate that the model reduces to a system of ordinary differential equations (ODEs) in this scenario.

We have also developed a finite element simulation of the full FLIP model which we will explain in section 5.3. We have been provided with FLIP data on yes-associated protein (YAP), for cancer-associated and normal fibroblasts. In section 5.4 we will fit both the ODE and the PDE models to empirical data to obtain information about YAP regulation in fibroblasts.

5.1 FLIP MODEL

To begin, it is necessary to formulate a model which is appropriate for yes-associated protein (YAP) data with which we have been supplied. First, suppose the cell is divided into two compartments; the nucleus and the cytoplasm. Let the set $\Omega_n \subset \mathbb{R}^d$ denote the nucleus and $\Omega_c \subset \mathbb{R}^d$ the cytoplasm ($d = 2, 3$), with $\partial\Omega_n$ and $\partial\Omega_c$ being their respective boundaries. We model the nuclear membrane, which separates the two compartments, as a curve (in two dimensions) or a surface (in three dimensions), denoted by Γ. Note that $\partial\Omega_n \cap \partial\Omega_c = \Gamma$. We also allow for internal impenetrable regions within the compartments (for example, nucleoli inside the nucleus). See figure 39 for a schematic representation of this breakdown of the cell. A suspected nucleolus is represented by a hole in the nucleus.

YAP interacts with chromatin in the nucleus to form a complex, just as in chapter 4. In the cytoplasm, YAP interacts with regulatory proteins which may anchor YAP molecules in the cytoplasm [300, 301]. We model YAP transport within each compartment with a pair of reaction-diffusion equations. Naturally, the flux of YAP into and out of impenetrable cellular structures is 0, as is the flux of YAP across the cell membrane. Some recent quantitative FLIP studies (for example [152]) have modelled the boundary between cellular compartments as a partially-permeable membrane. However, the nuclear membrane is impassable large molecules, which must be translocated across nuclear pores via active transport [298]. This transport is bi-directional, so proteins can be selectively added to or removed from the nucleus [299]. It is known that YAP nucleocytoplasmic shuttling is an

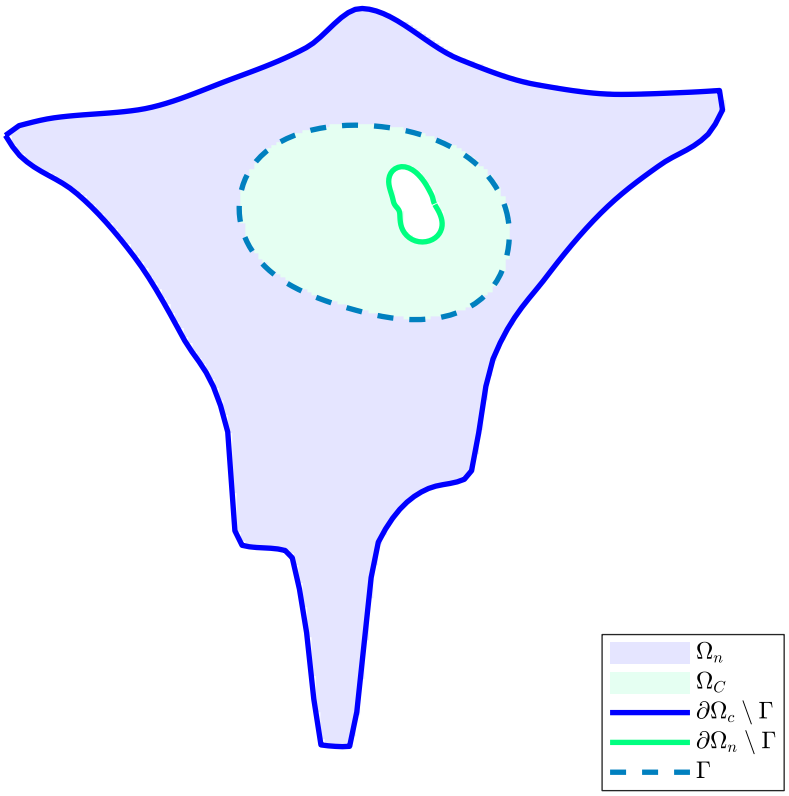


Figure 39: A sketch of a cell broken into two regions; the nucleus ,Ω_n, and the cytoplasm, Ω_c. Solid lines denote impermeable boundaries, while the dashed line, Γ, denotes the permeable membrane separating the nucleus and cytoplasm.

active transport process [302]. Because shuttling is an active, rather than a passive process, it is possible for there to exist a concentration gradient of unbound protein across the nuclear membrane at equilibrium.

We assume that protein transport in the nucleus is governed by the following system of equations,

$$\begin{cases} \frac{\partial u_n}{\partial t} = -k_n^+ u_n + k_n^- v_n + D_{u_n} \nabla^2 u_n - \alpha I(\mathbf{x}, t) u_n, \\ \frac{\partial v_n}{\partial t} = k_n^+ u_n - k_n^- v_n + D_{v_n} \nabla^2 v_n - \alpha I(\mathbf{x}, t) v_n, \end{cases} \tag{287}$$

where u_n is the concentration of unbound protein and v_n is the concentration of bound protein in the nucleus, and u_c and v_c are respectively the

concentrations of unbound and bound protein in the cytoplasm. Likewise, the cytoplasm equations are

$$\begin{cases} \frac{\partial u_c}{\partial t} = -k_c^+ u_c + k_c^- v_c + D_{u_c} \nabla^2 u_c, \\ \frac{\partial v_c}{\partial t} = k_c^+ u_c - k_c^- v_c + D_{v_c} \nabla^2 v_c. \end{cases} \tag{288}$$

The two systems of equations, (287) and (288), are coupled at the nuclear membrane, Γ, by the Robin boundary conditions

$$D_{u_c} \nabla^2 u_c \cdot \hat{\mathbf{n}} \mid_\Gamma = k_{\text{out}} u_n - k_{\text{in}} u_c, \tag{289}$$

and

$$D_{u_n} \nabla^2 u_n \cdot \hat{\mathbf{n}} \mid_\Gamma = k_{\text{in}} u_c - k_{\text{out}} u_n. \tag{290}$$

The boundary conditions, (289) and (290), are intended to model the asymmetric shuttling of protein between the nucleus and cytoplasm by active transport. These boundary conditions may be contrasted with the homogeneous Neumann boundary conditions assumed for the FRAP model in chapter 4. As we saw in section 4.7.1, the duration of the FRAP experiment is so short that protein transport across the nuclear membrane is effectively negligible, but this is not the case for FLIP. In the special case $k_{\text{in}} = k_{\text{out}}$ the boundary conditions coincide with a passive transport model. Finally, the homogeneous Neumann conditions imposed on the rest of the compartment boundaries,

$$\nabla u_n \cdot \hat{\mathbf{n}} \mid_{\partial\Omega_n \setminus \Gamma} = 0, \quad \nabla v_n \cdot \hat{\mathbf{n}} \mid_{\partial\Omega_n} = 0, \tag{291}$$

and

$$\nabla u_c \cdot \hat{\mathbf{n}} \mid_{\partial\Omega_c \setminus \Gamma} = 0, \quad \nabla v_c \cdot \hat{\mathbf{n}} \mid_{\partial\Omega_c} = 0, \tag{292}$$

close the model for given initial conditions. It is also helpful to define the total fluorescent protein concentration in each compartment,

$$w_n(\mathbf{x}, t) = u_n(\mathbf{x}, t) + v_n(\mathbf{x}, t), \quad w_c(\mathbf{x}, t) = u_c(\mathbf{x}, t) + v_c(\mathbf{x}, t). \tag{293}$$

The quantity f_n is the fraction of protein which is freely diffusing, or unbound, inside the nucleus at equilibrium. It is given by

$$f_n = \frac{k_n^-}{k_n^+ + k_n^-}, \tag{294}$$

and likewise for the cytoplasm,

$$f_c = \frac{k_c^-}{k_c^+ + k_c^-}. \tag{295}$$

5.2 ASYMPTOTIC ANALYSIS OF THE FLIP MODEL

Having posed the FLIP model, we will now consider an asymptotic limit in which the model reduces to a system of ordinary differential equations. Let $[x]$ denote units of length, $[t]$ denote units of time. Given that

$$[D_{u_n}] = \frac{[x]^2}{[t]}, \quad [\nabla u_n \cdot \hat{\mathbf{n}}] = \frac{[u_n]}{[x]},$$

from the boundary condition (297), we can infer that

$$[k_{\text{in}}] = [k_{\text{out}}] = \frac{[x]}{[t]}.$$

Hence we can make the substitution,

$$\mathbf{x} = L_n \mathbf{x}', \quad t = L_n t' / k_{\text{in}},$$

where $\mathbf{x}'$ and t' are dimensionless variables. The length scale, L_n, is the diameter of the nucleus

$$L_n = \sup\{\|\mathbf{x} - \mathbf{y}\| | \mathbf{x}, \mathbf{y} \in \Omega_n\}.$$

Under this substitution, (287) becomes

$$\begin{cases} \frac{k_{\text{in}}}{L_n} \frac{\partial u_n}{\partial t} = -k_n^+ u_n + k_n^- v_n + \frac{D_{u_n}}{L_n^2} \nabla'^2 u_n - \alpha I u_n, \\ \frac{k_{\text{in}}}{L_n} \frac{\partial v_n}{\partial t} = k_n^+ u_n - k_n^- v_n + \frac{D_{v_n}}{L_n^2} \nabla'^2 v_n - \alpha I v_n. \end{cases} \tag{296}$$

Likewise, the Robin boundary condition (297) becomes

$$\frac{D_{u_n}}{L_n} \nabla' u_n \cdot \hat{\mathbf{n}} \mid_\Gamma = k_{\text{in}} u_c - k_{\text{out}} u_n. \tag{297}$$

Rearranging gives

$$\begin{cases} \frac{\partial u_n}{\partial t} = \frac{k_n^+ L_n}{k_{\text{in}}}(-u_n + \kappa_n v_n) + \frac{D_{u_n}}{k_{\text{in}} L_n} \nabla'^2 u_n - \frac{\alpha I L_n}{k_{\text{in}}} u_n, \\ \frac{\partial v_n}{\partial t} = \frac{k_n^+ L_n}{k_{\text{in}}}(u_n - \kappa_n v_n) + \frac{D_{u_n}}{k_{\text{in}} L_n} \delta_n \nabla'^2 v_n - \frac{\alpha I L_n}{k_{\text{in}}} v_n, \end{cases} \tag{298}$$

with the boundary condition

$$\nabla' u_n \cdot \hat{\mathbf{n}} \mid_\Gamma = \frac{k_{\text{in}} L_n}{D_{u_n}} (u_c - \rho u_n), \tag{299}$$

where

$$\delta_n = \frac{D_{v_n}}{D_{u_n}}, \quad \kappa_n = \frac{k_n^-}{k_n^+}, \quad \rho = \frac{k_{\text{out}}}{k_{\text{in}}},$$

are all dimensionless parameters. Now, set

$$\epsilon = \frac{k_{\text{in}} L_n}{D_{u_n}},$$

and multiply (298) by ϵ to get

$$\begin{cases} \epsilon \frac{\partial u_n}{\partial t} = \frac{k_n^+ L_n^2}{D_{u_n}} (-u_n + \kappa_n v_n) + \nabla'^2 u_n - \lambda u_n, \\ \epsilon \frac{\partial v_n}{\partial t} = \frac{k_n^+ L_n^2}{D_{u_n}} (u_n - \kappa_n v_n) + \delta_n \nabla'^2 v_n - \lambda v_n. \end{cases} \tag{300}$$

Boundary condition (299) becomes

$$\nabla' u_n \cdot \hat{\mathbf{n}} \mid_\Gamma = \epsilon (u_c - \rho u_n). \tag{301}$$

Note that the dimensionless parameter λ is given by

$$\lambda = \frac{\alpha I L_n^2}{D_{u_n}} = \frac{L_n^2}{D_{u_n}} \div \frac{1}{\alpha I} = \frac{\tau_D}{\tau_\alpha},$$

which is the ratio of the timescale of diffusion across the compartment $\tau_D = L_n^2 / D_{u_n}$ to the time scale of bleaching $\tau_\alpha = 1/(\alpha I)$. Now, take $\epsilon \to 0$, $\delta_n \to 0$ and $\lambda \to 0$, giving

$$\begin{cases} 0 = \frac{k_c^+ L_n^2}{D_{u_n}} (-u_n + \kappa_n v_n) + \nabla'^2 u_n, \\ 0 = \frac{k_c^+ L_n^2}{D_{u_n}} (u_n - \kappa_n v_n), \end{cases} \tag{302}$$

and

$$\nabla' u_n \cdot \hat{\mathbf{n}} \mid_\Gamma = 0. \tag{303}$$

Adding the two equations in (302) yields

$$\nabla'^2 u_n = 0. \tag{304}$$

Equations (303) and (304) together imply that u_n is spatially uniform, such that $u_n = u_n(t)$. By equation (302), $u_n = \kappa_n v_n$, hence

$$v_n(t) = \frac{u_n(t)}{\kappa_n} = \frac{k_n^+}{k_n^-} u_n(t). \tag{305}$$

Recalling that $w_n = u_n + v_n$, $f_n = k_n^- / (k_n^- + k_n^+)$ and $b_n = 1 - f_n$, it follows that

$$u_n = f_n w_n, \quad v_n = b_n w_n.$$

By adding the pair of equations in system (287), we get

$$\frac{\partial}{\partial t}(u_n + v_n) = D_{u_n} \nabla^2 u_n + D_{v_n} \nabla^2 v_n - \alpha I (u_n + v_n), \tag{306}$$

which can be integrated to give,

$$\int_{\Omega_c} \frac{\partial}{\partial t}(w_c) \mathrm{d}V = \int_{\Omega_c} D_{u_c} \nabla^2 u_c \mathrm{d}V + \int_{\Omega_c} D_{v_c} \nabla^2 v_c \mathrm{d}V - \int_{\Omega_c} \alpha I w_c \mathrm{d}V. \tag{307}$$

By the divergence theorem,

$$\frac{\mathrm{d}}{\mathrm{d}t} \int_{\Omega_n} (w_n) \mathrm{d}V = \oint_{\Omega_n} D_{u_n} \nabla u_n \cdot \hat{\mathbf{n}} \mathrm{d}S + \oint_{\Omega_n} D_{v_n} \nabla v_n \cdot \hat{\mathbf{n}} \mathrm{d}S - \int_{\Omega_n} \alpha I w_n \mathrm{d}V. \tag{308}$$

The surface integrals in (308) can be replaced using the boundary conditions (297),

$$\frac{\mathrm{d}}{\mathrm{d}t} \int_{\Omega_n} (w_n) \mathrm{d}V = \oint_{\Gamma} (k_{\text{out}} u_n - k_{\text{in}} u_n) \mathrm{d}S - \int_{\Omega_n} \alpha I w_n \mathrm{d}V. \tag{309}$$

If we were to take the limit $k_{\text{in}} L_c / D_{u_c} \to 0$, we would find, through a derivation which is essentially identical to the one we have just seen, that $u_c = f_c w_c(t)$. In this case, (309) would yield,

$$\frac{\mathrm{d}w_c}{\mathrm{d}t} |\Omega_c| = |\Gamma| (k_{\text{out}} u_n - k_{\text{in}} u_c) - \beta w_c, \tag{310}$$

where

$$|\Omega_c| = \int_{\Omega_c} \mathrm{d}V, \quad |\Gamma| = \oint_{\Gamma} \mathrm{d}S, \quad \beta(t) = \int_{\Omega_c} \alpha I(\mathbf{x}, t) \mathrm{d}V.$$

Equivalently,

$$|\Omega_n| \frac{\mathrm{d}w_n}{\mathrm{d}t} = |\Gamma| \left(k_{\text{in}} f_c w_c - k_{\text{out}} f_n w_n \right) - \beta w_n, \tag{311}$$

and

$$|\Omega_c| \frac{\mathrm{d}w_c}{\mathrm{d}t} = |\Gamma| \left(k_{\text{out}} f_n w_n - k_{\text{in}} f_c w_c \right), \tag{312}$$

which can be rewritten as

$$\frac{\mathrm{d}w_c}{\mathrm{d}t} = \frac{|\Omega_n|}{|\Omega_c|} \left(\frac{|\Gamma|}{|\Omega_n|} k_{\text{out}} f_n w_n - \frac{|\Gamma|}{|\Omega_n|} k_{\text{in}} f_c w_c \right), \tag{313}$$

and

$$\frac{\mathrm{d}w_n}{\mathrm{d}t} = \frac{|\Gamma|}{|\Omega_n|}k_{\text{in}}f_c w_c - \frac{|\Gamma|}{|\Omega_n|}k_{\text{out}}f_n w_n - \frac{\beta}{|\Omega_n|}w_n. \tag{314}$$

In summary, we are left with the system of linear ODEs

$$\begin{cases} \frac{\mathrm{d}w_c}{\mathrm{d}t} = r_V(r_{\text{out}}w_n - r_{\text{in}}w_c), \\ \frac{\mathrm{d}w_n}{\mathrm{d}t} = (r_{\text{in}}w_c - r_{\text{out}}w_n) - \beta w_n, \end{cases} \tag{315}$$

where

$$r_S = \frac{|\Gamma|}{|\Omega_n|}, \quad r_{\text{out}} = r_S k_{\text{out}} f_n, \quad r_{\text{in}} = r_S k_{\text{in}} f_c, \quad r_V = \frac{|\Omega_n|}{|\Omega_c|}.$$

Note that the pre-experiment steady state gives a constraint on r_{out} and r_{in},

$$r_{\text{out}}w_n(0) = r_{\text{in}}w_c(0), r_{\text{out}} = r_{\text{in}}\frac{w_c(0)}{w_n(0)}.$$

By setting

$$r'_{\text{in}} = \frac{|\Gamma|k_{\text{in}}f_c}{|\Omega_c|}, \quad r'_{\text{out}} = \frac{|\Gamma|k_{\text{out}}f_n}{|\Omega_n|},$$

we can rewrite (315), to get

$$\begin{cases} \frac{\mathrm{d}W_n}{\mathrm{d}t} = r'_{\text{in}}W_c - r'_{\text{out}}W_n - \beta' w_n, \\ \frac{\mathrm{d}W_c}{\mathrm{d}t} = r'_{\text{out}}W_n - r'_{\text{in}}W_c, \end{cases} \tag{316}$$

where W_n=$|\Omega_n|w_n$ and $W_c = |\Omega_c|w_c$. The ODE model (316) has appeared in previous quantitative FRAP studies [148, 149]. Fitting (316) to data certainly reveals information about the aggregate rate of transport between compartments, but not about the individual factors which affect protein transport; binding (f_n,f_c), cross-membrane flux (k_{in}, k_{out}) and cell geometry ($|\Gamma|$, $|\Omega_n|$, $|\Omega_c|$). Given complete information about a cell, $|\Omega_n|$, $|\Omega_n|$ and $|\Gamma|$ may be known. However, in practice we are often only supplied with a two dimensional image of a cell when we technically require information about its three dimensional structure. Given the form of equation (315), the volume ratio of cellular compartments, r_V is a parameter which can be inferred by model fitting, yet it remains to estimate the surface area to volume ratio of the nucleus, r_S. Once this is done, we can estimate the flux parameters, k_{in} and k_{out}, as long as we have estimates of f_n and f_c, which can either be obtained by FRAP experiments or by simulating the PDE model numerically (see section 5.3).

5.2.1 *Nucleus shape and the surface area to volume ratio*

Even if we cannot observe the three dimensional structure of the nucleus, we can estimate its surface-area-to-volume ratio, r_S, under certain assumptions about its shape. Most cell nuclei are approximately spherical or ellipsoidal [303]. If we assume that the nucleus is spherical, we can fit a circle to the nuclear boundary as it appears in the raw data. Then, assuming that the best-fit radius, R, is the radius of the nucleus, we have

$$r_S \text{ (sphere)} = \frac{3}{R}. \tag{317}$$

Alternatively, we can suppose the nucleus is an ellipsoid with principal semi-axes of length a, b and c, and fit an ellipse to the image of nuclear boundary. Let a and b be the lengths of the semi-major and semi-minor axes of the best-fit ellipse respectively (hence $a \geq b$ necessarily). This leaves c as an unknown. However, we might assume that c would be of similar scale to a and b. We therefore split the elliptical model into two limiting sub-cases: $c = a$ and $c = b$. In either case, the surface-area-to-volume ratio can be approximated by

$$r_S \text{ (ellipsoid)} \approx \frac{3}{abc}\left(\frac{(ab)^p + (ac)^p + (bc)^p}{3}\right)^{\frac{1}{p}}, \tag{318}$$

where $p = 1.6$.

We can also assume (rather unrealistically) that the cell is two dimensional, in which case $|\Gamma|$ and $|\Omega_n|$ (hence r_S) can be computed directly.

We computed r_S for the average NF and CAF under these various assumptions (table 5.2.1). The different three dimensional nucleus models give fairly consistent estimates of r_S for both CAFs and NFs, only the two dimensional model significantly differs. This is reassuring as it indicates that r_S is quite robustly estimable, even if the full geometry of the nucleus is unknown.

Figure 40 illustrates an example of ODE model fitting to data. Figure 40A indicates that the ODE model (315) approximates this particular cell

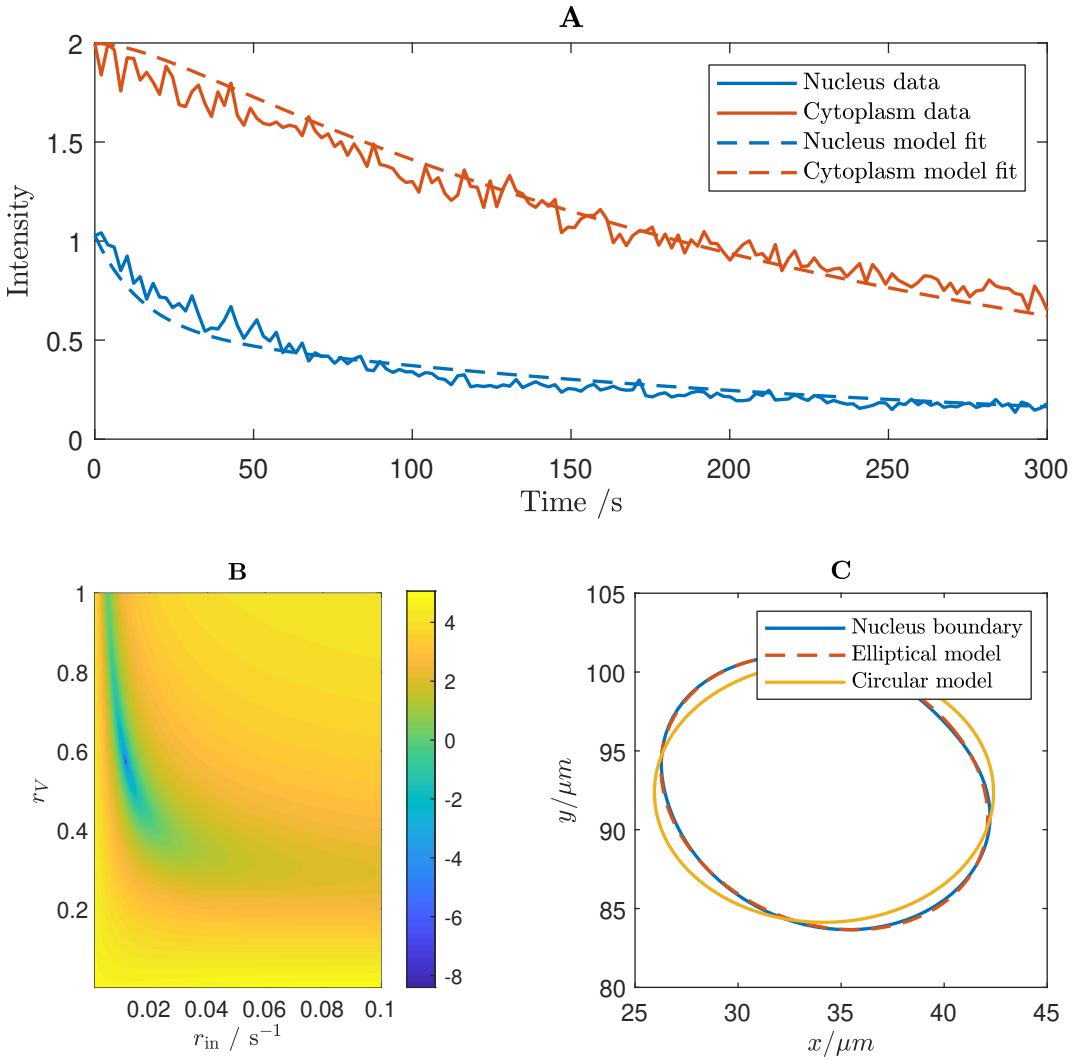


Figure 40: (A) Fit of the ODE model (315) to empirical NF data. (B) The residual sum of square errors between NF data and the ODE model for varying values of r_V and r_{in}. (C) Two dimensional image of a NF nuclear membrane fitted with an ellipse and a circle.

reasonably well, while the plot of the residual sum of square errors in 40B suggests that the fit of r_{in} and r_V is unique. Figure 40C gives an example of fitting the circular and elliptical nucleus models to empirical data. The elliptical model clearly follows the data much more closely. Notwithstanding, the spherical nucleus model will be used for the remainder of this chapter, since the estimates of r_S do not vary substantially between different models, and it eliminates the need to introduce the additional unknown, c.

	Ellipsoid ($c = b$)	Spherical	Ellipsoid ($c = a$)	2D
NF	0.4528	0.4075	0.4011	0.2865
CAF	0.3563	0.3308	0.3261	0.2281

Table 10: Average surface-area-to-volume ratios calculated from a sample of 24 real NFs and CAFs under four different modelling assumptions: the spherical model (317), the ellipsoidal model (318) for two different assumptions about the unknown semi-axis length c, and the two dimensional model. The differences between CAFs and NFs are caused by the fact that CAFs are significantly larger cells with larger nuclei.

5.3 NUMERICAL SIMULATION OF THE FLIP MODEL

In this section, we explain, with reference to an example, the process we used to simulate FLIP experiments numerically. Following the example of previous quantitative FLIP studies [151, 152], we used a finite element method which we implemented in MATLAB. To begin, it is obviously necessary to identify, from an image of a cell, the nucleus and the cytoplasm. Fortunately, to this end we can employ precisely the same method used to identify cell nuclei described in chapter 4.4.1.

5.3.1 *Compensating for cell motion*

FLIP experiments typically take considerably longer than FRAP. The experiments analysed in this chapter had a duration of approximately 300 seconds. Because the cells under investigation are motile, they can move appreciably in the course of a FLIP experiment. It is necessary to make adjustments to the data which compensate for cellular motion, or else it will be a source of error when attempting to fit the numerical model. Figure 41 features four images of a target cell which are taken 100 seconds apart. It is clear that,

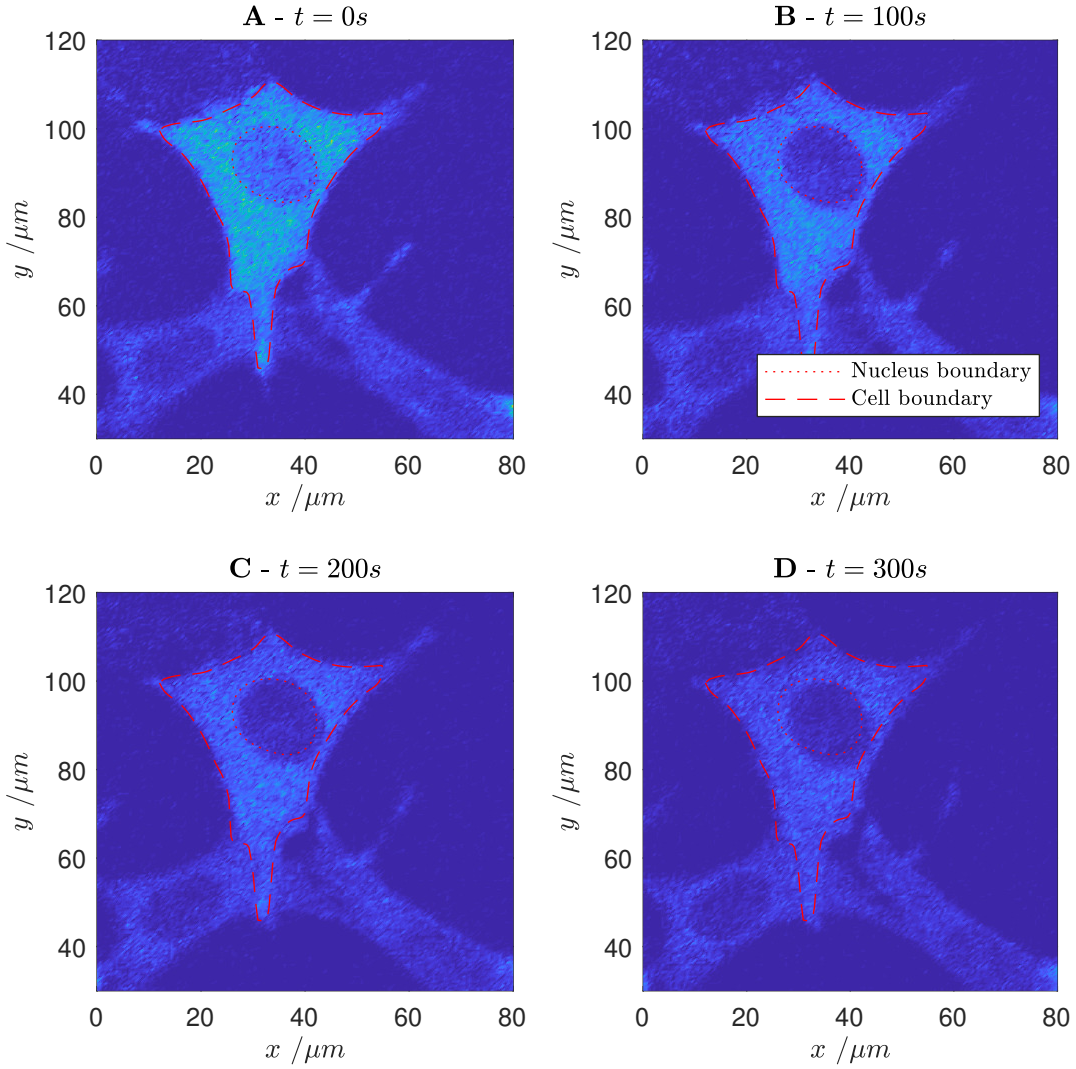


Figure 41: (A-D) Four images of the target cell in a FLIP experiment. The original positions of the nuclear membrane and the external cell membrane are also plotted. The cell drifts further from its original position as the experiment proceeds.

by the end of the experiment, the nucleus and cytoplasm of the cell are not aligned with their original positions at the start of the experiment.

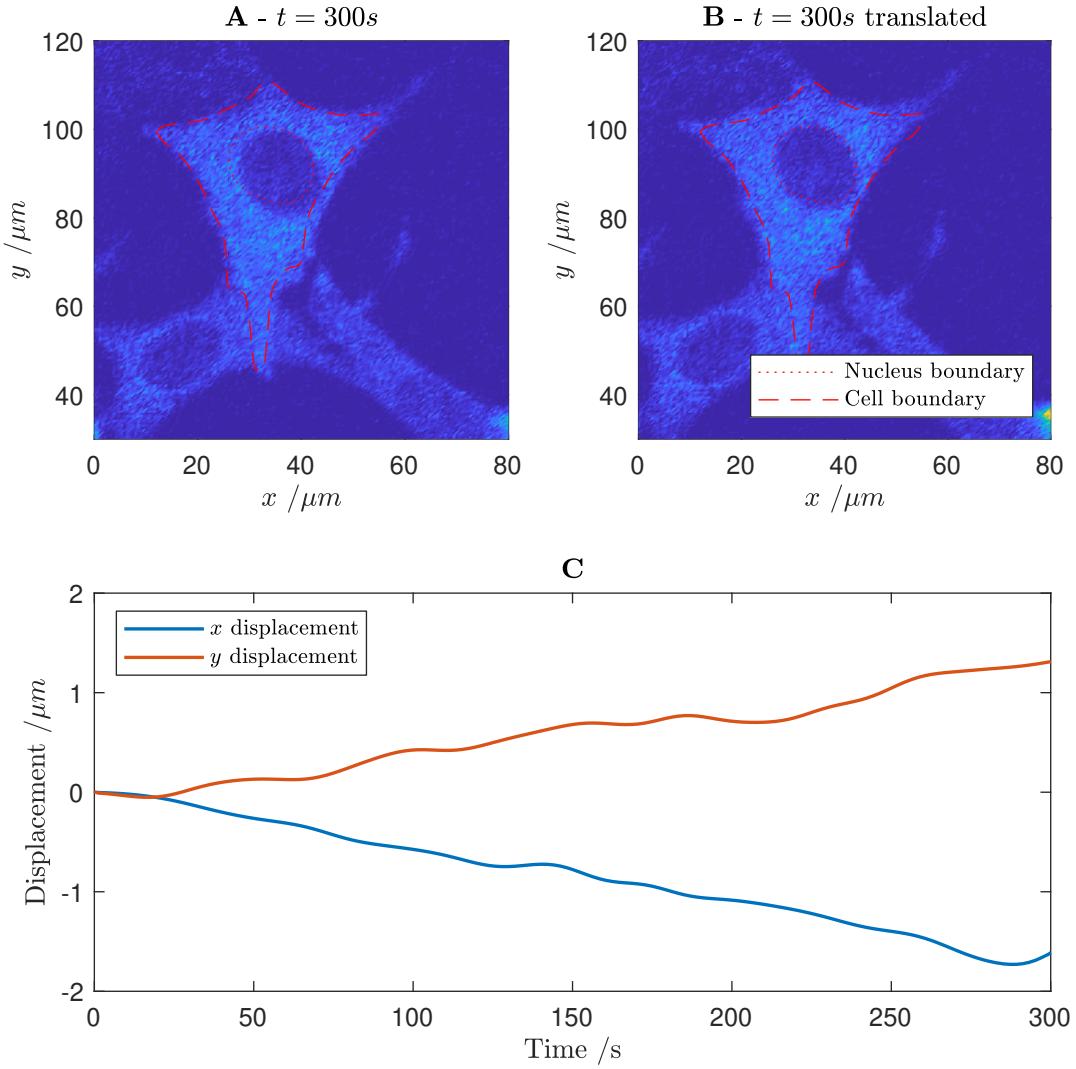


Figure 42: (A) The position of the cell 300 seconds after the beginning of the experiment. (B) The translated image of the cell 300 seconds after the beginning of the experiment. The nucleus is now realigned with its original position at the start of the experiment. (C) A plot of the x and y cell displacements, $x_d(t)$ and $y_d(t)$, against time.

The motion tracking problem is complicated somewhat by two factors. First, the recording of the cell is noisy. Secondly, the image of the cell becomes incrementally darker in each cell due to photobleaching. We found that an effective method is to established a map which translates the empirical fluorescence intensity profile, $w(x, y, t)$ by (x_d, y_d). In this way, we are

left with an optimisation problem: at each time point, t, for which we have data: find x_d and y_d which minimise the objective function,

$$\phi_t(x_d, y_d) = \int_{\Omega_n} \left[\frac{w_(x + x_d, y + y_d, t)}{\int_{\Omega_n} w_(x + x_d, y + y_d, t) \mathrm{d}x\mathrm{d}y} - \frac{w(x, y, 0)}{\int_{\Omega_n} w(x, y, 0) \mathrm{d}x\mathrm{d}y} \right]^2 \mathrm{d}x\mathrm{d}y, \tag{319}$$

Note that this definition of ϕ_t compensates for the loss of fluorescence intensity over time.

Figure 42 contains images of the target cell before and after translation. After translation, the nucleus is realigned with its original position. However, the entire cell is not quite perfectly aligned since it is a non-rigid structure and it has deformed during the experiment. Nevertheless, the deformation is rather slight and the translation is certainly an improvement over nothing.

5.3.2 *The bleaching laser*

As the target cell moves, the position of the bleaching laser will move relative to the cell. This dynamic laser is a feature we have built into our numerical FLIP model. Unlike the FRAP experiments featured in chapter 4, the laser profile used in the FLIP experiments was a 1.848 $\mu m \times 1.848$ μm square box. Regrettably we were unable to determine the laser profile empirically as we did in chapter 4.3 with H2B, due to a lack of data. Instead, we assumed that the laser intensity to be a square step function,

$$I(\mathbf{x}, t) = \begin{cases} 1 \text{ if } \mathbf{x} \in [x_{\mathrm{bl}}(t), x_{\mathrm{bl}}(t) + \Delta x] \cap [y_{\mathrm{bl}}(t), y_{\mathrm{bl}}(t) + \Delta y], \\ 0 \text{ otherwise,} \end{cases} \tag{320}$$

where $\Delta x = \Delta y = 1.848$ μm, with $(x_{\mathrm{bl}}(t), y_{\mathrm{bl}}(t))$ being the bottom left corner of the square at time t. Having already determined the translation which restores the cell nucleus to its original position, $(x_d(t), y_d(t))$, we have $(x_{\mathrm{bl}}(t), y_{\mathrm{bl}}(t)) = (x_{\mathrm{bl}}(0) + x_d(t), y_{\mathrm{bl}}(0) + y_d(t))$.

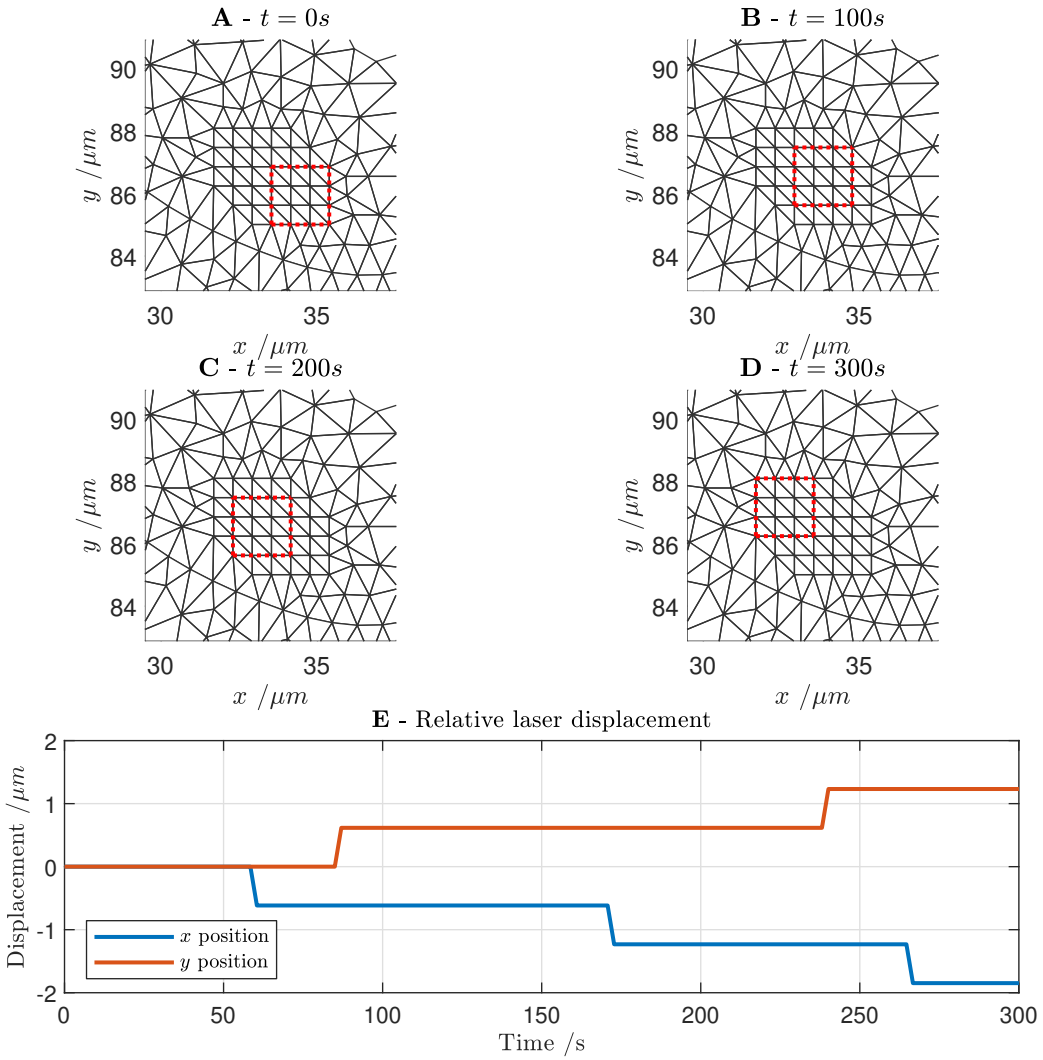


Figure 43: (A-D) Set of mesh points, B (322), embedded within an unstructured mesh. The position of the laser at the indicated time is marked by a red square. (E) A plot of the x and y coordinates of the laser displacement, $(\hat{x}_{\text{bl}}(t) - \hat{x}_{\text{bl}}(0), \hat{y}_{\text{bl}}(t) - \hat{y}_{\text{bl}}(0))$, interpolated onto the grid G.

The square step function laser profile cannot readily be approximated on a general unstructured mesh, so we must be careful to include within the simulation mesh a set of points, B, which are appropriate for the square laser geometry. Define,

$$\delta x = \frac{\Delta x}{n_x - 1}, \quad \delta y = \frac{\Delta y}{n_y - 1},$$

for some $n_x, n_y \in \mathbb{N}$. Then define the set of rectangular grid points,

$$G = \{(x_{\text{bl}}(0) + i\delta x, y_{\text{bl}}(0) + j\delta y) | i, j \in \mathbb{Z}\}.$$

We interpolate $(x_{\text{bl}}, y_{\text{bl}})$ onto the grid G, letting $(\hat{x}_{\text{bl}}(t), \hat{y}_{\text{bl}}(t)) \in G$ be the interpolations. Now define,

$$B(t) = \{(\hat{x}_{\text{bl}}(t) + i\delta x, \hat{y}_{\text{bl}}(t) + j\delta y) | i \in \{0, 1, ..., n_x - 1\}, j \in \{0, 1, ..., n_y - 1\}\}, \tag{321}$$

which is the set of mesh points covered by the laser at time t. Finally, define B as the union of the sets $B(t)$ at each discrete time point in the simulation,

$$B = \bigcup_{k=1}^{n_t} B(t_k). \tag{322}$$

As indicated in figure 43, the relative motion of the laser is modelled as a series of discrete jumps between mesh points.

5.3.3 *The simulation mesh*

Separate meshes are generated for the nucleus and the cytoplasm. We begin by generating a set, $\hat{\Gamma}$, of evenly spaced points which lie along the curve, Γ, that separates the cytoplasm from the nucleus. It is essential that the elements of $\hat{\Gamma}$ are contained within both $\hat{\Omega}_n$ and $\hat{\Omega}_c$ since there must be exchange of protein between the two compartments on their shared boundary. We also generate $\partial\hat{\Omega}_n \setminus \hat{\Gamma}$, which is the set of points lying along the closed curves at the boundary of the nucleoli, contained within the nucleus. The set of points, B, is also added to the mesh.

Turning our attention to the cytoplasm mesh, as well as $\hat{\Gamma}$ we add $\partial\hat{\Omega}_c \setminus \hat{\Gamma}$ which is a set of evenly spaced points lying along the exterior boundary of the cell (the cell membrane). Having specified the points which must be including, mesh generation is completed using a constrained Delaunay triangulation with the mesh2d MATLAB function [304]. See figure 44 for an example mesh.

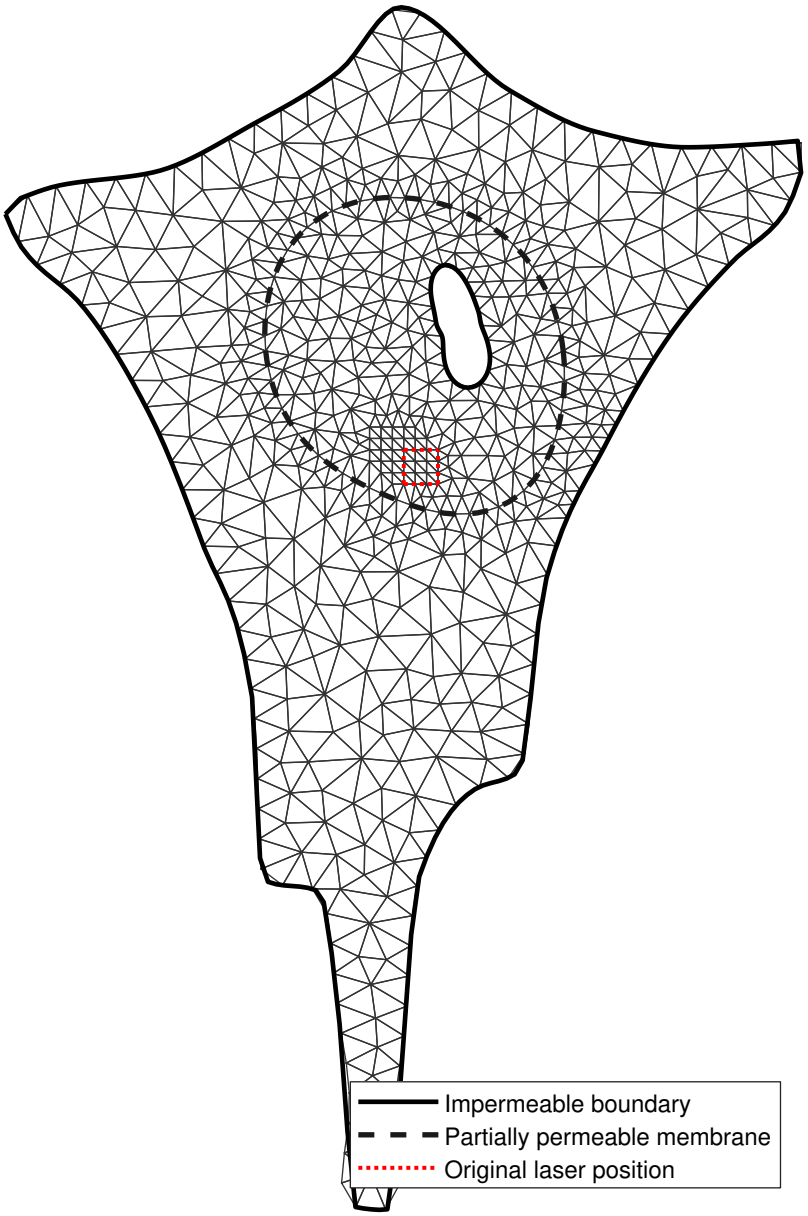


Figure 44: A mesh generated from NF data.

5.3.4 *Finite element matrices*

Having assembled the mesh, the next stage is to reduce the PDE model to a 'semi-discrete' approximation. Consider the equation,

$$\frac{\partial u_n}{\partial t} = -k_n^+ u_n + k_n^- v_n + D_{u_n} \nabla^2 u_n. \tag{323}$$

The first step of the finite element method is to multiply by an arbitrary function, $b(\mathbf{x})$, and integrate over Ω_n,

$$\int_\Omega \frac{\partial u_n}{\partial t} b \mathrm{d}V = -k_n^+ \int_\Omega u_n b \mathrm{d}V + k_n^- \int_\Omega v_n b \mathrm{d}V + \int_\Omega D_{u_n} \nabla^2 u_n b \mathrm{d}V. \tag{324}$$

By Green's first identity, it follows that

$$\int_\Omega D_u \nabla^2 u_n b \mathrm{d}V = \oint_{\partial\Omega} b(D_{u_n} \nabla u_n \cdot \hat{\mathbf{n}}) \mathrm{d}S - \int_\Omega D_{u_n} \nabla u_n \cdot \nabla b \mathrm{d}V, \tag{325}$$

hence

$$\oint_{\partial\Omega} b(D_{u_n} \nabla u_n \cdot \hat{\mathbf{n}}) \mathrm{d}S = \oint_\Gamma b(D_{u_n} \nabla u_n \cdot \hat{\mathbf{n}}) \mathrm{d}S = \oint_\Gamma b(k_{\mathrm{in}} u_c - k_{\mathrm{out}} u_n) \mathrm{d}S. \tag{326}$$

At this stage, we make the substitution

$$u_n(\mathbf{x}, t) = \sum_{j=1}^{p} u_{nj}(t) b_j(\mathbf{x}), \quad v_n(\mathbf{x}, t) = \sum_{j=1}^{p} v_{nj}(t) b_j(\mathbf{x}), \tag{327}$$

from which it follows that

$$\int_\Omega u_n(t, \mathbf{x}) b_i(\mathbf{x}) \mathrm{d}V = \int_\Omega \sum_{j=1}^{p} u_{nj}(t) b_j(\mathbf{x}) b_i(\mathbf{x}) \mathrm{d}V = \sum_{j=1}^{p} u_{nj}(t) \int_\Omega b_j(\mathbf{x}) b_i(\mathbf{x}) \mathrm{d}V, \tag{328}$$

and

$$\int_\Omega \nabla u_n(t, \mathbf{x}) \cdot \nabla b_i(\mathbf{x}) \mathrm{d}V = \sum_{j=1}^{p} u_{nj}(t) \int_\Omega \nabla b_i(\mathbf{x}) \cdot \nabla b_j(\mathbf{x}) \mathrm{d}V. \tag{329}$$

Now we turn our attention to the surface integral,

$$\oint_\Gamma b_i(\mathbf{x}) u_n(t) \mathrm{d}S = \sum_{j=1}^{p} u_{nj}(t) \oint_\Gamma b_j(\mathbf{x}) \mathrm{d}S, \tag{330}$$

which becomes

$$\oint_\Gamma b_i(\mathbf{x}) u_n(t) \mathrm{d}S = \sum_{j=1}^{p} u_{nj}(t) \oint_\Gamma b_i(\mathbf{x}) b_j(\mathbf{x}) \mathrm{d}S. \tag{331}$$

If we also make the substitution

$$u_c(\mathbf{x},t) = \sum_{j'=1}^{q} u_{cj'}(t) b_{j'}(\mathbf{x}), \quad v_c(\mathbf{x},t) = \sum_{j'=1}^{q} v_{nj'}(t) b_{j'}(\mathbf{x}), \tag{332}$$

we get

$$\oint_\Gamma b_i(\mathbf{x}) u_c(t) \mathrm{d}S = \sum_{j'=1}^{q} u_{cj'}(t) \oint_\Gamma b_i(\mathbf{x}) b_{j'}(\mathbf{x}) \mathrm{d}S. \tag{333}$$

For clarity, we will always use i and j to denote indices in the nucleus mesh and i' and j' to denote indices in the cytoplasm mesh. At this stage, we can define the vectors,

$$\mathbf{u}_n = (u_{n1}, ..., u_{np})^T, \quad \mathbf{v}_n = (v_{n1}, ..., v_{np})^T,$$

and

$$\mathbf{u}_c = (u_{c1}, ..., u_{cq})^T, \quad \mathbf{v}_c = (v_{c1}, ..., v_{cq})^T,$$

which enables us to reduce (323) to the semi-discrete approximation

$$m_n \dot{\mathbf{u}}_n = -k_n^+ m_n \mathbf{u}_n + k_n^- m_n \mathbf{v}_n + D_{u_n} l_n \mathbf{u}_n + k_{\text{in}} \phi_c \mathbf{u}_c - k_{\text{out}} \phi_n \mathbf{u}_n, \tag{334}$$

where we have used identities (328), (329), (331) and (333). The matrices m_n, l_n, ϕ_n and ϕ_c are defined as follows,

$$(m_n)_{ij} = \int_{\Omega_n} b_i(\mathbf{x}) b_j(\mathbf{x}) \mathrm{d}V, \tag{335}$$

$$(l_n)_{ij} = -\int_{\Omega_n} \nabla b_i(\mathbf{x}) \cdot \nabla b_j(\mathbf{x}) \mathrm{d}V, \tag{336}$$

$$(\phi_n)_{ij} = \oint_\Gamma b_i(\mathbf{x}) b_j(\mathbf{x}) \mathrm{d}S, \tag{337}$$

which are all $p \times p$ matrices, and

$$(\phi_c)_{ij'} = \oint_\Gamma b_i(\mathbf{x}) b_{j'}(\mathbf{x}) \mathrm{d}S, \tag{338}$$

which is a $p \times q$ matrix. Next we consider the simplified system

$$\frac{\partial u_n}{\partial t}(\mathbf{x},t) = -\alpha I(\mathbf{x},t) u(\mathbf{x},t). \tag{339}$$

Using identity (328) we get

$$\int_\Omega \frac{\partial u_n}{\partial t}(\mathbf{x},t)b(\mathbf{x})\mathrm{d}V = \int_\Omega I(\mathbf{x},t)u(\mathbf{x},t)b(\mathbf{x})\mathrm{d}V. \tag{340}$$

We also make the substitution,

$$I(\mathbf{x},t)u(\mathbf{x},t) = \sum_{j=1}^{p} I_j(t)u_j(t)b_j(\mathbf{x}), \tag{341}$$

so that (340) becomes

$$\sum_{j=1}^{p} \dot{u}_j(t)\int_{\Omega_n} b_i(\mathbf{x})b_j(\mathbf{x})\mathrm{d}V = -\alpha\sum_{j=1}^{p} I_j(t)u_j(t)\int_\Omega b_i(\mathbf{x})b_j(\mathbf{x})\mathrm{d}V, \tag{342}$$

which can be re-written as

$$m_n\dot{\mathbf{u}}_n = -\alpha\mathcal{I}(t)m_n\mathbf{u}_n. \tag{343}$$

The matrix $\mathcal{I}(t)$ is defined as

$$\mathcal{I}_{ij}(t) = \begin{cases} I_j(t) \text{ if } i = j, \\ 0 \text{ otherwise,} \end{cases} \tag{344}$$

where

$$I_j(t) = \begin{cases} 1 \text{ if } \mathbf{x}_j \in B(t), \\ 0 \text{ otherwise.} \end{cases} \tag{345}$$

Set B is defined in equation (321), the set of mesh points which are covered by the laser at time t.

Having considered the simplified equations (323) and (339), the full FLIP model can be reduced to the semi-discrete approximation,

$$\begin{cases} m_n\dot{\mathbf{u}}_n = -k_n^+m_n\mathbf{u}_n + k_n^-m_n\mathbf{v}_n + D_{u_n}l_n\mathbf{u}_n + k_{\text{in}}\phi_c\mathbf{u}_c - k_{\text{out}}\phi_n\mathbf{u}_n - \alpha\mathcal{I}(t)m_n\mathbf{u}_n, \\ m_n\dot{\mathbf{v}}_n = k_n^+m_n\mathbf{u}_n - k_n^-m_n\mathbf{v}_n + D_{v_n}l_n\mathbf{u}_n - \alpha\mathcal{I}(t)m_n\mathbf{u}_n, \\ m_c\dot{\mathbf{u}}_c = -k_c^+m_c\mathbf{u}_c + k_c^-m_c\mathbf{v}_c + D_{u_c}l_c\mathbf{u}_c + k_{\text{out}}\phi_n'\mathbf{u}_n - k_{\text{in}}\phi_c'\mathbf{u}_c, \\ m_c\dot{\mathbf{v}}_c = k_c^+m_c\mathbf{u}_c - k_c^-m_c\mathbf{v}_c + D_{v_c}l_c\mathbf{u}_c. \end{cases} \tag{346}$$

The remaining matrices are defined by

$$(m_c)_{i'j'} = \int_{\Omega_c} b_{i'}(\mathbf{x})b_{j'}(\mathbf{x})\mathrm{d}V, \tag{347}$$

$$(l_c)_{i'j'} = -\int_{\Omega_c} \nabla b_{i'}(\mathbf{x}) \cdot \nabla b_{j'}(\mathbf{x}) \mathrm{d}V, \tag{348}$$

$$(\phi_n')_{i'j} = \oint_{\Gamma} b_{i'}(\mathbf{x}) b_j(\mathbf{x}) \mathrm{d}S, \tag{349}$$

and

$$(\phi_c')_{i'j'} = \oint_{\Gamma} b_{i'}(\mathbf{x}) b_{j'}(\mathbf{x}) \mathrm{d}S. \tag{350}$$

It remains to decide on a set of basis function $b_i(\mathbf{x})$, $i = 1, ..., p$ and $b_{i'}(\mathbf{x})$, $i' = 1, ..., q$. We choose piece-wise linear functions satisfying,

$$b_i(\mathbf{x}) = \begin{cases} 1 \text{ if } \mathbf{x} = \mathbf{x}_i, \\ 0 \text{ if } \mathbf{x} = \mathbf{x}_j, j \neq i, \end{cases} \tag{351}$$

where $\mathbf{x}_i$ and $\mathbf{x}_j$ are mesh points. All the matrices in equation (346) are then sparse, since $(m_n)_{ij} = 0$ if $\mathbf{x}_i$ and $\mathbf{x}_j$ are not adjacent, and likewise for all other matrices.

5.3.5 *Example simulations*

In this section we include two example simulations of the FLIP model. In simulation 1, parameters have been chosen which ensure that the timescale of exchange of protein between cellular compartments is significantly greater than the timescale of protein redistribution within compartments. This condition theoretically ensures the validity of the ODE approximation (315). As the analysis of section 5.2 would predict, the distribution of fluorescent protein remains approximately uniform across both cellular compartments (figure 45).

Simulation 2 is intended to contrast simulation 1, the simulation parameters being chosen so that the ODE model ought not to be applicable. The loss in fluorescence intensity is localised to the bleach region and that part of the cytoplasm which is closest to the nucleus (figure 46).

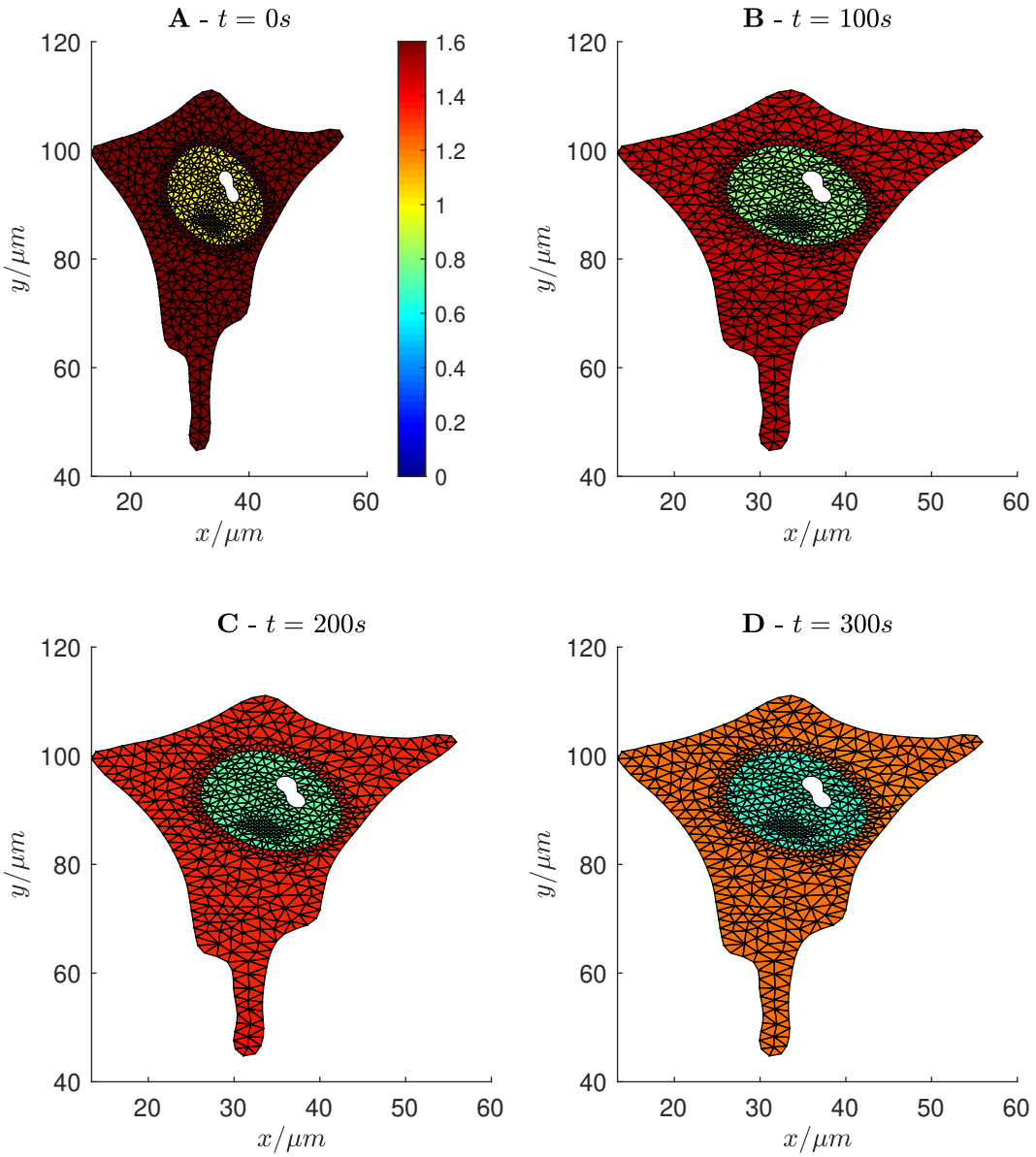


Figure 45: (A-D) Snapshots from a finite element FLIP simulation taken at the indicated times. The simulation parameters were $D_{u_n} = D_{u_c} = 40\mu m^2 s^{-1}$, $\alpha = 0.3Jm^{-2}s^{-2}$, $k_{\text{in}} = 0.21\mu m s^{-1}$, $k_{\text{out}} = 0.3\mu m s^{-1}$, $k_n^- = k_c^+ = 1s^{-1}$, $k_n^+ = 0.43s^{-1}$, $k_c^+ = 0.62s^{-1}$

As expected, the ODE model (315) is a good approximation to simulation 1, but not simulation 2 (figure 47). In particular, the ODE model overestimates the rate of loss of intensity in the cytoplasm, while underestimating intensity loss in the nucleus, which indicates that the ODE model overestimates the continuity between the two compartments. This is just as we

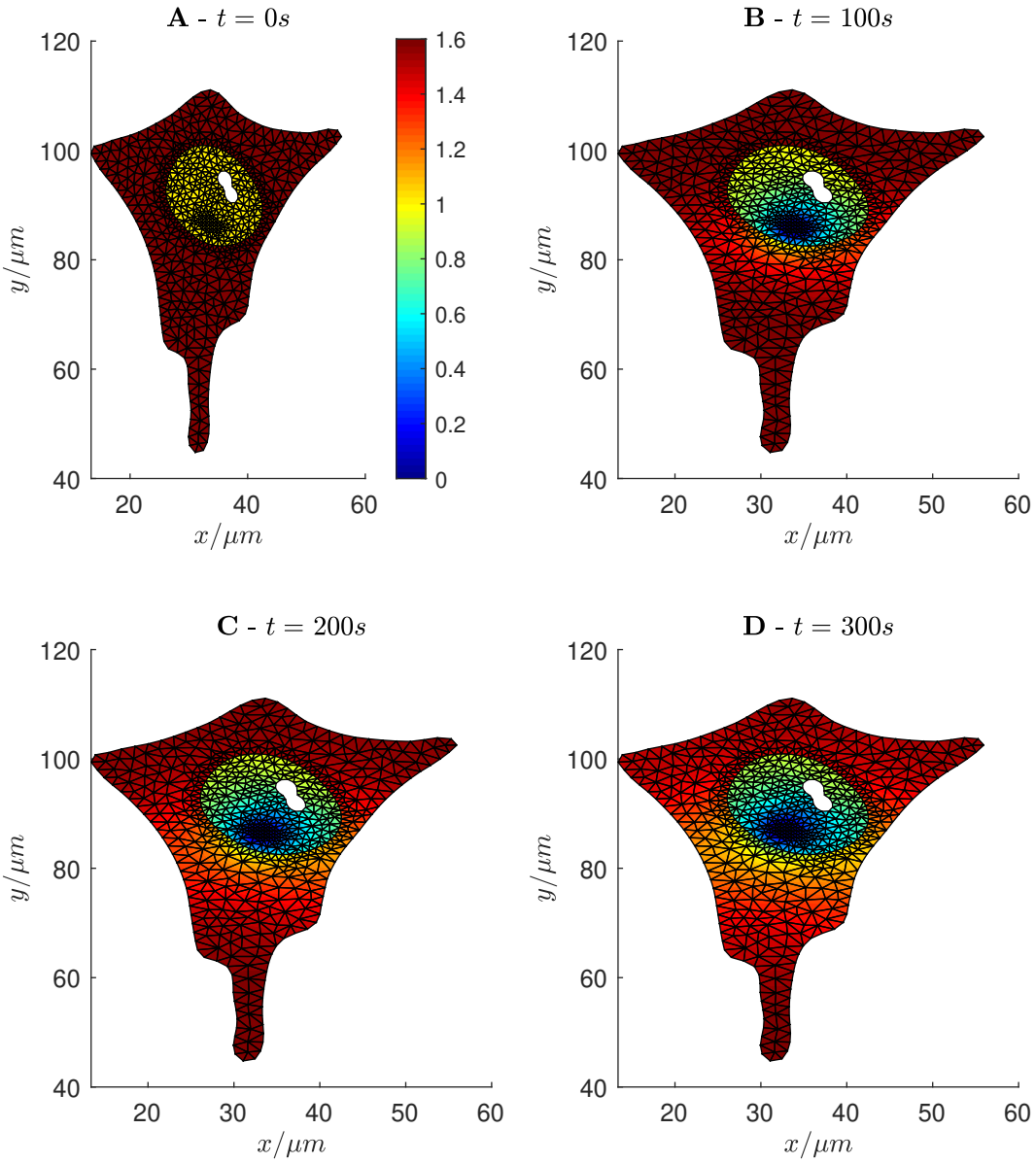


Figure 46: (A-D) Snapshots from a finite element FLIP simulation taken at the indicated times. The simulation parameters were $D_{u_n} = D_{u_c} = 1\mu m^2 s^{-1}$, $\alpha = 5Jm^{-2}s^{-2}$, $k_{\text{in}} = 6\mu m s^{-1}$, $k_{\text{out}} = 10\mu m s^{-1}$, $k_n^- = k_c^+ = 1s^{-1}$, $k_n^+ = 1s^{-1}$, $k_c^+ = 1.22s^{-1}$

would predict, as the ODE model assumes that the diffusivity of the protein within each compartment is not a limiting factor. In simulation 2, intra-compartmental diffusion is quite slow compared with inter-compartmental transport, so this assumption does not hold.

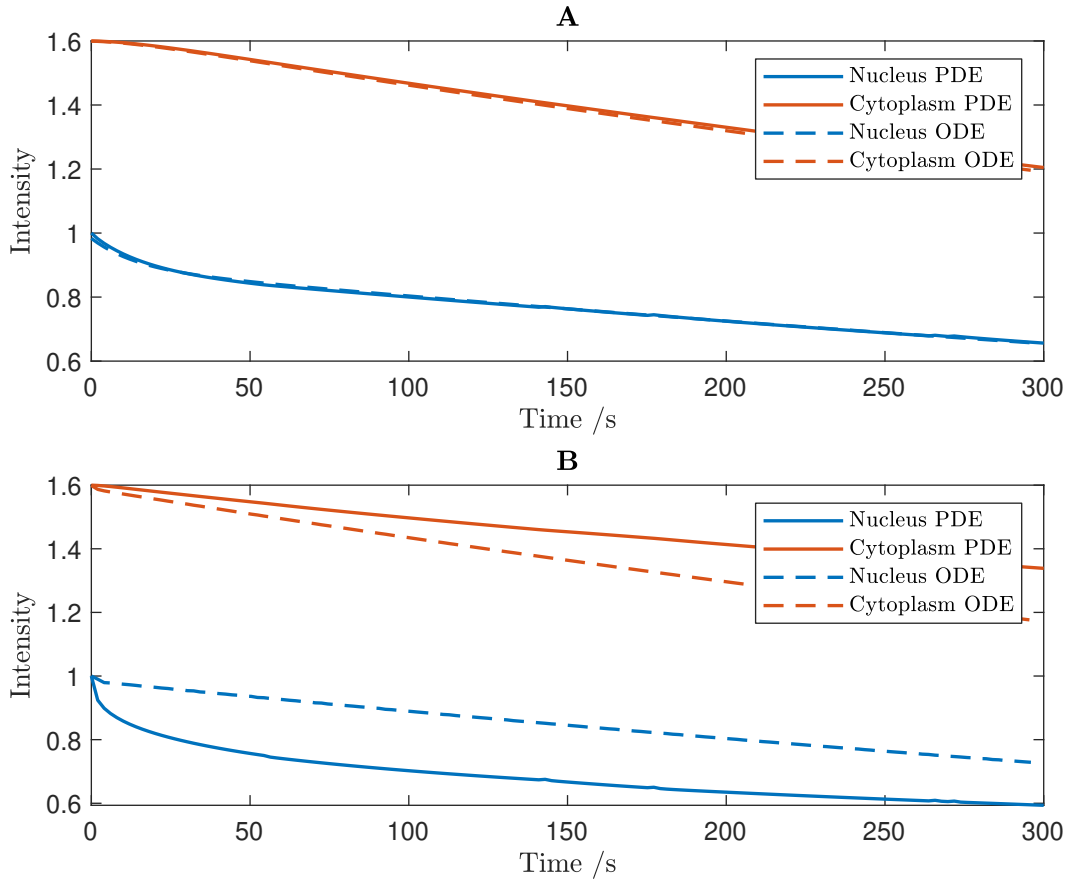


Figure 47: Average fluorescence intensities across the nucleus and cytoplasm against time taken from finite element FLIP simulations, contrasted with the predictions of the ODE model (315). The PDE FLIP model was run using (A) the same parameters as the simulation featured in figure 45 and (B) the same parameters as in figure 46.

5.4 METHODOLOGY

We have been supplied with a sample of FLIP data on wild-type YAP in 24 NFs and 23 CAFs. In this section, we outline the methods used to analyse the data, with reference to the previous sections in this chapter, and present the results. In particular, we are interested in obtaining estimates of the cross-membrane flux parameters, k_{in} and k_{out} because these are not estimable from FRAP data, as we discussed in section 4.7.1, due to the very limited data amount of data acquired in the cytoplasm.

First the cell data are normalised to account for unintentional photobleaching caused by the imaging laser. A cell which is not subject to intentional phototbleaching is chosen as an external control. We subtract the background intensity (*i.e.* the intensity of a region which contains no cells), then normalise by the average intensity of the external control cell. We call the total fluorescence intensity (after normalisation) at point $\mathbf{x}$ and time t $w_{\text{Data}}(\mathbf{x}, t)$.

For each cell we manually select two reporting regions, one in the nucleus, Ω_{nr}, and one in the cytoplasm Ω_{cr}. The average intensities across the reporting regions are

$$w_{n\text{Data}}(t) = \frac{1}{|\Omega_{nr}|}\int_{\Omega_{nr}} w_{\text{Data}}(\mathbf{x}, t)\mathrm{d}V, \quad w_{c\text{Data}}(t) = \frac{1}{|\Omega_{cr}|}\int_{\Omega_{cr}} w_{\text{Data}}(\mathbf{x}, t)\mathrm{d}V.$$

Let $w_n(t;\theta)$, $w_c(t;\theta)$ be a solution to the ODE model (315) for a set of parameter values, θ. Define the objective function, ϕ as

$$\phi(\theta) = \int_0^T (w_{n\text{Data}}(t) - w_n(t;\theta))^2\mathrm{d}t + \int_0^T (w_{c\text{Data}}(t) - w_c(t;\theta))^2\mathrm{d}t.$$

We then solve a constrained optimisation problem, minimising ϕ, yielding estimates of r_{in} and r_{out}, the total rates of nuclear import and export. We then calculate the mean radius, R, of the nucleus and determine the surface area-to-volume ratio, r_S, as described in section 5.2.1.

Continuing, we carry out a numerical PDE simulation, following section 5.3. Let $w(\mathbf{x}, t)$ be the total fluorescence intensity at $\mathbf{x}$ and t predicted by the numerical solution of the PDE FLIP model. We define the second objective function, ϕ_{Space}, as follows,

$$\phi_n(\theta) = \int_0^T \int_{\Omega_n} (w_{\text{Data}}(\mathbf{x}, t) - w_n(\mathbf{x}, t;\theta))^2\mathrm{d}V\mathrm{d}t,$$

$$\phi_c(\theta) = \int_0^T \int_{\Omega_c} (w_{\text{Data}}(\mathbf{x}, t) - w_c(\mathbf{x}, t;\theta))^2\mathrm{d}V\mathrm{d}t,$$

$$\phi_{\text{Space}}(\theta) = \phi_n(\theta) + \phi_c(\theta).$$

By finding the minimum of ϕ_{Space}, we are provided with estimates of f_n and f_c (the fractions of unbound protein at equilibrium in the nucleus and

cytoplasm respectively). To reduce the degrees of freedom, we set D_{u_n} for each cell equal to the mean estimate obtained by FRAP in chapter 4 and set $D_{u_c} = D_{u_n}$. These assumptions are unlikely to be a great source of error, as we have already established that the fast diffusivity coefficient is a sloppy parameter. Having firmly established with H2B data in section 4.3 that $D_{v_n} = 0$, as chromatin is immobile, we also assume that $D_{v_c} = 0$. This assumption enables us to investigate the extent of YAP immobilisation in the cytoplasm in NFs and CAFs.

By this process we additionally end up with estimates of k_{in} and k_{out}, but these are not recorded because the simulation is two dimensional so we cannot ensure that the estimates are accurate. Instead, we set

$$k_{\text{in}} = \frac{r_{\text{in}}}{r_S f_c}, \quad k_{\text{out}} = \frac{r_{\text{out}}}{r_S f_n},$$

using estimates of r_{in} and r_{out} from the ODE model, and estimates of f_n and f_c from the PDE model. To establish fully the differences between CAFs and NFs we measure several equilibrium constants: the YAP concentration in the nucleus,

$$N = \frac{1}{|\Omega_n|} \int_{\Omega_n} w_{\text{Data}}(\mathbf{x}, 0) \mathrm{d}V,$$

the YAP concentration in the cytoplasm,

$$C = \frac{1}{|\Omega_c|} \int_{\Omega_c} w_{\text{Data}}(\mathbf{x}, 0) \mathrm{d}V,$$

and the total mass of YAP across the whole cell

$$M = \int_{\Omega_n} w_{\text{Data}}(\mathbf{x}, 0) \mathrm{d}V + \int_{\Omega_c} w_{\text{Data}}(\mathbf{x}, 0) \mathrm{d}V.$$

5.5 RESULTS

YAP is a target of the Hippo tumour suppressing pathway [170]. YAP suppression occurs by a variety of mechanisms: nuclear exclusion, sequestration in the cytoplasm and degradation [10, 175, 176, 196]. YAP suppression can theoretically be measured by parameter estimation with the FLIP model.

Nuclear exclusion will lower k_{in} and/or raise k_{out}, while cytoplasmic sequestration will tend to lower f_c (in particular, interactions between YAP and 14-3-3 proteins). The FLIP model does not measure protein degradation, but the total mass of protein in a cell, M, is an indirect measure of the rate of degradation, as we would expect that M would tend to be lower in cells with a greater degradation rate. Of course, this is an imperfect measure, since M is also affected by the rate of protein production by translation. In this section we will present parameter fitting results and check whether they are consistent with biological understanding.

The results in this section are grouped into three main tables. Table 11 includes measurements of equilibrium constants, M, N and C. Tables 12 and 13 contain parameter estimates obtained via the ODE and PDE models respectively. The statistical difference (Cohen's d) in each variable between CAFs and NFs is calculated and classified (small, medium, large etc.) according to canonical classification of effect size [285].

	CAF			NF			
	Lower	Mean	Upper	Lower	Mean	Upper	d (CAF-NF)
M	297	395	492	217	280	343	+0.6 (medium)
N	0.41	0.46	0.51	0.22	0.25	0.28	+1.99 (huge)
C	0.28	0.32	0.36	0.42	0.48	0.54	-1.31 (very large)

Table 11: Calculations of the total mass of protein per cell, M, nuclear protein concentration, N, and cytoplasm protein concentration, C. Lower and upper estimates are the 95% confident intervals. The rightmost column is Cohen's d, an effect size measure of the difference between CAFs and NFs.

We notice that N is much greater in CAFs while C is much greater in NFs, which is consistent with the sequestration of YAP in cytoplasm in NFs (table 11). We find that M is moderately greater in CAFs which is consistent with (though does not prove) a greater rate of YAP degradation in NFs.

	CAF			NF			
	Lower	Mean	Upper	Lower	Mean	Upper	d (CAF-NF)
r_{in}	0.036	0.045	0.054	0.020	0.025	0.031	+1.16 (large)
r_{out}	0.025	0.031	0.036	0.038	0.048	0.058	-1.02 (large)
r_{in}/r_S	0.11	0.14	0.17	0.049	0.62	0.75	+1.46 (very large)
r_{in}/r_S	0.076	0.095	0.011	0.0.096	0.12	0.14	-0.52 (medium)

Table 12: Estimates of the aggregate transport rates, r_{in} and r_{out}, obtained by fitting the ODE model (315) to data. Also, the aggregate transport rates normalised by nucleus surface-area-to-volume ratio, r_S. Lower and upper estimates are the 95% confident intervals. The rightmost column is Cohen's d, an effect size measure of the difference between CAFs and NFs.

	CAF			NF			
	Lower	Mean	Upper	Lower	Mean	Upper	d (CAF-NF)
f_n	0.14	0.23	0.39	0.23	0.32	0.41	-0.43 (medium)
f_c	0.32	0.44	0.56	0.23	0.36	0.50	+0.26 (small)
k_{in}	0.021	0.83	1.65	0.14	0.47	0.83	+0.24 (small)
k_{out}	0.53	0.96	1.38	0.29	1.14	1.98	-0.13 (small)

Table 13: Estimates of the fraction of protein unbound at equilibrium in the nucleus and cytoplasm, f_n and f_c respectively, obtained by fitting the PDE model to data. Also, the cross-membrane flux parameters, k_{in} and k_{out} which are estimated as follows. First estimate r_{out}/r_S with ODE model fitting (see table 12), then set $k_{\text{out}} = (r_{\text{out}}/r_S)/f_n$ where f_n is estimated by PDE model fitting (and likewise for r_{in}). Lower and upper estimates are the 95% confident intervals. The rightmost column is Cohen's d, an effect size measure of the difference between CAFs and NFs.

Similarly, ODE model fitting yielded large differences between CAFs and NFs in terms of the aggregate transport rates, r_{in} and r_{out} (table 12). PDE model fitting (table 13) revealed differences which were fully consistent with biological expectation: f_c and k_{in} were greater in CAFs, while k_{out} was lower

(f_n was also lower in CAFs which suggests greater interaction between YAP and chromatin).

The effect sizes for each of these differences individually were small to moderate, which suggests that there is no single dominant regulatory mechanism responsible for the cytoplasmic sequestration of YAP in normal fibroblasts. Greater YAP degradation, binding with cytoplasmic regulatory proteins, a reduced rate of nuclear import and a greater rate of export via nuclear pore complexes all have an individually small, but collectively significant, effect.

5.5.1 *Concordance between FRAP and FLIP*

There is some overlap between the FLIP results in this chapter, and the FRAP results in chapter 4. Both yield estimates of the unbound protein fraction in the nucleus, f_n. It is appropriate to check if the two different methods produce consistent results.

	FLIP		FRAP		
	Mean	σ	Mean	σ	d (FLIP-FRAP)
CAF	0.23	0.21	0.27	0.078	-0.30 (small)
NF	0.32	0.22	0.30	0.14	+0.096 (very small)

Table 14: Mean estimates of f_n obtained by FLIP and FRAP model fitting, as well as the standard deviation σ of the estimates. Effect size calculations, reveal only small differences between the two methods.

Table 14 contrasts FLIP and FRAP results. It is clear from the smaller standard deviation in parameter estimates that FRAP gives superior results, but this is to be expected given the lower temporal resolution of FLIP. Nevertheless, we found only statistically small differences between the two methods, which is an encouraging validation of the FLIP methodology.

5.6 CHAPTER SUMMARY

In this chapter we began by posing a PDE model of FLIP. This model was fairly generic and could be applied to a wide variety of proteins. Although ODE modelling has been applied to FLIP in previous studies, to our knowledge the relevant ODE has never been formally derived as an asymptotic limit case until now. The formal derivation also enabled us to account for the transport of protein across the nuclear membrane in three dimensions, even when only two dimensional imaging data are available. We derived a new (to our knowledge) finite element FLIP simulation procedure which can compensate for cellular motion during experiments.

Parameter fitting yielded results which were both consistent with current biological understanding of YAP and concordant with previous FRAP results. We found that the sequestration of YAP in the cytoplasm in normal fibroblasts is the result of a combination of several regulatory mechanisms. Anchoring by proteins in the cytoplasm, reduced nuclear import, increased nuclear export, and reduced binding with chromatin all contribute a small amount to the cytoplasmic sequestration of YAP in NFs. Collectively, they produce a large effect, with cytoplasmic YAP concentrations being much greater in NFs and nuclear YAP concentration being much greater in CAFs.

An interesting weakness of the FLIP model is that it cannot distinguish different states in which the protein of interest has similar mobility. Suppose that the protein binds with another mobile protein in the cytoplasm to form a complex with diffusivity, D_{v_c}, where $D_{v_c} \approx D_{u_c}$. Even though this complex is part of the bound fraction of protein, it would be detected as part of the free fraction of protein due to its high mobility. Suppose further that this protein complex is not translocated to the nucleus. The model assumes that all free protein molecules in the cytoplasm may be imported into the nucleus, yet in this case there would be protein molecules which were (erroneously) identified as free which were not susceptible to nuclear import. While the presence of such a highly mobile bound fraction in fact constitutes

a reduction of f_c (relative to a cell which is identical, except that it does not form these high mobility protein complexes), it would be detected by model fitting as a reduction in the import flux, k_{in}. This is significant, as we might assume that k_{in} and k_{out} are determined by the properties of the nuclear pore complexes, but this is not entirely true. It must be taken into consideration that the FLIP model does not give a totally accurate characterisation of a cell, and that information about many different cellular processes may be compressed into a single model parameter.

6

CONCLUSION

Yes-associated protein (YAP) is a potent onctoprotein which promotes malignant behaviour in cancer cells when it is localised to the nucleus [170]. This thesis was originally motivated by an empirical question: what explains the elevated nuclear concentration of YAP in cancer-associated fibroblasts? YAP localisation is proximally regulated by four mechanisms which can be investigated by FRAP/FLIP: binding reactions in the cytoplasm, nuclear export, binding reactions in the nucleus and nuclear import. Additionally, YAP is regulated by proteasomal degradation, although this cannot be investigated directly by either FRAP or FLIP. This led to the main theoretical question of the thesis: under what conditions can protein binding kinetics be dissected quantitatively using FRAP?

6.1 MATHEMATICAL ANALYSIS OF FRAP

The content of chapter 2 was wholly theoretical. We derived a generalisation of a well-known FRAP asymptotic approximation formula. From this formula, we explicitly computed the Fisher information matrix and determined conditions which guarantee viable parameter estimation in conventional (*i.e.* recovery curve-based) FRAP. We expanded a simplified version of the asymptotic formula to first order to determine conditions guaranteeing parameter estimability in pixel-based scanning FRAP.

Additionally, we considered models of three interacting species and derived new (to our knowledge) approximation formulas in certain limiting cases. We also found that FRAP could theoretically be used to determine the order of reaction in three-species systems; the number of exponential functions required to fit a recovery curve is an indicator of order of reaction.

6.2 NUMERICAL ANALYSIS OF FRAP AND A GENERAL PARAMETER FITTING SCHEME

In chapter 3 we ran *in silico* FRAP experiments to test the predictions of chapter 2, finding good agreement. We also found that fitting multiple fluorescence recoveries with different bleach region radii reduces parameter multiplicity in noisy systems. We then proposed a general FRAP fitting protocol. Each cell is bleached twice and the fluorescence recoveries are fitted with a computational model. Constrained model fits are used to determine the parameter regime of the data. In the rapid equilibration regime ($D_u/(k^+ r_n^2) \gg 1$) it is possible to estimate all model parameters. Outside of this regime, it is necessary to run separate experiments to estimate the diffusivities, D_u and D_v. Theoretically, it is always possible to determine the bound fraction of protein at equilibrium, if not the individual reaction rates.

6.3 INVESTIGATING YAP WITH FRAP MODEL FITTING

We implemented a pixel-based finite difference numerical model of FRAP in the cell nucleus (chapter 4). This model allowed for inhomogeneous distribution of binding sites, and time dependent photobleaching which might be caused by laser intensity fluctuations. It also benefited from an empirical bleaching intensity profile derived from the immobile nuclear protein, H2B.

This model was fitted to YAP data from both CAFs and NFs. In addition to wild type YAP, data on YAP mutants 5SA and S94A were also investigated. The 5SA mutation causes YAP to resist phosphorylation (hence inhibition) by the Hippo signalling pathway, while the S94A mutation makes YAP unable to bind with TEAD transcription factors. We included, as a control, data on unassociated enhanced green fluorescent protein, EGFP.

Our expectation was that the bound fraction of YAP would be greater and/or bonds between YAP and chromatin would be more stable in CAFs than NFs. We would expect that the S94A mutation would significantly decrease the bound fraction of YAP in both CAFs and NFs. The control, EGFP, is not known to interact with anything in the nuclei of human cells and so was expected to have a bound fraction of approximately 0. Our results showed good agreement with all of these predictions. Further, we found that, although the bound fraction of S94A YAP was reduced relative to wild-type YAP, it was not reduced to 0, which is evidence of TEAD-independent interactions with chromatin. We also found that the 5SA mutation boosted the bound fraction of YAP which we did not expect based on our review of the YAP literature in chapter 1 (section 1.6). This result implies that phosphorylation of YAP by Hippo signalling diminishes its affinity with chromatin.

6.4 FLUORESCENCE LOSS IN PHOTOBLEACHING

In chapter 5 we turned our attention to FLIP. We developed a finite element model of FLIP which included internal obstructions within the nucleus, active transport across the nuclear membrane, and cell motion during the experiment. To our knowledge, no previous model has incorporated all of these features.

We used parameter fitting of our FLIP model to study wild-type YAP in CAFs and NFs. We expected the nuclear import rate, and bound fraction in the nucleus to be greater in CAFs, and the nuclear export rate and

bound fraction in the cytoplasm to be greater in NFs. Results were in good agreement with these expectations.

6.5 SUMMARY OF EMPIRICAL RESULTS: THE DIFFERENCE BETWEEN CAFS AND NFS

YAP localisation to the nucleus is influenced by five variables which we are able to measure: the mobile fraction in the nucleus, f_n, the mobile fraction in the cytoplasm, f_c, the import and export flux terms, k_{in} and k_{out}, and the total cellular mass of YAP, M (this is indirectly a measure of degradation and production, as a higher rate of degradation will drive down M, while a higher rate of production will increase it). An advantage of quantification is that we are able to rank-order these factors by importance. At equilibrium, the total mass of YAP in the nucleus, N, is given by

$$N = M\frac{k_{\text{in}}f_c r_V}{k_{\text{out}}f_n + r_V k_{\text{in}}f_c}, \tag{352}$$

where r_V is the volume ratio of the nucleus to the cytoplasm. We can take the mean estimates of f_c, k_{in}, k_{out}, M and r_V from FLIP data, and f_n from FRAP data (FLIP also provided estimates of f_n but the FRAP estimates had tighter confidence intervals). We computed the value of N for a theoretical average NF, then switched each parameter value individually to the mean estimate in CAFs and recorded the proportional change in N.

	k_{in}	M	k_{out}	f_c	f_n
Nuclear YAP boost	64.5%	41.1%	32.5%	20.0%	9.30%

Table 15: Percentage change in theoretical nuclear YAP mass when switching one parameter value from the NF average to the CAF average. The percentages do not add to 100% because there are diminishing returns on changing two or more parameter values simultaneously.

Results (table 15) clearly indicate that the import flux, k_{in} is the single most important factor distinguishing CAFs from NFs. Recall that k_{in} is

boosted by extra-cellular matrix (ECM) tensile forces, which are transmitted to the nucleus via actomyosin filaments, and open nuclear pore complexes on the apical surface of the nucleus [247]. Since CAFs remodel the ECM to boost its rigidity, increasing the tensile force exerted on nearby cells [18], this result suggests a highly significant role for fibroblasts in boosting YAP localisation to the nucleus, and hence in the progression of solid tumours.

6.6 POSSIBILITIES FOR FUTURE WORK

The empirical results of chapters 4 and 5 could be strengthened with additional data. For example, only FLIP data on wild type YAP were available, but it would be interesting to know the rates of nucleocytoplasmic shuttling for the 5SA and S94A mutants also. In particular, since the 5SA mutant is resistant to phosphorylation by the Hippo pathway, FLIP could be used to determine what effect Hippo signalling has on the nuclear import and export of YAP. This is a good example of how quantitative FRAP/FLIP analysis can lead to qualitative insights about protein regulation.

The mathematical model fitting applied to YAP here could quite readily be applied to other proteins, particularly to proteins which have been less extensively studied than YAP, which could yield important information about protein dynamics. This would be also a good opportunity to test the model fitting protocol proposed in chapter 3.

Indeed, the case for further collaboration between modellers and experimentalists is quite strong generally. Despite the wealth of FRAP models that have been published, researchers have often been content with exponential formula fitting that gives a general picture of protein mobility, but not much more [90]. Due to the difficulty of solving even a simple two species reaction-diffusion equation analytically, proper analysis of binding kinetics realistically requires numerical methods. Yet numerical methods, requiring dedicated programming, have had a rather limited impact; one fairly recent review which was co-authored by a large team of FRAP ex-

perts surmised "their use has been and most likely will be limited to very specific cases" [44]. It is likely that, without direct collaboration between modellers and researchers, much FRAP data will be under-analysed.

Another more speculative direction for future work would be modelling of newer experimental techniques, such as optogenetics. Optogenetics is a technique that has emerged over the past decade which can be used to investigate protein mobility in live cells. Briefly, a photo-responsive complex is used to sequester a fluorophore-tagged protein under investigation on the surface of the mitochondria. Illumination with blue light releases protein molecules from the mitochondria. Their subsequent spread throughout the cell, including entry into the nucleus, is observed. Cessation of blue light illumination leads to re-sequestration on the surface of mitochondria [305]. This process could potentially be modelled by an adaptation of the FLIP model in chapter 5. The required modifications would include explicit inclusion of mitochondria and modelling of the reversible sequestration of protein on the mitochondrial surface.

BIBLIOGRAPHY

[1] Dong J, Feldmann G, Huang J, *et al. Elucidation of a universal size-control mechanism in Drosophila and mammals.* Cell. 2007;130(6):1120-1133. doi:10.1016/j.cell.2007.07.019

[2] Santinon G, Brian I, Pocaterra A, *et al. dNTP metabolism links mechanical cues and YAP/TAZ to cell growth and oncogene-induced senescence.* EMBO J. 2018;37(11):e97780. doi:10.15252/embj.201797780

[3] Zanconato F, Forcato M, Battilana G, *et al. Genome-wide association between YAP/TAZ/TEAD and AP-1 at enhancers drives oncogenic growth.* Nat Cell Biol. 2015;17(9):1218-1227. doi:10.1038/ncb3216

[4] Lamar JM, Stern P, Liu H, Schindler JW, Jiang ZG, Hynes RO. *The Hippo pathway target, YAP, promotes metastasis through its TEAD-interaction domain.* Proc Natl Acad Sci U S A. 2012;109(37):E2441-E2450. doi:10.1073/pnas.1212021109

[5] Moya IM, Halder G. *Hippo-YAP/TAZ signalling in organ regeneration and regenerative medicine.* Nat Rev Mol Cell Biol. 2019;20(4):211-226. doi:10.1038/s41580-018-0086-y

[6] Panciera T, Azzolin L, Fujimura A, *et al. Induction of Expandable Tissue-Specific Stem/Progenitor Cells through Transient Expression of YAP/TAZ.* Cell Stem Cell. 2016;19(6):725-737. doi:10.1016/j.stem.2016.08.009

[7] Yui S, Azzolin L, Maimets M, *et al. YAP/TAZ-Dependent Reprogramming of Colonic Epithelium Links ECM Remodeling to Tissue Regeneration.* Cell Stem Cell. 2018;22(1):35-49.e7. doi:10.1016/j.stem.2017.11.001

[8] Ma S, Meng Z, Chen R, Guan KL. *The Hippo Pathway: Biology and Pathophysiology.* Annu Rev Biochem. 2019;88:577-604. doi:10.1146/annurev-biochem-013118-111829

[9] Zanconato F, Cordenonsi M, Piccolo S. YAP/TAZ at the Roots of Cancer. Cancer Cell. 2016;29(6):783-803. doi:10.1016/j.ccell.2016.05.005

[10] Zhao B, Li L, Lei Q, Guan KL. *The Hippo-YAP pathway in organ size control and tumorigenesis: an updated version.* Genes Dev. 2010;24(9):862-874. doi:10.1101/gad.1909210

[11] Harvey KF, Zhang X, Thomas DM. *The Hippo pathway and human cancer.* Nat Rev Cancer. 2013;13(4):246-257. doi:10.1038/nrc3458

[12] Johnson R, Halder G. The two faces of Hippo: targeting the Hippo pathway for regenerative medicine and cancer treatment. Nat Rev Drug Discov. 2014;13(1):63-79. doi:10.1038/nrd4161

[13] Liu JY, Li YH, Lin HX, *et al. Overexpression of YAP 1 contributes to progressive features and poor prognosis of human urothelial carcinoma of the bladder.* BMC Cancer. 2013;13:349. Published 2013 Jul 19. doi:10.1186/1471-2407-13-349

[14] Huang HL, Wang S, Yin MX, *et al. Par-1 regulates tissue growth by influencing hippo phosphorylation status and hippo-salvador association.* PLoS Biol. 2013;11(8):e1001620. doi:10.1371/journal.pbio.1001620

[15] Warren JSA, Xiao Y, Lamar JM. *YAP/TAZ Activation as a Target for Treating Metastatic Cancer.* Cancers (Basel). 2018;10(4):115. Published 2018 Apr 10. doi:10.3390/cancers10040115

[16] Kalluri R, Zeisberg M. Fibroblasts in cancer. Nat Rev Cancer. 2006;6(5):392-401. doi:10.1038/nrc1877

[17] Gaggioli C, Hooper S, Hidalgo-Carcedo C, et al. Fibroblast-led collective invasion of carcinoma cells with differing roles for RhoGT-

Pases in leading and following cells. Nat Cell Biol. 2007;9(12):1392-1400. doi:10.1038/ncb1658

[18] Calvo F, Ege N, Grande-Garcia A, *et al. Mechanotransduction and YAP-dependent matrix remodelling is required for the generation and maintenance of cancer-associated fibroblasts.* Nat Cell Biol. 2013;15(6):637-646. doi:10.1038/ncb2756

[19] Tsien RY. *The green fluorescent protein.* Annu Rev Biochem. 1998;67:509-544. doi:10.1146/annurev.biochem.67.1.509

[20] Giepmans BN, Adams SR, Ellisman MH, Tsien RY. *The fluorescent toolbox for assessing protein location and function.* Science. 2006;312(5771):217-224. doi:10.1126/science.1124618

[21] White J, Stelzer E. Photobleaching GFP reveals protein dynamics inside live cells. Trends Cell Biol. 1999;9(2):61-65. doi:10.1016/s0962-8924(98)01433-0

[22] Meyvis TK, De Smedt SC, Van Oostveldt P, Demeester J. Fluorescence recovery after photobleaching: a versatile tool for mobility and interaction measurements in pharmaceutical research. Pharm Res. 1999;16(8):1153-1162. doi:10.1023/a:1011924909138

[23] Reits EA, Neefjes JJ. From fixed to FRAP: measuring protein mobility and activity in living cells. Nat Cell Biol. 2001;3(6):E145-E147. doi:10.1038/35078615

[24] Carrero G, McDonald D, Crawford E, de Vries G, Hendzel MJ. Using FRAP and mathematical modeling to determine the in vivo kinetics of nuclear proteins. Methods. 2003;29(1):14-28. doi:10.1016/s1046-2023(02)00288-8

[25] Lippincott-Schwartz J, Snapp EL, Phair RD. The Development and Enhancement of FRAP as a Key Tool for Investigating Protein Dynamics. Biophys J. 2018;115(7):1146-1155. doi:10.1016/j.bpj.2018.08.007

[26] Mielenz KD. On the Diffraction Limit for Lensless Imaging. J Res Natl Inst Stand Technol. 1999;104(5):479-485. doi:10.6028/jres.104.029

[27] Shaw PJ, Rawlins DJ. *The point spread function of a confocal microscope: its measurement and use in deconvolution of 3 [U+2010]D data.* J. Microsc. 1991;163(2):151-165. doi:10.1111/j.1365-2818.1991.tb03168.x

[28] Axelrod D, Elson EL, Schlessinger J, Koppel DE. *Reminiscences on the "Classic" 1976 FRAP Article in Biophysical Journal.* Biophys J. 2018;115(7):1156-1159. doi:10.1016/j.bpj.2018.08.037

[29] Axelrod D, Koppel DE, Schlessinger J, Elson E, Webb WW. *Mobility measurement by analysis of fluorescence photobleaching recovery kinetics.* Biophys J. 1976;16(9):1055-1069. doi:10.1016/S0006-3495(76)85755-4

[30] Soumpasis DM. Theoretical analysis of fluorescence photobleaching recovery experiments. Biophys J. 1983;41(1):95-97. doi:10.1016/S0006-3495(83)84410-5

[31] Cone RA. Rotational diffusion of rhodopsin in the visual receptor membrane. Nat New Biol. 1972;236(63):39-43. doi:10.1038/newbio236039a0

[32] Poo M, Cone RA. Lateral diffusion of rhodopsin in the visual receptor membrane. J Supramol Struct. 1973;1(4):354. doi:10.1002/jss.400010411

[33] Poo M, Cone RA. Lateral diffusion of rhodopsin in the photoreceptor membrane. Nature. 1974;247(5441):438-441. doi:10.1038/247438a0

[34] Peters R, Peters J, Tews KH, Bähr W. A microfluorimetric study of translational diffusion in erythrocyte membranes. Biochim Biophys Acta. 1974;367(3):282-294. doi:10.1016/0005-2736(74)90085-6

[35] Jacobson K, Derzko Z, Wu ES, Hou Y, Poste G. Measurement of the lateral mobility of cell surface components in single, living cells by fluorescence recovery after photobleaching. J Supramol Struct. 1976;5(4):565(417)-576(428. doi:10.1002/jss.400050411

[36] Edidin M, Zagyansky Y, Lardner TJ. Measurement of membrane protein lateral diffusion in single cells. Science. 1976;191(4226):466-468. doi:10.1126/science.1246629

[37] Koppel DE. *Fluorescence redistribution after photobleaching. A new multipoint analysis of membrane translational dynamics.* Biophys J. 1979;28(2):281-291. doi:10.1016/S0006-3495(79)85176-0

[38] Yguerabide J, Schmidt JA, Yguerabide EE. *Lateral mobility in membranes as detected by fluorescence recovery after photobleaching.* Biophys J. 1982;40(1):69-75. doi:10.1016/S0006-3495(82)84459-7

[39] Kubitscheck U, Wedekind P, Peters R. *Lateral diffusion measurement at high spatial resolution by scanning microphotolysis in a confocal microscope.* Biophys J. 1994;67(3):948-956. doi:10.1016/S0006-3495(94)80596-X

[40] Cutts LS, Robberts PA, Adler J, Davies MC, Melia CD. *Determination of localized diffusion-coefficients in gels using confocal scanning laser microscopy* J Microsc. 1995;180:131-139. doi:10.1111/j.1365-2818.1995.tb03668.x

[41] Seiffert S, Oppermann W. *Systematic evaluation of FRAP experiments performed in a confocal laser scanning microscope.* J Microsc. 2005;220(Pt 1):20-30. doi:10.1111/j.1365-2818.2005.01512.x

[42] Wedekind P, Kubitscheck U, Heinrich O, Peters R. *Line-scanning microphotolysis for diffraction-limited measurements of lateral diffusion.* Biophys J. 1996;71(3):1621-1632. doi:10.1016/S0006-3495(96)79366-9

[43] Blonk JCG, Don A, Van AALST H, Birmingham JJ. *Fluorescence photobleaching recovery in the confocal scanning light microscope* J. Microsc. 1993;169:363-74. doi:10.1111/j.1365-2818.1993.tb03312.x

[44] Loren, N., Hagman, J., Jonasson, J., Deschout, H., Bernin, D., Cella-Zanacchi, F., . . . Braeckmans, K. (2015). Fluorescence recovery after photobleaching in material and life sciences: Putting the-

ory into practice. Quarterly Reviews of Biophysics, 48(3), 323-387. doi:10.1017/S0033583515000013

[45] Weiss M. *Challenges and artifacts in quantitative photobleaching experiments.* Traffic. 2004;5(9):662-671. doi:10.1111/j.1600-0854.2004.00215.x

[46] Braga J, Desterro JM, Carmo-Fonseca M. *Intracellular macromolecular mobility measured by fluorescence recovery after photobleaching with confocal laser scanning microscopes.* Mol Biol Cell. 2004;15(10):4749-4760. doi:10.1091/mbc.e04-06-0496

[47] Pucadyil TJ, Chattopadhyay A. *Confocal fluorescence recovery after photobleaching of green fluorescent protein in solution.* J Fluoresc. 2006;16(1):87-94. doi:10.1007/s10895-005-0019-y

[48] Kang M, Day CA, Drake K, Kenworthy AK, DiBenedetto E. *A generalization of theory for two-dimensional fluorescence recovery after photobleaching applicable to confocal laser scanning microscopes.* Biophys J. 2009;97(5):1501-1511. doi:10.1016/j.bpj.2009.06.017

[49] Jonasson JK, Lorén N, Olofsson P, Nydén M, Rudemo M. *A pixel-based likelihood framework for analysis of fluorescence recovery after photobleaching data.* J Microsc. 2008;232(2):260-269. doi:10.1111/j.1365-2818.2008.02097.x

[50] Kao HP, Abney JR, Verkman AS. *Determinants of the translational mobility of a small solute in cell cytoplasm.* J Cell Biol. 1993;120(1):175-184. doi:10.1083/jcb.120.1.175

[51] Seksek O, Biwersi J, Verkman AS. *Translational diffusion of macromolecule-sized solutes in cytoplasm and nucleus.* J Cell Biol. 1997;138(1):131-142. doi:10.1083/jcb.138.1.131

[52] Lukacs GL, Haggie P, Seksek O, Lechardeur D, Freedman N, Verkman AS. *Size-dependent DNA mobility in cytoplasm and nucleus.* J Biol Chem. 2000;275(3):1625-1629. doi:10.1074/jbc.275.3.1625

[53] Verkman AS. *Diffusion in cells measured by fluorescence recovery after photobleaching.* Methods Enzymol. 2003;360:635-648. doi:10.1016/s0076-6879(03)60132-1

[54] Karpova TS, Chen TY, Sprague BL, McNally JG. *Dynamic interactions of a transcription factor with DNA are accelerated by a chromatin remodeller.* EMBO Rep. 2004;5(11):1064-1070. doi:10.1038/sj.embor.7400281

[55] Sanders NN, De Smedt SC, Demeester J. *The physical properties of biogels and their permeability for macromolecular drugs and colloidal drug carriers.* J Pharm Sci. 2000;89(7):835-849. doi:10.1002/1520-6017(200007)89:7<835::AID-JPS1>3.0.CO;2-6

[56] Olmsted SS, Padgett JL, Yudin AI, Whaley KJ, Moench TR, Cone RA. *Diffusion of macromolecules and virus-like particles in human cervical mucus.* Biophys J. 2001;81(4):1930-1937. doi:10.1016/S0006-3495(01)75844-4

[57] Pluen A, Boucher Y, Ramanujan S, et al. *Role of tumor-host interactions in interstitial diffusion of macromolecules: cranial vs. subcutaneous tumors.* Proc Natl Acad Sci U S A. 2001;98(8):4628-4633. doi:10.1073/pnas.081626898

[58] Ramanujan S, Pluen A, McKee TD, Brown EB, Boucher Y, Jain RK. *Diffusion and convection in collagen gels: implications for transport in the tumor interstitium.* Biophys J. 2002;83(3):1650-1660. doi:10.1016/S0006-3495(02)73933-7

[59] Peeters L, Sanders NN, Braeckmans K, et al. *Vitreous: a barrier to nonviral ocular gene therapy.* Invest Ophthalmol Vis Sci. 2005;46(10):3553-3561. doi:10.1167/iovs.05-0165

[60] Peters R, Kubitscheck U. *Scanning microphotolysis: three-dimensional diffusion measurement and optical single-transporter recording.* Methods. 1999;18(4):508-517. doi:10.1006/meth.1999.0819

[61] Braeckmans K, Peeters L, Sanders NN, De Smedt SC, Demeester J. *Three-dimensional fluorescence recovery after photobleaching with the*

confocal scanning laser microscope. Biophys J. 2003;85(4):2240-2252. doi:10.1016/S0006-3495(03)74649-9

[62] Braeckmans K, Remaut K, Vandenbroucke RE, Lucas B, De Smedt SC, Demeester J. *Line FRAP with the confocal laser scanning microscope for diffusion measurements in small regions of 3-D samples.* Biophys J. 2007;92(6):2172-2183. doi:10.1529/biophysj.106.099838

[63] Mazza D, Braeckmans K, Cella F, et al. *A new FRAP/FRAPa method for three-dimensional diffusion measurements based on multiphoton excitation microscopy.* Biophys J. 2008;95(7):3457-3469. doi:10.1529/biophysj.108.133637

[64] Braeckmans K, Stubbe BG, Remaut K, Demeester J, De Smedt SC. Anomalous photobleaching in fluorescence recovery after photobleaching measurements due to excitation saturation–a case study for fluorescein. J Biomed Opt. 2006;11(4):044013. doi:10.1117/1.2337531

[65] Deschout H, Hagman J, Fransson S, et al. *Straightforward FRAP for quantitative diffusion measurements with a laser scanning microscope.* Opt Express. 2010;18(22):22886-22905. doi:10.1364/OE.18.022886

[66] Smisdom N, Braeckmans K, Deschout H, *et al. Fluorescence recovery after photobleaching on the confocal laser-scanning microscope: generalized model without restriction on the size of the photobleached disk.* J Biomed Opt. 2011;16(4):046021. doi:10.1117/1.3569620

[67] Kubitscheck U, Tschödrich-Rotter M, Wedekind P, Peters R. *Two-photon scanning microphotolysis for three-dimensional data storage and biological transport measurements.* J Microsc. 1996;182(Pt 3):225-233. doi:10.1046/j.1365-2818.1996.60424.x

[68] Brown EB, Wu ES, Zipfel W, Webb WW. *Measurement of molecular diffusion in solution by multiphoton fluorescence photobleaching recovery.* Biophys J. 1999;77(5):2837-2849. doi:10.1016/S0006-3495(99)77115-8

[69] Kaufman EN, Jain RK. *Quantification of transport and binding parameters using fluorescence recovery after photobleaching. Potential for in vivo applications.* Biophys J. 1990;58(4):873-885. doi:10.1016/S0006-3495(90)82432-2

[70] Sprague BL, Pego RL, Stavreva DA, McNally JG. *Analysis of binding reactions by fluorescence recovery after photobleaching.* Biophys J. 2004;86(6):3473-3495. doi:10.1529/biophysj.103.026765

[71] Hinow P, Rogers CE, Barbieri CE, Pietenpol JA, Kenworthy AK, DiBenedetto E. *The DNA binding activity of p53 displays reaction-diffusion kinetics.* Biophys J. 2006;91(1):330-342. doi:10.1529/biophysj.105.078303

[72] Beaudouin J, Mora-Bermúdez F, Klee T, Daigle N, Ellenberg J. *Dissecting the contribution of diffusion and interactions to the mobility of nuclear proteins.* Biophys J. 2006;90(6):1878-1894. doi:10.1529/biophysj.105.071241

[73] Mueller F, Wach P, McNally JG. *Evidence for a common mode of transcription factor interaction with chromatin as revealed by improved quantitative fluorescence recovery after photobleaching.* Biophys J. 2008;94(8):3323-3339. doi:10.1529/biophysj.107.123182

[74] Tsibidis GD. *Quantitative interpretation of binding reactions of rapidly diffusing species using fluorescence recovery after photobleaching.* J Microsc. 2009;233(3):384-390. doi:10.1111/j.1365-2818.2009.03132.x

[75] Braga J, McNally JG, Carmo-Fonseca M. *A reaction-diffusion model to study RNA motion by quantitative fluorescence recovery after photobleaching.* Biophys J. 2007;92(8):2694-2703. doi:10.1529/biophysj.106.096693

[76] Kang M, Day CA, Di Benedetto E, Kenworthy AK. *A quantitative approach to analyze binding diffusion kinetics by confocal FRAP.* Biophys J. 2010;99(9):2737-2747. doi:10.1016/j.bpj.2010.09.013

[77] Berkovich R, Wolfenson H, Eisenberg S, *et al. Accurate quantification of diffusion and binding kinetics of non-integral membrane proteins by FRAP.* Traffic. 2011;12(11):1648-1657. doi:10.1111/j.1600-0854.2011.01264.x

[78] Montero Llopis P, Sliusarenko O, Heinritz J, Jacobs-Wagner C. *In vivo biochemistry in bacterial cells using FRAP: insight into the translation cycle.* Biophys J. 2012;103(9):1848-1859. doi:10.1016/j.bpj.2012.09.035

[79] Kapitza HG, McGregor G, Jacobson KA. *Direct measurement of lateral transport in membranes by using time-resolved spatial photometry.* Proc Natl Acad Sci U S A. 1985;82(12):4122-4126. doi:10.1073/pnas.82.12.4122

[80] Fritzsche M, Charras G. *Dissecting protein reaction dynamics in living cells by fluorescence recovery after photobleaching.* Nat Protoc. 2015;10(5):660-680. doi:10.1038/nprot.2015.042

[81] Calizo RC, Scarlata S. *Discrepancy between fluorescence correlation spectroscopy and fluorescence recovery after photobleaching diffusion measurements of G-protein-coupled receptors.* Anal Biochem. 2013;440(1):40-48. doi:10.1016/j.ab.2013.04.033

[82] Kroschwald S, Maharana S, Mateju D, *et al. Promiscuous interactions and protein disaggregases determine the material state of stress-inducible RNP granules.* Elife. 2015;4:e06807. Published 2015 Aug 4. doi:10.7554/eLife.06807

[83] Molliex A, Temirov J, Lee J, *et al. Phase separation by low complexity domains promotes stress granule assembly and drives pathological fibrillization.* Cell. 2015;163(1):123-133. doi:10.1016/j.cell.2015.09.015

[84] Banani SF, Rice AM, Peeples WB, *et al. Compositional Control of Phase-Separated Cellular Bodies. Cell.* 2016;166(3):651-663. doi:10.1016/j.cell.2016.06.010

[85] Guillén-Boixet J, Buzon V, Salvatella X, Méndez R. *CPEB4 is regulated during cell cycle by ERK2/Cdk1-mediated phosphorylation and its assembly into liquid-like droplets.* Elife. 2016;5:e19298. Published 2016 Nov 1. doi:10.7554/eLife.19298

[86] Jain S, Wheeler JR, Walters RW, Agrawal A, Barsic A, Parker R. *ATPase-Modulated Stress Granules Contain a Diverse Proteome and Substructure.* Cell. 2016;164(3):487-498. doi:10.1016/j.cell.2015.12.038

[87] Feric M, Vaidya N, Harmon TS, *et al. Coexisting Liquid Phases Underlie Nucleolar Subcompartments.* Cell. 2016;165(7):1686-1697. doi:10.1016/j.cell.2016.04.047

[88] Banerjee PR, Milin AN, Moosa MM, Onuchic PL, Deniz AA. *Reentrant Phase Transition Drives Dynamic Substructure Formation in Ribonucleoprotein Droplets.* Angew Chem Int Ed Engl. 2017;56(38):11354-11359. doi:10.1002/anie.201703191

[89] Gupta S, Sutter M, Remesh SG, *et al. X-ray radiolytic labeling reveals the molecular basis of orange carotenoid protein photoprotection and its interactions with fluorescence recovery protein.* J Biol Chem. 2019;294(22):8848-8860. doi:10.1074/jbc.RA119.007592

[90] Taylor NO, Wei MT, Stone HA, Brangwynne CP. *Quantifying Dynamics in Phase-Separated Condensates Using Fluorescence Recovery after Photobleaching.* Biophys J. 2019;117(7):1285-1300. doi:10.1016/j.bpj.2019.08.030

[91] Seabrooke S, Qiu X, Stewart BA. *Nonmuscle Myosin II helps regulate synaptic vesicle mobility at the Drosophila neuromuscular junction.* BMC Neurosci. 2010;11:37. Published 2010 Mar 16. doi:10.1186/1471-2202-11-37

[92] Firmino J, Tinevez JY, Knust E. Crumbs affects protein dynamics in anterior regions of the developing Drosophila embryo. PLoS One. 2013;8(3):e58839. doi:10.1371/journal.pone.0058839

[93] Kisiel M, McKenzie K, Stewart B. *Localization and mobility of synaptic vesicles in Myosin VI mutants of Drosophila.* PLoS One. 2014;9(7):e102988. Published 2014 Jul 25. doi:10.1371/journal.pone.0102988

[94] Sakurai-Yageta M, Maruyama T, Suzuki T, Ichikawa K, Murakami Y. *Dynamic regulation of a cell adhesion protein complex in-*

cluding CADM1 by combinatorial analysis of FRAP with exponential curve-fitting. PLoS One. 2015;10(3):e0116637. Published 2015 Mar 17. doi:10.1371/journal.pone.0116637

[95] Eroshkin FM, Nesterenko AM, Borodulin AV, *et al. Noggin4 is a long-range inhibitor of Wnt8 signalling that regulates head development in Xenopus laevis.* Sci Rep. 2016;6:23049. Published 2016 Mar 14. doi:10.1038/srep23049

[96] McGrath JL, Tardy Y, Dewey CF Jr, Meister JJ, Hartwig JH. *Simultaneous measurements of actin filament turnover, filament fraction, and monomer diffusion in endothelial cells.* Biophys J. 1998;75(4):2070-2078. doi:10.1016/S0006-3495(98)77649-0

[97] Kang M, Andreani M, Kenworthy AK. *Validation of Normalizations, Scaling, and Photofading Corrections for FRAP Data Analysis.* PLoS One. 2015;10(5):e0127966. Published 2015 May 27. doi:10.1371/journal.pone.0127966

[98] Mai J, Trump S, Lehmann I, Attinger S. Parameter importance in FRAP acquisition and analysis: a simulation approach. Biophys J. 2013;104(9):2089-2097. doi:10.1016/j.bpj.2013.03.036

[99] Kingsley JL, Bibeau JP, Mousavi SI, *et al. Characterization of Cell Boundary and Confocal Effects Improves Quantitative FRAP Analysis.* Biophys J. 2018;114(5):1153-1164. doi:10.1016/j.bpj.2018.01.013

[100] Sniekers YH, van Donkelaar CC. Determining diffusion coefficients in inhomogeneous tissues using fluorescence recovery after photobleaching. Biophys J. 2005;89(2):1302-1307. doi:10.1529/biophysj.104.053652

[101] Vinnakota KC, Mitchell DA, Deschenes RJ, Wakatsuki T, Beard DA. Analysis of the diffusion of Ras2 in Saccharomyces cerevisiae using fluorescence recovery after photobleaching. Phys Biol. 2010;7(2):026011. Published 2010 Jun 4. doi:10.1088/1478-3975/7/2/026011

[102] González-Pérez V, Schmierer B, Hill CS, Sear RP. Studying Smad2 intranuclear diffusion dynamics by mathematical modelling of FRAP experiments. Integr Biol (Camb). 2011;3(3):197-207. doi:10.1039/coib00098a

[103] Erdel F, Rippe K. *Quantifying transient binding of ISWI chromatin remodelers in living cells by pixel-wise photobleaching profile evolution analysis.* Proc Natl Acad Sci U S A. 2012;109(47):E3221-E3230. doi:10.1073/pnas.1209579109

[104] Blumenthal D, Goldstien L, Edidin M, Gheber LA. *Universal Approach to FRAP Analysis of Arbitrary Bleaching Patterns. Sci Rep. 2015;5:11655.* Published 2015 Jun 25. doi:10.1038/srep11655

[105] Bläßle A, Soh G, Braun T, et al. Quantitative diffusion measurements using the open-source software PyFRAP. Nat Commun. 2018;9(1):1582. Published 2018 Apr 20. doi:10.1038/s41467-018-03975-6

[106] Moraru II, Schaff JC, Slepchenko BM, et al. Virtual Cell modelling and simulation software environment. IET Syst Biol. 2008;2(5):352-362. doi:10.1049/iet-syb:20080102

[107] Nicolau DV Jr, Hancock JF, Burrage K.

[108] Biophys J. 2007;92(6):1975-1987. doi:10.1529/biophysj.105.076869

[109] Groeneweg FL, van Royen ME, Fenz S, *et al. Quantitation of glucocorticoid receptor DNA-binding dynamics by single-molecule microscopy and FRAP.* PLoS One. 2014;9(3):e90532. Published 2014 Mar 14. doi:10.1371/journal.pone.0090532

[110] Tsay TT, Jacobson KA. *Spatial Fourier analysis of video photobleaching measurements. Principles and optimization.* Biophys J. 1991;60(2):360-368. doi:10.1016/S0006-3495(91)82061-6

[111] Jönsson P, Jonsson MP, Tegenfeldt JO, Höök F. A method improving the accuracy of fluorescence recovery after photobleaching analysis. Biophys J. 2008;95(11):5334-5348. doi:10.1529/biophysj.108.134874

[112] Röding M, Lacroix L, Krona A, Gebäck T, Lorén N. *A Highly Accurate Pixel-Based FRAP Model Based on Spectral-Domain Numerical Methods.* Biophys J. 2019;116(7):1348-1361. doi:10.1016/j.bpj.2019.02.023

[113] Bernadi C, Maday Y. *Handbook of numerical analysis* Volume 5 (1997): pp.209-485

[114] Lin L, Othmer HG. *Improving Parameter Inference from FRAP Data: an Analysis Motivated by Pattern Formation in the Drosophila Wing Disc.* Bull Math Biol. 2017;79(3):448-497. doi:10.1007/s11538-016-0241-6

[115] Jung P, Brown A. *Modeling the slowing of neurofilament transport along the mouse sciatic nerve.* Phys Biol. 2009;6(4):046002. Published 2009 Aug 21. doi:10.1088/1478-3975/6/4/046002

[116] Li Y, Brown A, Jung P. *Deciphering the axonal transport kinetics of neurofilaments using the fluorescence photoactivation pulse-escape method.* Phys Biol. 2014;11(2):026001. doi:10.1088/1478-3975/11/2/026001

[117] Newby JM, Bressloff PC. *Quasi-steady state reduction of molecular motor-based models of directed intermittent search.* Bull Math Biol. 2010;72(7):1840-1866. doi:10.1007/s11538-010-9513-8

[118] Chen J, Lippincott-Schwartz J, Liu J. Intracellular spatial localization regulated by the microtubule network. PLoS One. 2012;7(4):e34919. doi:10.1371/journal.pone.0034919

[119] Ciocanel MV, Kreiling JA, Gagnon JA, Mowry KL, Sandstede B. Analysis of Active Transport by Fluorescence Recovery after Photobleaching. Biophys J. 2017;112(8):1714-1725. doi:10.1016/j.bpj.2017.02.042

[120] Feder TJ, Brust-Mascher I, Slattery JP, Baird B, Webb WW. *Constrained diffusion or immobile fraction on cell surfaces: a new interpretation.* Biophys J. 1996;70(6):2767-2773. doi:10.1016/S0006-3495(96)79846-6

[121] Smith PR, Morrison IE, Wilson KM, Fernández N, Cherry RJ. *Anomalous diffusion of major histocompatibility complex class I molecules on HeLa cells determined by single particle tracking.* Biophys J. 1999;76(6):3331-3344. doi:10.1016/S0006-3495(99)77486-2

[122] Banks DS, Fradin C. *Anomalous diffusion of proteins due to molecular crowding.* Biophys J. 2005;89(5):2960-2971. doi:10.1529/biophysj.104.051078

[123] Saxton MJ. *A biological interpretation of transient anomalous subdiffusion. I. Qualitative model. Biophys J. 2007;92(4):1178-1191.* doi:10.1529/biophysj.106.092619

[124] Wu J, Berland KM. *Propagators and time-dependent diffusion coefficients for anomalous diffusion.* Biophys J. 2008;95(4):2049-2052. doi:10.1529/biophysj.107.121608

[125] Weron A, Burnecki K, Akin EJ, *et al. Ergodicity breaking on the neuronal surface emerges from random switching between diffusive states.* Sci Rep. 2017;7(1):5404. Published 2017 Jul 14. doi:10.1038/s41598-017-05911-y

[126] Saxton MJ. *Anomalous diffusion due to binding: a Monte Carlo study.* Biophys J. 1996;70(3):1250-1262. doi:10.1016/S0006-3495(96)79682-0

[127] Soula H, Caré B, Beslon G, Berry H. *Anomalous versus slowed-down Brownian diffusion in the ligand-binding equilibrium.* Biophys J. 2013;105(9):2064-2073. doi:10.1016/j.bpj.2013.07.023

[128] Berry H, Chaté H. *Anomalous diffusion due to hindering by mobile obstacles undergoing Brownian motion or Orstein-Ulhenbeck processes.* Phys Rev E Stat Nonlin Soft Matter Phys. 2014;89(2):022708. doi:10.1103/PhysRevE.89.022708

[129] McLaughlin S, Murray D. *Plasma membrane phosphoinositide organization by protein electrostatics.* Nature. 2005;438(7068):605-611. doi:10.1038/nature04398

[130] van den Bogaart G, Meyenberg K, Risselada HJ, *et al. Membrane protein sequestering by ionic protein-lipid interactions.* Nature. 2011;479(7374):552-555. Published 2011 Oct 23. doi:10.1038/nature10545

[131] De Clercq B, Cleuren B, Deschout H, Braeckmans K, Ameloot M. *Distinguishing free and anomalous diffusion by rectangular fluorescence recovery after photobleaching: a Monte Carlo study.* J Biomed Opt. 2013;18(7):76012. doi:10.1117/1.JBO.18.7.076012

[132] Lubelski A, Klafter J. *Fluorescence recovery after photobleaching: the case of anomalous diffusion.* Biophys J. 2008;94(12):4646-4653. doi:10.1529/biophysj.107.119081

[133] Saxton MJ. *Anomalous subdiffusion in fluorescence photobleaching recovery: a Monte Carlo study.* Biophys J. 2001;81(4):2226-2240. doi:10.1016/S0006-3495(01)75870-5

[134] Kang M, Day CA, Kenworthy AK, DiBenedetto E. *Simplified equation to extract diffusion coefficients from confocal FRAP data.* Traffic. 2012;13(12):1589-1600. doi:10.1111/tra.12008

[135] Kang M, Day CA, Kenworthy AK. *A novel computational framework for D(t) from Fluorescence Recovery after Photobleaching data reveals various anomalous diffusion types in live cell membranes.* Traffic. 2019;20(11):867-880. doi:10.1111/tra.12690

[136] van Oostveldt P, Bauwens S *Quantitative fluorescence in confocal microscopy. The effect of the detection pinhole aperture on the re[U+2010]absorption and inner filter phenomena.* Journal of Microscopy. 1990;158:121–132. doi: 10.1111/j.1365-2818.1990.tb02985.x

[137] Herman B. *Fluorescence microscopy.* Curr Protoc Immunol. 2002;Chapter 21:. doi:10.1002/0471142735.im2102s48

[138] Henderson JN, Ai HW, Campbell RE, Remington SJ. *Structural basis for reversible photobleaching of a green fluorescent protein homologue.* Proc Natl Acad Sci U S A. 2007;104(16):6672-6677. doi:10.1073/pnas.0700059104

[139] Mueller F, Morisaki T, Mazza D, McNally JG. *Minimizing the impact of photoswitching of fluorescent proteins on FRAP analysis.* Biophys J. 2012;102(7):1656-1665. doi:10.1016/j.bpj.2012.02.029

[140] Costantini LM, Fossati M, Francolini M, Snapp EL. *Assessing the tendency of fluorescent proteins to oligomerize under physiologic conditions.* Traffic. 2012;13(5):643-649. doi:10.1111/j.1600-0854.2012.01336.x

[141] Chudakov DM, Matz MV, Lukyanov S, Lukyanov KA. *Fluorescent proteins and their applications in imaging living cells and tissues.* Physiol Rev. 2010;90(3):1103[U+2010]1163. doi:10.1152/physrev.00038.2009

[142] Gonneau M, Höfte H, Vernhettes S. *Fluorescent tags to explore cell wall structure and dynamics.* Front Plant Sci. 2012;3:145. Published 2012 Jul 3. doi:10.3389/fpls.2012.00145

[143] Bolognesi A., Sliwa-Gonzalez A., Prasad R., Barral Y. (2016) *Fluorescence Recovery After Photo-Bleaching (FRAP) and Fluorescence Loss in Photo-Bleaching (FLIP) Experiments to Study Protein Dynamics During Budding Yeast Cell Division.* In: Sanchez-Diaz A., Perez P. (eds) Yeast Cytokinesis. Methods in Molecular Biology, vol 1369. Humana Press, New York, NY

[144] Snapp EL, Altan N, Lippincott-Schwartz J. Measuring protein mobility by photobleaching GFP chimeras in living cells. Curr Protoc Cell Biol. 2003;Chapter 21:. doi:10.1002/0471143030.cb2101s19

[145] Dundr M, Misteli T. *Measuring dynamics of nuclear proteins by photobleaching.* Curr Protoc Cell Biol. 2003;Chapter 13:. doi:10.1002/0471143030.cb1305s18

[146] Lippincott-Schwartz J, Altan-Bonnet N, Patterson GH. Photobleaching and photoactivation: following protein dynamics in living cells. Nat Cell Biol. 2003;Suppl:S7[U+2010]S14.

[147] Luedeke C, Frei SB, Sbalzarini I, Schwarz H, Spang A, Barral Y. Septin-dependent compartmentalization of the endoplasmic reticulum during yeast polarized growth. J Cell Biol. 2005;169(6):897-908. doi:10.1083/jcb.200412143

[148] Wüstner D, Solanko LM, Lund FW, Sage D, Schroll HJ, Lomholt MA. *Quantitative fluorescence loss in photobleaching for analysis of protein transport and aggregation.* BMC Bioinformatics. 2012;13:296. Published 2012 Nov 13. doi:10.1186/1471-2105-13-296

[149] Ege N, Dowbaj AM, Jiang M, *et al. Quantitative Analysis Reveals that Actin and Src-Family Kinases Regulate Nuclear YAP1 and Its Export.* Cell Syst. 2018;6(6):692-708.e13. doi:10.1016/j.cels.2018.05.006

[150] Guo M, Gelman H, Gruebele M. *Coupled protein diffusion and folding in the cell.* PLoS One. 2014;9(12):e113040. Published 2014 Dec 1. doi:10.1371/journal.pone.0113040

[151] Hansen, C.V., Schroll, H.J. Wüstner, D. Computational modeling of fluorescence loss in photobleaching. Comput. Visual Sci. 17, 151–166 (2015). https://doi.org/10.1007/s00791-015-0259-6

[152] Hansen CV, Schroll HJ, Wüstner D. A Discontinuous Galerkin Model for Fluorescence Loss in Photobleaching. Sci Rep. 2018;8(1):1387. Published 2018 Jan 23. doi:10.1038/s41598-018-19159-7

[153] Xiong R, Vandenbroucke RE, Broos K, *et al. Sizing nanomaterials in biofluids by cFRAP enables protein aggregation measurements and diagnosis of bio-barrier permeability.* Nat Commun. 2016;7:12982. Published 2016 Sep 22. doi:10.1038/ncomms12982

[154] Gordon GW, Chazotte B, Wang XF, Herman B. *Analysis of simulated and experimental fluorescence recovery after photobleaching. Data for two diffusing components.* Biophys J. 1995;68(3):766-778. doi:10.1016/S0006-3495(95)80251-1

[155] Shore J, Johnson R. *Axiomatic derivation of the principle of maximum entropy and the principle of minimum cross-entropy.* IEEE Transactions on Information Theory. 1980;26(1):26-37. doi:10.1109/TIT.1980.1056144

[156] Braeckmans K, Buyens K, Bouquet W, *et al. Sizing nanomatter in biological fluids by fluorescence single particle tracking.* Nano Lett. 2010;10(11):4435-4442. doi:10.1021/nl103264u

[157] White A, Tolman M, Thames HD, Withers HR, Mason KA, Transtrum MK. *The Limitations of Model-Based Experimental Design and Parameter Estimation in Sloppy Systems.* PLoS Comput Biol. 2016;12(12):e1005227. Published 2016 Dec 6. doi:10.1371/journal.pcbi.1005227

[158] Rao CR. (1992) *Information and the Accuracy Attainable in the Estimation of Statistical Parameters.* In: Kotz S, Johnson NL (eds) *Breakthroughs in Statistics.* Springer Series in Statistics (Perspectives in Statistics). Springer, New York, NY. doi:10.1007/978-1-4612-0919-$5_1$6

[159] Akaike H. (1998) *Information Theory and an Extension of the Maximum Likelihood Principle.* In: Parzen E, Tanabe K, Kitagawa G (eds). *Selected Papers of Hirotugu Akaike.* Springer Series in Statistics (Perspectives in Statistics). Springer, New York, NY. doi:10.1007/978-1-4612-1694-$0_1$5

[160] Gutenkunst RN, Waterfall JJ, Casey FP, Brown KS, Myers CR, Sethna JP. *Universally sloppy parameter sensitivities in systems biology models.* PLoS Comput Biol. 2007;3(10):1871-1878. doi:10.1371/journal.pcbi.0030189

[161] Daniels BC, Chen YJ, Sethna JP, Gutenkunst RN, Myers CR. *Sloppiness, robustness, and evolvability in systems biology.* Current opinion in biotechnology. 2008; 19(4):389–395.

[162] Machta BB, Chachra R, Transtrum MK, Sethna JP. *Parameter space compression underlies emergent theories and predictive models.* Science. 2013;342(6158):604-607. doi:10.1126/science.1238723

[163] Transtrum MK, Machta BB, Brown KS, Daniels BC, Myers CR, Sethna JP. *Perspective: Sloppiness and emergent theories in physics, biology, and beyond.* J Chem Phys. 2015;143(1):010901. doi:10.1063/1.4923066

[164] Hanahan D, Weinberg RA. *The hallmarks of cancer.* Cell. 2000;100(1):57-70. doi:10.1016/s0092-8674(00)81683-9

[165] French AS. *Mechanotransduction.* Annu Rev Physiol. 1992;54:135-152. doi:10.1146/annurev.ph.54.030192.001031

[166] Butler GS, Overall CM. *Proteomic identification of multitasking proteins in unexpected locations complicates drug targeting.* Nat Rev Drug Discov. 2009;8(12):935-948. doi:10.1038/nrd2945

[167] Kau TR, Way JC, Silver PA. *Nuclear transport and cancer: from mechanism to intervention.* Nat Rev Cancer. 2004;4(2):106-117. doi:10.1038/nrc1274

[168] Hung MC, Link W. *Protein localization in disease and therapy.* J Cell Sci. 2011;124(Pt 20):3381-3392. doi:10.1242/jcs.089110

[169] Pocaterra A, Romani P, Dupont S. *YAP/TAZ functions and their regulation at a glance.* J Cell Sci. 2020;133(2):jcs230425. Published 2020 Jan 29. doi:10.1242/jcs.230425

[170] Piccolo S, Dupont S, Cordenonsi M. *The biology of YAP/TAZ: hippo signaling and beyond.* Physiol Rev. 2014;94(4):1287-1312. doi:10.1152/physrev.00005.2014

[171] Zhao B, Ye X, Yu J, *et al. TEAD mediates YAP-dependent gene induction and growth control.* Genes Dev. 2008;22(14):1962-1971. doi:10.1101/gad.1664408

[172] Zhao B, Tumaneng K, Guan KL. *The Hippo pathway in organ size control, tissue regeneration and stem cell self-renewal.* Nat Cell Biol. 2011;13(8):877-883. Published 2011 Aug 1. doi:10.1038/ncb2303

[173] Dhanasekaran N, Premkumar Reddy E. *Signaling by dual specificity kinases.* Oncogene. 1998;17(11 Reviews):1447-1455. doi:10.1038/sj.onc.1202251

[174] Zhao B, Lei QY, Guan KL. *The Hippo-YAP pathway: new connections between regulation of organ size and cancer.* Curr Opin Cell Biol. 2008;20(6):638-646. doi:10.1016/j.ceb.2008.10.001

[175] Lei QY, Zhang H, Zhao B, *et al. TAZ promotes cell proliferation and epithelial-mesenchymal transition and is inhibited by the hippo pathway.* Mol Cell Biol. 2008;28(7):2426-2436. doi:10.1128/MCB.01874-07

[176] Liu CY, Zha ZY, Zhou X, *et al. The hippo tumor pathway promotes TAZ degradation by phosphorylating a phosphodegron and recruiting the SCFbeta-TrCP E3 ligase.* J Biol Chem. 2010;285(48):37159-37169. doi:10.1074/jbc.M110.152942

[177] Dupont S, Morsut L, Aragona M, *et al. Role of YAP/TAZ in mechanotransduction.* Nature. 2011;474(7350):179-183. Published 2011 Jun 8. doi:10.1038/nature10137

[178] Scoles DR, Yong WH, Qin Y, Wawrowsky K, Pulst SM. *Schwannomin inhibits tumorigenesis through direct interaction with the eukaryotic initiation factor subunit c (eIF3c).* Hum Mol Genet. 2006;15(7):1059-1070. doi:10.1093/hmg/ddl021

[179] Yi C, Troutman S, Fera D, *et al. A tight junction-associated Merlin-angiomotin complex mediates Merlin's regulation of mitogenic signaling and tumor suppressive functions.* Cancer Cell. 2011;19(4):527-540. doi:10.1016/j.ccr.2011.02.017

[180] Yin F, Yu J, Zheng Y, Chen Q, Zhang N, Pan D. *Spatial organization of Hippo signaling at the plasma membrane mediated by the tumor suppressor Merlin/NF2.* Cell. 2013;154(6):1342-1355. doi:10.1016/j.cell.2013.08.025

[181] Furukawa KT, Yamashita K, Sakurai N, Ohno S. *The Epithelial Circumferential Actin Belt Regulates YAP/TAZ through Nucleocytoplasmic Shuttling of Merlin.* Cell Rep. 2017;20(6):1435-1447. doi:10.1016/j.celrep.2017.07.032

[182] Gumbiner BM, Kim NG. *The Hippo-YAP signaling pathway and contact inhibition of growth.* J Cell Sci. 2014;127(Pt 4):709-717. doi:10.1242/jcs.140103

[183] Humphrey JD, Dufresne ER, Schwartz MA. *Mechanotransduction and extracellular matrix homeostasis.* Nat Rev Mol Cell Biol. 2014;15(12):802-812. doi:10.1038/nrm3896

[184] Hao J, Zhang Y, Wang Y, *et al. Role of extracellular matrix and YAP/TAZ in cell fate determination. Cell Signal.* 2014;26(2):186-191. doi:10.1016/j.cellsig.2013.11.006

[185] Elbediwy A, Vanyai H, Diaz-de-la-Loza MD, Frith D, Snijders AP, Thompson BJ. *Enigma proteins regulate YAP mechanotransduction.* J Cell Sci. 2018;131(22):jcs221788. Published 2018 Nov 22. doi:10.1242/jcs.221788

[186] Hsu PC, Yang CT, Jablons DM, You L. The Crosstalk between Src and Hippo/YAP Signaling Pathways in Non-Small Cell Lung Cancer (NSCLC). Cancers (Basel). 2020;12(6):1361. Published 2020 May 26. doi:10.3390/cancers12061361

[187] Halder G, Dupont S, Piccolo S. *Transduction of mechanical and cytoskeletal cues by YAP and TAZ.* Nat Rev Mol Cell Biol. 2012;13(9):591-600. doi:10.1038/nrm3416

[188] Grinnell F. *Fibroblast biology in three-dimensional collagen matrices.* Trends Cell Biol. 2003;13(5):264-269. doi:10.1016/s0962-8924(03)00057-6

[189] Maller O, DuFort CC, Weaver VM. *YAP forces fibroblasts to feel the tension.* Nat Cell Biol. 2013;15(6):570-572. doi:10.1038/ncb2777

[190] Peters JM, Franke WW, Kleinschmidt JA. *Distinct 19 S and 20 S subcomplexes of the 26 S proteasome and their distribution in the nucleus and the cytoplasm.* J Biol Chem. 1994;269(10):7709-7718.

[191] Carragher NO, Frame MC. *Focal adhesion and actin dynamics: a place where kinases and proteases meet to promote invasion.* Trends Cell Biol. 2004;14(5):241-249. doi:10.1016/j.tcb.2004.03.011

[192] Marfori M, Mynott A, Ellis JJ, *et al. Molecular basis for specificity of nuclear import and prediction of nuclear localization.* Biochim Biophys Acta. 2011;1813(9):1562-1577. doi:10.1016/j.bbamcr.2010.10.013

[193] Sudol M. Yes-associated protein (YAP65) is a proline-rich phosphoprotein that binds to the SH3 domain of the Yes proto-oncogene product. Oncogene. 1994;9(8):2145-2152.

[194] Silvis MR, Kreger BT, Lien WH, *et al. α-catenin is a tumor suppressor that controls cell accumulation by regulating the localization and activity of the transcriptional coactivator Yap1.* Sci Signal. 2011;4(174):ra33. Published 2011 May 24. doi:10.1126/scisignal.2001823

[195] Santucci M, Vignudelli T, Ferrari S, *et al. The Hippo Pathway and YAP/TAZ-TEAD Protein-Protein Interaction as Targets for Regenerative Medicine and Cancer Treatment.* J Med Chem. 2015;58(12):4857-4873. doi:10.1021/jm501615v

[196] Zhao B, Wei X, Li W, *et al. Inactivation of YAP oncoprotein by the Hippo pathway is involved in cell contact inhibition and tissue growth control.* Genes Dev. 2007;21(21):2747-2761. doi:10.1101/gad.1602907

[197] Ota M, Sasaki H. *Mammalian Tead proteins regulate cell proliferation and contact inhibition as transcriptional mediators of Hippo signaling.* Development. 2008;135(24):4059-4069. doi:10.1242/dev.027151

[198] Azzolin L, Panciera T, Soligo S, *et al. YAP/TAZ incorporation in the β-catenin destruction complex orchestrates the Wnt response.* Cell. 2014;158(1):157-170. doi:10.1016/j.cell.2014.06.013

[199] Varelas X, Miller BW, Sopko R, *et al. The Hippo pathway regulates Wnt/beta-catenin signaling.* Dev Cell. 2010;18(4):579-591. doi:10.1016/j.devcel.2010.03.007

[200] Camargo FD, Gokhale S, Johnnidis JB, *et al. YAP1 increases organ size and expands undifferentiated progenitor cells* [published correction appears in Curr Biol. 2007 Dec 4;17(23):2094]. Curr Biol. 2007;17(23):2054-2060. doi:10.1016/j.cub.2007.10.039

[201] Astone M, Lai JKH, Dupont S, Stainier DYR, Argenton F, Vettori A. *Zebrafish mutants and TEAD reporters reveal essential functions for Yap and Taz in posterior cardinal vein development.* Sci Rep. 2018;8(1):10189. Published 2018 Jul 5. doi:10.1038/s41598-018-27657-x

[202] Kim J, Kim YH, Kim J, *et al. YAP/TAZ regulates sprouting angiogenesis and vascular barrier maturation.* J Clin Invest. 2017;127(9):3441-3461. doi:10.1172/JCI93825

[203] Wang X, Freire Valls A, Schermann G, et al. YAP/TAZ Orchestrate VEGF Signaling during Developmental Angiogenesis. Dev Cell. 2017;42(5):462-478.e7. doi:10.1016/j.devcel.2017.08.002

[204] Wang J, Liu S, Heallen T, Martin JF. The Hippo pathway in the heart: pivotal roles in development, disease, and regeneration. Nat Rev Cardiol. 2018;15(11):672-684. doi:10.1038/s41569-018-0063-3 Crawford2018 Crawford JJ, Bronner SM, Zbieg JR. Hippo pathway inhibition by blocking the YAP/TAZ-TEAD interface: a patent review. Expert Opin Ther Pat. 2018;28(12):867-873. doi:10.1080/13543776.2018.1549226

[205] Croci O, De Fazio S, Biagioni F, *et al. Transcriptional integration of mitogenic and mechanical signals by Myc and YAP.* Genes Dev. 2017;31(20):2017-2022. doi:10.1101/gad.301184.117

[206] Galli GG, Carrara M, Yuan WC, *et al. YAP Drives Growth by Controlling Transcriptional Pause Release from Dynamic Enhancers.* Mol Cell. 2015;60(2):328-337. doi:10.1016/j.molcel.2015.09.001

[207] Stein C, Bardet AF, Roma G, *et al. YAP1 Exerts Its Transcriptional Control via TEAD-Mediated Activation of Enhancers.* PLoS Genet. 2015;11(8):e1005465. Published 2015 Aug 21. doi:10.1371/journal.pgen.1005465

[208] Liu X, Li H, Rajurkar M, *et al. Tead and AP1 Coordinate Transcription and Motility.* Cell Rep. 2016;14(5):1169-1180. doi:10.1016/j.celrep.2015.12.104

[209] Zheng Y, Pan D. *The Hippo Signaling Pathway in Development and Disease.* Dev Cell. 2019;50(3):264-282. doi:10.1016/j.devcel.2019.06.003

[210] Schlegelmilch K, Mohseni M, Kirak O, *et al. Yap1 acts downstream of α-catenin to control epidermal proliferation.* Cell. 2011;144(5):782-795. doi:10.1016/j.cell.2011.02.031

[211] Kwan J, Sczaniecka A, Heidary Arash E, *et al. DLG5 connects cell polarity and Hippo signaling protein networks by linking PAR-1 with MST1/2.* Genes Dev. 2016;30(24):2696-2709. doi:10.1101/gad.284539.116

[212] Li P, Silvis MR, Honaker Y, Lien WH, Arron ST, Vasioukhin V. *E-catenin inhibits a Src-YAP1 oncogenic module that couples tyrosine kinases and the effector of Hippo signaling pathway.* Genes Dev. 2016;30(7):798-811. doi:10.1101/gad.274951.115

[213] Szymaniak AD, Mahoney JE, Cardoso WV, Varelas X. *Crumbs3-Mediated Polarity Directs Airway Epithelial Cell Fate through the Hippo Pathway Effector Yap.* Dev Cell. 2015;34(3):283-296. doi:10.1016/j.devcel.2015.06.020

[214] Benham-Pyle BW, Pruitt BL, Nelson WJ. *Cell adhesion. Mechanical strain induces E-cadherin-dependent Yap1 and β-catenin activation to drive cell cycle entry.* Science. 2015;348(6238):1024-1027. doi:10.1126/science.aaa4559

[215] Cordenonsi M, Zanconato F, Azzolin L, et al. The Hippo transducer TAZ confers cancer stem cell-related traits on breast cancer cells. Cell. 2011;147(4):759-772. doi:10.1016/j.cell.2011.09.048

[216] Hirata H, Samsonov M, Sokabe M. *Actomyosin contractility provokes contact inhibition in E-cadherin-ligated keratinocytes.* Sci Rep. 2017;7:46326. Published 2017 Apr 13. doi:10.1038/srep46326

[217] Choi HJ, Zhang H, Park H, *et al. Yes-associated protein regulates endothelial cell contact-mediated expression of angiopoietin-2.* Nat Commun. 2015;6:6943. Published 2015 May 12. doi:10.1038/ncomms7943

[218] Herr KJ, Tsang YH, Ong JW, *et al. Loss of α-catenin elicits a cholestatic response and impairs liver regeneration.* Sci Rep. 2014;4:6835. Published 2014 Oct 30. doi:10.1038/srep06835

[219] Bertocchi C, Wang Y, Ravasio A, et al. Nanoscale architecture of cadherin-based cell adhesions. Nat Cell Biol. 2017;19(1):28-37. doi:10.1038/ncb3456

[220] Mege RM, Ishiyama N. *Integration of Cadherin Adhesion and Cytoskeleton at Adherens Junctions.* Cold Spring Harb Perspect Biol. 2017;9(5):a028738. Published 2017 May 1. doi:10.1101/cshperspect.a028738

[221] Gladden AB, Hebert AM, Schneeberger EE, McClatchey AI. *The NF2 tumor suppressor, Merlin, regulates epidermal development through the establishment of a junctional polarity complex.* Dev Cell. 2010;19(5):727-739. doi:10.1016/j.devcel.2010.10.008

[222] Yonemura S, Wada Y, Watanabe T, Nagafuchi A, Shibata M. alpha-Catenin as a tension transducer that induces adherens junction development. Nat Cell Biol. 2010;12(6):533-542. doi:10.1038/ncb2055

[223] Yao M, Qiu W, Liu R, *et al. Force-dependent conformational switch of -catenin controls vinculin binding* [published correction appears in Nat Commun. 2015;6:6568]. Nat Commun. 2014;5:4525. Published 2014 Jul 31. doi:10.1038/ncomms5525

[224] Chicurel ME, Singer RH, Meyer CJ, Ingber DE. *Integrin binding and mechanical tension induce movement of mRNA and ribosomes to focal adhesions.* Nature. 1998;392(6677):730-733. doi:10.1038/33719

[225] Wozniak MA, Modzelewska K, Kwong L, Keely PJ. *Focal adhesion regulation of cell behavior.* Biochim Biophys Acta. 2004;1692(2-3):103-119. doi:10.1016/j.bbamcr.2004.04.007

[226] Fenner J, Stacer AC, Winterroth F, Johnson TD, Luker KE, Luker GD. *Macroscopic stiffness of breast tumors predicts metastasis.* Sci Rep. 2014;4:5512. Published 2014 Jul 1. doi:10.1038/srep05512

[227] Mouw JK, Yui Y, Damiano L, *et al. Tissue mechanics modulate microRNA-dependent PTEN expression to regulate malignant progression.* Nat Med. 2014;20(4):360-367. doi:10.1038/nm.3497

[228] Katsumi A, Orr AW, Tzima E, Schwartz MA. *Integrins in mechanotransduction.* J Biol Chem. 2004;279(13):12001-12004. doi:10.1074/jbc.R300038200

[229] Vogel V, Sheetz M. *Local force and geometry sensing regulate cell functions.* Nat Rev Mol Cell Biol. 2006;7(4):265-275. doi:10.1038/nrm1890

[230] Plotnikov SV, Pasapera AM, Sabass B, Waterman CM. *Force fluctuations within focal adhesions mediate ECM-rigidity sensing to guide directed cell migration.* Cell. 2012;151(7):1513-1527. doi:10.1016/j.cell.2012.11.034

[231] Burridge K, Guilluy C. *Focal adhesions, stress fibers and mechanical tension.* Exp Cell Res. 2016;343(1):14-20. doi:10.1016/j.yexcr.2015.10.029

[232] Burridge K, Chrzanowska-Wodnicka M. *Focal adhesions, contractility, and signaling.* Annu Rev Cell Dev Biol. 1996;12:463-518. doi:10.1146/annurev.cellbio.12.1.463

[233] Kim S, Coulombe PA. *Emerging role for the cytoskeleton as an organizer and regulator of translation.* Nat Rev Mol Cell Biol. 2010;11(1):75-81. doi:10.1038/nrm2818

[234] Schwartz MA. *Integrins and extracellular matrix in mechanotransduction.* Cold Spring Harb Perspect Biol. 2010;2(12):a005066. doi:10.1101/cshperspect.a005066

[235] Jaalouk DE, Lammerding J. *Mechanotransduction gone awry.* Nat Rev Mol Cell Biol. 2009;10(1):63-73. doi:10.1038/nrm2597

[236] Mammoto A, Ingber DE. *Cytoskeletal control of growth and cell fate switching.* Curr Opin Cell Biol. 2009;21(6):864-870. doi:10.1016/j.ceb.2009.08.001

[237] Wozniak MA, Chen CS. *Mechanotransduction in development: a growing role for contractility.* Nat Rev Mol Cell Biol. 2009;10(1):34-43. doi:10.1038/nrm2592

[238] Wada K, Itoga K, Okano T, Yonemura S, Sasaki H. *Hippo pathway regulation by cell morphology and stress fibers.* Development. 2011;138(18):3907-3914. doi:10.1242/dev.070987

[239] Mo JS, Yu FX, Gong R, Brown JH, Guan KL. *Regulation of the Hippo-YAP pathway by protease-activated receptors (PARs).* Genes Dev. 2012;26(19):2138-2143. doi:10.1101/gad.197582.112

[240] Kim NG, Gumbiner BM. Adhesion to fibronectin regulates Hippo signaling via the FAK-Src-PI3K pathway. J Cell Biol. 2015;210(3):503-515. doi:10.1083/jcb.201501025

[241] Sansores-Garcia L, Bossuyt W, Wada K, *et al. Modulating F-actin organization induces organ growth by affecting the Hippo pathway.* EMBO J. 2011;30(12):2325-2335. Published 2011 May 10. doi:10.1038/emboj.2011.157

[242] Janmey PA, Fletcher DA, Reinhart-King CA. *Stiffness Sensing by Cells.* Physiol Rev. 2020;100(2):695-724. doi:10.1152/physrev.00013.2019

[243] McBeath R, Pirone DM, Nelson CM, Bhadriraju K, Chen CS. *Cell shape, cytoskeletal tension, and RhoA regulate stem cell lineage commitment.* Dev Cell. 2004;6(4):483-495. doi:10.1016/s1534-5807(04)00075-9

[244] Puliafito A, Hufnagel L, Neveu P, *et al. Collective and single cell behavior in epithelial contact inhibition.* Proc Natl Acad Sci U S A. 2012;109(3):739-744. doi:10.1073/pnas.1007809109

[245] Streichan SJ, Hoerner CR, Schneidt T, Holzer D, Hufnagel L. Spatial constraints control cell proliferation in tissues. Proc Natl Acad Sci U S A. 2014;111(15):5586-5591. doi:10.1073/pnas.1323016111

[246] Shiu JY, Aires L, Lin Z, Vogel V. *Nanopillar force measurements reveal actin-cap-mediated YAP mechanotransduction.* Nat Cell Biol. 2018;20(3):262-271. doi:10.1038/s41556-017-0030-y

[247] Elosegui-Artola A, Andreu I, Beedle AEM, *et al. Force Triggers YAP Nuclear Entry by Regulating Transport across Nuclear Pores.* Cell. 2017;171(6):1397-1410.e14. doi:10.1016/j.cell.2017.10.008

[248] Gill MK, Christova T, Zhang YY, *et al. A feed forward loop enforces YAP/TAZ signaling during tumorigenesis.* Nat Commun. 2018;9(1):3510. Published 2018 Aug 29. doi:10.1038/s41467-018-05939-2

[249] Moroishi T, Park HW, Qin B, *et al. A YAP/TAZ-induced feedback mechanism regulates Hippo pathway homeostasis.* Genes Dev. 2015;29(12):1271-1284. doi:10.1101/gad.262816.115

[250] Yuan WC, Pepe-Mooney B, Galli GG, *et al. NUAK2 is a critical YAP target in liver cancer.* Nat Commun. 2018;9(1):4834. Published 2018 Nov 16. doi:10.1038/s41467-018-07394-5

[251] Nardone G, Oliver-De La Cruz J, Vrbsky J, *et al. YAP regulates cell mechanics by controlling focal adhesion assembly.* Nat Commun. 2017;8:15321. Published 2017 May 15. doi:10.1038/ncomms15321

[252] Porazinski S, Wang H, Asaoka Y, *et al. YAP is essential for tissue tension to ensure vertebrate 3D body shape.* Nature. 2015;521(7551):217-221. doi:10.1038/nature14215

[253] Qiao Y, Chen J, Lim YB, *et al. YAP Regulates Actin Dynamics through ARHGAP29 and Promotes Metastasis.* Cell Rep. 2017;19(8):1495-1502. doi:10.1016/j.celrep.2017.04.075

[254] Clevers H. *Wnt/beta-catenin signaling in development and disease.* Cell. 2006;127(3):469-480. doi:10.1016/j.cell.2006.10.018

[255] Niehrs C, Acebron SP. *Mitotic and mitogenic Wnt signalling.* EMBO J. 2012;31(12):2705-2713. doi:10.1038/emboj.2012.124

[256] Scherz-Shouval R, Santagata S, Mendillo ML, *et al. The reprogramming of tumor stroma by HSF1 is a potent enabler of malignancy.* Cell. 2014;158(3):564-578. doi:10.1016/j.cell.2014.05.045

[257] Salamanca HH, Antonyak MA, Cerione RA, Shi H, Lis JT. Inhibiting heat shock factor 1 in human cancer cells with a potent RNA aptamer. PLoS One. 2014;9(5):e96330. Published 2014 May 6. doi:10.1371/journal.pone.0096330

[258] Ferrari N, Ranftl R, Chicherova I, *et al. Dickkopf-3 links HSF1 and YAP/TAZ signalling to control aggressive behaviours in cancer-associated fibroblasts.* Nat Commun. 2019;10(1):130. Published 2019 Jan 10. doi:10.1038/s41467-018-07987-0

[259] Levental KR, Yu H, Kass L, *et al. Matrix crosslinking forces tumor progression by enhancing integrin signaling.* Cell. 2009;139(5):891-906. doi:10.1016/j.cell.2009.10.027

[260] Liu F, Mih JD, Shea BS, *et al. Feedback amplification of fibrosis through matrix stiffening and COX-2 suppression.* J Cell Biol. 2010;190(4):693-706. doi:10.1083/jcb.201004082

[261] Marinkovic A, Mih JD, Park JA, Liu F, Tschumperlin DJ. *Improved throughput traction microscopy reveals pivotal role for matrix stiffness in fibroblast contractility and TGF-β responsiveness.* Am J Physiol Lung Cell Mol Physiol. 2012;303(3):L169-L180. doi:10.1152/ajplung.00108.2012

[262] Liu F, Lagares D, Choi KM, *et al. Mechanosignaling through YAP and TAZ drives fibroblast activation and fibrosis.* Am J Physiol Lung Cell Mol Physiol. 2015;308(4):L344-L357. doi:10.1152/ajplung.00300.2014

[263] Liu F, Lagares D, Choi KM, *et al. Mechanosignaling through YAP and TAZ drives fibroblast activation and fibrosis.* Am J Physiol Lung Cell Mol Physiol. 2015;308(4):L344-L357. doi:10.1152/ajplung.00300.2014

[264] Murray JD. *Mathematical Biology II: Spatial Models and Biomedical Applications*, Third Edition, 2004, pp. 548.

[265] Gradshteyn IS, Ryzhik IM, *Table of Integrals, Series, and Products*, Fifth edition, 1994, pp. 739, 6.633

[266] Abramowitz M, Stegun IA, *Handbook of Mathematical Functions with Formulas, Graphs, and Mathematical Tables*, Tenth printing, 1972, pp. 484, 11.3.20

[267] *Ibid.* pp. 377, 9.7.1

[268] *Ibid.* pp. 376, 9.6.16

[269] *Ibid.* pp. 484, 11.3.14

[270] Bulinski JC, Odde DJ, Howell BJ, Salmon TD, Waterman-Storer CM. *Rapid dynamics of the microtubule binding of ensconsin in vivo.* J Cell Sci. 2001 Nov; 114(Pt 21): 3885-97.

[271] Dundr M, Hoffmann-Rohrer U, Hu Q, Grummt I, Rothblum LI, Phair RD, Misteli T. *A kinetic framework for a mammalian RNA polymerase in vivo.* Science. 2002 Nov 22; 298(5598): 1623-6.

[272] Phair RD, Scaffidi P, Elbi C, Vecerová J, Dey A, Ozato K, Brown DT, Hager G, Bustin M, Misteli T. *Global nature of dynamic protein-chromatin interactions in vivo: three-dimensional genome scanning and dynamic interaction networks of chromatin proteins.* Mol Cell Biol. 2004 Jul; 24(14):6393-402.,

[273] Rabut G, Doye V, Ellenberg J. *Mapping the dynamic organization of the nuclear pore complex inside single living cells.* Nat Cell Biol. 2004 Nov; 6(11): 1114-21.

[274] Crank, J. 1975. *The Mathematics of Diffusion.* Oxford University Press, New York. 326-51.

[275] Orlova DY, Bártová E, Maltsev VP, Kozubek S, Chernyshev AV. *A nonfitting method using a spatial sine window transform for inhomogeneous effective-diffusion measurements by FRAP.* Biophys J. 2011 Jan 19; 100(2): 507-16.

[276] van Royen ME, Farla P, Mattern KA, Geverts B, Trapman J, Houtsmuller AB. *Fluorescence recovery after photobleaching (FRAP) to study nuclear protein dynamics in living cells.* Methods Mol Biol. 2009; 464: 363-85.

[277] Phair RD, Misteli T. *High mobility of proteins in the mammalian cell nucleus.* Nature. 2000 Apr 6; 404(6778): 604-9.

[278] Nelder JA, Mead R. *A Simplex Method for Function Minimization.* Comput J. 1965 Jan; 7(4): 308-313.

[279] Olsson DM, Nelson LS. *The Nelder-Mead Simplex Procedure for Function Minimization.* Technometrics 1975; 17(1): 45-51.

[280] Schnell EA, Eikenes L, Tufto I, Erikson A, Juthajan A, Lindgren M, de Lange Davies C. *Diffusion measured by fluorescence recovery after photobleaching based on multiphoton excitation laser scanning microscopy.* J Biomed Opt. 2008 Nov-Dec; 13(6): 064037.

[281] Sun ZW, Allis CD *Ubiquitination of histone H2B regulates H3 methylation and gene silencing in yeast.* Nature. 2002 Jul 4;418(6893):104-8. Epub 2002 Jun 23.

[282] Phair RD, Scaffidi P, Elbi C, Vecerová J, Dey A, Ozato K, Brown DT, Hager G, Bustin M, Misteli T. *Global nature of dynamic protein-chromatin interactions in vivo: three-dimensional genome scanning and dynamic interaction networks of chromatin proteins.* Mol Cell Biol. 2004 Jul; 24(14):6393-402.

[283] Nakagawa S, Cuthill IC. *Effect size, confidence interval and statistical significance: a practical guide for biologists.* Biol Rev Camb Philos Soc. 2007 Nov; 82(4): 591-605.

[284] Lee DK. *Alternatives to P value: confidence interval and effect size.* Korean J Anesthesiol. 2016 Dec; 69(6): 555-562.

[285] Sawilowsky SS. *New Effect Size Rules of Thumb.* J Mod Appl Stat Methods. 2009 Nov; 8(2), 597 – 599.

[286] Wedekind P, Kubitscheck U, Peters R. *Scanning microphotolysis: a new photobleaching technique based on fast intensity modulation of a scanned laser beam and confocal imaging.* J Microsc. 1994 Oct;176(Pt 1):23-33.

[287] Raska I, Shaw PJ, Cmarko D. *Structure and function of the nucleolus in the spotlight.* Curr Opin Cell Biol. 2006 Jun;18(3):325-34.

[288] Zhao B, Ye X, Yu J, Li L, Li W, Li S, Yu J, Lin JD, Wang CY, Chinnaiyan AM, Lai ZC, Guan KL. *TEAD mediates YAP-dependent gene induction and growth control.* Genes Dev. 2008 Jul 15;22(14):1962-71.

[289] Hansen CG, Ng YL, Lam WL, Plouffe SW, Guan KL. *The Hippo pathway effectors YAP and TAZ promote cell growth by modulating amino acid signaling to mTORC1.* Cell Res. 2015 Dec;25(12):1299-313.

[290] Moroishi T, Hansen CG, Guan KL. *The emerging roles of YAP and TAZ in cancer.* Nat Rev Cancer. 2015 Feb;15(2):73-79.

[291] Zhou Y, Huang T, Cheng AS, Yu J, Kang W1, To KF. *The TEAD Family and Its Oncogenic Role in Promoting Tumorigenesis.* Int J Mol Sci. 2016 Jan 21;17(1).

[292] Lee Y, Kim NH, Cho ES, Yang JH, Cha YH, Kang HE, Yun JS, Cho SB, Lee SH, Paclikova P, Radaszkiewicz TW, Bryja V, Kang CG, Yuk YS, Cha SY, Kim SY, Kim HS, Yook JI. *Dishevelled has a YAP nuclear export function in a tumor suppressor context-dependent manner.* Nat Commun. 2018 Jun 12;9(1):2301.

[293] Shreberk-Shaked M, Oren M. *New insights into YAP/TAZ nucleo-cytoplasmic shuttling: new cancer therapeutic opportunities?* Mol Oncol. 2019 Jun;13(6):1335-1341.

[294] Xia Y, Chang T, Wang Y, Liu Y, Li W, Li M, Fan HY. *YAP promotes ovarian cancer cell tumorigenesis and is indicative of a poor prognosis for ovarian cancer patients.* PLoS One. 2014 Mar 12;9(3):e91770.

[295] Kim M, Kim 2, Johnson RL, Lim DS. *Transcriptional co-repressor function of the hippo pathway transducers YAP and TAZ.* Cell Rep. 2015 Apr 14;11(2):270-82.

[296] Han D, Byun SH, Park S, Kim J, Kim I, Ha S, Kwon M, Yoon K. *YAP/TAZ enhance mammalian embryonic neural stem cell characteristics in a Tead-dependent manner.* Biochem Biophys Res Commun. 2015 Feb 27;458(1):110-6.

[297] Zhang G, Gurtu V, Kain SR. *An enhanced green fluorescent protein allows sensitive detection of gene transfer in mammalian cells.* Biochem Biophys Res Commun. 1996 Oct 23;227(3):707-11.

[298] Cooper GM. The Cell: A Molecular Approach. 2nd edition. Sunderland (MA): Sinauer Associates; 2000. The Nuclear Envelope and Traffic between the Nucleus and Cytoplasm. Available from: https://www.ncbi.nlm.nih.gov/books/NBK9927/

[299] Wente SR, Rout MP. *The nuclear pore complex and nuclear transport.* Cold Spring Harb Perspect Biol. 2010;2(10):a000562. doi:10.1101/cshperspect.a000562

[300] Freeman AK, Morrison DK. 14-3-3 Proteins: diverse functions in cell proliferation and cancer progression. Semin Cell Dev Biol. 2011;22(7):681[U+2010]687. doi:10.1016/j.semcdb.2011.08.009

[301] Moon S, Kim W, Kim S, et al. Phosphorylation by NLK inhibits YAP-14-3-3-interactions and induces its nuclear localization. EMBO Rep. 2017;18(1):61[U+2010]71. doi:10.15252/embr.201642683

[302] Dobrokhotov O, Samsonov M, Sokabe M, Hirata H. *Mechanoregulation and pathology of YAP/TAZ via Hippo and non-Hippo mechanisms.* Clin Transl Med. 2018;7(1):23. Published 2018 Aug 13. doi:10.1186/s40169-018-0202-9

[303] Webster M, Witkin KL, Cohen-Fix O. *Sizing up the nucleus: nuclear shape, size and nuclear-envelope assembly.* J Cell Sci. 2009;122(Pt 10):1477[U+2010]1486. doi:10.1242/jcs.037333

[304] D. Engwirda D. *Locally-optimal Delaunay-refinement and optimisation-based mesh generation.* Ph.D. Thesis, School of Mathematics and Statistics, The University of Sydney, http://hdl.handle.net/2123/13148, 2014.

[305] Dowbaj AM, Jenkins RP, Hahn K, Montagner M, Sahai E. emphAn optogenetic method for interrogating YAP1 and TAZ nuclear-cytoplasmic shuttling. Anna M. Dowbaj, Robert P. Jenkins, Klaus Hahn, Marco Montagner, Erik Sahai bioRxiv 2020.06.08.140228; doi: https://doi.org/10.1101/2020.06.08.140228